IN-CYLINDER FLOW AND COMBUSTION STUDIES IN AN AIR-ASSISTED DIRECT INJECTION GASOLINE ENGINE

A thesis submitted for the degree of Doctor of Philosophy

by

Ben Thomas Leach

Department of Mechanical Engineering
Brunel University
United Kingdom

August 2004

Contents

Page Number

Brunel University
Department of Mechanical Engineering
United Kingdom

Ben Thomas Leach

In-cylinder flow and combustion studies in an air-assisted direct injection gasoline engine

July 2004, PhD

Abstract

In-cylinder flows and CAI combustion were investigated in a single cylinder, air-assisted gasoline direct injection engine. CAI was promoted and controlled by internal exhaust gas recirculation, achieved by employing short duration camshafts and early exhaust valve closure. The effects of valve and injection timing and engine speed on exhaust emissions, fuel consumption, combustion phasing and operating region were investigated.

The results show that valve timing mainly affects engine load and CAI combustion phasing through changes in trapped residual levels and stratification of fresh and residual gases respectively. Injection of fuel into residual gases during the recompression process was found to increase the operating region and reduce uHC emissions though charge cooling effects and increased fuel ignitability via internal fuel reformation. The increased ignitability of the mixture also advanced ignition timing, resulting in increased in-cylinder temperatures and NO_x concentrations. It was found that, compared to SI combustion in the same engine, CAI operation reduced NO_x emissions by between 98% and 80% while fuel consumption was reduced by between 9% and 17%.

The in-cylinder flows of intake air and fuel droplets from the air-assisted injection system and cylinder head were investigated using the PIV technique. No significant large-scale flow structures were found in the in-cylinder airflow and the fuel spray appeared unaffected by the in-cylinder air motion.

In addition, the in-cylinder fuel distribution from the air-assisted injection system was measured using laser induced exiplex fluorescence. A combination of naphthalene and DMA in isooctane were used to form an exiplex and simultaneous qualitative images of the liquid and vapour fuel phases were obtained. When using a late injection strategy, a well stratified mixture was formed at the end of the compression stroke, while injection during the intake stroke left a well mixed homogenous charge.

Acknowledgements

First of all I would like to express sincere gratitude to my supervisor, Professor Hua Zhao for his help and guidance through this project. I must also thank him for giving me opportunity to attend and present some of this work at several international conferences, which has improved my confidence, allowed me to greatly deepen my knowledge and make valuable contacts within the industry.

Secondly, I would like to give my deepest thanks to my colleague Dr Yufeng Li for the large amount of help and support has provided me both in and out of the lab.

Equally important to the success of this work has been the support of the various members of staff who run and maintain the laboratory facilities. Mr Bob Webb has been invaluable in this respect and, along with Mr John Langdon, have always ensured the supply of the various materials, products and services as required. I must also express sincere thanks to Mr Clive Barratt for designing and building the various electronic control and driver systems that were central to the completion of this work and also for his assistance in trouble shooting other electronic problems encountered along the way. My thanks must also be given to Mr Len Soames, Mr Brian Deer and Mr John Tierney for machining and fabricating many of the components required for this work. I would also like to thank my friend and colleague, Mr John Williams for developing and commissioning the data acquisition system used during this work and also for his prompt and generous assistance around laboratory whenever it was required.

I would also like to thank my parents, Trevor and Marion Leach, for their help and support that has allowed me to progress to this point.

Finally, I am indebted to my partner Carol, for listening, supporting and encouraging me through this period of my life.

Nomenclature

General Abbreviations

ABDC	After Bottom Dead Centre
AC	Alternating Current
AFR	Air /Fuel Ratio
ARC	Active Radical Combustion
ATAC	Active Thermo-Atmospheric Combustion
ATDC	After TDC
BBDC	Before Bottom Dead Centre
BMEP	Brake Mean Effective Pressure
BS	British Standard
BTDC	Before Top Dead Centre
CA	Crank Angle
CAI	Controlled Auto Ignition
CARB	California Air Resources Board
CCD	Charge Coupled Device
CFD	Computational Fluid Dynamics
CI	Compression Ignition
CIHC	Compression Ignited Homogenous Charge
COVimep	Coefficient of Variation in IMEP
COVpmax	Coefficient of Variation in Maximum Cylinder Pressure
CR	Compression Ratio
DAQ	Data Acquisition
DC	Direct Current
DI	Direct Injection
EA	Ensemble Average
EGR	Exhaust gas Recirculation
EGT	Exhaust Gas Temperature
EOFI	End of Fuel Injection
EOI	End of Injection
EVC	Exhaust Valve Closure
Ex	Exhaust
FFT	Fast Fourier Transform
FID	Flame Ionisation Detector

FMEP	Friction Mean Effective Pressure
FWHM	Full Width Half Maximum
GDI	Gasoline Direct Injection
HC	Hydrocarbons
HCCI	Homogenous Charge Compression Ignition
HSDI	High Speed Direct Injection
HWA	Hot Wire Anemometry
Hz	Hertz
kW	Kilowatt
IC	Internal Combustion
ICCD	Intensified Charge Coupled Device
IEGR	Internal Exhaust Gas Recirculation
IMEP	Indicated Mean Effective Pressure
In	Intake
ISFC	Indicated Specific Fuel Consumption
IVC	Intake Valve Closure
LDA	Laser Doppler Anemometry
LDV	Laser Doppler Velocimetry
LEV	Low Emission Vehicle
LGV	Light Goods Vehicle
LIF	Laser Induced Fluorescence
LIEF	Laser Induced Exiplex Fluorescence
LRS	Laser Rayleigh scattering
MAP	Manifold Absolute Pressure
MBT	Minimum Spark Advance for Best Torque
MFB	Mass Fraction Burned
MON	Motor Octane Number
MPI	Manifold Port Inector/Injection
m	Mass
m/s	metres per second
NDIR	Non-Dispersive Infrared
NEDC	New Emission Drive Cycle
NMOG	Non-Methane Organic Compounds
ON	Octane Number
PC	Personal Computer, Pico Coulomb
PCCI	Premixed Charge Compression Ignition

PFI	Port Fuel Injector/Injection
PIV	Particle Image Velocimetry
PLIF	Planar Laser Induced Fluorescence
PM	Particulate Matter
PMEP	Pumping Mean Effective Pressure
ppm	parts per million
PTV	Particle Tracking Velocimetery
RAM	Random Access Memory
RMS	Root Mean Squared
RON	Research Octane Number
RPM	Revolutions per Minute
SI	Spark Ignition
SOFI	Start of Fuel Injection
SOI	Start of Injection
SR	Swirl Ratio
SRS	Spontaneous Raman Scattering
SULEV	Super Low Emissions Vehicle
TDC	Top Dead Centre
TLEV	Transitional Low Emissions Vehicle
TR	Tumble Ratio
uHC	Unburned Hydrocarbons
UK	United Kingdom
ULEV	Ultra Low Emissions Vehicle
VCA	Vehicle Certification Agency
VOC	Volatile Organic Compounds
VVA	Variable Valve Actuation
WOT	Wide Open Throttle
ZEV	Zero Emissions Vehicle

General Notation

A	Constant
a	Crank radius, wet molar fraction of fuel
B	Constant
b	H/C ratio of fuel
c	O/C ratio of fuel

c_p	Specific heat capacity at constant pressure
c_v	Specific heat capacity at constant volume
D	Displacement vector
d	Wet molar fraction of intake air
d_i	Generic displacement in direction I
E_b	Bias voltage
f	Wet molar fraction of exhaust products in intake mixture
g	Wet molar fraction of CO_2
h	Wet molar fraction of CO
I	Angular Inertia
i	Numerical index, denotes intake species
j	Wet molar fraction of O_2
k	Wet molar fraction of N_2
l	Connecting rod length, Wet molar fraction of H_2O, litre
M	Magnification Factor
m	Wet molar fraction of NO
m_f	Mass flow rate of fuel
m_r	Mass flow rate of reactants
m_x	molecular mass (where x is CH_bO_c, CO_2, CO, O_2, N_2, H_2O, CH_4 or O)
N	Engine speed, number of cycles
n	Polytropic coefficient, number of crank revolutions per power stroke
n_f	Number of moles of fuel in intake charge
n_r	Number of moles of reactants
n_p	Number of moles of products
P,p	Pressure
P_c	In-cylinder pressure
P_i	Indicated power
Q	Heat transfer
Q_{hv}	Lower heating value of fuel
q	Heat transfer
δQ_{hr}	Heat released during combustion
δQ_{ht}	Heat exchange with chamber walls
R	Universal gas constant
s	Wet molar fraction of unburned hydrocarbons, distance between crank and piston pin axis
T	Temperature

ΔT	Time interval
t	Time, Wet molar fraction of H_2
$\vec{U}$	Velocity vector
dU	Systematic change in internal energy
u	Velocity component on the x direction
V	Volume
V_c	Clearance Volume
V_d	Displacement volume
v	Velocity component in the y direction
W, w	Work transfer
δW	Work done by cylinder gases on the piston
x	Generic wet molar fraction

Greek Symbols

γ	Ratio of specific heats
λ	Relative air/fuel ratio
θ	Crank angle
Ø	Diameter
σ	Standard deviation
Ψ	State of particle ensemble

Chemical Symbols and Abbreviations

C_1, C_2	Carbon
CH4	Methane
CH_bO_c	Generic fuel type
CO	Carbon monoxide
CO_2	Carbon dioxide
DMA	Dimethylaniline
H_2O	Water
NO	Nitrogen oxide
NO_2	Nitrogen dioxide
NO_x	Combined oxides of nitrogen
O	Oxygen Radical
O_2	Oxygen

O_3	Ozone
PTFE	Polytetrafluroethylene
R	Radical
TEL	Tetra ethyl lead
TEM	Tetra methyl lead
TMN	Trimethylnapthalene

Chapter 1

Introduction

Chapter 1 Introduction

1.1 Introduction

Since their introduction around a century ago, IC engines have played a key role, both socially and economically, in shaping of the modern world. Their suitability as an automotive power plant, coupled with a lack of practical alternatives, means road transport in its present form could not exist without them. However, in recent decades, serious concerns have been raised with regard to the environment impact of the gaseous and particulate emissions arising from operation of these engines. As a result, ever tightening legislation, that restricts the levels of pollutants that may be emitted from vehicles, has been introduced by governments around the world. In addition, concerns about the world's finite oil reserves and, more recently, climate change brought about CO_2 emissions has lead, particularly in Europe, to heavy taxation of road transport, mainly via on duty on fuel. These two factors have lead to massive pressure on vehicle manufacturers to research, develop and produce ever cleaner and more fuel efficient vehicles. Though there are technologies that could theoretically provide a much environmentally sound alternatives to the IC engine, such as fuel cells, practicality, cost, efficiency and power density issues will prevent from them displacing IC in the near future.

The absence of viable competing technologies has left no alternative but to continually improve the IC engine, both in terms of increased fuel efficiency and reduced pollutant production. One major area of development has been the introduction of gasoline direct injection (GDI) and high-speed direct injection diesel units into the market place, which offer significant reductions in fuel consumption. However, optimum operation of both these combustion systems requires that both in-cylinder fuel distribution and airflow be controlled to a very high level. This has lead to the development and use of various techniques to measure these parameters as they happen inside the engine.

In this work, the in-cylinder airflow of a GDI engine equipped with an air assisted injection system is measured using a technique known as particle image velocimetry (PIV). In this method, the in-cylinder airflow is tracked by seeding particles introduced into the intake flow. These are illuminated using a laser sheet and the light scattered recorded by a CCD camera. By taking two images separated by a very small, but known time period, the displacement of each particle, and hence the flow field, can be determined. The system has also been applied to the study of the liquid fuel spray from the Orbital air assisted injection system. Here, the technique is applied in a very similar way, although no seeding material is added, with the fuel droplets themselves acting as markers. Since the Orbital injection system is intended for GDI operation where a late injection strategy can be employed to achieve a stratified charge, adequate control of fuel motion after it has left the injection is paramount. Also in this work, laser induced exiplex fluorescence is used to visualise in-cylinder fuel distribution in both liquid and vapour phases distinctly and simultaneously. The technique involves adding tracer dopants to a non-fluorescing substitute fuel. During the injection, the fuel is excited using a laser sheet and the resulting fluorescence emission is collected via an ICCD camera.

Despite the gains made by these technologies, major difficulties exist in achieving simultaneous reductions in fuel consumption and exhaust emissions. The introduction of high pressure direct injection diesel and direct injection gasoline (GDI) has proved particularly problematic in this respect, with potentially large efficiency gains stifled by the need for maintain low NOx emissions.

Over the last 30 years, an alternative combustion technology has emerged that has the potential to achieve efficiencies in excess of GDI units and approaching those of current CI engines, but with levels of raw NOx emissions up to two levels of magnitude lower than either. These abilities offer the potential to meet current and future emissions legislation, without the need for expensive, complex and inefficient exhaust gas aftertreatment systems. Various names (and acronyms) have been applied to this type of combustion including controlled auto ignition (CAI) and homogenous charge compression ignition (HCCI).

Though CAI combustion has been productionised in limited numbers by Honda with the two-stroke ARC250 engine, its application to four stroke units suitable for powering passenger cars still presents a considerable challenge. Although there are various means of achieving CAI combustion, the method that has emerged as most suitable for a multi cylinder unit capable of the good transient response essential for automotive applications is the use of radical valve timings to trap large amounts of burned gas prior to induction. This provides both the thermal energy needed to initiate the combustion and the high levels of charge dilution required to temper the subsequent heat release rate to sustainable levels. The major drawback of this method is that the large levels of trapped gas required reduces the space available for the fresh charge, severely compromising power density. However, it is envisaged that a productionised engine would be capable of using an intelligent valve timing system to switch to conventional SI mode when the CAI operating region is breached, returning when the load or speed demand falls.

Since gas exchange process, and hence engine load, is controlled almost exclusively by the valve timing, its effects on CAI combustion with regard to exhaust emissions, fuel consumption and operating range have been investigated. The application of a GDI injection system to the CAI concept adds another dimension of combustion control. For this reason the effects of injection timing were also studied.

1.2 Objectives of Project

The objectives of this project are to:

i) Investigate and define the in-cylinder flow and liquid fuel spray characteristics of the Orbital prototype cylinder head and air-assisted injection system, including any interaction between the two motions.

ii) Complete qualitative measurements of the in-cylinder liquid and vapour fuel distribution obtained from the Orbital air-assisted injection system.

iii) Investigate the effect of valve and injection timing on the operating range, exhaust emissions and fuel consumption on a GDI engine with CAI combustion.

1.3 Outline of Thesis

Following this introduction, Chapter 2 is a review of relevant literature relating to the project and is split into five main parts. First of all, the current and future emissions legislation with regard to vehicles is outlined in order to give context for the motivation for research and development of IC engines. Secondly, the current state of the art technologies that are either being used or actively researched in order to meet this legislation are discussed. The third section is devoted to the review of papers published on CAI combustion, providing a basis for this section of the research. In the fourth section, a range of papers relating to the field of in-cylinder flow field measurement are reviewed. Here, the historical development of the various techniques, along with the current state of the art methods, are discussed. The final section is a review of papers related to the measurement of in-cylinder fuel distribution. As with the previous section, the development of the field will be discussed, along with various methods available.

Chapter Three details the general set-up of the test facility. Specifications of the engine and test bed are discussed, along with details of the cylinder head, optical access windows and gaskets. Also, the air-assisted injection system used throughout the research is introduced, along with the fuel supply, ignition and control systems.

Chapter Four covers the in-cylinder flow field and liquid fuel spray measurements performed on the engine. Following a brief summary of the techniques available for in-cylinder flow field measurement, the PIV technique is introduced and its application to IC engines detailed. Next, details of the experiments performed are discussed, along with the methods employed to post process the resulting data. Finally the results obtained are presented and discussed.

The subject of Chapter Five is the characterisation of the in-cylinder fuel distribution from the Orbital air assisted injection system using laser induced exiplex fluorescence (LIEF). The first section introduces the various techniques available for measuring in cylinder fuel distribution along with their various merits and limitations. Next the principle of laser induced fluorescence is discussed, followed by the considerations required in its application to IC engines. The exiplex system used in this work is then detailed, including the selection and evaluation of dopants used. Finally, after describing the experimental set-up and the tests performed, the results obtained are presented and discussed.

Chapter Six is used to present information relating to the changes in experimental set-up required for the fired engine work, the results of which are presented in Chapter 7. The preparation of the engine and fuel supply system for fired operation is covered, along with a discussion of the additional temperature, emissions and in-cylinder pressure measurement equipment required. In addition, the analytical processing of in-cylinder pressure data that is used to extract information regarding various combustion parameters is discussed.

Chapter Seven begins by presenting the experimental details of the fired engine work, including the valve timing strategy to achieve CAI and test methodology. The rest of the chapter is devoted to presenting and discussing the results obtained from the CAI and SI tests.

Chapter Eight begins by presenting the general conclusions that could be drawn as a result of the knowledge gained during this project. The conclusions are essentially a compilation of the summary sections included at the end of Chapters 4, 5 and 7. The chapter also contains recommendations for further work. Suggestions have arisen from the limitations of the techniques that have become apparent during the work. In addition, discoveries made as a result of experiments have prompted further important questions that cannot be answered without additional work.

Appendix A contains detail drawing of various engine components manufactured during the project. They are included as a reference resource for researchers that may use the equipment in the future.

Chapter 2

Literature Review

Chapter 2 Literature Review

2.1 Emissions Legislation

The vast majority of past and present research in the field of IC engines for automotive applications has been concerned with reducing the environmental damage caused by their operation. UK greenhouse gas emissions from the transport sector make up 21% of the total and this is predicted to rise to 26% by 2050 [1]. Greenhouse gases arising from transport consist of CO_2, NOx and volatile organic compounds (VOC). Concerns over global climate change, as a result of greenhouse gas emissions, has prompted the development of the Kyoto protocol, an agreement whereby many nations have pledged to cut their greenhouse gas emissions over the coming years, with the UK committed to reduction of 12% by 2010 [2].

The symptoms arising from burning of hydrocarbon fuels can generally be divided into local and global environment effects. On a local level, the reaction of ground level NOx and VOC's emissions with oxygen in the presence of sunlight forms photochemical smog, which can cause respiratory problems. Additionally, incomplete carbon oxidation (to CO_2) leads to the formation of carbon monoxide (CO), which can lead to unconsciousness and respiratory failure if inhaled in sufficient concentrations. Inhalation of particulate matter (PM), usually formed with fuel rich combustion, can cause lung problems and is also, along with other hydrocarbons such as benzene, carcinogenic.

Over the last 30 years, levels of NOx, CO and VOC emissions from vehicles have been dramatically reduced and this has largely been achieved by the use of exhaust gas after-treatment systems, such as the catalytic converter. This has been motivated by a continually tightening band of legislation related to emission of these pollutants that has been enforced in the United States (USA), Japan and Europe (EU). Table 2.1 shows the permitted emission levels for the EU and California Air Resources Board (CARB) for passenger cars [3], [4].

Table 2.1 Current and Future EU and CARB Legislated Emissions Levels for Passenger Cars [3], [4].

Euro Standard	Year	Engine Type	CO (g/km)	HC/NMOG (g/km)	NOx (g/km)	HC+NOx (g/km)	PM (g/km)
Euro III	2001	SI	2.3	0.2	0.15	-	-
		CI	0.64	-	0.5	0.56	0.05
Euro IV	2005	SI	1.00	0.2	0.08	-	-
		CI	0.5	-	0.25	0.3	0.025
CARB (LEV II)			**2**	**0.033**	**0.04**		**-**
TLEV	2004-10		-	-	-		-
LEV			4.2	0.056	0.07		0.01
ULEV			2.1	0.034	0.07		0.01
SULEV			1	0.006	0.02		0.01

*After 100,000 Miles

EU emissions legislation demands that all vehicles comply with the particular standard that is in force at that time they are manufactured. The permitted emission levels are given on a specific basis and are the maximum permitted over a standard drive cycle, intended to be representative of a typical vehicle journey. Legislation from CARB is included in Table 2.1 because it is currently the most stringent in the world. The US legislation is significantly different from the EU standards in that it operates a 'fleet-averaged' system, where the average emissions output from the total sales of a manufacturers product range must be within the prescribed limits. In this way, a manufacturer can, for example, use sales of SULEVS to offset the higher emissions from TLEVS to keep within the required limits. In addition, differences in the test drive cycle and the measurement method of VOC's make direct comparison of the 'Euro' and CARB standards impossible. Johnson [5] has shown, through normalisation of the US and European standards, that the levels of uHC permitted by the US LEV II and EURO IV standards are roughly similar. However, he also concluded that the US standard permits approximately half the amount of NOx emissions, which was likely to seriously limit the penetration of HSDI Diesel and GDI engines into this market until adequate exhaust gas aftertreatment systems are developed.

In addition to standards concerned with limiting local pollution, government policy is used to reduce global climate change by attempting to limit vehicle CO_2 emissions. In the UK and much of Europe this takes the form of heavy taxation of fuel, discounts on Road Fund Duty for small capacity vehicles and, most recently, the introduction of sliding scale of 'company car tax' that heavily penalises the operation of vehicles with high CO_2 emissions. As part of this, CO_2 emission levels for all new passenger cars and LGV's must be published. Driven by this strong desire to reduce CO_2 emissions, a voluntary agreement has been reached between many of the major European car manufacturers to reduce their fleet average fuel consumption by 25% by 2008 [6]. In the US, legislation was introduced in the 1970's that required manufacturers to achieve certain levels of fleet average fuel consumption for passenger cars and light trucks, though the motivation for this was based largely on concerns regarding the supply of oil, rather than the consequences of high CO_2 emissions.

2.2 Current Technologies and Future Developments

The ultimate target of emissions legislation is to push technology to the point where a practical, affordable zero emissions vehicle (ZEV) with acceptable performance becomes a reality. Although the technology exists to produce true ZEV's, powered by a fuel cell that consumes hydrogen produced from water by electricity generated from renewable sources, it is highly unlikely that the resulting vehicle would even come close to meeting any of the other criteria listed above. For this reason, the bulk of vehicle research and development resources are still being applied to the IC engine.

Wiess et al. [7] used the 'well to wheels efficiency' concept to quantify the total 'energy cost' and subsequent environment impact of different vehicle technologies. The study attempted to assess and compare current and emerging technologies, with developments projected to 2020. In each case, the total energy cost was evaluated, including vehicle production, fuel processing and running costs. They concluded that, in terms of energy consumption per unit distance travelled, diesel/electric and gasoline/electric hybrids offered the best solution. Fuel cell vehicles, that use a reformer to produce their hydrogen fuel from gasoline, were found to be least energy efficient. The added problems of poor range and performance suffered with today's batteries, plus the major problems that must be solved before the introduction of a hydrogen supply infrastructure, also added weight to the conclusion that IC engines will be the dominant means of powering transport for the foreseeable future. Since this report, both Honda and Toyota have introduced gasoline/electric hybrids onto the world-wide market. Uptake of these vehicles has been slow, but this is likely to be as a result of their poor value for money, in pure economic terms, even when considering their fuel consumption benefits. As the technology inevitably decreases in price and consumers become more aware of the need to reduce fossil fuel use, their popularity can be expected to increase.

While hybrid vehicles may prove to be a stepping stone to a ZEV, recent developments in traditional SI and CI engine technology have allowed large improvements in emission and fuel consumption to be made. In terms of emissions, the adoption of the 3-way catalytic converter has allowed engine-out emissions of CO, uHC and NOx to be reduced by over 90%. However, in order to maintain these conversion efficiencies, this unit, can only be used with an engine operating within a few percent of stoichiometry [8]. This fine level of AFR control is beyond the capabilities of the once ubiquitous carburettor so has tended to be displaced by electronically controlled closed loop fuel injection systems, adding significantly to vehicle cost. More importantly, the requirement for continuous stoichiometric operation prevents the engine from operating with a lean AFR at part load, leading to a small but significant increase in overall fuel consumption.

The requirement of SI engines with a 3-way catalyst to operate with a homogenous charge, and at lambda = 1, means that engine air and fuel flow must be controlled simultaneously to vary engine load. Airflow control is generally accomplished by intake throttling and this leads to an increase in pumping losses that reduce engine efficiency by up to 20%. However, diesel, and more recently, stratified charge gasoline direct injection (GDI) engines permit lean combustion by allowing fuel flow rate (and hence load), to be varied independently of airflow. These approaches can therefore achieve significant reductions in fuel consumption, particularly at part load. However, their operation away from stoichiometry prevents the effective use of traditional exhaust after-treatments for reducing NOx emissions. Though the technology to achieve NOx reduction from lean burn engines is available [9], it is currently very expensive and can suffer from durability problems. Another problem with diesel engines is their tendency to produce high levels of particulate matter (PM). The Euro IV and US Tier 2 emissions legislation demands levels PM control that can only be achieved with the use of particulate filters within the exhaust. The systems that are currently available require the filter be periodically purged by post-injecting fuel so that the catalyst can raise the exhaust temperature to around 550°C in order to oxidise the carbon in to CO_2. This incurs a fuel consumption penalty of 3-4%, negating some of advantages of lean combustion and systems are currently expensive and cannot yet last the life of the engine [10].

As alternative to SI and CI engines, a new type of combustion has emerged that has the potential to allow both low emissions and high efficiency to be achieved simultaneously. Controlled auto ignition (CAI) combustion, as it has become known, involves the auto ignition of a homogenous charge. In practical terms, this is achieved by subjecting part or all of the cylinder contents to temperatures above those required for auto-ignition of the reacting species. If left unchecked, the heat release rates of the subsequent combustion are high enough to cause severe engine damage, and as a result, must be tempered by large amounts of excess air and/or exhaust gas.

2.3 Controlled Auto Ignition Combustion

2.3.1 Introduction and Current Strategies

The roots of the current interest in CAI combustion may be traced back to work on ignition theory by Semenov in the 1930's [11]. However, it is generally considered that the first systematic investigation on the new combustion process was carried out by Onishi [12] and Noguchi [13]. This line of research has culminated in the introduction, by Honda, of the first (and only) production CAI engine, the two-stroke ARC 250 unit [14]. With this unit, which uses the thermal energy of residual gases to promote CAI, Honda claims to reduce fuel consumption by up to 29% while simultaneously halving uHC emissions.

Despite the apparent appeal of this engine, being based on a 2-stroke unit it suffers from several problems that make it unsuitable for mainstream automotive applications. Firstly, lack of low pressure during the intake process necessitates that the fresh charge be pumped into the cylinder. In most cases, this is achieved by initially inducting the fresh charge into the crankcase as the piston rises and subsequently using crankcase pressure generated by the descending piston to push the charge into the cylinder. However, this configuration prevents the use of a closed, recirculating lubrication system, meaning a total loss system where lubricating oil is mixed with fuel must be used, leading to intolerable levels of uHC emissions. This problem can be overcome by using a separate pump to drive in the charge but leads to increased cost, complexity, weight and parasitic losses that increase fuel consumption. In addition, the strong influence of gas flow dynamics on the gas exchange process dictates that torque is strongly related to engine speed, leading to driveability problems. Also, during high load operation, the simultaneous opening of the intake and exhaust ports inevitably leads to some of the fuel 'short circuiting' combustion, resulting in unacceptable levels of uHC emissions, though this can be improved by the use of a GDI injection system [15].

The apparent potential of CAI to reduce emissions and fuel consumption, coupled with serious shortfalls of the 2 stroke ported engine as an automotive power unit, led to an investigation into the application of CAI to 4 stroke engines by Najt and Foster [16]. In this study, high intake air temperature was used to initiate CAI combustion, while a highly diluted charge was employed to control the subsequent heat release rate. Although this approach has been used in many fundamental studies into CAI combustion, its long-term practical application is limited by the small speed and load ranges where acceptable CAI combustion can be realised. In addition, the large thermal inertias associated with intake air heating, coupled with the highly transient nature of automotive applications, will ultimately make the control of CAI by this method very hard to achieve. Also, unless waste heat rejected from the engine coolant or exhaust is used to heat the intake, large amounts of extra energy would need to be added, leading to an increase in fuel consumption. Despite these practical problems, Najt and Fosters' early work [16], proved the potential of CAI in a 4-stroke engine to reduce fuel consumption.

A solution to the problem of inadequate operating region was proposed by Lavy et al. through the use of a CAI / SI hybrid strategy [17]. Here SI operation would be employed whenever the CAI region is breached, leading to an overall reduction in fuel consumption and emissions over SI operation alone.

Another means that has been successfully used to achieve CAI combustion is to increase the compression ratio to the point where the required temperature and pressure for auto ignition are achieved through compression alone [18]. However, as with intake heating, this method also requires the use of ultra lean air/fuel mixtures to prevent excessive heat release rates and, as such, suffers from similar constraints regarding its operating region. In this case, it would not be possible to apply the hybridisation strategy described above, since the compression ratio would be far too high for SI operation without suffering catastrophic levels of knocking combustion, unless a variable compression ratio system is used.

Variation in fuel blend has also been used by Olsson and Johnson [19] to achieve CAI combustion. This method, that also employed supercharging and intake air heating, used combinations of isoctane and heptane to achieve CAI combustion over a large speed and load range. Although it was found to work reasonably well, a complex control system, with closed loop control of heat release rate and intake temperature was required. In addition, since it requires heated intake air to function correctly, its ability to deal with transient situations must also be called into question. Its potential as a method of achieving CAI in future production engines is also limited by the current lack of infrastructure to supply the required fuels.

More recently CAI combustion has been achieved in 4 stroke engines by using large amounts of residual gases, trapped in the cylinder by early closure of the exhaust valve(s), to heat the incoming fresh charge to the point where auto ignition takes place around TDC [17], [20], [21]. This method of trapping large amounts exhaust gas in the cylinder is often referred to as internal exhaust gas recirculation (IEGR). The retention of burned gases not only heats the charge, but also serves to dilute the air/fuel mixture, restraining heat release rates to sustainable levels. In this type of engine, load is primarily controlled by the valve timing, with more retarded exhaust valve timing producing greater load. In many cases, this has been achieved in practice by using specially modified short duration camshafts to achieve CAI and the camshaft phasers now found on many production engines [22]. Although, because of the requirement for the presence of both residual and fresh gases in the cylinder, this system suffers from similar speed and load constraints as other methods, several means of increasing the operating range have been suggested, such as the CAI/SI hybrid strategy mentioned above. Successful implementation of such a strategy would almost certainly require the use an active valve control system that could switch instantaneously between the two radically different valve timings. Though not currently available on production engines many such systems are in development and have even been used in the research of this type of CAI engine [23]. Another solution to increase the power density is that of supercharging, thus allowing sufficient fresh charge to be burned to achieve reasonable outputs, whilst also maintaining the requisite quantity of residual gases in the cylinder. This approach has been successfully applied by Aoyama et al. [24] who succeeded in increasing the charging efficiency of their engine from 85% in naturally aspirated form to 120% with forced induction.

Over the last few years, the IEGR method of initiating and controlling CAI has proved to be increasingly popular with researchers since it appears to offer the best chance of producing a feasible production CAI/SI hybrid unit in the short to medium term. In addition, the method is likely to be prove popular with motor manufacturers since it should be relatively cheap to implement and, apart from the addition of a new valve train and control system, requires no radical (expensive) changes to vehicle or engine architecture. Indeed, as part of the 4-space project, Li et al. [22] took a production 4 cylinder engine and achieved CAI combustion over a reasonable speed and load range with only the addition of modified camshafts.

2.3.2 Heat Release Considerations

Although the issues of combustion phasing and heat release are of obvious importance and of interest to researchers of SI and CI combustion, the inherent lack of a direct control link to ignition timing with CAI combustion has ensured the subject has received a large amount of attention. Researchers of CAI engines have several means of controlling ignition timing at their disposal and Christensen and Johansson [25] list these as:

- Compression ratio
- Inlet mixture temperature
- Inlet manifold pressure
- Fuel
- Air/fuel ratio
- EGR rate
- Engine speed
- Coolant temperature

With the adoption of GDI injection systems into CAI research, the variable of injection timing should also be added to this list [20].

Oakley [26] who studied CAI combustion over a wide range of lambda and EGR rates found that for most operating conditions AFR had very little effect on ignition timing, except at EGR rates over 40%, where reducing the AFR was found to retard ignition timing significantly. Work by Christensen and Johansson [27] studied the effect of compression ratio, inlet air temperature and fuel octane number (ON) on the ignition timing a CAI engine. Initially, they tested fuels with constant ON and adjusted the intake air temperature and compression ratio to achieve ignition at TDC in each case. It was found that as the fuel ON was increased, the compression ratio has to be increased to advance the ignition timing to TDC. Also, as the intake air temperature was increased, a lower compression ratio was required to achieve ignition timing at TDC. In another study, this time using a GDI injection system, Sjoberg et al. [28] found that, under some conditions, use of a late injection, stratified charge strategy could promote very advanced ignition and lead to knocking combustion, while use of a homogenous charge under the same conditions, resulted in much later ignition.

With regard to burn duration, work on SI and CI engines has generally been concerned with speeding up combustion, in order to increase the knock limit and improve maximum output respectively [29]. However, with CAI combustion, in almost all cases provision must be made to reduce heat release rates and hence increase combustion duration to prevent knocking combustion [30]. The earliest 2 stroke studies by Onishi et al. [12] and Noguchi et al.[13] found that the duration of CAI combustion, (from ignition to end of combustion), was considerably reduced. Onishi et al.[12] reported that, under certain conditions, heat release rate was increased by 30%. This publication also includes a good qualitative explanation why CAI combustion is often faster that SI combustion an adaption of which is included in Figure 2.1.

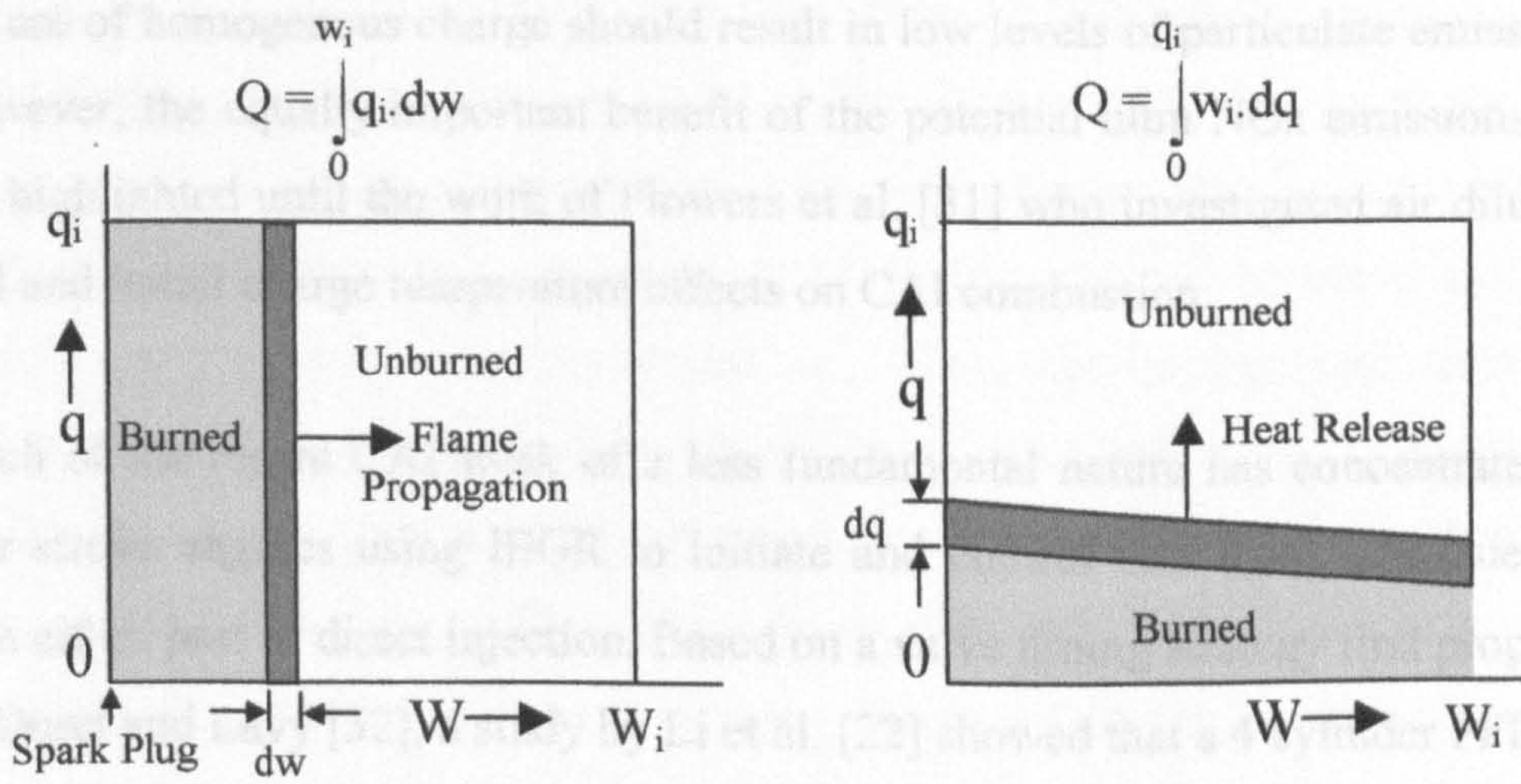

(a) Spark Ignition Combustion **(b) CAI Combustion**

Figure 2.1 Ideal Models of Spark Ignition and CAI Combustion [12]

Figure 2.1 (a) and 2.1 (b) show ideal models of SI and CAI combustion respectively. In each case, the x-axis represents the fraction of total mixture mass, while the y-axis represents the specific heating value of the fuel. During SI combustion, each element of the fuel is burned completely while in the flame region, shown as *dw* in the figure. Conversely, during CAI operation, combustion occurs in almost all parts of the charge simultaneously, and *dq* represents the total heating value of the intermediate reactants that continue the chain branching reactions. In this way, with CAI combustion, minimum duration is limited chemically by kinetic reaction rates, while minimum SI combustion duration is limited by the physics of flame propagation.

2.3.3 Exhaust Emissions

The primary motivation of early investigations into CAI in two stroke engines by Onishi et al. [12] and Noguchi et al. [13] was to reduce uHC and fuel consumption at light load through increased combustion stability and elimination of misfires. However, since the four-stroke engine does not tend to suffer in this way, these benefits were of little consequence for automotive applications. Early four-stroke work by Thring [30] noted improved fuel consumption benefits from CAI via lean, homogenous, unthrottled operation at low load. He also noted that the use of homogenous charge should result in low levels of particulate emissions. However, the equally important benefit of the potential ultra NOx emissions was not highlighted until the work of Flowers et al. [31] who investigated air dilution, fuel and initial charge temperature effects on CAI combustion.

Much of the recent CAI work of a less fundamental nature has concentrated on four stroke engines using IEGR to initiate and control CAI using gasoline fuel with either port or direct injection. Based on a valve timing strategy first proposed by Duret and Lavy [32], a study by Li et al. [22] showed that a 4 cylinder PFI four stroke production engine could be made to run in the CAI mode simply by exchanging the original camshafts for a pair with much reduced lift and duration. The study concluded that, in the reasonable operating region attainable, NOx emissions could be reduced by between 90% and 99% over SI operation of the same engine, prompting the assertion that the use of a 3-way catalyst might be negated by the adoption of this technology. A reduction in CO emissions of between 10 and 40% over SI operation was also noted, although HC emissions were found to increase by as much as 160%. In addition, fuel consumption was found to be reduced by up to 30%, through the reduced pumping losses and rapid heat addition of the CAI combustion. Follow up work by Zhao et al. [33]

compared the performance of a hypothetical CAI/SI hybrid engine with a similar one operating in the SI mode only over the European New Emission Drive Cycle (NEDC). It was found that, over the cycle, fuel consumption was reduced by 4.7%, NOx emissions were down by 12.7% and emission of CO dropped by 3.7% while and increase in HC emissions of 16.9% was observed.

A novel approach to the problem of high uHC emissions from CAI engines has been proposed by Hultqvist et al. [34]. In this study, ceramic and catalytic coatings were applied to the surfaces of the combustion chamber, piston crown and cylinder liner in the hope that they support the oxidation of the near wall unburned hydrocarbons. Although they found that a thin thermal barrier could reduce uHc and CO emissions, catalytic coatings actually gave increased levels of uHC emissions, which was attributed to catalytic flame quenching.

A study by Sjoberg et al. [28] analysed the effects of GDI injection timing and air swirl on the exhaust emissions of a CAI engine. Interestingly, the engine used was a heavy duty 6 cylinder diesel engine with one cylinder running in CAI mode. CAI was initiated by the application of EGR from one of the diesel cylinders and/or electrical heating of the intake air. They showed that, with their GDI injection system, a homogenous charge was produced when injection was performed around 70 °CA ATDC during the intake stroke, resulting in low NOx and smoke emissions. They also found that the high fuel consumption encountered under very lean, homogenous charge conditions, could be improved by delaying injection and creating stratification in the cylinder. However, they also state that if injection is too late then NOx emissions rise and the engine has a tendency to run into knocking combustion, demonstrating a trade-off between engine efficiency and NOx emissions. They also noticed that the enhanced air/fuel mixing afforded under high swirl conditions reduced HC, CO and smoke emissions, particularly when very early or late injection was used.

CAI combustion has also been shown to improve combustion stability in 2-stroke engines [12, 13], while 4-stroke CAI units tend to produce similar levels of COVpmax and COVimep to their SI counterparts [23]. Koopmans et al. [23] found that cycle to cycle variations in cylinder pressure in CAI engines is caused by variation in the auto-ignition temperature of the air-fuel mixture. They discovered that cycles with late combustion had much higher levels of uHC in the exhaust stream than those with early combustion. Investigation of the cylinder pressure during the recompression of residual gases following a cycle with late combustion revealed combustion was present. This increased the residual gas temperature, resulting in early ignition of the next cycle. Since the early combustion cycle left less unburned hydrocarbons in the residual gases, no combustion was detected during the recompression and there was not gas temperature increase. As a result combustion in the next cycle was later.

2.3.4 Operating Region

Regardless of the means employed to achieve CAI combustion, the attainable operating range is always greatly reduced from that of an equivalent engine operating the SI or CI mode [23]. If the heat energy required for auto-ignition is introduced into the charge by intake air heating or increased compression ratio [26], over lean mixtures or copious amounts of dilution with exhaust gas must be used to limit the heat release rates. If the heat energy is supplied by IEGR [20, 22], then space must be allotted for the requisite quantity of exhaust gas, which conveniently also provides the required charge dilution. In both the cases, the amount of fuel that can be burned in any cycle is drastically reduced when compared to SI and CI engines, limiting maximum torque output.

When using IEGR to initiate and control CAI, the dual roles of the residual gases in heating and diluting the charge means that the upper torque limit may be limited by one of two reasons, depending on the in-cylinder conditions. As load is increased, the amount residual gases must be reduced to make space for the extra fresh charge [30]. If the residual gases can continue to supply sufficient local temperatures for auto-ignition to occur, it may be knocking combustion, as a result of insufficient dilution, that limits the attainable load. However, a situation can also occur where insufficient heat energy is available for auto-ignition while the charge is still sufficiently dilute. At the lower load limit, the residual gas temperature is too low to facilitate auto-ignition [30]. A study by

Urushihrara et al.[20] attempted to expand the operating region of a GDI IEGR engine. Here, injection during the recompression of the residual gases, following the early EVC, increased the combustion stability at higher AF ratios, dramatically increasing the useable operating region. Although no formal chemical analysis was completed, the phenomenon was attributed to some form of fuel reformation that took place when injecting into the hot residual gas.

2.4 In-Cylinder Flow Field Measurement

Air motion within the cylinder has a fundamental effect on the combustion, emissions formation and performance of internal combustion engines [35]. Motivated by emissions legislation and high levels of fuel duty, vehicle manufacturers are continuously striving to produce engines with reduced emissions and increased efficiency. In conventional homogenous charge SI engines, large scale flow structures, such as swirl or tumble are often used to maintain the flow's kinetic energy until the end of the compression stroke, where they break down into micro scale turbulence, promoting early flame kernel growth and increased flame speed [35]. This can be used to increase the engines knock limit, allowing the use of increased compression ratios that result in increase fuel efficiency and reduced CO_2 emissions. In addition, the technique can allow operation at lean air/fuel ratios that reduce fuel consumption through reduced pumping losses and increased cycle efficiency. More recently, combustion systems that rely heavily on particular in-cylinder flow regimes to perform optimally have been introduced. These include high swirl DI diesel systems and stratified charge GDI engines. Despite the development of ever more powerful CFD modelling tools that are of great value to designers of such combustion systems, their limitations mean that experimental validation of models using such techniques as particle image velocimetry (PIV) will still be required for the foreseeable future.

In a similar manner, PIV has more recently been used to the study the motion of liquid fuel droplets emerging from fuel injectors. Though less widespread than the study of in-cylinder flows the technique has been applied to both diesel and GDI injection systems [6, 36].

Optimisation of these advanced combustion systems has largely been made possible through the development of various techniques that allow the measurement of in-cylinder flow fields. The first attempts to characterise in-cylinder flows within IC engines used single point measurements techniques such as hot wire anemometry (HWA) and laser Doppler anemometry/velocimetry (LDA/LDV) [37-41]. Whilst providing useful point wise data, these studies have shown that flow within the cylinder varies not only with time, but also that it differs spatially at any one instant. For this reason, the time-averaged data that can be obtained from a limited amount of point wise measurements cannot fully describe the unsteady flow encountered with the IC engine. As a result of this, techniques capable of measuring the whole flow field have been developed. Though in the early development of IC engines, qualitative flow measurements were obtained by the introduction of such mediums as smoke and feathers into the cylinder [42], the era of quantitative whole field measurement began with the development of particle tracking velocimetry (PTV) [43-45] and particle image velocimetry (PIV) [46-48]. These techniques have enabled the recording of instantaneous, cycle resolved, two-dimensional velocity maps across extended measurement planes within the cylinder. With these measurements systems, small seeding particles are introduced to the flow, normally via the intake port, and are subjected to intense stroboscopic illumination that allows their position to be recorded either electronically or photographically at two or more instants in time. In PTV measurements, particles are identified and matched between two exposures within a known timeframe, enabling their velocity to be determined. PTV has been used to characterise induction like flows in water analogue engines [49] and cyclic variability in a motored engine [50], and, more recently, the effects of intake port geometry on large scale flows [51]. While these studies prove that useful data can be obtained using PTV, there are several difficulties with the technique that limits it application. Firstly, a light source that can provide long pulses is required, and this tends to mean that illumination is of low power density. Because of this, large seed particles must be used in order to scatter sufficient light. In addition, in order to avoid confusion of seed pairs during analysis, only sparse seeding can be used, resulting in lean flow fields that require significant interpretation or ensemble averaging.

The development of the PIV technique and its application to IC engines has allowed in-cylinder flow field measurement to be obtained with high spacial resolution. In these measurements the movement of seed particles is captured by two short duration, high energy, thin laser sheet pulses. From this, the mean velocity within each small interrogation area of the image is determined via spacial correlation such that no identification of distinct, individual particles is required. This allows the use of high seeding densities and hence a more comprehensive velocity map than can be obtained than with PTV. The use of a power dense illumination source allows the use of micron sized particles that can track high frequency flows and the technique appears suitable for the measurement of both large scale and small-scale motions. Among the first researchers to apply PIV to IC engines were Reuss et al. [46] who used the technique to acquire instantaneous in-cylinder planar velocity measurements. From this data they derived flow parameters such as large-scale vorticity and strain rate in an attempt to understand the effect of the flow field on the burn rate of laminar and turbulent flames. Subsequently, the technique was used to study unburned gas behaviour under combustion conditions [47, 52]. In these, and many other early applications of PIV [46, 48, 52], the particle images were generally captured on photographic film and the velocity vectors calculated using the auto-correlation method. Unfortunately, this method has a limited dynamic range and suffers from directional ambiguity. In addition, it is not practical to obtain and process more than a few images at a particular crank angle, and even then, only from non-consecutive cycles, preventing the construction of ensemble-averaged flow maps. Although, owing to its high resolution, film allows the analysis of small-scale structures, the flow field of individual cycles may hardly resemble the ensemble averaged flow behaviour if large bulk flow variation is present. More recently the availability of high resolution charge coupled device (CCD) cameras has allowed PIV studies to use digital systems to capture and process the images [29, 53, 54]. This method allows the capture of two frames within a very short time via the 'frame straddle' technique. This then allows the velocity vectors to be calculated using the two frame cross-correlation method, which eliminates direction ambiguity and increases dynamic range. The high rate at which the digital system allows images to be captured and stored on a PC computer means that large numbers of PIV image pairs can be taken from consecutive engine cycles in short period of engine testing. This then allows ensemble averaged and cycle-resolved flow parameters to be obtained.

Though in the area of IC engine research, the PIV technique is primarily applied to the study of airflow, it has also been used to measure the motion of liquid fuel sprays [6, 36]. This application of the technique is essentially the same as that described above but, in this case, the liquid fuel droplets are used as markers and no extra seed particles are added. Though there are problems associated with this use of the technique, mainly concerning the obvious lack of control over the size and density of the seeding particles, some studies have yielded useful results [6, 36].

2.5 In-Cylinder Fuel Distribution Measurement

The fuel distribution and mixture formation process within an IC engine can greatly affect its ignition, combustion and pollutant formation processes as well as its fuel consumption. This is particularly true for stratified charge direct injection gasoline (GDI) engines where the guiding of the charge to the vicinity of the spark plug at the time of ignition is vital for optimised operation.

In order to provide these in-cylinder conditions, the ability to measure the fuel concentration and air/fuel ratio distribution in the combustion chamber is almost essential. To this end, several non-intrusive laser based spectroscopic diagnostic techniques have been developed to allow in-cylinder fuel concentration measurement. These are based on three different light scattering processes, namely Rayleigh scattering, Raman scattering and laser induced fluorescence.

Laser Rayleigh scattering (LRS) is a simple, and easy to use method for measuring gaseous species concentration. The light scattered by the Rayleigh method is the strongest of the techniques mentioned above and hence has the potential to facilitate 2D dimensional in-cylinder measurements. The main problem associated with the application of this technique to engines is the interference of the Rayleigh signal by Mie scattered light from both solid and liquid particles and the cylinder walls. Despite this, LRS has been successfully applied to the measurement of fuel vapour distribution with in the cylinder of motored IC engines. The first application of LRS to the measurement of fuel concentrations in IC engines was by Acroumanis et al [55]. In this work Freon-12 was injected into a motored model engine through a permanently open, axisymmetrically located valve, intended to represent a diesel injection process. The work was subsequently extended by Acroumanis et al [56] and Green et al [57] to a four-stroke diesel engine. The technique was then developed for application to the mixture formation in a SI engine. The initial work, completed on a steady flow rig was presented in a series of papers by Kadota et al [58] and Zhao et al [59]. Zhao et al then applied the technique to a motored SI engine. Later, quantitative measurements of fuel vapour concentrations were obtained in an evaporating and combusting spray using planar LRS by Espey et al [60] in an optical DI diesel engine under fired and motored conditions.

The spontaneous Raman scattering (SRS) technique allows direct detection of in-cylinder air/fuel ratio via simultaneous multiple-species measurements of stable species such as N_2, O_2, CO_2, etc. Though this technique theoretically has potential to providing full and accurate spatially resolved information of the cylinder contents, the weak nature of the Raman signal often means it is limited to single point measurements. An early application of SRS to IC engines to measure air/fuel ratio was by Johnston [61]. The experiment was completed on a motored, direct injection, stratified charge engine with gaseous propane fuel. The same arrangement was later used to measure the air fuel ratio near the spark plug electrode [62]. Problems associated with the small Raman scattering cross section, interference from other scattered light processes or flame luminosity can be serious for SRS. For this reason little further progress was made with the technique until improvements in lasers and mutli-channel detectors in the 1990's brought about a resurgence of interest, leading to new developments in the multi-point, multi-species SRS measurements [63, 64].

Probably the most widely used method of obtaining measurements of in-cylinder fuel distribution at present is laser-induced fluorescence (LIF). Its popularity mainly stems from its ability to provide planar 2D images of fuel distribution with a good signal to noise ratio and, with careful calibration, the potential for quantitative air/fuel ratio measurements. Zhao et al. [65] used the PLIF technique to measure the cyclic variation of mixture concentration in a low speed, motored, SI engine using nitrogen dioxide N_2O as the fluorescence tracer. A mixture of N_2O and N_2 was injected into the intake port to simulate fuel injection and mixing of fuel and air. Excitation of the N_2O was achieved with Nd:YAG laser with an output of 532mn and fluorescence was detected at around 580nm. From the measurements they were able to conclude that, while the mixture was homogenous in the late stage of the compression stroke, the cyclic variation of the homogeneity was large. However, it is important to note that this is not representative of normal SI engine operation, since the vaporisation of gasoline will affect the mixture formation.

The fuel distribution in a SI engine was measured using the PLIF technique by Baritaud and Heinze [66] and Deschamps et al [67]. The fluorescing dopant used was biacetyl, selected because its boiling point of 88°C is close to that of the isooctane (99°C) used as the substitute fuel. When excited at 355nm by the third harmonic output of an Nd:YAG laser, biacetyl fluoresces from the first excited singlet state (lifetime: 50ns, wavelength: 440-480nm), and, after internal conversion, it may phosphoresce from a triplet state (lifetime: 1.2 ms, wavelength: 510-600nm), or it may quenched. However, in practice the phosphoresce was found to be totally quenched, with only the fluorescence being observed. Replacing the intake air with pure nitrogen showed that less than 8% of the fluorescence was quenched by the oxygen in air. 2-6% of biacetyl in isooctane was found to produce strong fluorescence with little absorption.

The PLIF technique has been used in several studies at the Nissan Research Centre to measure the air/fuel ratio in a transparent piston, single cylinder, optical engine [68-70]. The dopant used was DMA (N,N-Dimethylaniline) in isooctane. It was found that DMA gravimetric concentrations of more than 2% lead to both oxygen and self quenching. Although 2% DMA gave the strongest fluorescence signal in the compression stroke, absorption problems mean this had to be reduced to 0.2% by volume. In an attempt to overcome absorption problems, KrF excimer laser beams at 248nm were introduced from both sides of the combustion chamber simultaneously. Peak fluorescence was observed at 335nm and a 280-400nm band pass filter was used to block both the scattered light from the laser and fluorescence from the quartz windows at 400nm.

While PLIF systems tend to be simple to set up and use, the selection of suitable dopants and compensation factors for phenomena that affect signal strength such as oxygen quenching and laser energy attenuation make the realisation of quantitative measurements very difficult. Another drawback of the classic planar LIF technique is that it is not suitable for use where fuel is present in both its liquid and vapour phases. This is because the range of signal levels between the very strong liquid phase emission and the weak vapour phase fluorescence is beyond the dynamic range of ICCD cameras currently available. Initially developed for application to diesel fuel sprays, but now also used in the study of GDI engines, laser induced exiplex fluorescence (LIEF) provides a solution to this problem [71-77]. In this technique, the emission from the liquid phase is spectrally red shifted with respect to that of the of the vapour phase, allowing, with suitable filtering, the capture of the fluorescence from each fuel phase separately.

As already stated, much of the early work on LIEF was directed towards the study of fuel distribution in diesel engines. Since the boiling point points of TMPD, (260°C), and naphthalene, (218°C), correspond to the middle boiling point of diesel fuel, Melton and Verdiect [78, 79] used these to form the exiplex compound for their initial work on LIEF. In this work, excitation was achieved using the 4th harmonic output of an Nd:YAG laser (261nm), though later the 3rd harmonic (355nm) was used by Bardsley et al [80] since it resulted in much less absorption by both components. The fuel used was a mixture of 90% decane, 9% naphthalene and 1% TMPD. A <450nm long-pass filter was used to isolate the liquid phase signal from the 400nm vapour phase emission. Oxygen quenching of the vapour phase fluorescence was found to be very strong during periods of high pressure within the engine. As a result, tests were completed using N_2 instead of air in a motored 2-stroke engine. The results showed that the vapour phase of the fuel penetrated further in a broader cone than the liquid phase and was deflected and converted by the swirling flow within the cylinder.

In the past, the application of the LIEF technique to port injected SI engines has often been concerned with visualisation of the fuel evaporation process that occurs in the intake manifold of these engines. However, with the recent interest in direct injection gasoline engine, the application of the LIEF technique to the in-cylinder fuel distribution of SI engines has become more widespread [71-81].

Many of the early studies of this type used the TMPD/naphthalene exiplex system, [71, 81, 82], popularised by researchers using it to study diesel engines. However, as the boiling point of TMPD, which dominates the vapour phase fluorescence, is 260°C, its ability to trace the evaporation of gasoline fuel is questionable. This has lead to a search for LIEF dopants that better match the evaporation properties of gasoline fuel. Following initial work by Melton [83], early work on a LIEF system to represent gasoline fuel focussed on mixtures of fluorobenzene, triethylamine (TEA) and isooctane. However, flurobenzene was found to evaporate much faster than isooctane, despite having a similar boiling point [84]. Ghandhi et al. [85] discovered that with blend of flurobenzene, diethylmethylamine (DEMA) and hexane, co-evaporation was more closely achieved between fluorobenzene and hexane. However, since the boiling point of hexane is low (68°C), the results obtained represent only the lighter fractions of gasoline fuel. With this LIEF system, excitation can be achieved using an Nd:YAG laser (266nm) and the emissions of the monomer (fluorobenzene) at 290nm and exiplex at 380nm are sufficiently spectrally separated to allow discrimination with suitable filters.

An alternative exiplex for gasoline fuel was used by Shimizu et al [86]. In this work a mixture of 5 % N,N-dimethylaniline (DMA), 5% naphthalene and 90% gasoline by mass was used to visualise both the liquid and vapour concentrations of the fuel. DMA was found to account for 85% of the fluorescence at λ_{max} = 355nm in the vapour phase when excited by an XeCl excimer laser at 308nm. The exiplex fluorescence was red shifted, its peak wavelength occurring at 410nm. A problem with this system is that, since DMA is used to trace the vapour phase and has a high boiling point that corresponds to the heavier end of gasoline(193°C), the true amount of vaporised fuel may be underestimated during the early stages of evaporation.

Kim et al [73] reported another exiplex system suitable for tracking gasoline fuel that consists of 5 % N,N-dimethylaniline (DMA), 7% 1,4,6-trimethylnapthalene (TMN) and 88% isooctane by mass. However, the high boiling point of DMA will still cause the problem of underestimation of the vapour phase as described above. Excitation at 308nm causes peak vapour and liquid emissions at 350nm and 405nm respectively. Both the spectral separation and exiplex formation were found to be stable at temperatures of up to 145 °C.

Another alternative gasoline exiplex system has been developed by Munch et al. [74]. The system uses a mixture of trimethylamine (TEA) and benzene, the boiling points of which, at 89 °C and 81 °C respectively, are close to that of the substitute fuel, isooctane (99 °C). When mixed at concentrations of 2.9% benzene and 2% TEA in isooctane, a red-shifted exiplex fluorescence was observed in the liquid phase with maximum emission around 350nm, while the vapour phase emission peaked at 290nm when exited at 248nm by a KrF excimer laser.

2.6 Summary

This literature review has shown that the modern engine researcher has many techniques and technologies at their disposal to reduce the fuel consumption and exhaust emissions from IC engines, in order to preserve both the environment and fossil fuel reserves.

Despite the many problems that must be overcome, CAI combustion offers the potential to give simultaneous reduction in both fuel consumption and exhaust emissions. Likewise, the laser diagnostics techniques available for the measurement of in-cylinder flow and fuel distribution have been shown to provide the means to improve engine design both in terms of current and future technologies. As improvements in IC engines continue, it is inevitable that the level of control over combustion that is required will increase. These tools provide means to achieve the highly optimal operating conditions required to maximise the potential of these new control and combustion technologies.

The survey has shown that, while ZEV's, powered by hydrogen generated from renewable sources, may be realised in the long term, there are no technologies available at present that can rival the IC engine in terms of cost and convenience.

The survey has also found that CAI combustion has the potential to achieve future emissions targets without the need for complex and expensive exhaust aftertreatment systems that are currently being developed for use with SI and CI engines. At present, the most efficient powertrain available for passenger cars is the high-speed direct injection diesel type. However, in terms of exhaust emissions, it is the homogenous charge, stoichiometric operated SI gasoline engines that, along with associated exhaust gas aftertreatment technologies, emit the lowest levels of NOx, HC, CO and particulate emissions. Studies reviewed here have shown that a CAI engine can operate at similar efficiencies to the best diesel engines, while emitting a tiny fraction of the NOx and particulate emissions. The required reduction of HC and CO can then be achieved with cheap and robust exhaust gas aftertreatment systems that are already available.

However, the survey has also shown that many problems with CAI must be addressed before it can be considered for series production. The best means of controlling combustion phasing in order to minimise fuel consumption and exhaust emissions is one such question. The application of gasoline direct injection technology to the CAI engine could prove effective in this, while the effect of valve timing on combustion certainly deserves further investigation.

Chapter 3

Experimental Test Facility

Chapter 3 Experimental Test Facility

3.1 Ricardo Hydra Research Engine

3.1.1 General description

The experimental work was completed on an engine test facility consisting of a Ricardo Hydra single cylinder research engine mounted on a Cusson's single cylinder engine test-bed. The engine test-bed comprises a 30 kW DC motor and associated water and oil conditioning systems, which are all controlled by a separate control unit.

During the research the engine was operated in two different configurations. For the PIV and LIEF work, optical accesses were added to the engine via a piston window and a transparent upper liner section. In this configuration the engine was operated in the motored condition only and was limited to a maximum speed of 1200rpm. For the engine experiments with combustion, the optical accesses were removed, allowing the engine to be operated in the fired condition and at engine speeds of up to 6000rpm.

Table 3.1 shows the specifications of the engine as used for the optical work

Table 3.1 Engine Specification

Bore (Extended piston)	80mm
Stroke	89mm
Compression ratio	10:1
Intake Valve Opening (IVO)	12°CA BTDC
Intake Valve Closure (IVC)	56°CA ABDC
Max valve lift (mm)	9
Engine Speed used during tests	1200 RPM

The lubrication system is of the wet sump type, with a remote gravity fed pressure pump powered by an AC motor. Oil is supplied to the crank and camshafts, allowing the bearing surfaces to be lubricated via radial feeds. The oil feed to the crankshaft lubricates the main, big end and small end bearings, the latter via a drilling near the big end of the connecting rod that squirts oil underneath the piston that subsequently falls onto the small end bearing. The piston and piston rings are splash lubricated by the action of the crankshaft passing through the sump oil.

A pair of electrical heaters are immersed in the sump oil to allow reduction in the engine warm up time or to increase the oil to normal operating temperature during motored or very low load operation. A mains water heat exchanger is also included in the oil system circuit and this is fitted with a closed loop control system that can automatically maintain the desired oil temperature. The coolant system also features an electric pump, immersion heater, mains water heat exchanger and closed loop control system.

The DC Dynamometer was used to drive the engine during motored operation, and brake it as required during fired testing. It also features a load cell that allows brake engine torque input/output to be measured. The dynamometer control system allows the desired engine speed to be set and be continually maintained regardless of the engine operating conditions, driving and braking as required.

3.1.2 Cylinder Head

The cylinder head used was a prototype single cylinder direct injection type, supplied by Orbital Engine Corporation Ltd. It featured a centrally mounted air-assisted injector, a pent roof combustion chamber with four valves and double overhead camshafts and mounting hole for a cylinder pressure transducer. Figure 3.1 shows the layout of the combustion chamber, clearly showing the close proximity of the spark plug and injector.

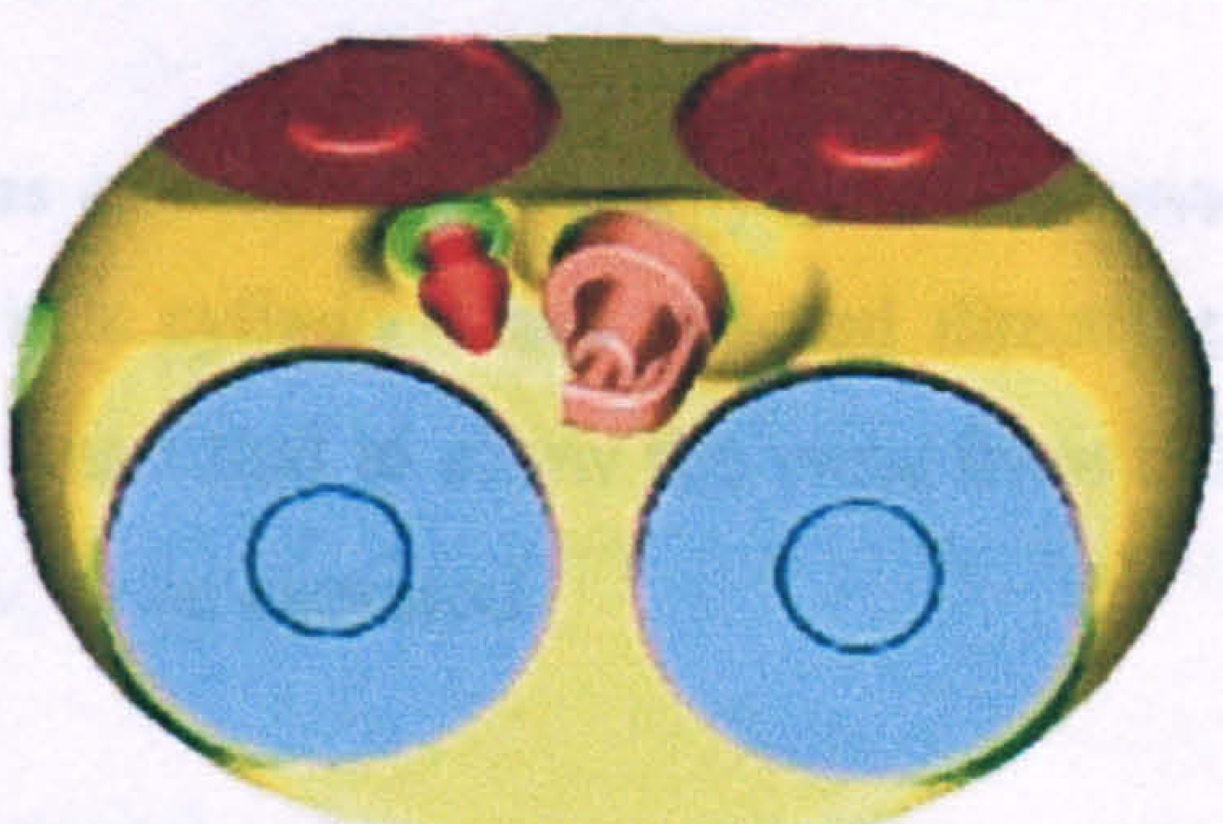

Figure 3.1 Combustion Chamber of Prototype Orbital Cylinder Head (Orbital Engine Corporation Ltd)

3.1.3 Optical Engine Configuration

3.1.3.1 Extended Piston, Cylinder Block and Piston Rings

The extended piston and cylinder block were used to allow optical access to the cylinder bore and combustion chamber via a window in the piston. The extended piston and cylinder block, (often referred to as a Bowditch extension) are shown in Figure 3.2

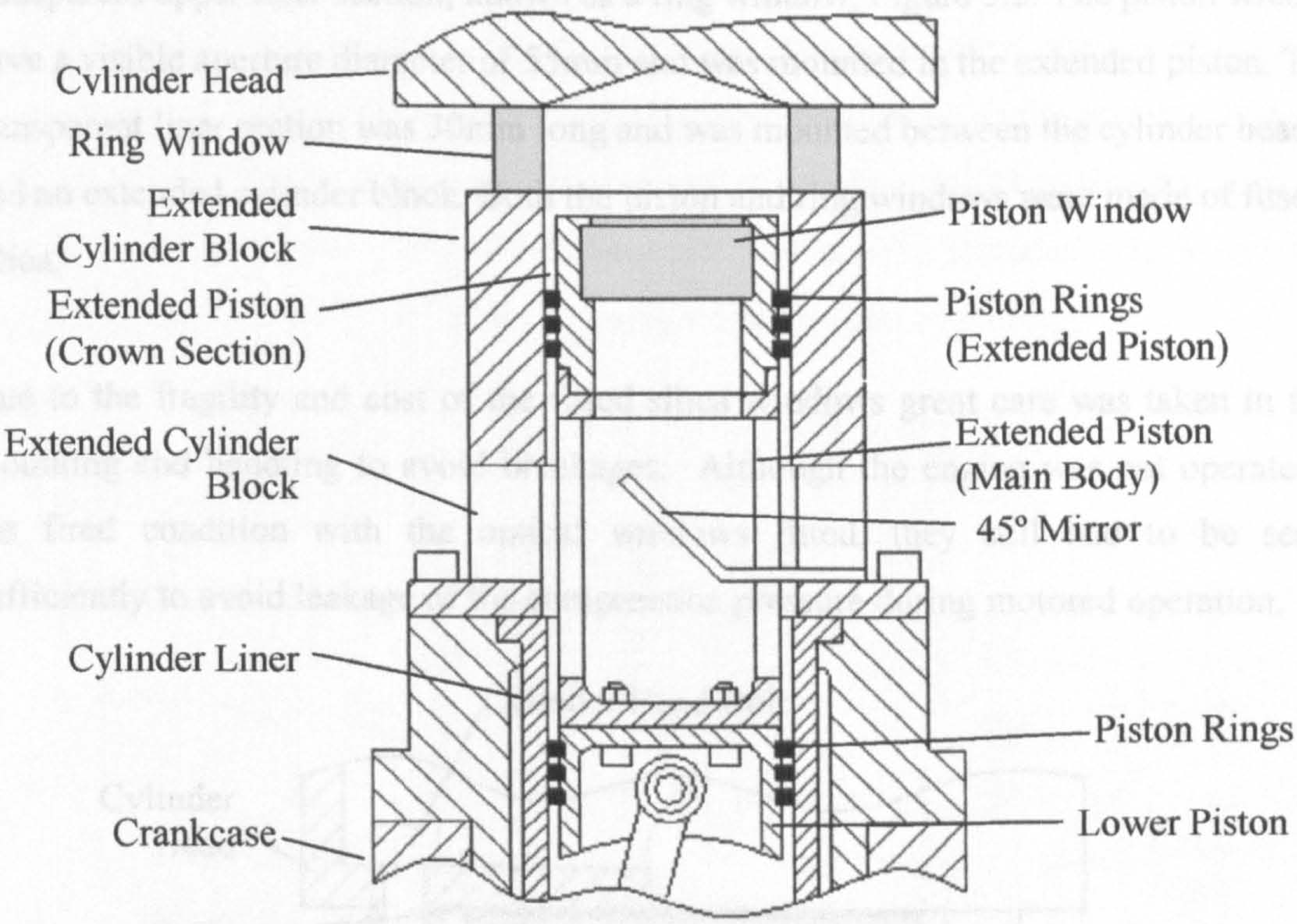

Figure 3.2 Sectional view of the optical engine set-up

The extended piston was attached to a specially modified lower piston by four nuts and bolts. The lower piston ran in a cylinder block attached directly to the engine crankcase. When required, a 45° mirror was fitted to allow the view from below the combustion chamber, via the piston window, to be captured.

To minimise contamination of the optical windows, it is necessary for the extended piston, piston rings and cylinder block to run together unlubricated and hence, conventional steel piston rings cannot not be used. Instead, 3 compression type piston rings made of a PTFE material known as PEEK were used and an engineering drawing for these is shown in Appendix A. Although the piston rings were capable of many hours of use before requiring replacement, their condition could be easily assessed by removing them from the piston and placing them into the cylinder bore. The resulting ring gap could then be measured using feeler gauges and any wear assessed. A gap of up to around 0.5mm was found to be tolerable.

3.1.3.2 Optical Access Windows

To allow the necessary optical access to the area around the combustion chamber during the laser diagnostic work, the engine was equipped with a piston window and a transparent upper liner section, known as a ring window, Figure 3.2. The piston window gave a visible aperture diameter of 55mm and was mounted in the extended piston. The transparent liner section was 30mm long and was mounted between the cylinder head and an extended cylinder block. Both the piston and ring windows were made of fused silica.

Due to the fragility and cost of the fused silica windows great care was taken in their mounting and handling to avoid breakages. Although the engine was not operated in the fired condition with the optical windows fitted, they still had to be sealed sufficiently to avoid leakage of the compression pressure during motored operation.

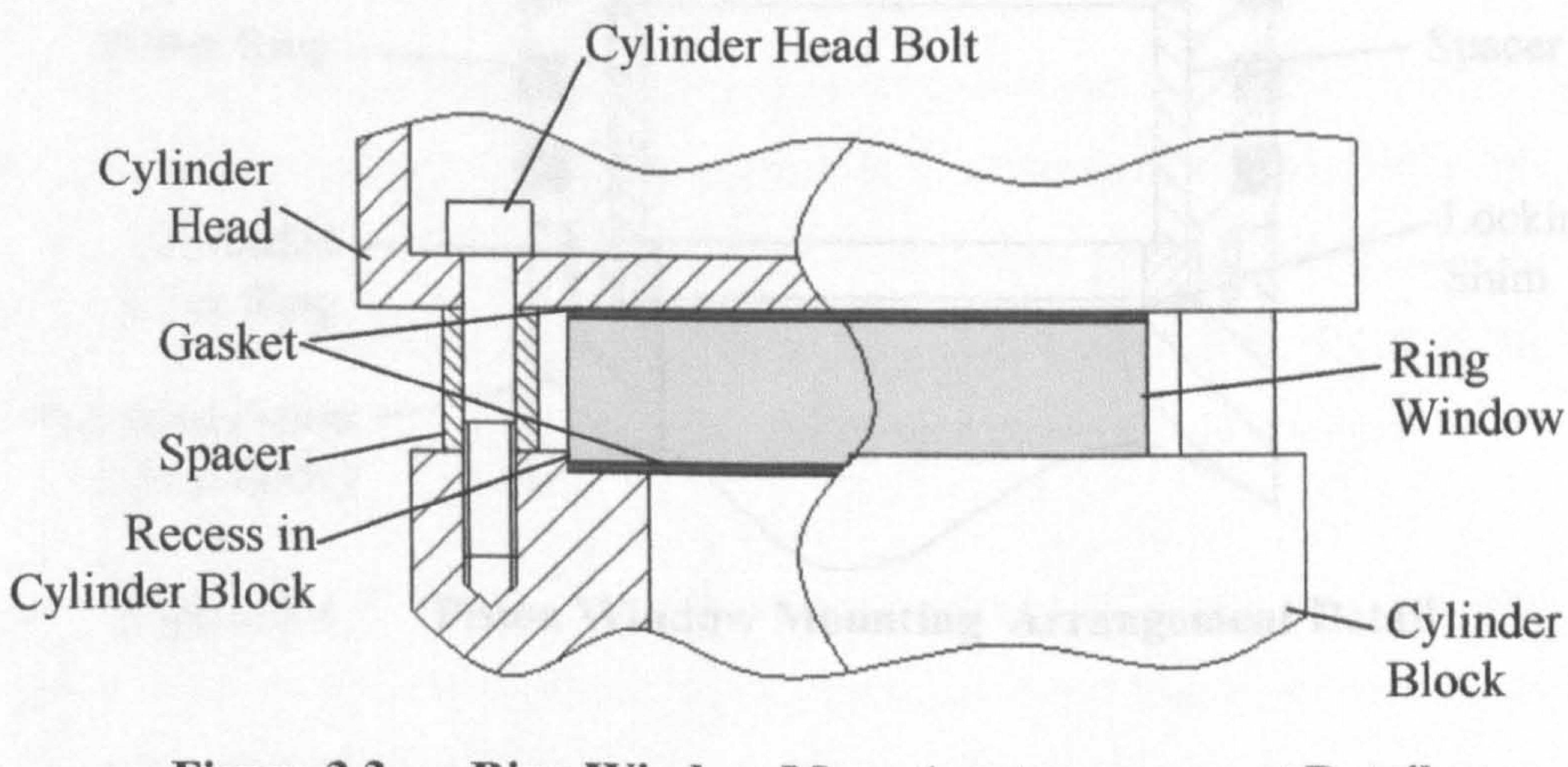

Figure 3.3 Ring Window Mounting Arrangement Detail

The mounting details of the ring window between the extended cylinder block and cylinder head are shown in Figure 3.3. It was located radially by a 3mm deep recess in the top face of the extended cylinder block and was sealed by a 1mm thick silicon rubber gasket on each side. The clamping force required to seal the gaskets was provided by the cylinder head bolts passing through the cylinder head into the cylinder block. In order to ensure that excessive loads were not passed to the ring window, carefully sized spacer posts were placed over the exposed section of the cylinder head bolts. The length of these spacers was chosen to ensure that during cylinder head bolt tightening, the upper and lower window gaskets were each compressed by around 0.3 mm before the spacers became clamped. Once the spacers were clamped further compression of the window gaskets was prevented, thus avoiding excessive loads on the window, whilst ensuring the cylinder head could be attached securely.

The piston window was held within a cavity in the crown section of the extended piston by a threaded ring and this is detailed in Figure 3.4. When fitting the window, the threaded ring was tightened firmly to ensure that the window was held tight but was not subjected to excessive pressure. The distance from the back face of the threaded ring to the bottom face of the piston crown was then measured using feeler gauges. A copper locking shim of this thickness was then manufactured and fitted between the lock ring and the main body of the extended piston This locked the threaded ring in position, preventing the window from becoming loose during engine operation.

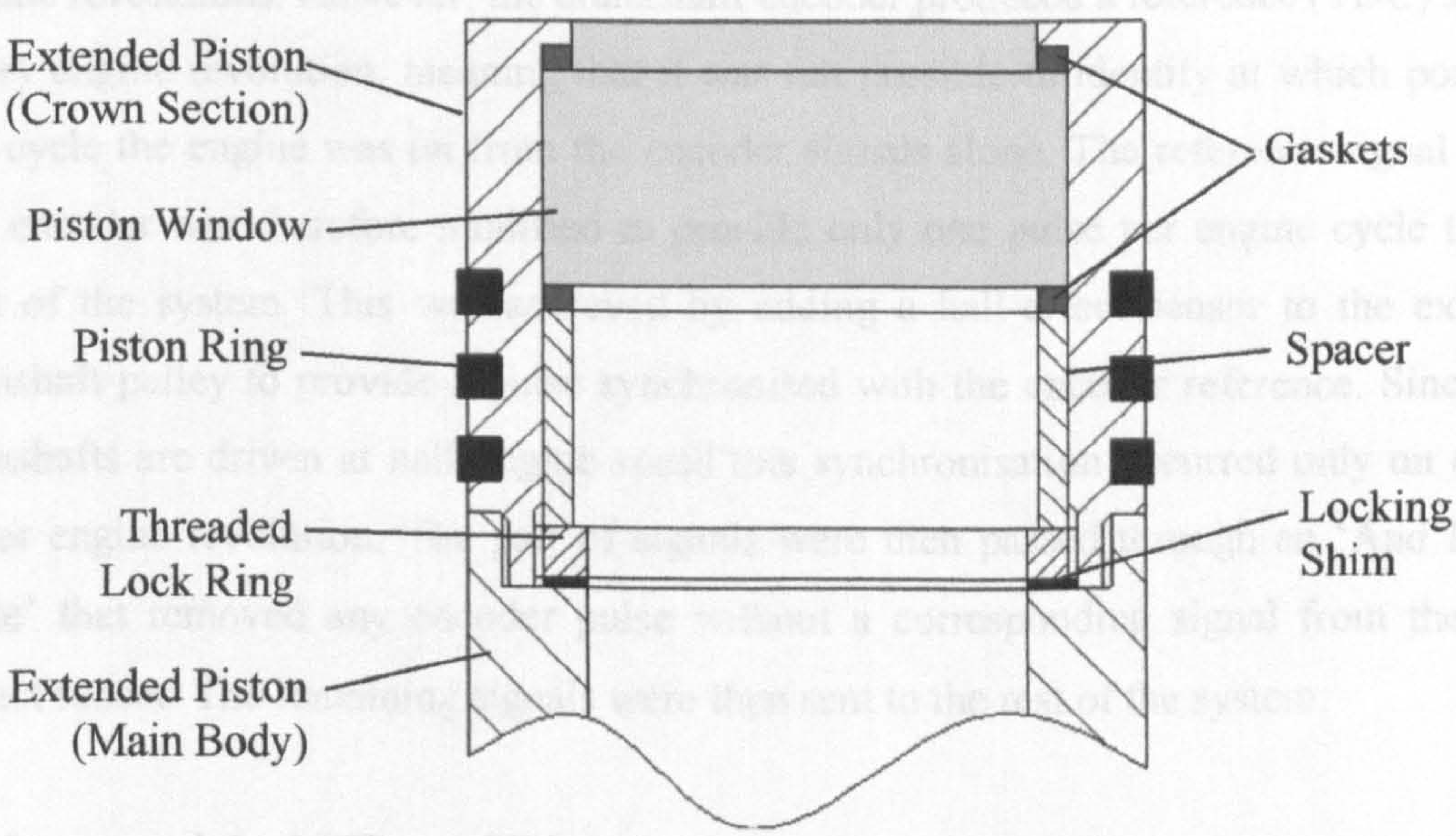

Figure 3.4 Piston Window Mounting Arrangement Detail

The gaskets used either side of the window were made from Klingersil high temperature gasket material of 1.5mm thickness. Following the installation of the piston window with new gaskets it was necessary to inspect and tighten the threaded ring after a short period of running to compensate for any 'settling' of the gaskets that may have occurred. Neglecting this adjustment may allow the window to become loose within the piston, resulting in leakage and damage to the window.

Access to the threaded ring was only possible after the separation of the piston crown and main body. This was accomplished by holding piston crown section in the 3–jaw chuck of a lathe and then unscrewing the main body. In order to minimise any damage to the piston crown section the chuck jaws used were specially modified by boring them to the same diameter as the piston. In order to provide extra support the bottom end of the piston was held using a centrepiece in the tailstock of the lathe.

3.1.4 Crankshaft Position System

To provide information regarding the angular position of the crankshaft, a shaft encoder was fitted to one end of crankshaft. This encoder generated a reference signal with a pulse once every engine revolution and a clock signal with a pulse every degree of rotation. This was then used to control and trigger the fuel injection timing, spark timing, camera exposure, cylinder pressure data acquisition system and laser firing.

Since the engine was of the four-stroke type each complete engine cycle required two engine revolutions. However, the crankshaft encoder produced a reference (TDC) signal every engine revolution, meaning that it was not possible to identify at which point of the cycle the engine was on from the encoder signals alone. The reference signal from the encoder was therefore modified to provide only one pulse per engine cycle to the rest of the system. This was achieved by adding a hall-effect sensor to the exhaust camshaft pulley to provide a pulse synchronised with the encoder reference. Since the camshafts are driven at half engine speed this synchronisation occurred only on every other engine revolution. The pair of signals were then passed through an 'And Logic Gate' that removed any encoder pulse without a corresponding signal from the hall effect sensor. The remaining signals were then sent to the rest of the system.

In the case of the LIEF and PIV optical work signals from the encoder were used to trigger a laser. In order to control the position of the laser trigger relative to crank angle a delay unit was introduced. This allowed the reference signal from the encoder to be delayed from 1 to 999 degrees in 1 degree increments before triggering the laser. Further details of the laser triggering and timing methods for the PIV and LIEF experiments are given in Chapters 4 and 5 respectively.

3.1.5 Air-Assisted Fuel Injection System

The air-assisted injector used was supplied by Orbital Engine Corporation Ltd and is a direct injection spray guided system intended for use on stratified charge SI engines. As shown in Figure 3.5, the system uses a conventional manifold port injector (MPI) injector to meter fuel into a chamber behind the main injector that is connected to the cylinder. The main injector then injects not only the fuel metered by the MPI injector but also a quantity of compressed air into the cylinder. This dramatically improves fuel atomisation, allowing the use of a very low injection pressure which in turn reduces the spray velocity and penetration of the fuel into the cylinder . A typical injection sequence is shown in Figure 3.5. Figure 3.6 shows a schematic of the complete fuel system. The injection system required pressurised supplies of both fuel and air. The air pressure was supplied from a cylinder of compressed air, using a regulator on the cylinder to set and control the supply pressure. The corrosive and degrading effects of the fuel dopants used for the LIF experiments meant that it was not possible to use a conventional fuel pump. Instead, the fuel was supplied by an accumulator type system where a compressed nitrogen cylinder was used to pressurise a sealed cylinder of fuel that was connected to the fuel injector.

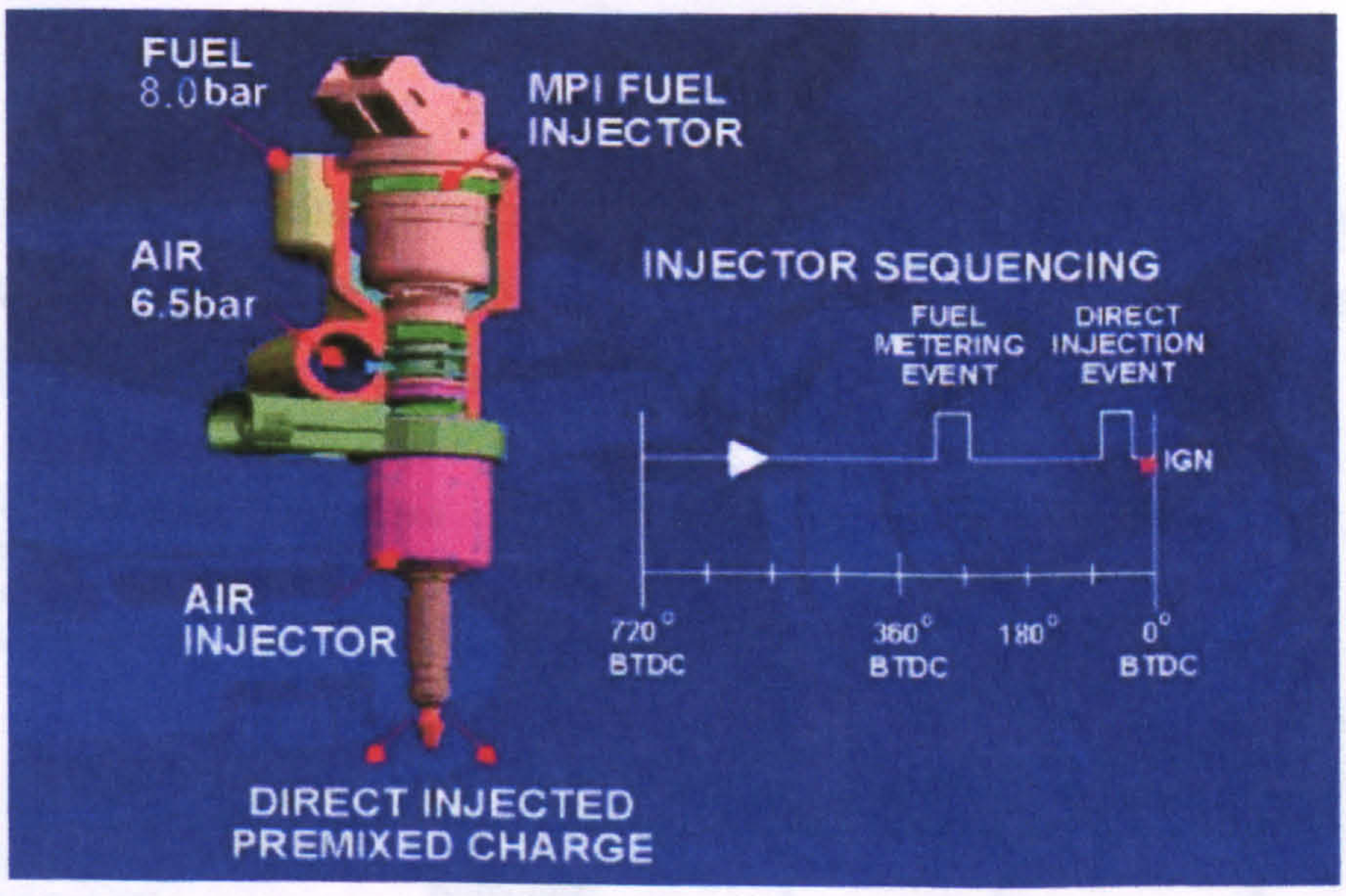

Figure 3.5 Orbital Air-assisted Injector with Typical Injection Sequence (Orbital Engine Corporation Ltd)

The start of injection (SOI) for each injector was controlled by a 2-channel delay unit built specifically for this project. This took the TDC signal from the crankshaft encoder and provided outputs that could be delayed in terms of crank angle to the desired SOI injection time for each injector. The delayed signals then passed to a 2-channel timer unit that was used to set the pulse width and hence end of injection (EOI) time, for each injector. The fuel and air pressures were set at 8 and 6.5 bar gauge pressure respectively.

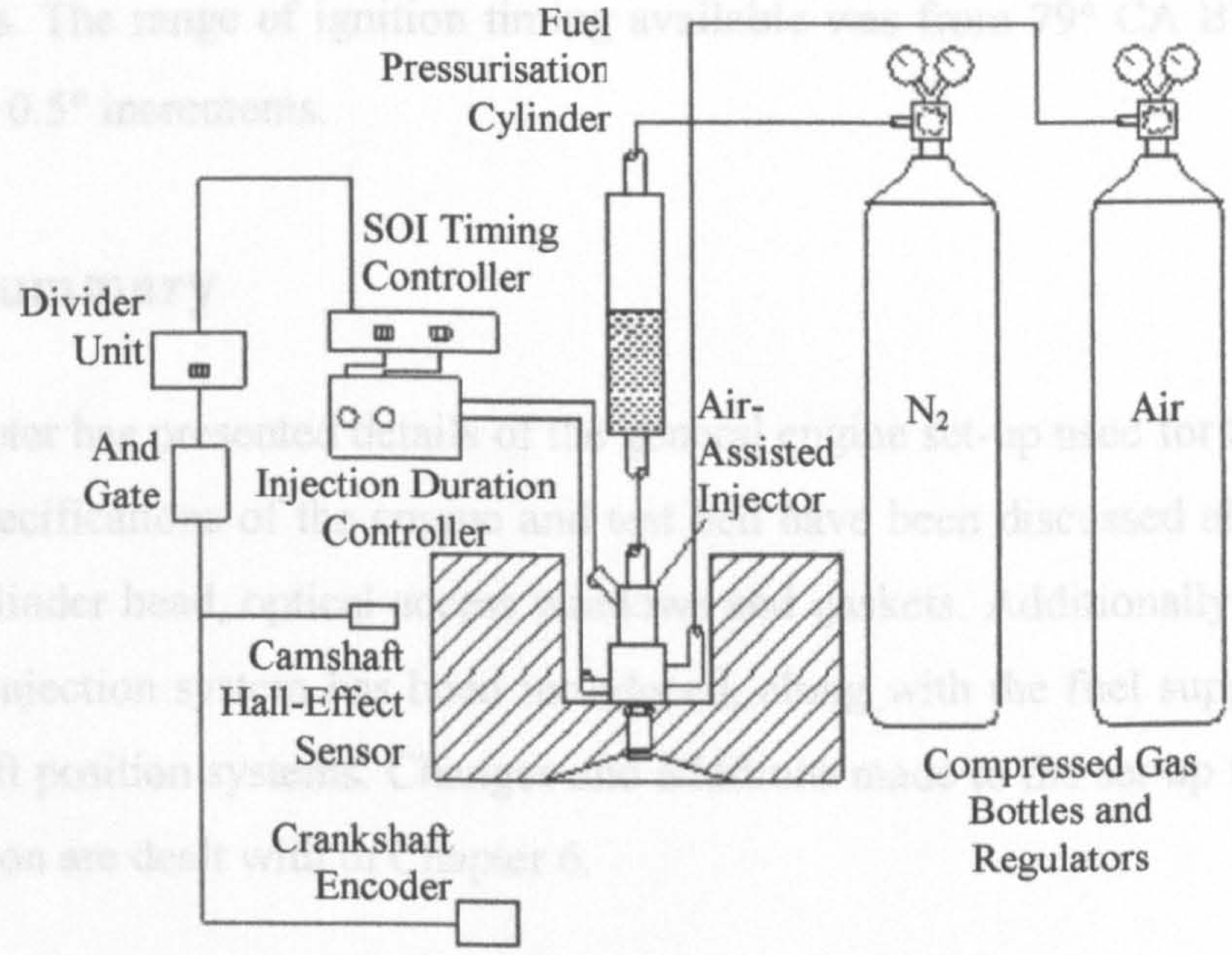

Fig 3.6 Schematic of the Air-assisted Injector Fuel System

3.1.6 Ignition System

Figure 3.7 shows a schematic diagram of the spark ignition system. Clock and reference signals are provided by the crankshaft encoder and camshaft sensor and are modified by the 'And gate' logic unit in the manner described in Section 3.1.4.

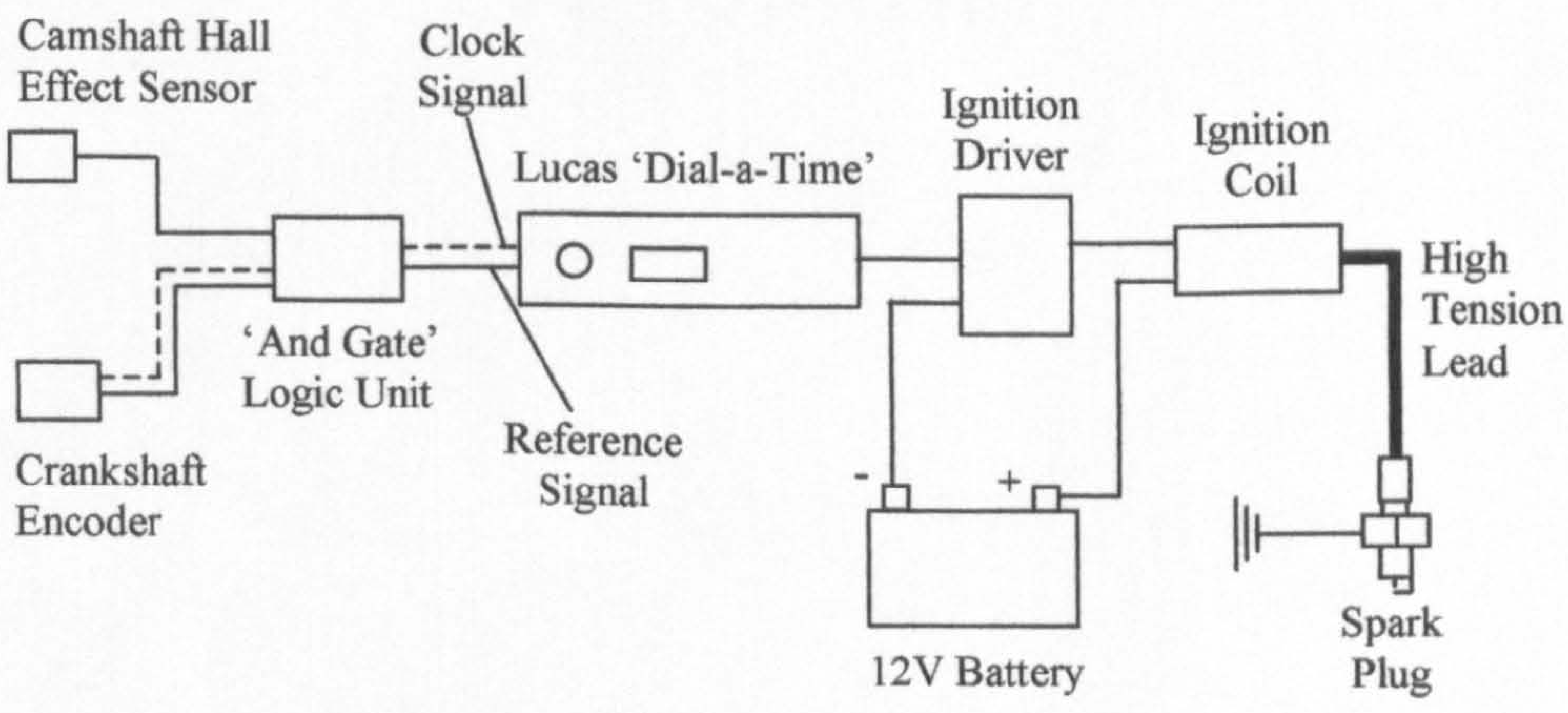

Figure 3.7 Schematic Diagram of Spark Ignition System

In order to allow the spark timing to be advanced from TDC the crankshaft encoder was set to provide the reference signal at 80° CA BTDC on the compression stroke. A Lucas 'Dial-a-Time' unit took the reference and clock signals and output a pulse with the desired ignition timing and coil-on (dwell) time. This was then amplified by the ignition driver unit whose output was used to charge the ignition coil. When the charging current was removed from the coil the field collapsed, causing a spark to jump the spark plug electrodes. The range of ignition timing available was from 79° CA BTDC to 45° CA ATDC in 0.5° increments.

3.2 Summary

This chapter has presented details of the general engine set-up used for the experimental work. Specifications of the engine and test bed have been discussed along with details of the cylinder head, optical access windows and gaskets. Additionally, the Orbital air-assisted injection system has been introduced, along with the fuel supply, ignition and crankshaft position systems. Changes and additions made to the set-up for the tests with combustion are dealt with in Chapter 6.

Chapter 4

In-Cylinder Flow Field and Liquid Fuel Spray Measurement using Particle Image Velocimetry

Chapter 4 In-Cylinder Flow Field and Liquid Fuel Spray Measurement using Particle Image Velocimetry

4.1 Introduction

It is known that the details of in-cylinder flow greatly affect performance and emissions of IC engines. The ever-increasing drive for reduced emissions and increased efficiency has lead to the introduction of combustion systems that rely heavily on particular in-cylinder flow regimes to perform optimally. These include high swirl DI diesel systems and, more recently, stratified charge GDI engines. In addition, large scale flow structures are often used in homogenous SI engines to maintain the flow's kinetic energy until the end of the compression stroke, where they break down into micro scale turbulence, promoting early flame kernel growth and increased flame speed. Despite the development of ever more powerful CFD modelling tools that are of great value to designers of such combustion systems, their limitations mean that experimental validation of models using such techniques as particle image velocimetry (PIV) will still be required for the foreseeable future.

In a similar manner, PIV has more recently been used to the study the motion of liquid fuel droplets emerging from fuel injectors. Though less widespread than the study of in-cylinder flows the technique has been applied to both diesel and GDI injection systems [6, 36].

After discussing the history of flow field measurement and the concept of particle image velocimetry, this chapter will go on to discuss the application of a PIV system to the Ricardo Hydra engine described in Chapter 3. This will be followed by a discussion of the results obtained.

4.1.1 History of Flow Field Measurement

The methods available for the measurement of in-cylinder flow fields can be categorised as either single point or whole field measurement techniques. Single point measurements can be completed using such techniques as hot wire anemometry (HWA) and laser Doppler anemometry/velocimetry (LDA/LDV). While these techniques, (particularly LDA), can provide useful point wise data, the in-cylinder flow within IC engines is complex, unsteady and turbulent. Though useful, the time-averaged data that can be obtained from a limited amount of point wise measurements cannot fully describe the unsteady flow encountered with the IC engine. For this reason, techniques capable of measuring the whole flow field have been developed. Though in the early development of IC engines qualitative flow measurements were obtained by the introduction of such mediums as smoke and feathers into the cylinder, the era of quantitative whole field measurement began with the development of particle tracking velocimetry (PTV) and particle image velocimetry (PIV). These techniques have enabled the recording of instantaneous, cycle resolved, two-dimensional velocity maps across extended measurement planes within the cylinder. With these measurements systems, small seeding particles are introduced to the flow, normally via the intake port, and are subjected to intense stroboscopic illumination that allows their position to be recorded either electronically or photographically at two or more instants in time. In PTV measurements, particles are identified and matched between two exposures within a known timeframe, enabling their velocity to be determined. However, there are several difficulties with PTV that, while not prohibitive to obtaining useful results, limit their applications. The requirement of a light source that can provide long pulses tends to mean that illumination is of low power density and hence requires the use for large seed particles in order to scatter sufficient light. In addition, low seeding densities must be used to avoid confusion of seed pairs during analysis, resulting in sparse flow fields that require significant interpretation or ensemble averaging.

The development of PIV has allowed flow field measurements to be obtained with high spacial resolution. In these measurements, the movement of seed particles is captured by two short duration, high energy, thin laser sheet pulses. From this, the mean velocity within each small interrogation area of the image is determined via spacial correlation such that no identification of distinct, individual particles is required. This allows the use of high seeding densities and hence a more comprehensive velocity map than can be obtained with PTV. The use of a power dense illumination source allows the use of micron sized particles that can track high frequency flows and the technique appears suitable for the measurement of both large scale and small-scale motions.

Though in the area of IC engine research, the PIV technique is primarily applied to the study of airflow, it has also been used to measure the motion of liquid fuel sprays. This application of the technique is essentially the same as that described above but in this case the liquid fuel droplets are used as markers and no extra seed particles are added. Though there are problems associated with this use of the technique, mainly concerning the obvious lack of control over the size and density of the seeding particles, some studies have yielded useful results.

For these reasons, the PIV technique has been adopted in this work to study the in-cylinder flow of air and liquid fuel spray within a single cylinder engine with an Orbital GDI cylinder head and air-assisted injection system.

4.2 Principle of Particle Image Velocimetry

A PIV system operates by calculating velocity vectors from the displacement of distinct elements of fluid within a flow field over a known time interval. In the most common set up, (also used in this study), a thin laser sheet is used to illuminate the measurement plane of interest, causing seeding particles introduced to the flow to scatter light. This scattered light is then detected and recorded digitally using a CCD camera placed perpendicular to the measurement plane. The light sheet is double pulsed at a very short and known time interval ΔT. If the scattered light from the two laser pulses are recorded separately, a pair of images showing the flow field frozen at each point in time can be obtained. The first of the two images will show the initial position of the seeding particles, while the second will show their final position caused by the displacement of the flow field. The area of the laser sheet intersected by the camera's field of view is known as the measurement region. The smallest resolvable area of the camera, known as the interrogation area, projected back onto the measurement region determines the interrogation volume that constitutes a single velocity vector.

The particle displacements at the camera, ΔX and ΔY along with the magnification factor M give the displacements at the measurement plane, Δx and Δy.

$$\Delta x = \frac{1}{M} \Delta X \text{ and } \Delta y = \frac{1}{M} \Delta Y \qquad (4.1)$$

Knowing the time interval, ΔT, between the two laser pulses, the velocities at the measurement plane, u and v, may be found from

$$u = \frac{\Delta x}{\Delta T} \text{ and } v = \frac{\Delta y}{\Delta T} \qquad (4.2)$$

If the process is repeated for each interrogation region, a velocity map can be built up showing the velocity vectors for the whole measurement region.

4.3 Experimental Set-up

4.3.1 Illumination

4.3.1.1 Laser

Use of a suitable illumination source is central to the realisation of successful PIV experiments. Not only is a source with a high energy density required to scatter sufficient light from the small particles in the densely seeded extended flow field, but also the pulse width must also be short enough to freeze the flow.

For these reasons lasers are ideally suited to this application. However, the suitability of laser types depends on their output wavelength. A wavelength in the green region is highly desirable since it will increase the average intensity of a particle image. Because of this, the most popular type for PIV experiments is the frequency doubled Nd:YAG pulsed laser.

The PIV technique requires the delivery of two laser pulses with very small separation and there are two means of achieving this with Nd:YAG lasers. One method is to gate one flash lamp discharge from a single cavity laser to provide the two pulses. This method has the disadvantage that both pulses will be of greatly reduced intensity compared to one pulse in the normal operating mode. In addition, pulse separations are typically limited to a range of 20μs - 200μs and pulse separation will affect both the intensity and width of the laser pulse. Therefore, use of a twin oscillator, twin amplifier type laser is preferred since this allows infinite and independent control over the separation, width and intensity of the pulses, though this can also be achieved by co-ordinating a pair of co-aligned single cavity lasers. For this work the latter option was chosen with the 2nd harmonic output of 532nm from a pair of frequency doubled, Nd: YAG lasers co-aligned using a beam combination optics box situated in front of the laser. Figure 4.1 shows a schematic of this PIV set-up. Control of the overall laser phasing, individual pulse timing and laser energy was achieved using a counter delay unit and pulse delay generator. Figure 4.2 shows a timing diagram for the PIV system. The counter unit was used to phase the overall laser outputs to the crankshaft position of interest. This unit takes an input of the clock signal from the crankshaft encoder at every degree of rotation and a reference pulse from the crankshaft encoder logic box every complete engine cycle. The crank angle of interest was set on a decade counter on the front of the unit. After receiving a reference pulse from the logic box, the unit then counted the reference pulses from the encoder until the programmed crank angle was reached. At this point the signal was then sent on to the pulse delay generator. This unit then sent out four appropriately timed signals to fire the flash lamps and Q switches of the two lasers respectively to deliver two light pulses with the required separation, intensity and pulse width.

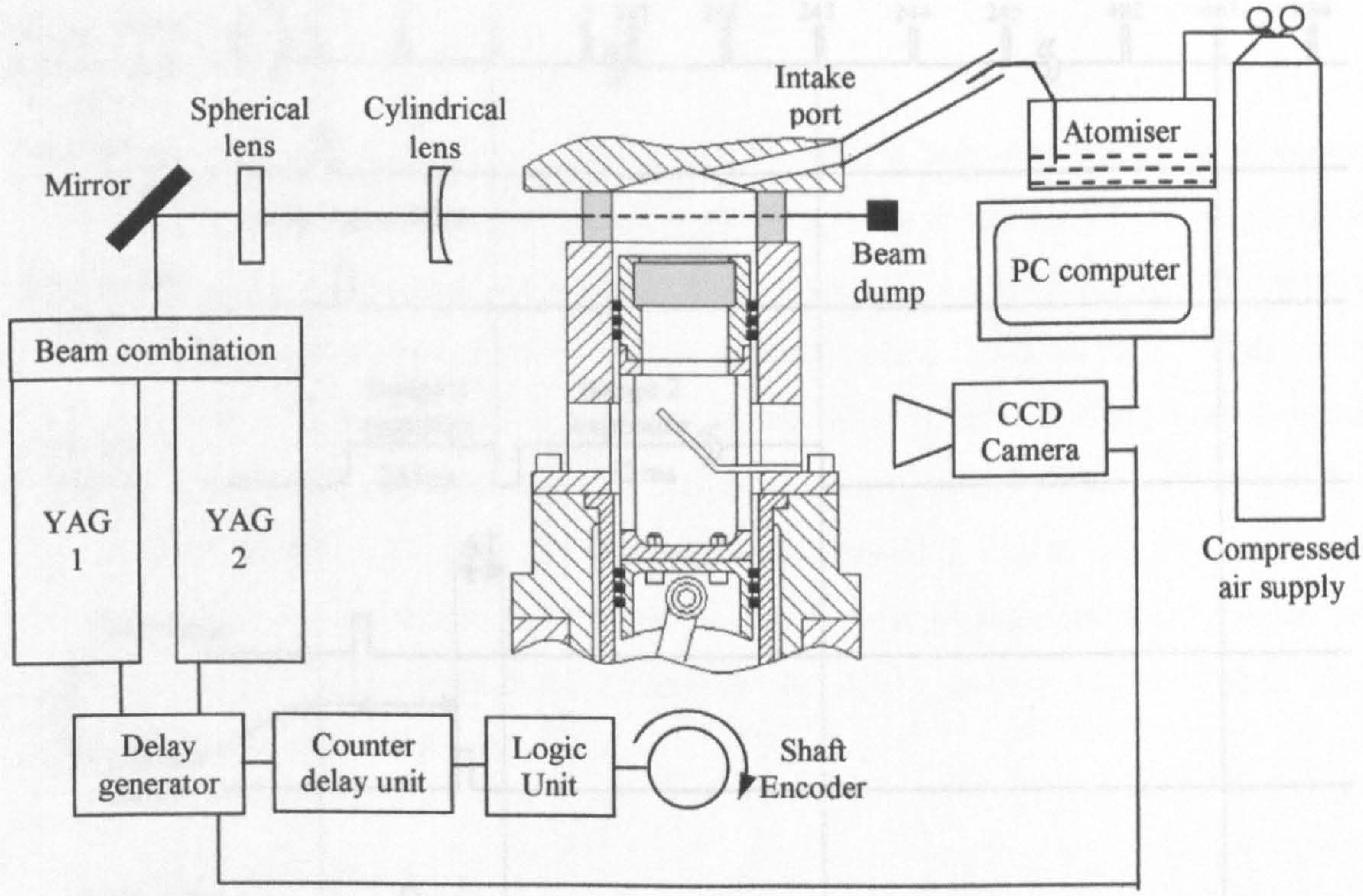

Figure 4.1 Schematic Diagram of the PIV System

4.3.1.2 Laser Optics

As already discussed, illumination for the PIV technique requires the generation of a thin, high intensity light sheet in order to illuminate the measurement plane within the cylinder. The output beam of the lasers used measured approximately 30mm diameter. The laser sheet was formed by first concentrating this beam down to a waist thickness of 425μm, using a spherical lens with a focal length of 1 metre. This was then expanded in one direction using a concave cylindrical lens with a –76mm focal length to form the laser sheet. The orientation of the cylindrical lens was changed according to whether a vertical or horizontal plane was to be measured. This arrangement is shown in Figure 4.1. Adjustment of the sheet thickness and sheet height was achieved by shifting the longitudinal positions of the two lenses in relation to the beam combination box and the desired measurement plane. Since the lasers were some distance away from the engine, a series of mirrors were used to deliver the beam/sheet to the measurement plane.

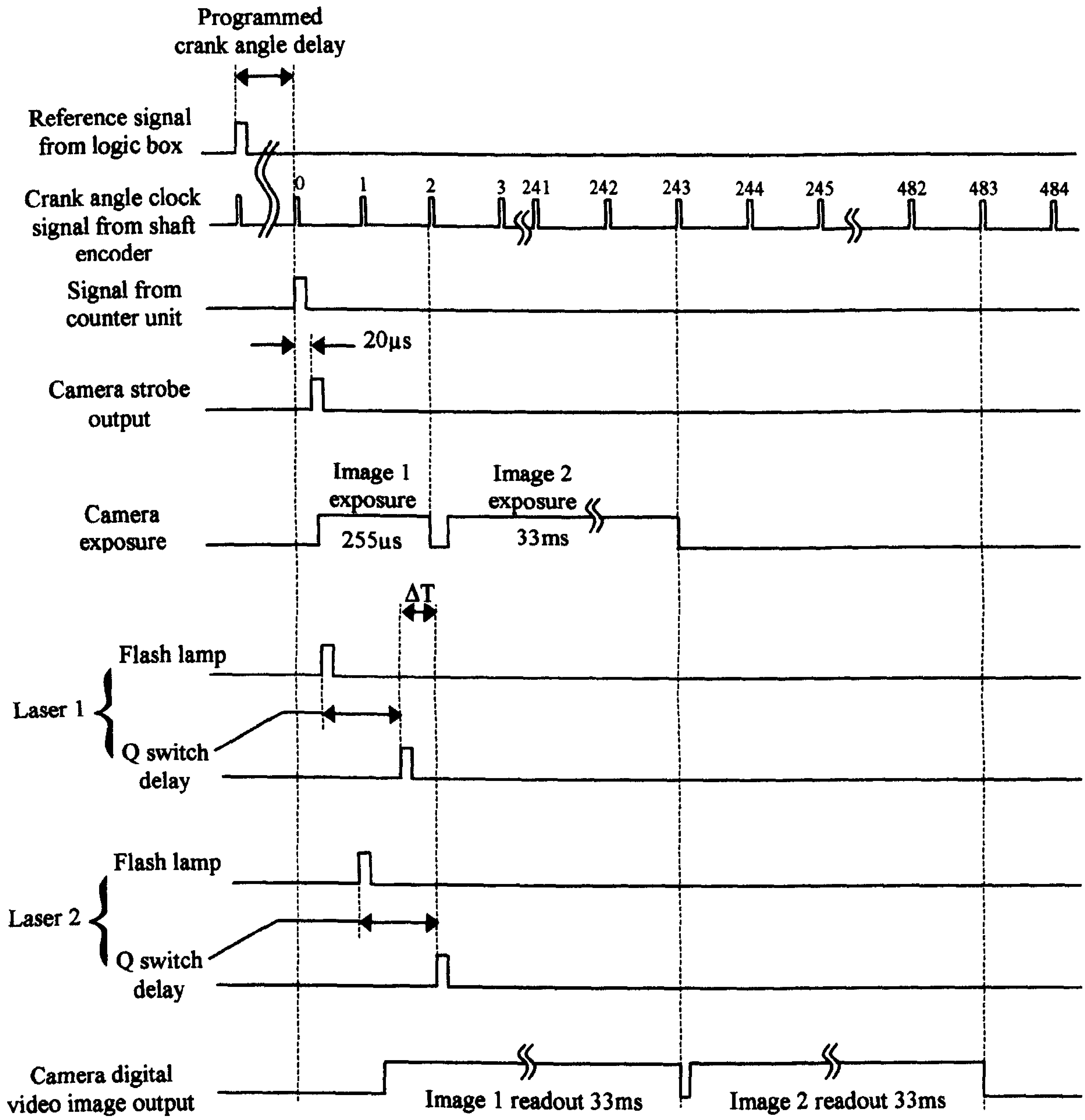

Figure 4.2 PIV System Timing Diagram

4.3.1.3 Flow Seeding

Selection of a suitable flow seeding medium is critical to the performance of a PIV system. Likewise, the flow seeding density must be carefully controlled if the system is to give the best results. When selecting the seed material the following properties must be considered:

- Ability to follow flow field faithfully
- Light scattering characteristics of particles
- Tendency to fowl optical windows
- Tendency to wear engine operating surfaces

- Ability to withstand in-cylinder temperatures during fired or motored operation as required

Solid particles are rarely used in engine measurements since they can cause large problems with regard to window fouling and engine wear. Therefore, a liquid aerosol is a common choice of seeding.

Some studies have used atomised vegetable oils as seeding but experiments by Reeves et al. [87] found that under some conditions this can evaporate at the end of the compression stroke. However, they also reported that high temperature silicon oil droplets could survive the complete engine cycle without difficulty. For this reason a fine mist of 0.5-5μm silicon oil droplets were used as the seeding medium. These were generated using a jet atomiser, manufactured by TSI Inc, which operated by passing compressed air at approximately 3 bar gauge pressure through a bath of silicon oil as illustrated in Figure 4.2. Precise control of the seeding density was achieved by adjusting a low-pressure regulator incorporated into the atomiser unit. The droplets were carried in the intake airflow to the engine via a flexible tube connected to the intake port.

4.3.2 Image Collection

4.3.2.1 Camera and Frame Straddle Technique

The pairs of particle images were recorded digitally using a Kodak Mega plus CCD camera with a resolution of 1008x1018 pixels and 9μm pixel spacing. The camera was operated in its 'triggered double exposure' mode that allowed a 'frame straddled' pair of particle images to be captured within 300μs of receiving an external trigger signal. The timing diagram shown in Figure 4.2 shows the various camera and laser events that take place during the capture of a pair of 'frame straddled' images. On receiving the external trigger signal from the delay generator, (Figure 4.1), the camera outputs a strobe trigger that initiates two exposure sequences in 20μs. The first exposure lasts 255μs, finishing about 2° CA after the external trigger signal is sent when operating at an engine speed of 1200 RPM. The second exposure lasts 33ms, ending about 243°CA after the trigger is received. Meanwhile, the delay generator also controls the firing of the two lasers. These delay times are set so that the first laser pulse is located towards the end of the first image exposure and the second laser pulse is sent near the start of the second exposure. In this way a pair of images separated by a short time interval, ΔT, are captured. The optimum value of ΔT is mainly dependant on the maximum flow velocity being measured at that time and therefore must be altered according to engine operating conditions, measurement plane and the point in the engine cycle being measured and will be discussed further in Section 4.3.3. Initially, the first image is stored in the on-board register. However, during the second exposure the data is transferred from the camera to a frame grabber in the PC computer. Once the second exposure is complete, it is transferred directly to the PC frame grabber. This immediately passes the image data on to the PC memory. This complete sequence takes about 483°CA to complete at an engine speed of 1200 RPM. When the next trigger signals arrive the sequence begins again.

4.3.2.2 PC Computer and Software

The PC computer used to store and process the PIV images was equipped with twin Intel Pentium II processors, 128MB of RAM and an image collection card by TSI Inc. The software package used to acquire the particle image pairs, perform the on-line post processing and display the velocity vectors was Insight 2.0 also by TSI Inc. Image post processing mainly involved the cropping of images down to the size of the optical window field of view, removal of spurious vectors and smoothing of the resulting vector map and will be discussed in further detail in Section 4.4. In addition, Tecplot software was installed on the PC and this was used to plot the raw vector data files as velocity vector flow maps. These images were then exported as TIFF image files that could be easily imported into Microsoft Word for presentation.

4.3.2.3 Optimisation of PIV Measurements

Optimisation of the PIV system involved finding the best settings for laser output and pulse duration and separation (ΔT) and seeding density as well as camera focus and f-number. These were found by trial and error during the system set-up and commissioning process.

In order to provide sharper particle images the camera was set to use a small f- number of 2.8 or 4. This had the advantage that less laser power was required, leading to less background light in the images from reflections etc. The magnification factors used were 1/1.78 for measurements in the vertical plane through the ring window and 1/10.2 for horizontal measurements through the piston window. This gave an estimated depth of field of 1.5mm, considerably larger than the light sheet thickness.

The laser energy and pulse width used were 200mJ and 30ns respectively. The laser separation, ΔT, was varied between 30μs during the compression stroke and 10μs during the intake stroke in order to compensate for changes in the flow velocities, while 15μs was found to be most suitable for the fuel spray measurements. For the airflow measurements seeding density was controlled by adjusting the pressure regulators on the atomiser and compressed air supply and the optimum settings were found to be 1.5 and 3 bar gauge respectively.

Accurate alignment of the two laser sheets was found to be paramount to the correct functioning of the PIV system. For this reason the sheet alignment was checked and adjusted as required before each set of measurements.

4.4 Evaluation of Displacement Vectors

Evaluation of the displacement vectors from the particle images was performed by the Insight software package, using the cross-correlation method. In this method, the particle images are subjected to an interrogation process where each image is divided into a number of square interrogation areas. The velocity vector in each interrogation area is then evaluated using the cross-correlation technique. Though the cross-correlation function is calculated by the software using FFT algorithms, the following text describes the mathematical background of the cross-correlation technique.

First of all, the particle image intensity distribution of each interrogation area for each exposure in the image pair must be found. In each interrogation area there is a random distribution of particle images that correspond to a certain pattern of N particles in the flow:

$$\Psi = \begin{pmatrix} x_1 \\ x_2 \\ \bullet \\ \bullet \\ x_N \end{pmatrix} \tag{4.3}$$

with

$$x_i = \begin{bmatrix} \mathrm{X}_i \\ \mathrm{y}_i \\ \mathrm{z}_i \end{bmatrix}$$

where Ψ is the state of the particle ensemble at a given time t and x_i is the position vector of the particle i at time t, in the interrogation volume of the laser sheet.

In the following analysis, capital case letters refer to the co-ordinates in the image plane so that:

$$\mathrm{X} = \begin{pmatrix} \mathrm{X} \\ \mathrm{Y} \end{pmatrix}$$

Lower case letters are used to represent the co-ordinates in the measurement plane so that, with magnification factor M;

$$\mathrm{x} = \mathrm{X/M} \quad \text{and} \quad \mathrm{y} = \mathrm{Y/M}$$

The image intensity of a single exposure can therefore be written as [88]:

$$\mathrm{I}\,(\mathrm{X}, \Psi) = \sum_{i=1}^{N} \mathrm{P}(x_i)\,.\,\tau\,(\mathrm{X} - \mathrm{X}_i) \tag{4.4}$$

Where $\tau\,(\mathrm{X} - \mathrm{X}_i)$ is the point spread function of the imaging lens and describes the impulse response of the imaging lens. $\mathrm{P}(x_i)$ is the system transfer function, giving the light energy of the image of an individual particle i inside the interrogation area IV and its conversion into an electronic signal.

The next stage is to calculate the cross correlation of the interrogation areas for the pair of exposures. At this point it is advantageous to offset the two interrogation areas according to an estimated mean particle displacement [89]. This increases the fraction of matched to unmatched particle images, thereby increasing the signal to noise ratio at the correlation peak. The cross correlation function for each pair of interrogation areas is then calculated and the peak displacement vector is determined, which corresponds to the particle image displacement vector.

In the following analysis, we assume that there is a constant displacement, d, of all particles inside the interrogation volume. Thus, the particle locations at the second exposure can be given by:

$$x'_i = x_i + \mathrm{d} = \begin{bmatrix} \mathrm{x}_i + d_x \\ \mathrm{y}_i + d_y \\ \mathrm{z}_i + d_z \end{bmatrix} \tag{4.5}$$

and the corresponding particle image displacement is given by:

$$D = \begin{bmatrix} M \,.\, d_x \\ M \,.\, d_y \end{bmatrix}$$

The intensity distribution of the interrogation area for the second exposure can therefore be described as:

$$I'(X, \Gamma) = \sum_{j=1}^{N} P'(x_j + d) \,.\, \tau (X - X_j - D) \tag{4.6}$$

Likewise for the first image

$$I (X, \Gamma) = \sum_{i=1}^{N} P(x_i) \,.\, \tau (X - X_i) \tag{4.7}$$

The cross-correlation function of the two interrogation areas can then be written as:

$$R_{II'} (s,\Psi,d) = \langle I (X, \Gamma) \,.\, I' (X + s, \Gamma)\rangle$$

$$= \frac{1}{A_I} \sum_{i,j}^{N} P(x_i) \,.\, P\tau (x_j + d) \int_{A_I} \tau (X - X_i) \,.\, \tau (X - X_j + s - D).\, dX \tag{4.8}$$

where s is the separation plane in the correlation plane. By distinguishing the $i \neq j$ terms, which represent the correlation of different particle images and therefore randomly distributed noise in the correlation plane, and the $i = j$ terms which contain the desired displacement data, we arrive at the following expression:

$$R_{II} (s,\Psi,d) = \frac{1}{A_I} \sum_{i\neq j} P(x_i) \,.\, P (x_j + d) \int_{A_I} \tau (X - X_i) \,.\, \tau (X - X_j + s - D).\, dX$$

$$+ \frac{1}{A_I} \sum_{i=j} P(x_i) \,.\, P (x_j + d) \int_{A_I} \tau (X - X_i) \,.\, \tau (X - X_i + s - D).\, dX$$

or

$$R_{II} (s,\Psi,d) = \sum_{i\neq j} P(x_i) \,.\, P (x_j + d).\ R_\tau (X_i - X_j + s - D)$$

$$+ R_\tau (s - D) \sum_{i=j} P(x_i) \,.\, P (x_i + d). \tag{4.9}$$

which can be split into three parts:

$$R_{II}(s,\Psi,d) = R_C(s,\Psi,d), R_F(s,\Psi,d), R_D(s,\Psi,d) \quad (4.10)$$

where the first two terms R_C and R_F contribute to the background noise in the correlation plane, both resulting from the $i \neq j$ terms. $R_D(s,\Psi,d)$ represents the component of the cross correlation function that corresponds to the correlation of images of particles obtained from the first exposure with images of identical particles obtained from the second exposure ($i = j$ terms) i.e.

$$R_D(s,\Psi,d) = R_\tau(s - D) \sum_{i=j} P(x_i) \,.\, P(x_i + d). \quad (4.11)$$

Hence, this displacement correlation reached its peak at $s = D$, which means that the average particle image displacement vector D can be determined from the maximum of the displacement correlation distribution in the correlation plane, with the sign of D defining the direction of flow.

Although the particle image displacement vector D can be calculated using Equation 4.8, the cross correlation calculations performed by the Insight software employs fast Fourier transform (FFT) algorithms.

The correlation theorem states that the cross-correlation of two functions is equivalent to a complex conjugate multiplication of their Fourier transforms,

$$R_{II} \Leftrightarrow \hat{\mathbf{I}} \,.\, \hat{\mathbf{I}}'^{*} \quad (4.12)$$

where $\hat{I}$ and $\hat{I}'$ are the Fourier transforms of the functions I and I' respectively. The cross correlation function can therefore be calculated by computing two two-dimensional FFT's on equal sized samples of the image, followed by a complex-conjugate multiplication of the resulting Fourier co-efficients.

In this work, the interrogation area used was either 32 x 32 or 64 x 64 pixels and the Gaussian algorithm was used to determine the correlation peak and hence, particle displacement in that region. The ratio of the velocity peak intensity to average intensity, (the summation of pixel intensities in the correlation area excluding zero peak and velocity peak areas), was used to judge whether the vector was valid or not.

4.5 Post Processing of PIV Data

4.5.1 Removal of Spurious Vectors

Following the capture and cross-correlation analysis of the particle image pairs, some degree of post processing is normally required. A typical in-cylinder vector map may contain 5 to 10% spurious velocity vectors, while spray PIV images may contain more than 40%. These may be caused by noise or rogue material in the images or missing particle pairs, due to large amounts of flow across the measurement plane, particularly during the intake stroke, may also result in spurious vectors. In addition, spurious vectors may arise in spray images from dense areas of spray or unsuitably sized fuel droplets. These outliners, as they are called, were removed using post-processing algorithms included in the Insight software. The one employed in this case was a standard deviation operator where any velocity vectors that exceed a user defined standard deviation from their neighbours were removed.

4.5.2 Smoothing Velocity Vector Maps

Since the removal of outliners leaves voids in the velocity map without vectors, the Insight software incorporates a smoothing function that allows these holes to be filled. The missing vectors are replaced with a mean velocity of the neighbouring vectors using a two dimensional linear interpolation method.

It is possible that some high frequency velocity fluctuations, due to random measurement errors, may be present due to the combined effects of velocity gradients, particle size and number and turbulence structure. Therefore, if required, continuity of the velocity map can also be improved by using the Insight smoothing function. In this case, vectors were smoothed using the convolution of the two-component vector with an axisymmetric Gaussian kernel [35].

4.6 Calculation of Flow Parameters

Results from airflow PIV experiments are normally presented as velocity maps of ensemble averaged data. Though these maps are useful and can be quite telling with regard the state of the in-cylinder flow, the calculation of certain flow parameters can yield quantitative, absolute data on the flow field, making assessment and comparison of the flow characteristics much easier. The following sections will discuss the various flow parameters calculated in this work.

4.6.1 Mean Velocity

The ensemble-averaged mean velocity was calculated at each crank angle as follows:

$$\vec{U}_{EA(x,y)} = \frac{1}{N}\sum_{i=1}^{N}\vec{U}_{(x,y,i)} \tag{4.13}$$

where N is the total number of cycles, $\vec{U}_{(x,y,i)}$ is the two-dimensional instantaneous velocity vector at the point (x, y) at the i^{th} the cycle.

4.6.2 Velocity Fluctuation

This is a measure of the cycle-to-cycle velocity fluctuation of the instantaneous velocity about the ensemble-averaged mean velocity and can be described using the following equation:

$$\vec{u}_{F(x,y,i)} = \vec{U}_{F(x,y,i)} - \vec{U}_{EA(x,y)} \tag{4.14}$$

In general, the ensemble averaged root mean square (RMS) of the fluctuating velocity is used to represent the fluctuation intensity and can be obtained from the following equation,

$$\vec{u}'_{F,EA(x,y)} = \sqrt{\frac{1}{N}\sum_{i=1}^{N} u^2_{F(x,y,i)}} \tag{4.15}$$

and

$$v'_{F,EA(x,y)} = \sqrt{\frac{1}{N}\sum_{i=1}^{N} v^2_{F(x,y,i)}}$$

where $\{u^2_{F(x,y,i)}, v^2_{F(x,y,i)}\}$ are the fluctuating velocity components along the two co-ordinate directions at a certain point (x, y). In addition, the kinetic energy of the velocity fluctuation can be calculated from the RMS fluctuating velocity as follows:

$$E_{F(x,y)} = \frac{1}{2}\, u'^2_{F,EA(x,y)} + v'^2_{F,EA(x,y)} \tag{4.16}$$

4.6.3 Vortex Ratio and Vortex Centre

Large-scale vortices within the in-cylinder airflow can have a large effect on mixture distribution and resulting combustion. Such vortices with their axis of rotation along the length of the cylinder are termed swirl, while charge motion on an axis parallel to the crankshaft is known as tumble. The ratio of the equivalent solid body vortex angular velocity to engine speed is a commonly used means of measuring vortex intensity and is known as the swirl or tumble ratio respectively. The vortex solid body equivalent can be obtained by dividing the total angular momentum by the moment of inertia of the measurement volume. Integrating the corresponding vector using Equation 4.17, will yield the total angular momentum with respect to the vortex centre, such that in a planar PIV vector field, the swirl ratio (SR) or tumble ratio (TR) can be expressed as:

$$\text{SR or TR} = \frac{\sum_{i=1}^{N} m_i \vec{r}_i . \vec{U}_i}{I\varpi_c} \quad (4.17)$$

where I is the angular inertia

$$I = \sum_{i=1}^{N} m_i \vec{r}_i . \vec{r}_i$$

and ϖ_c is the crankshaft angular speed. $\vec{r}_i$ is the distance of the cell position of the i^{th} velocity vector to the vortex centre. It is common to assume that m_i, the mass of fluid located in the cell, is uniformly distributed within the cylinder.

Since the vortex intensity and the position of its rotational axis vary due to cycle-to-cycle variation of the bulk flow, standard deviation can be used to describe the amount of cyclic variation of the vortex ratio and centre.

$$r_\sigma = \sqrt{\frac{1}{N} \sum_{i=1}^{N} [(x_i - x_o)^2 + (y_i - y_o)^2]} \quad (4.18)$$

$$SR_\sigma = \sqrt{\frac{1}{N} \sum_{i=1}^{N} [SR_i - SR_o]^2} \quad (4.19)$$

$$TR_\sigma = \sqrt{\frac{1}{N} \sum_{i=1}^{N} [TR_i - TR_o]^2} \quad (4.20)$$

Where r_σ, SR_σ and TR_σ are the standard deviations of the cyclic variations of the vortex centre and swirl and tumble ratios respectively. (x_i, x_i) and SR_i / TR_i represent the vortex centre and the swirl/tumble ratio of the instantaneous velocity field in the i^{th} cycle. (x_o, x_o) and SR_o / TR_o are the vortex centre and swirl/tumble ratio of the ensemble average of the flow field.

In many cases the position of the instantaneous vortex centre can appear ambiguous, leading to difficulties in locating it. To avoid problems of this nature in this work, a two-dimensional spatial low pass filtering method, based on a FFT, was employed to remove the velocity fluctuation, providing an easy and reliable means location of the vortex centre [35]. When using the FFT, a spatial frequency of $0.05mm^{-1}$ was used as a cut off frequency.

4.7 PIV Experiments

The PIV experiments were completed using the optical engine set-up described in Chapter 3 and PIV system described earlier in this chapter. The engine speed used was 1200 RPM. While this engine speed was wholly suitable for the experiment, it was primarily dictated by the laser output frequency of 10 Hz. In an attempt to minimise condensation of the fuel spray and flow seeding onto the optical windows all tests were completed with the engine coolant heated to 80°C.

4.7.1 Characterisation of In-Cylinder Flow Field

For each crank angle where measurements were taken, 80 image pairs were recorded. Following the cross-correlation analysis the data were ensemble averaged to provide an average flow field for that point in the engine cycle. Since images were recorded on consecutive engine cycles, insufficient time was available to write the data directly to the PC hard disc. For this reason, it was initially written to the PC RAM before being copied to disc immediately after the experiment. Unfortunately, since the RAM was only capable of holding 40 pairs of images at any one time, each test had to be completed in two halves with the first 40 image pairs being saved disc before continuing with the experiment.

4.7.1.1 Measurement Planes

In order to provide a better insight into the behaviour of the in-cylinder flow, the planar two dimensional PIV experiments were completed in four different planes, in as shown in Figure 4.3. These planes were created by moving the intersection of the laser sheet and camera field of view.

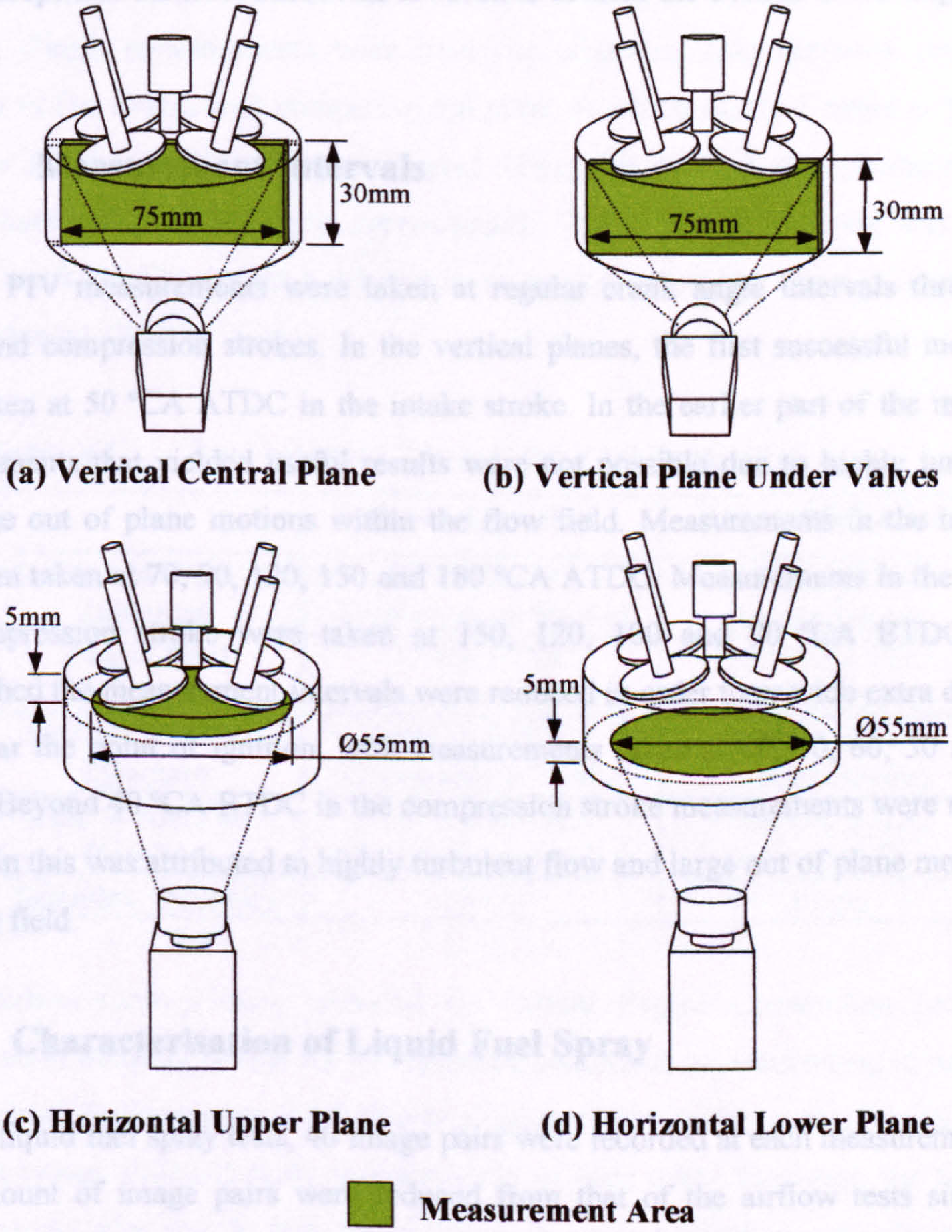

Figure 4.3 PIV measurement planes

Figure 4.3 (a) shows the vertical plane located in the centre of the cylinder. Here, both illumination and light collection were completed via the ring window at the top of the cylinder. Though the cylinder bore measured 80mm, the spacers between the cylinder head and block restricted the field of view to 75mm x 30mm. Figure 4.3 (b) shows the second vertical measurement plane located under the centreline of the intake and exhaust valves nearest the camera. The field of view with this arrangement was also 75mm x 30mm.

Figure 4.3 (c) shows the measurement region for the upper horizontal plane. This plane was positioned as close to the cylinder head face as practically possible, allowing the best view of the horizontal flow from the intake valves. Light detection by the camera was completed via the piston window and 45° mirror and hence the field of view was limited to the diameter of the piston window, which measured Ø55mm. The arrangement of the lower horizontal measurement plane shown in Figure 4.3 (d) was identical to that described above except that the laser sheet was lowered to as near the bottom of the ring window as possible.

4.7.1.2 Measurement Intervals

Airflow PIV measurements were taken at regular crank angle intervals throughout the intake and compression strokes. In the vertical planes, the first successful measurements were taken at 50 °CA ATDC in the intake stroke. In the earlier part of the intake stroke, measurements that yielded useful results were not possible due to highly turbulent flow and large out of plane motions within the flow field. Measurements in the intake stroke were then taken at 70, 90, 120, 150 and 180 °CA ATDC. Measurements in the first half of the compression stroke were taken at 150, 120, 100 and 90 °CA BTDC. As TDC approached the measurement intervals were reduced in order to provide extra details of the flow near the point of ignition, with measurements taken at 80, 70, 60, 50 and 40 °CA BTDC. Beyond 40 °CA BTDC in the compression stroke measurements were not possible, and again this was attributed to highly turbulent flow and large out of plane motions within the flow field.

4.7.2 Characterisation of Liquid Fuel Spray

For the liquid fuel spray tests, 40 image pairs were recorded at each measurement interval. The amount of image pairs were reduced from that of the airflow tests since window fouling from the fuel spray did not allow the capture of 80 image pairs in one running session.

4.7.2.1 Injection Timings

Experiments were completed using two injection timings, details of which are shown in Table 4.1, along with the quantity of fuel injected. Initially, timings representing an 'early' injection strategy that might be used during full load homogenous operation were used.

Following this, the tests were repeated using a 'late' injection strategy, intended to simulate a stratified, part load condition of at 3.0 bar IMEP with an overall AFR of 40:1.

The injection timings shown in Table 4.1 are the actual times at which either injector was required to open or close. In practice, there is a small time delay between the electrical signal being sent to the injector and it actually opening and flowing. Therefore, these delays were measured and compensated for when setting the timings on the injector control drivers. These measurements were made by obtaining Mie scattered images of the injection in the engine and comparing the point at which the fuel spray as first seen to when the electrical signal was actually sent. Using this method, the opening delay for the air/fuel injector was found to be approximately 7°CA. The fuel injector was assumed to have a much smaller opening delay due to its much smaller internal inertia and was estimated to be 3°CA.

Table 4.1 Fuel Injection Timings for Fuel Spray PIV

	'Late' Injection	**'Early' Injection**
Start of Fuel Injection	88°CA BTDC (Compression Stroke)	59°CA ATDC (Intake Stroke)
End of Fuel Injection	72°CA BTDC (Compression Stroke)	118°CA ATDC (Intake Stroke)
Start of Air/Fuel Injection	70°CA BTDC (Compression Stroke)	120°CA ATDC (Intake Stroke)
End of Air/Fuel Injection	32°CA BTDC (Compression Stroke)	160°CA BTDC (Compression Stroke)
Injection Quantity	10 mg	30 mg

The injection timings were provided by Orbital Engine Corporation Ltd and were considered to be fairly typical for the operating conditions we were trying to reproduce. As discussed briefly in Section 3.1.5, the two injectors that make up the Orbital air assisted injection system function fairly independently of each other. However, the timing of the fuel metering injection, in relation to the main air/fuel injection, can affect the overall injection characteristics. Though the study of these effects would be an interesting area of future research, for this work minimum delay between the two injections was maintained for both injection strategies.

4.7.2.2 Measurement Plane

The fuel spray PIV experiments were completed on a measurement plane on the central vertical plane. In the case of the late injection tests, a fairly narrow spray and good stratification of the fuel spray meant that the liquid droplets were confined to the central area of the cylinder. This allowed the measurement area to be reduced to 50mm x 30mm, meaning the camera could be moved closer to the engine, increasing the resolution and clarity of the spray images. This configuration is shown in Figure 4.4. For experiments completed with the early injection timing this set-up was also used during the early stages of the injection event, up to 19° CA after SOI. However, as the spray developed, the spread of the fuel spray droplets beyond this field of view dictated the return to a measurement area that encompassed the whole available, as shown in Figure 4.3 (a).

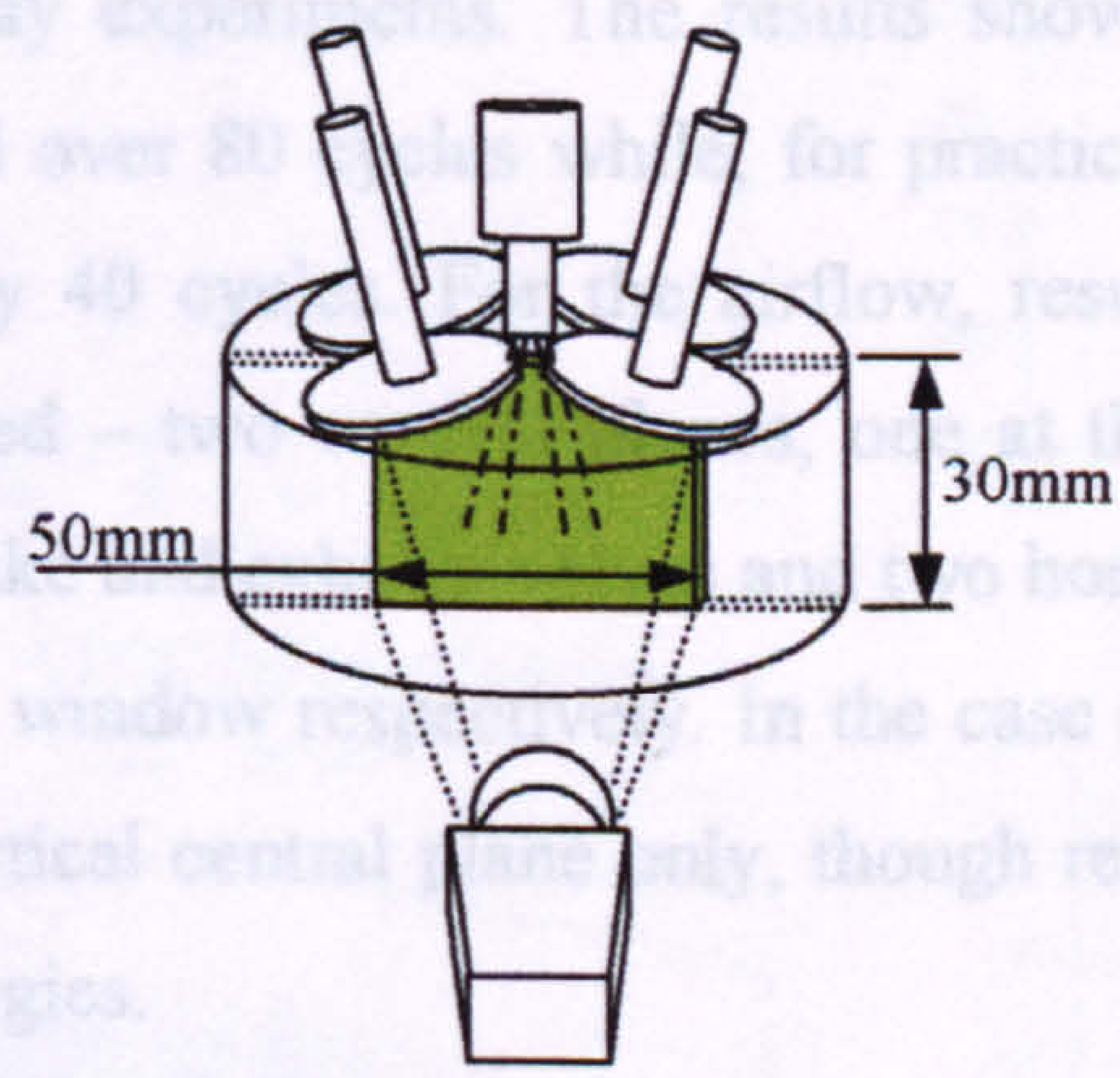

Figure 4.4 Fuel Spray PIV Measurement Area with Late injection Timing

4.7.2.3 Measurement Intervals

PIV measurements of the fuel spray were taken at regular intervals throughout the injection period for both injection strategies. With the early injection strategy, measurements were taken at 3 °CA intervals from the start of injection until 9 °CA into the injection. From then on measurements were taken every 10 °CA until 59 °CA ASOI when insufficient liquid fuel markers were present to make measurements. For the late injection case, measurements were taken every 3 °CA throughout the injection period.

4.7.3 Calibration of PIV Images

In order to enable the calculated vectors to be expressed in terms of velocity, the PIV system must be calibrated both spatially and temporally. Temporal calibration was completed by simply entering the time interval, ΔT, used during that particular test into the Insight software, prior to the evaluating the vectors. For the spatial calibration, a card printed with lines a known distance apart was placed within the ring window within the measurement plane of interest and an image recorded. Then, using the calibration function of the Insight software, the distance between the lines on the image was measured in terms of pixels. The distance between the lines divided by the measured number of pixels gives the spatial calibration value that must also be entered into the Insight software prior to image processing. This process must be completed each time the camera position or field of view is changed.

4.8 Results and Discussion

The following sections discuss the PIV results obtained for both the in-cylinder airflow and injector liquid spray experiments. The results shown for the in-cylinder flow field are ensemble averaged over 80 cycles while, for practical reasons, the fuel spray maps were averaged over only 40 cycles. For the airflow, results from four separate measurement planes are presented – two vertical planes, one at the centreline of the cylinder and one under a pair of intake and exhaust valves and two horizontal planes, 5mm from the top and bottom of the ring window respectively. In the case of the fuel spray, measurements were obtained in the vertical central plane only, though results are presented for both early and late injection strategies.

4.8.1 Analysis of In-Cylinder Flow Field

4.8.1.1 General Description of Flow Characteristics

This section contains a general description of the in-cylinder flow field measured using the PIV technique. Prior to obtaining the results it was expected that the flow description could be enhanced by calculating the vortex centre and vortex ratio for the tumble and swirl motion often present in the cylinder, as detailed in Section 4.7.3. However, as the following results will show, the lack of any strong large-scale vortices prevented this.

In the vertical measurement planes the 'X and Y' axes refer to horizontal and vertical directions respectively. In the horizontal measurement planes 'X' and 'Y' axes refer to the directions parallel and perpendicular to the crankshaft axis respectively.

Central Vertical Plane

Figure 4.5 displays the results from the PIV experiments with the measurement plane vertical, and on the centre line of the cylinder, perpendicular to the crankshaft axis. In Figure 4.5 (a) the airflow into the cylinder at 50 °CA ATDC during the intake stroke is

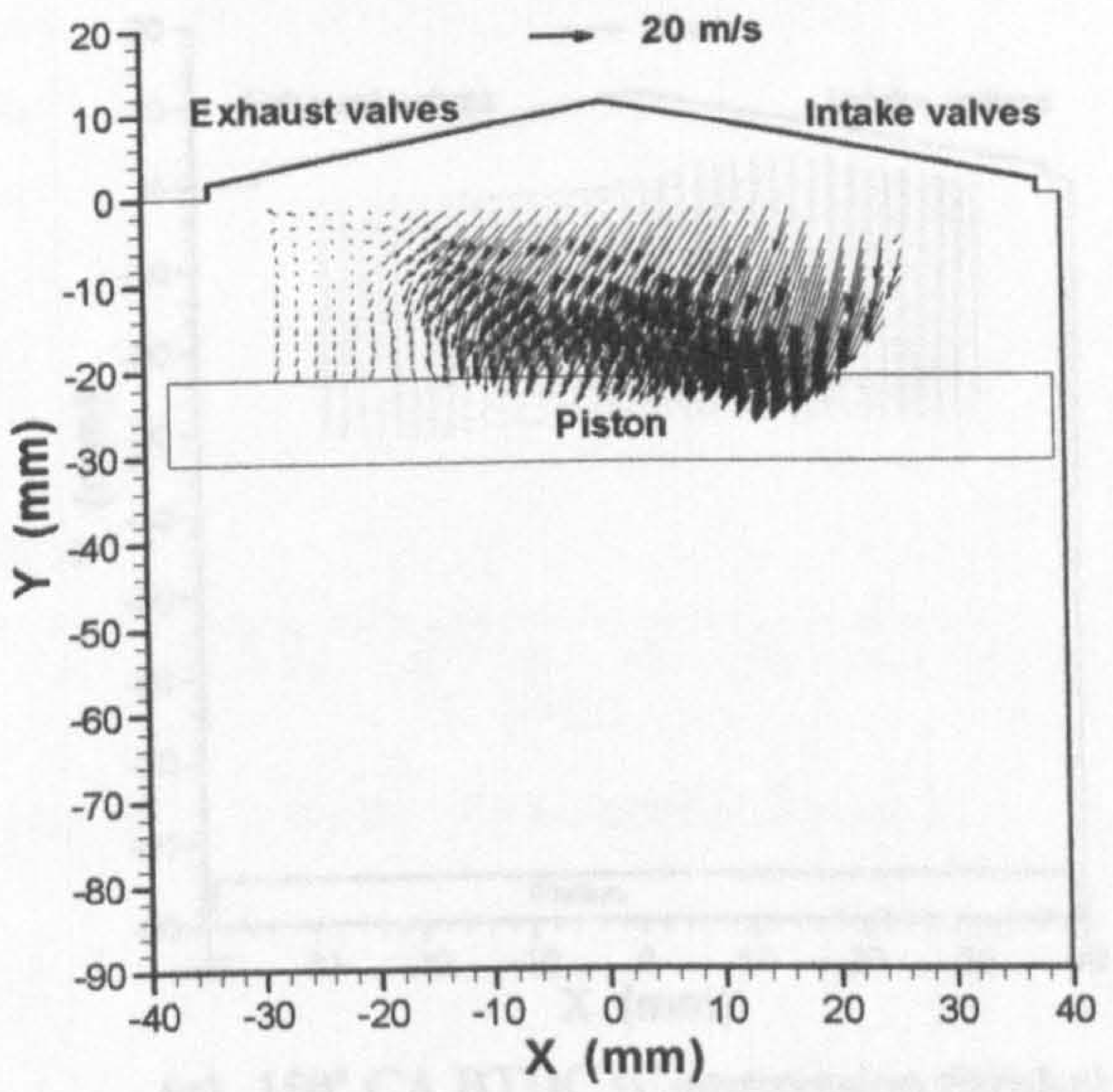

(a) 50° CA ATDC (Intake Stroke)

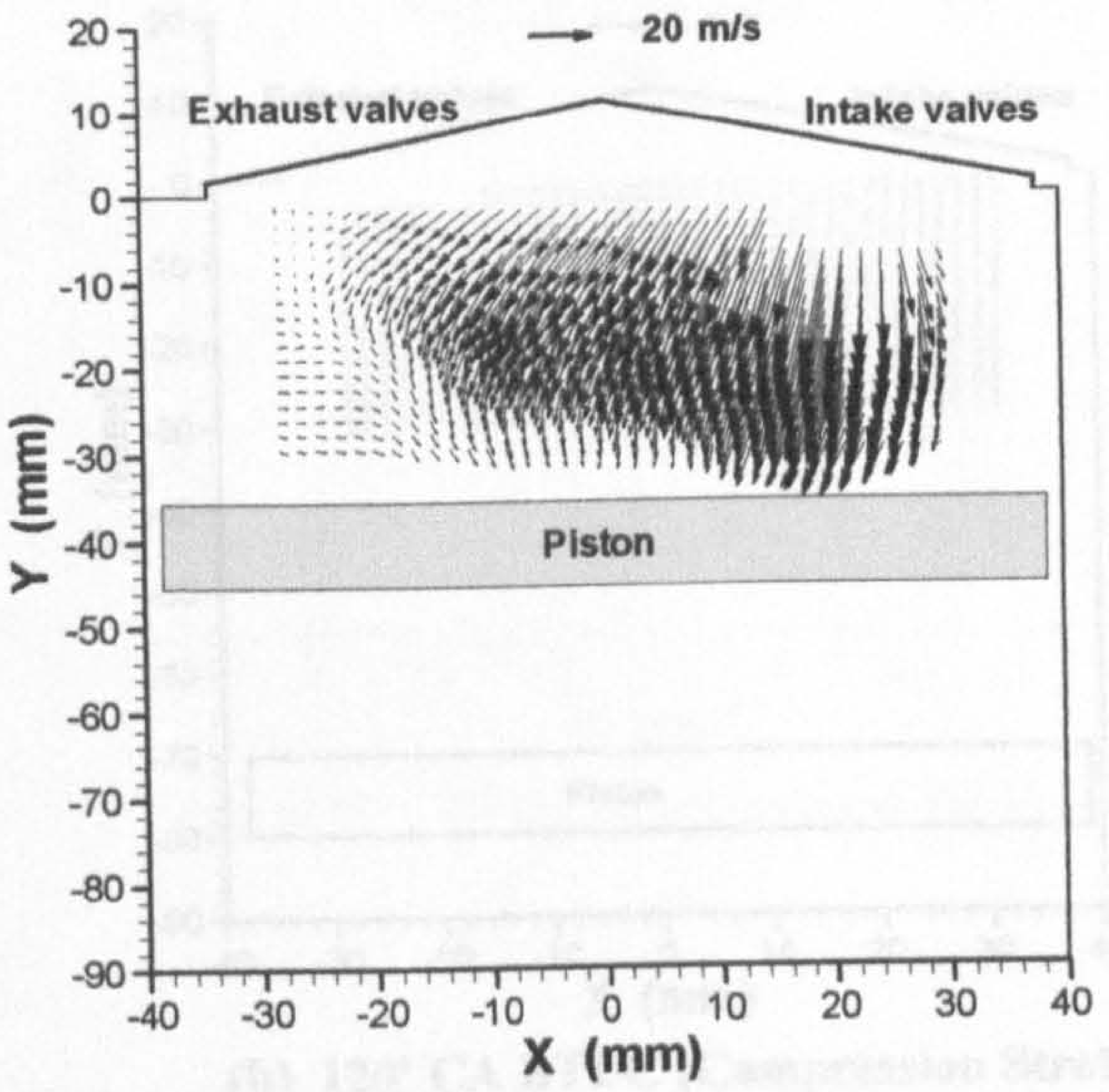

(b) 70° CA ATDC (Intake Stroke)

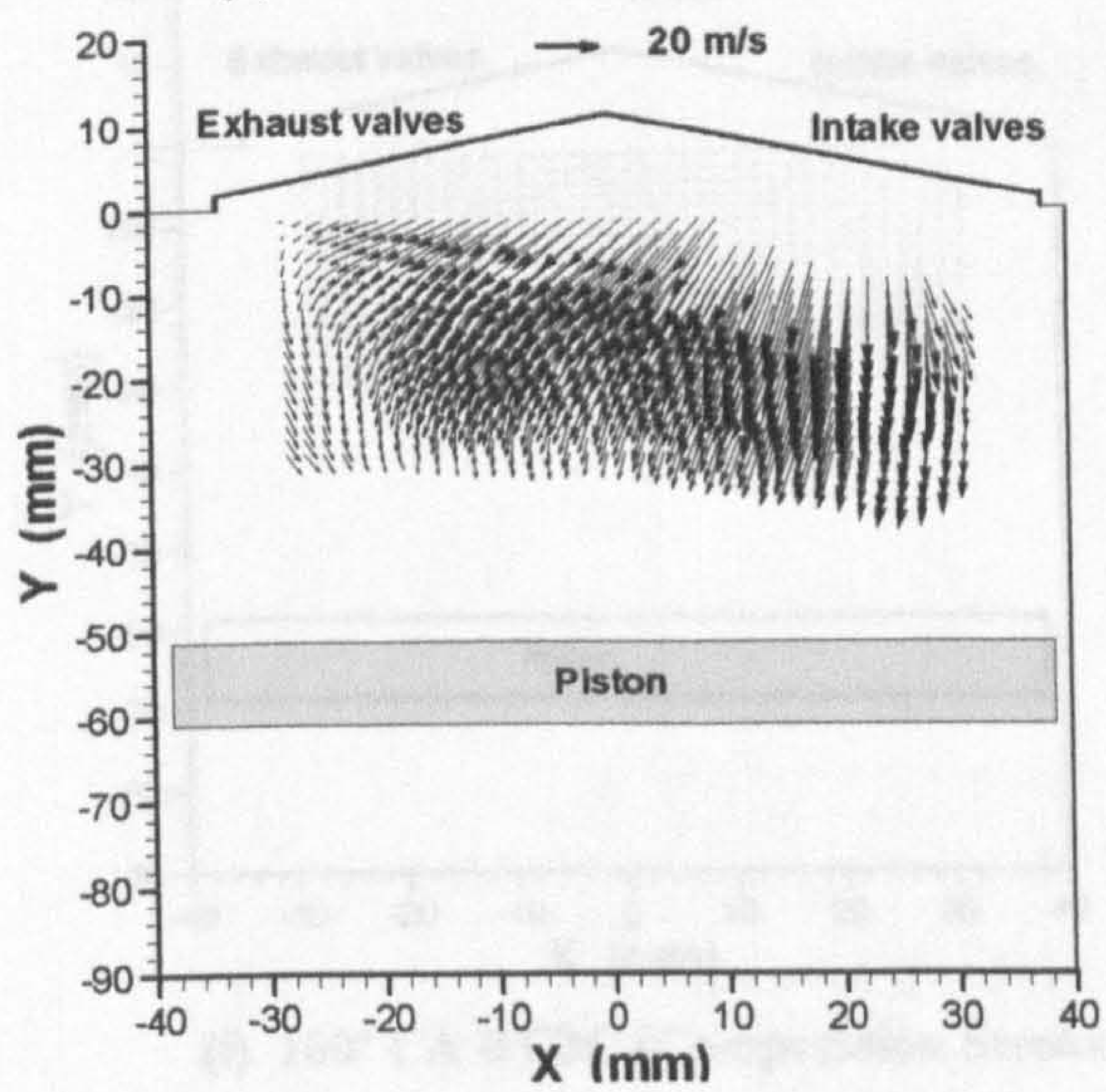

(c) 90° CA ATDC (Intake Stroke)

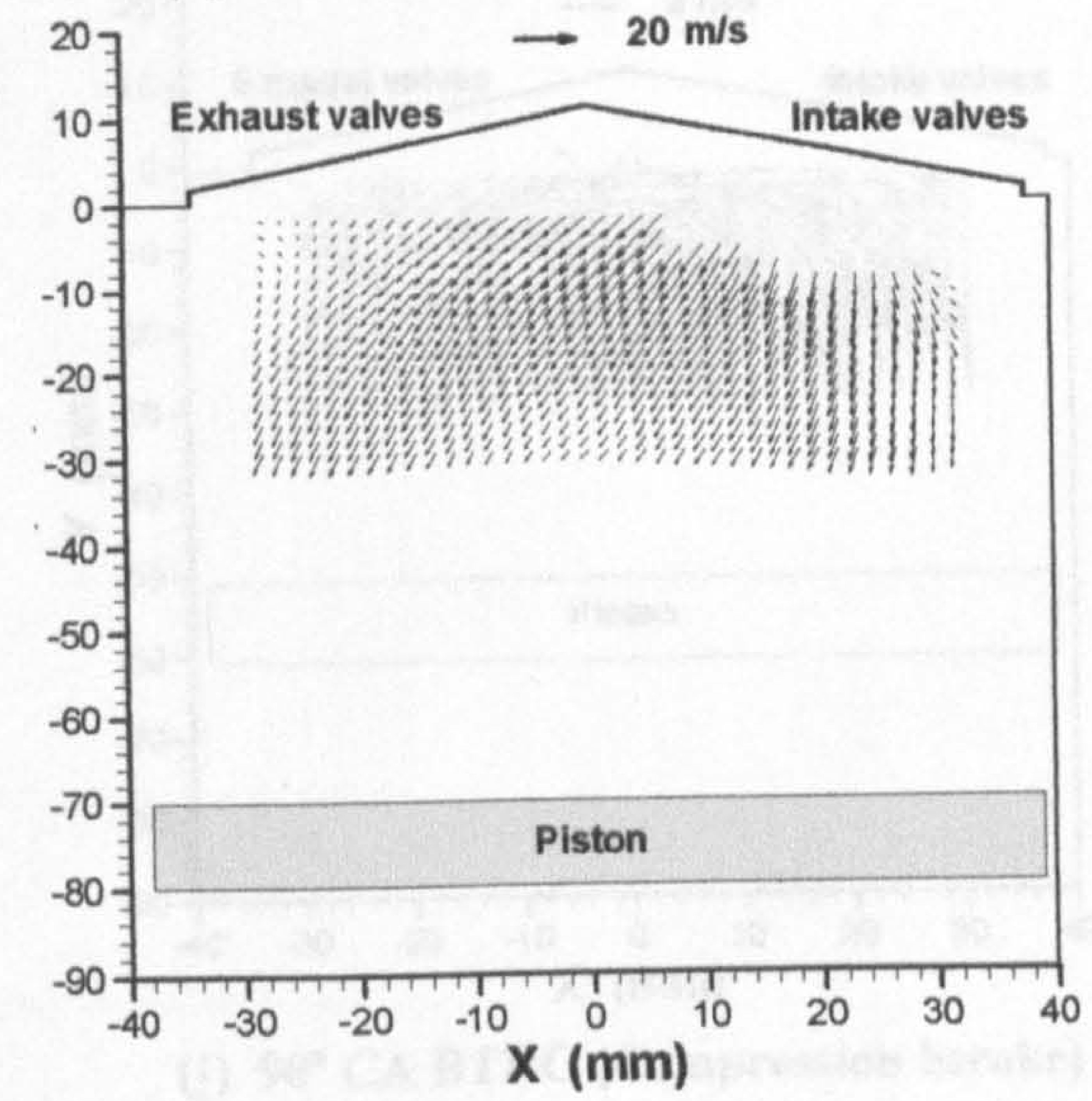

(d) 120° CA ATDC (Intake Stroke)

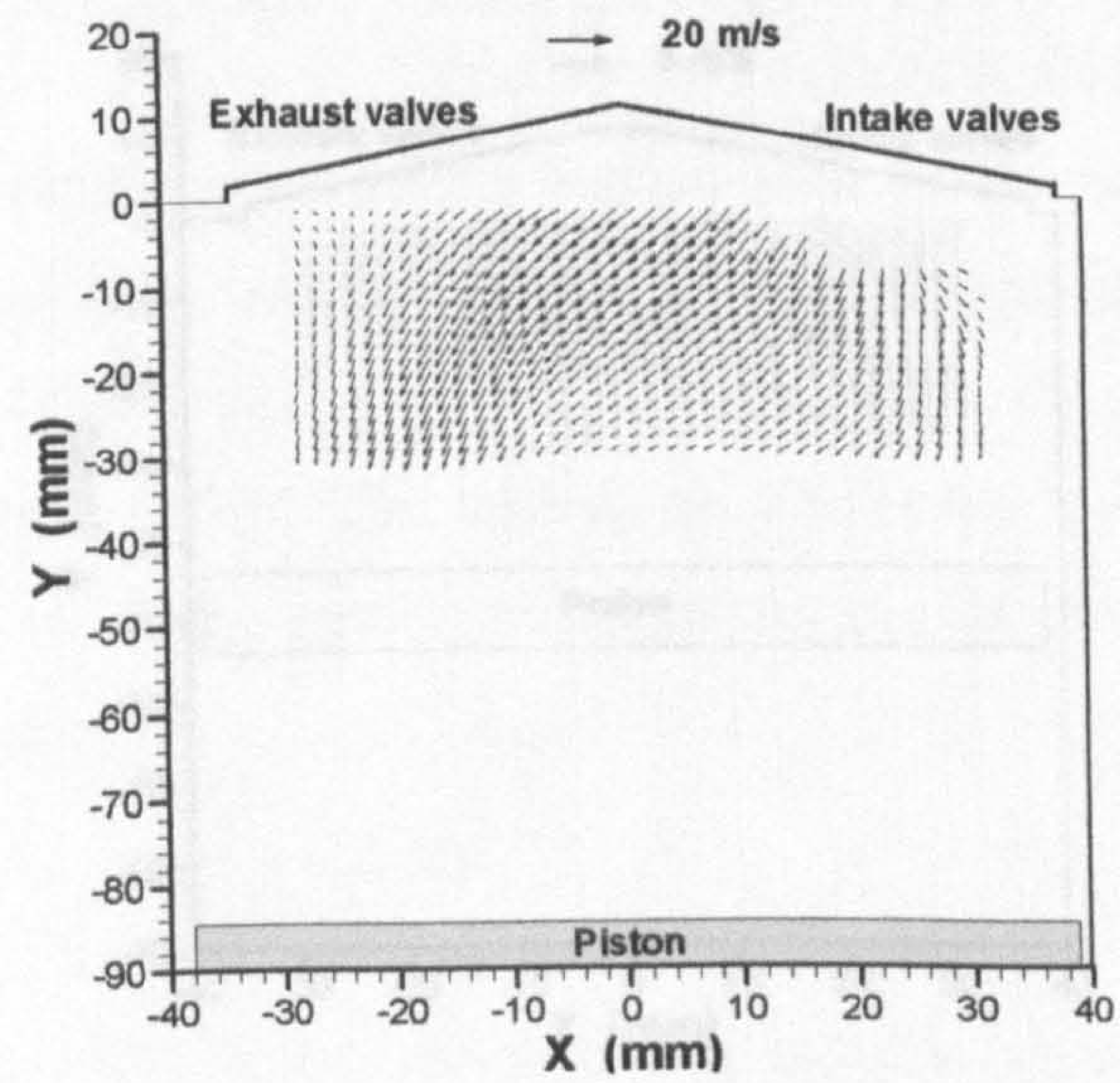

(e) 150° CA ATDC (Intake Stroke)

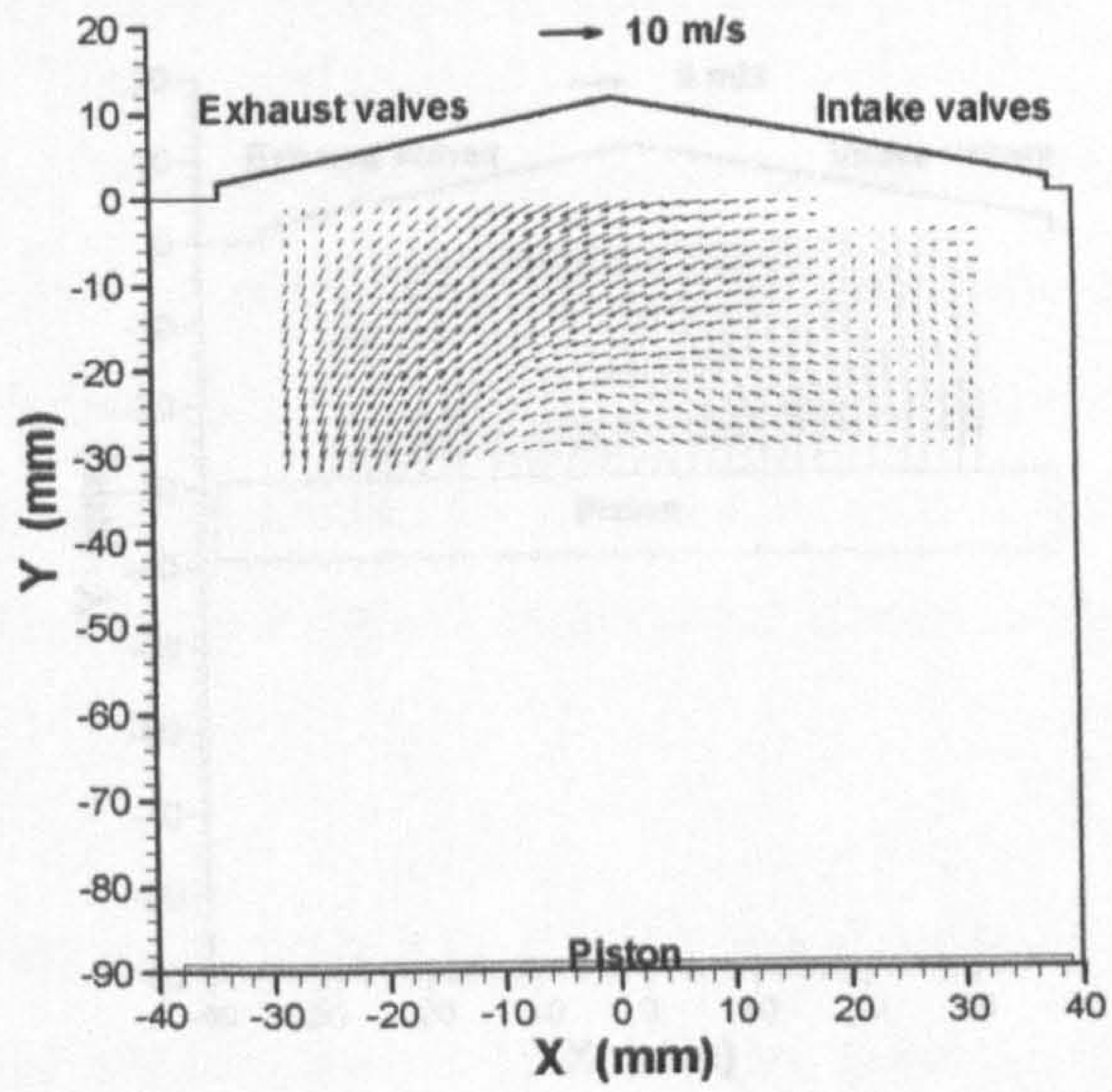

(f) BDC (Intake/Compression Stroke)

Figure 4.5 Ensemble Averaged PIV In-Cylinder Flow Field Results for Central Vertical Measurement Plane

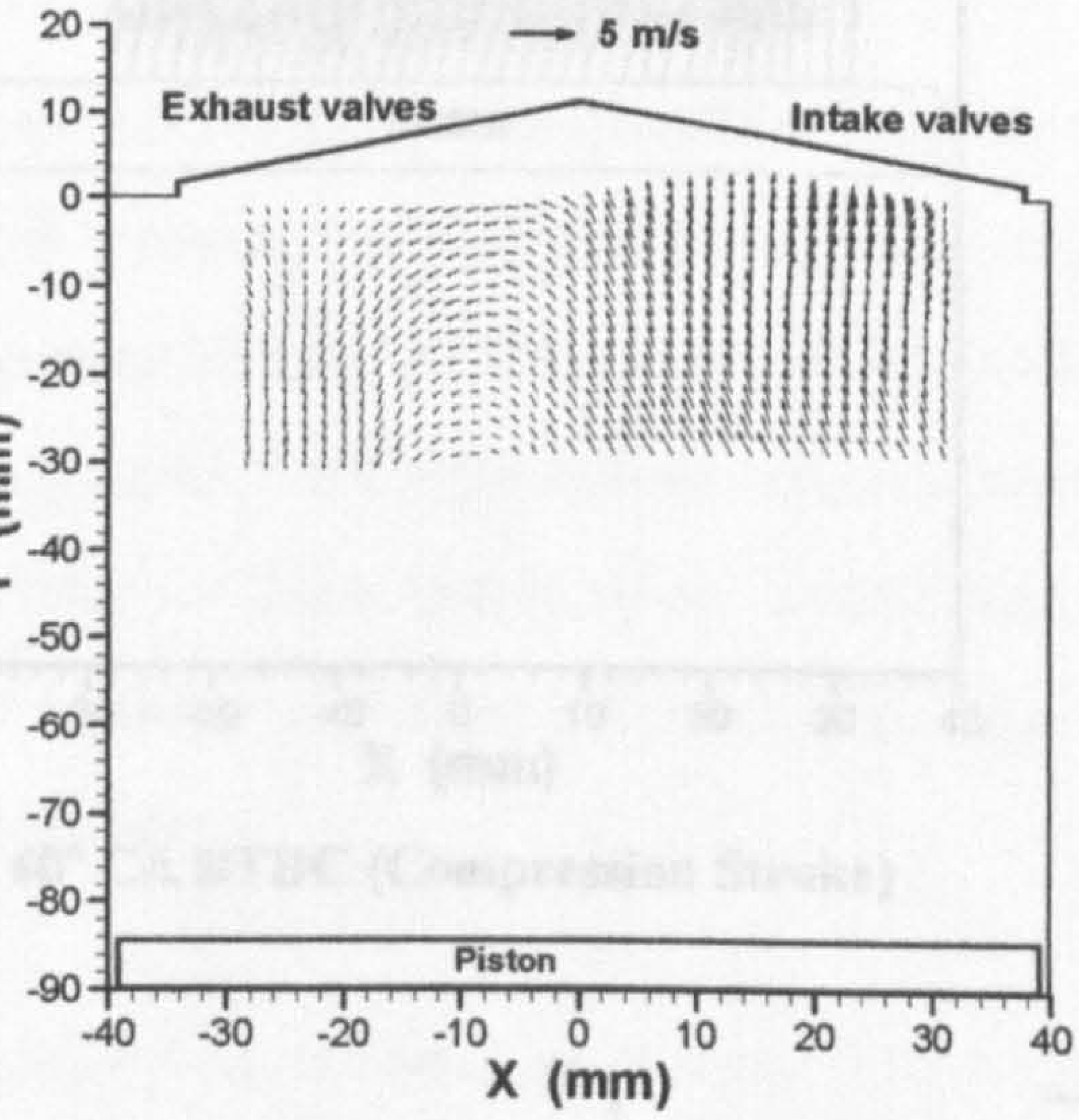

(g) 150° CA BTDC (Compression Stroke)

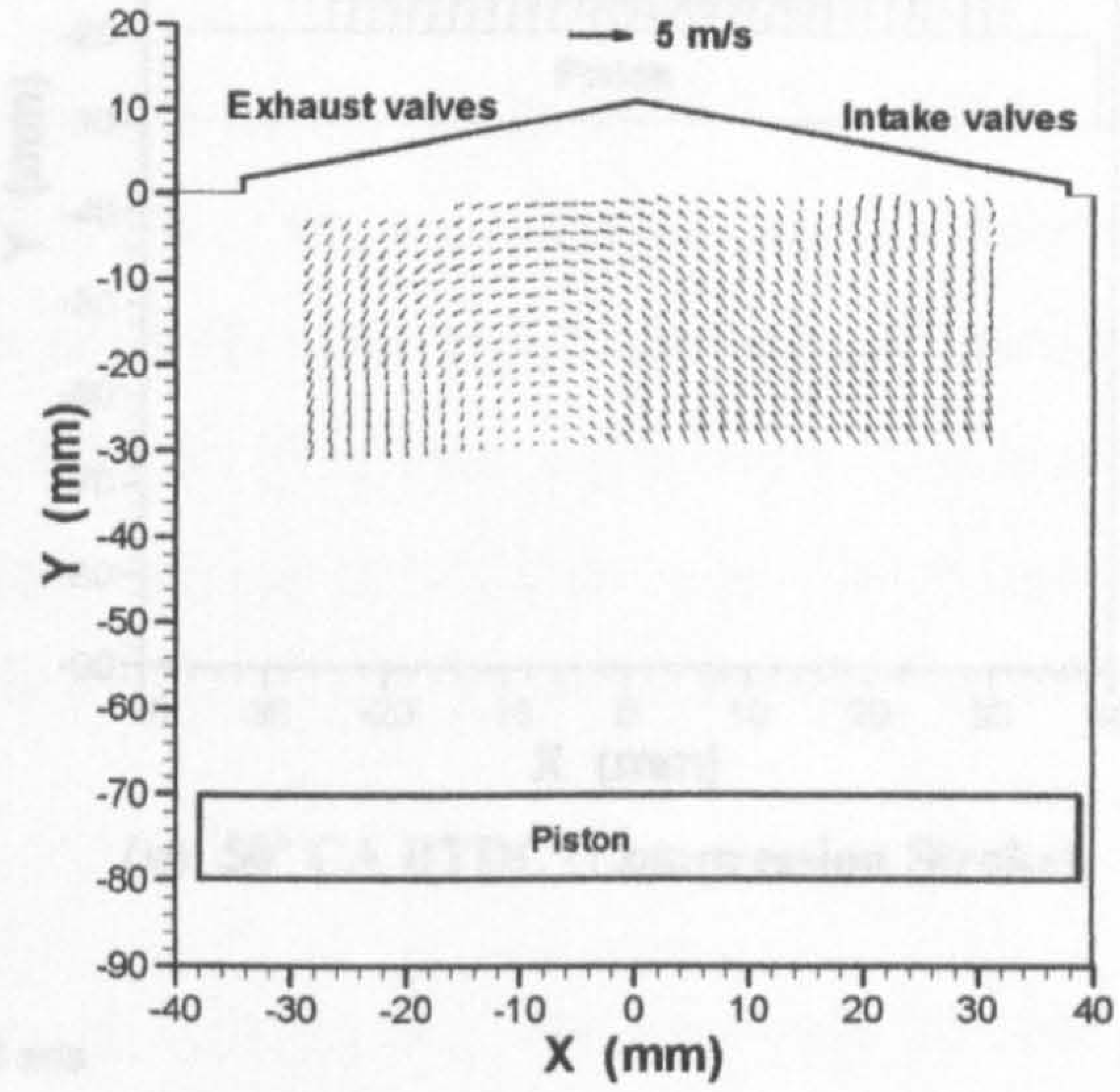

(h) 120° CA BTDC (Compression Stroke)

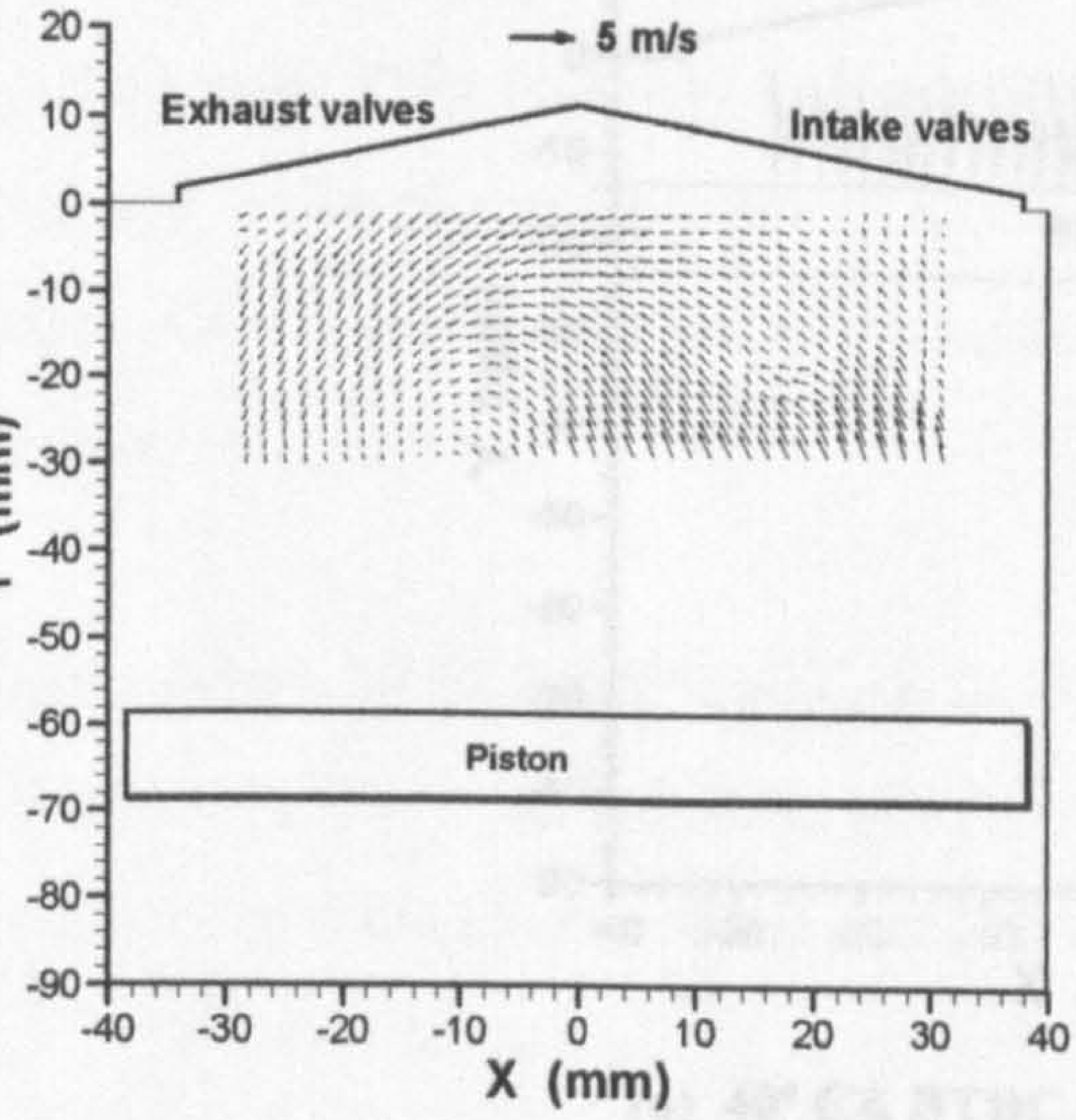

(i) 100° CA BTDC (Compression Stroke)

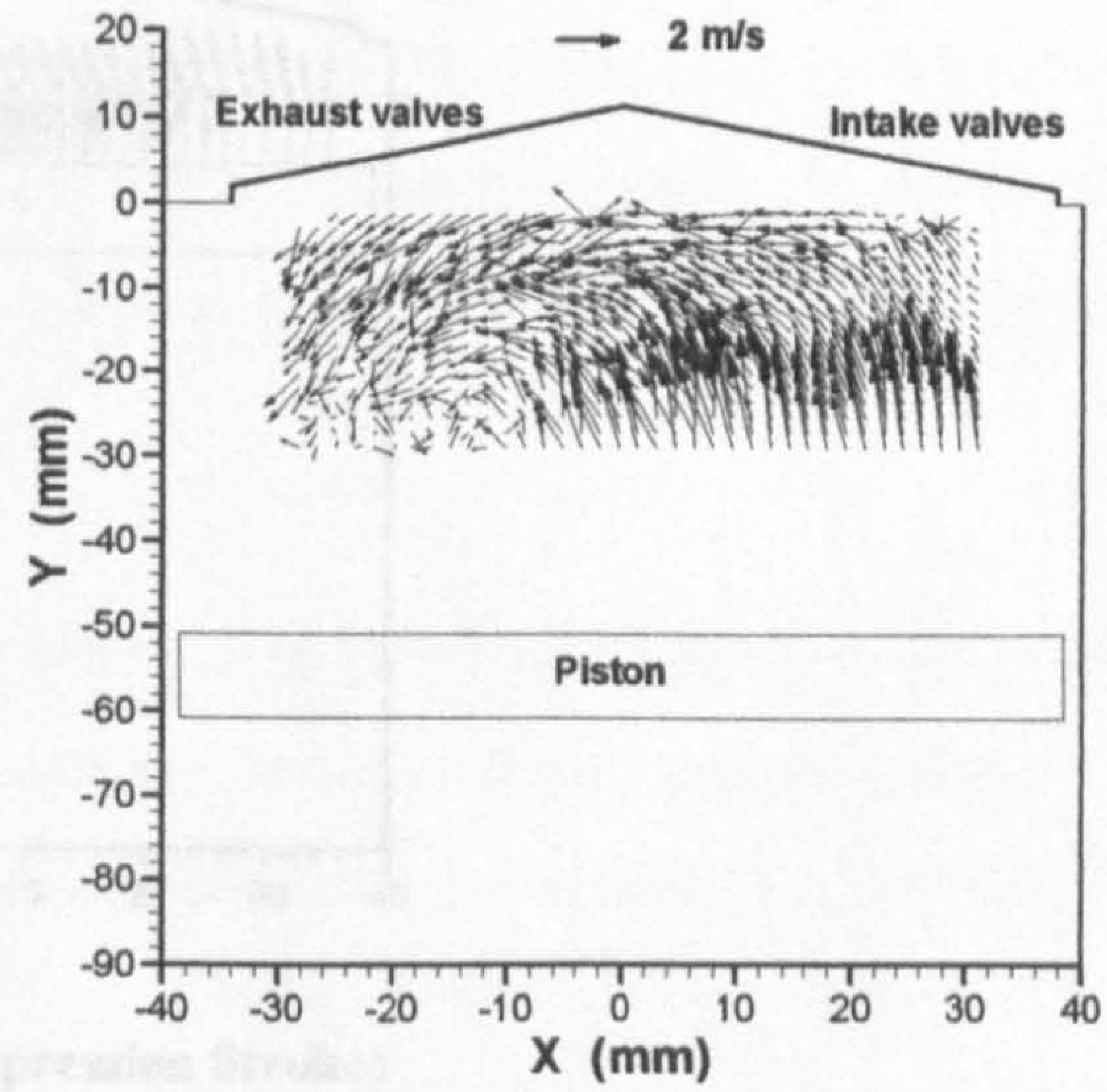

(j) 90° CA BTDC (Compression Stroke)

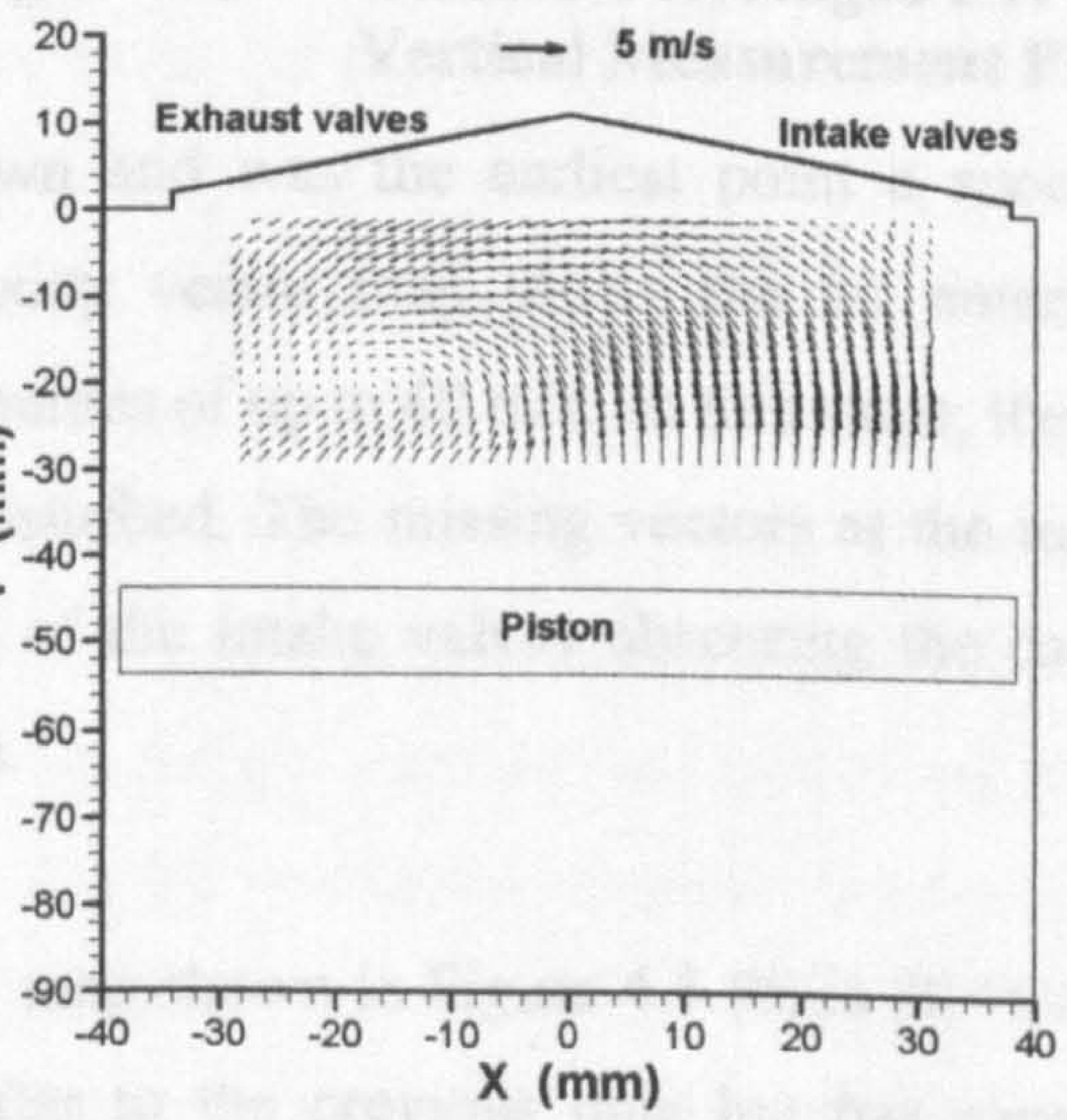

(k) 80° CA BTDC (Compression Stroke)

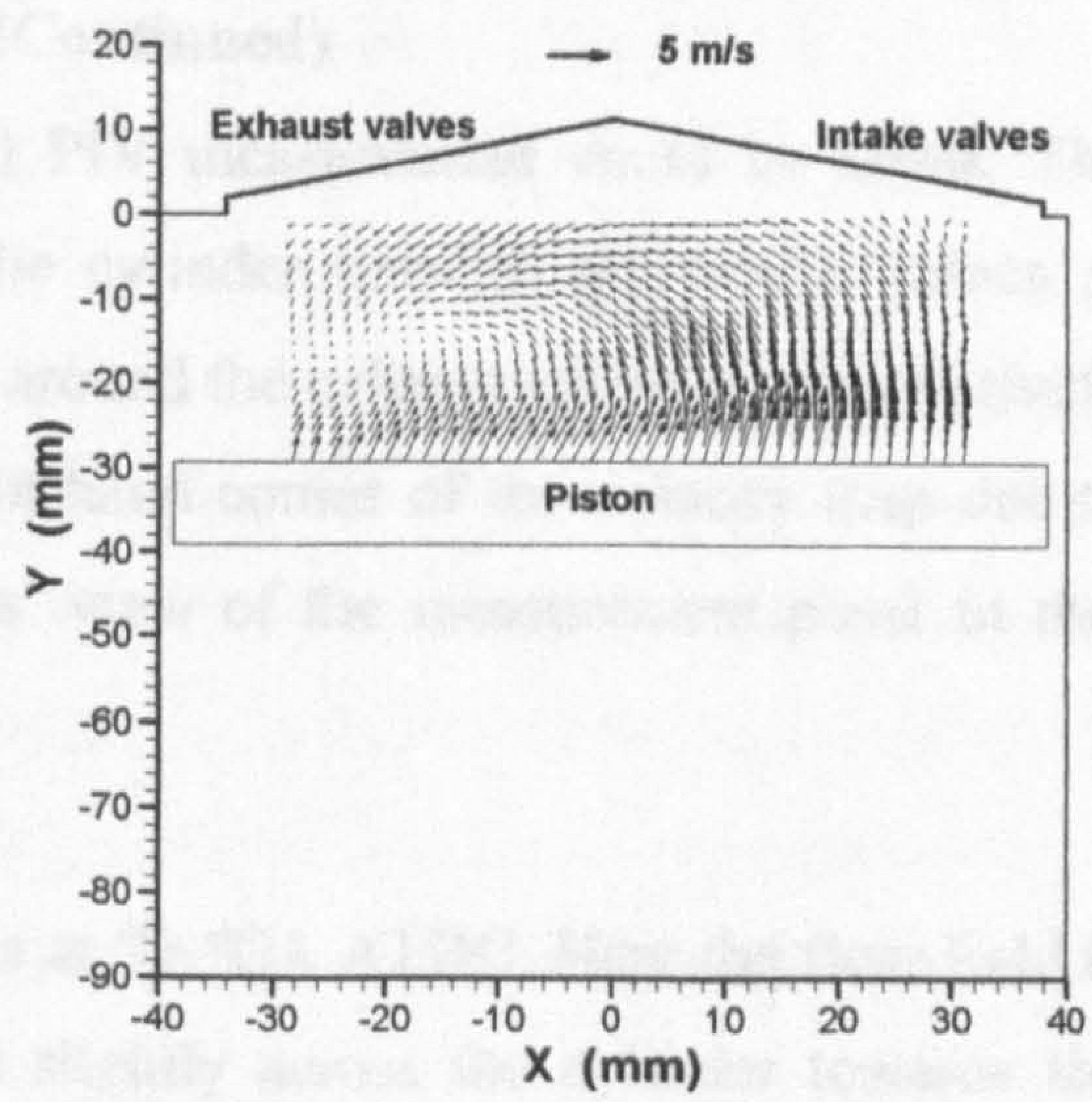

(l) 70° CA BTDC (Compression Stroke)

Figure 4.5 Ensemble Averaged PIV In-Cylinder Flow Field Results for Central Vertical Measurement Plane (Continued)

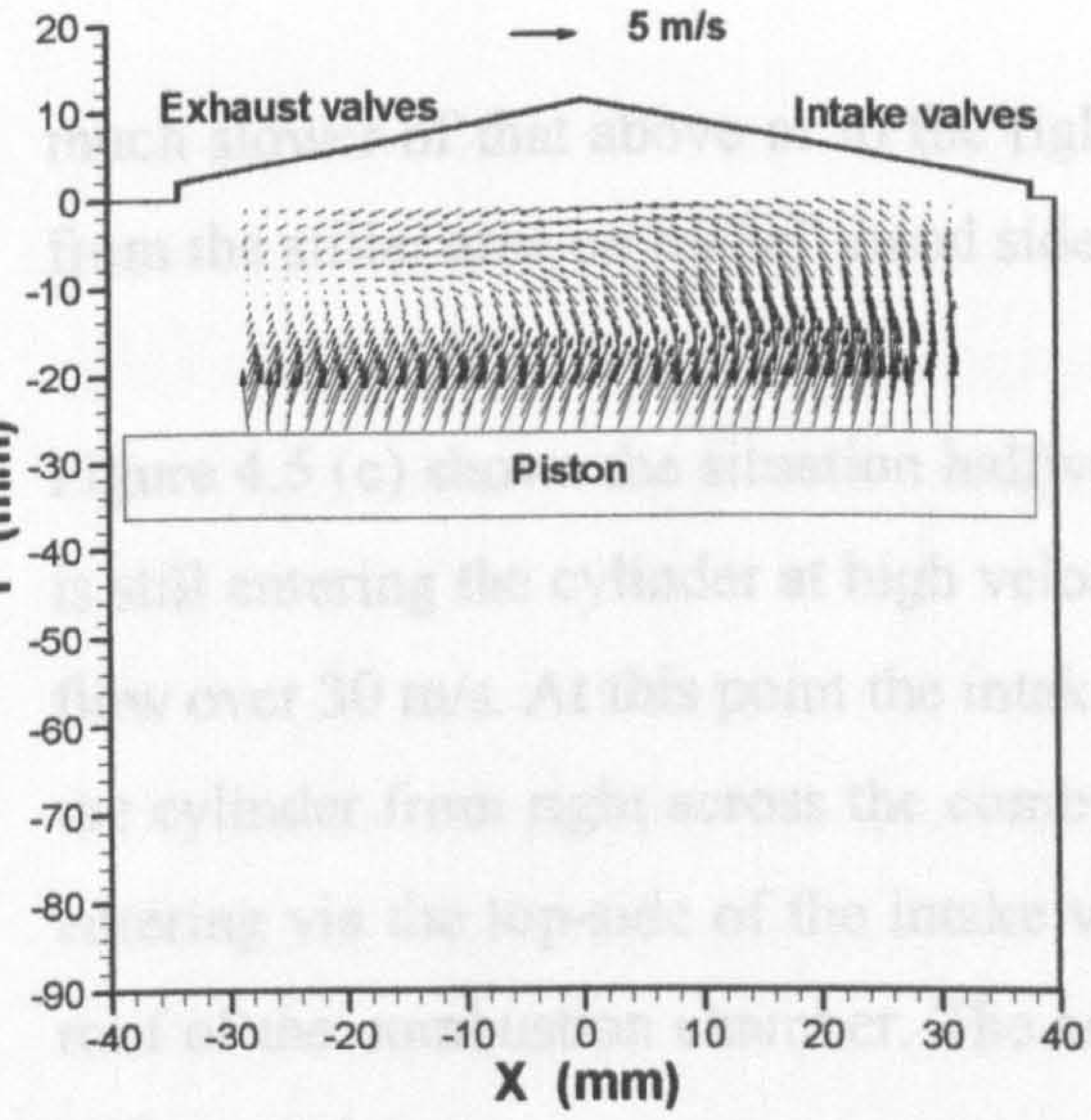

(m) 60° CA BTDC (Compression Stroke)

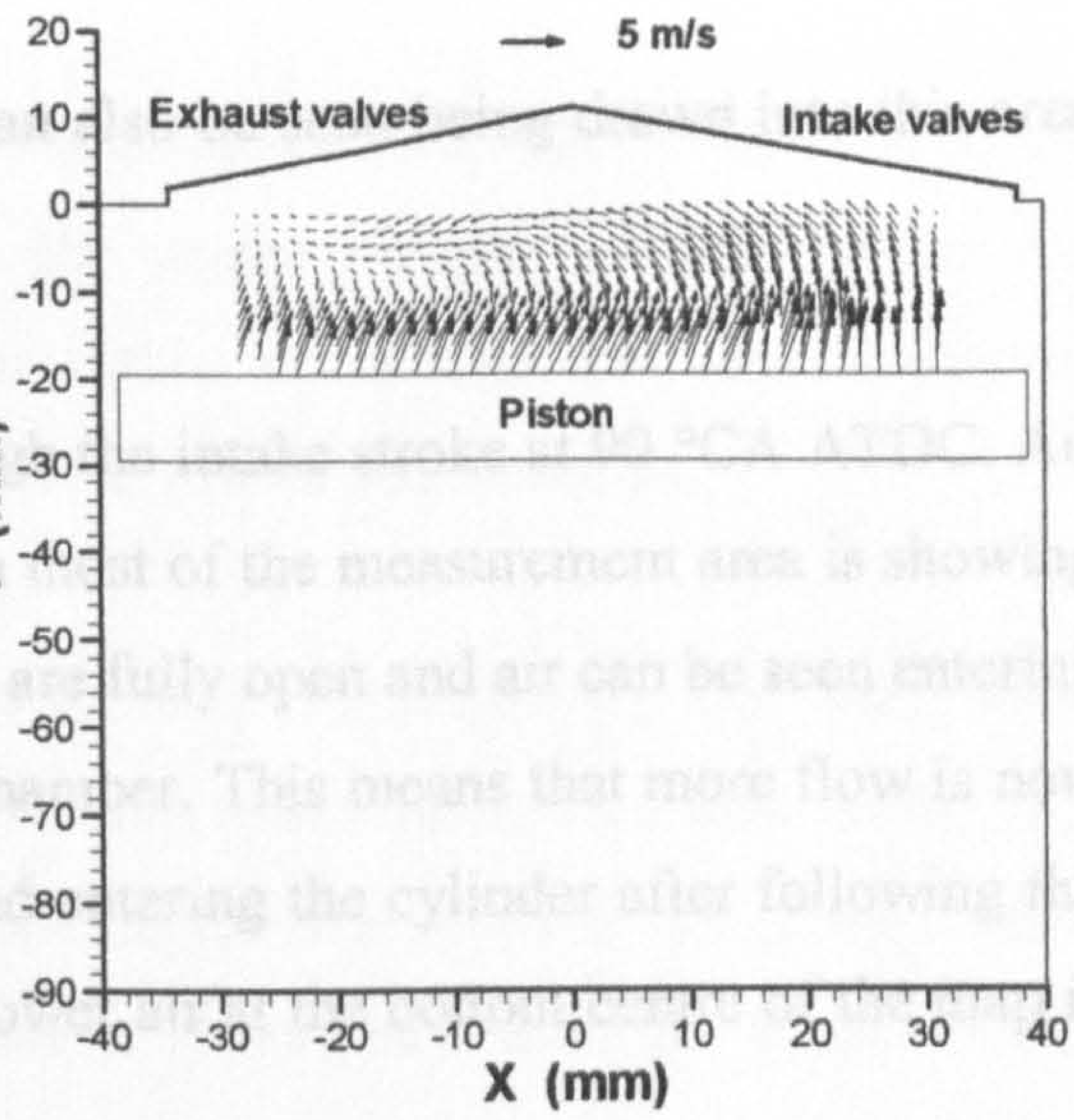

(n) 50° CA BTDC (Compression Stroke)

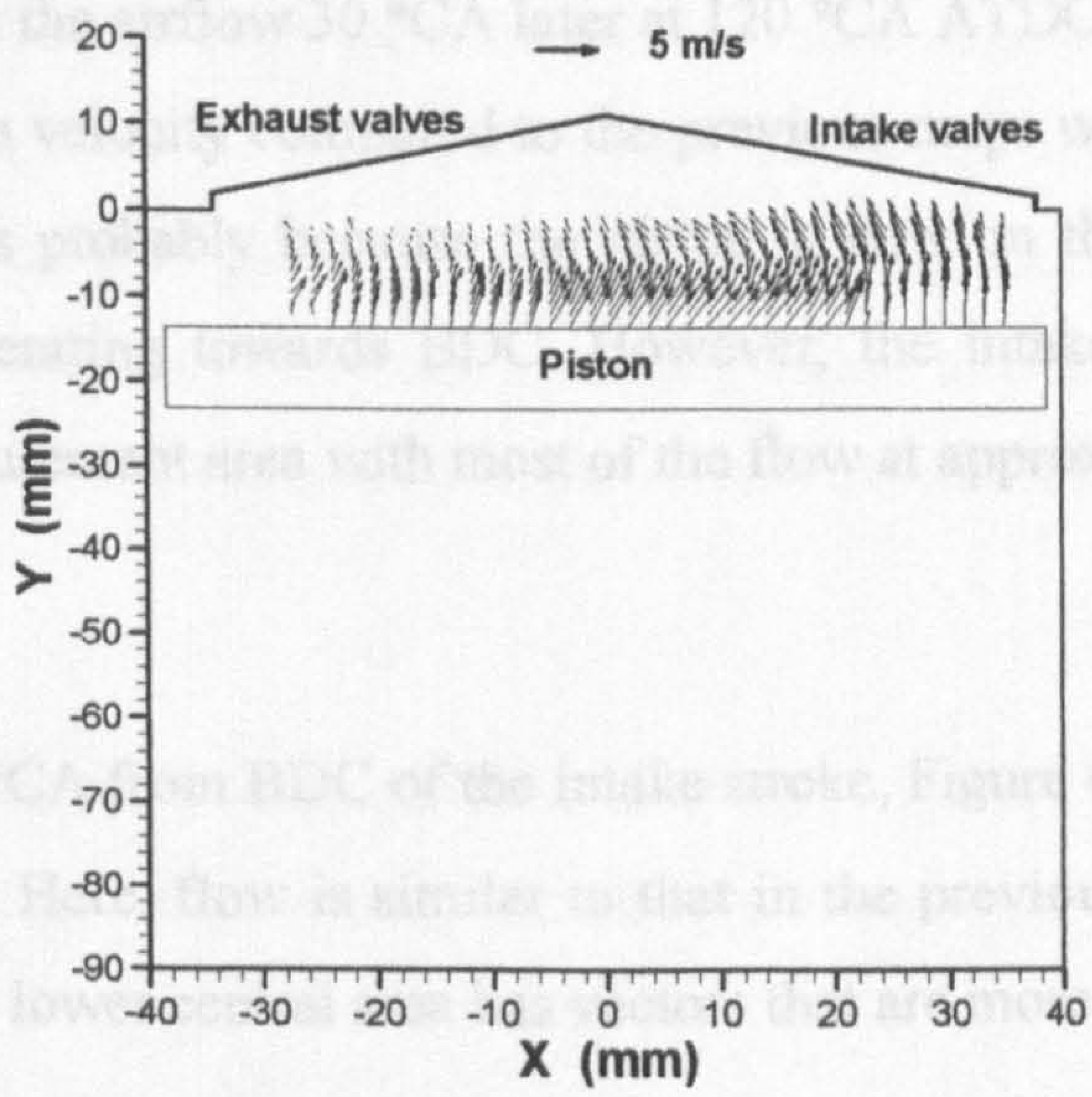

(o) 40° CA BTDC (Compression Stroke)

Figure 4.5 Ensemble Averaged PIV In-Cylinder Flow Field Results for Central Vertical Measurement Plane (Continued)

shown and was the earliest point a successful PIV measurement could be taken. The velocity vector map shows the air entering the cylinder through the intake valves at velocities of up to 40 m/s. At this stage, the area around the exhaust valves is still relatively undisturbed. The missing vectors at the top right hand corner of the velocity map due to one of the intake valves obscuring the cameras' view of the measurement plane in this area.

The map shown in Figure 4.5 (b) is 20 °CA later at 70 °CA ATDC. Here the flow field is similar to the previous map but has expanded slightly across the cylinder towards the exhaust valves. However, the lower, central, area of the map shows an area of flow that is much slower of that above or to the right. Air can also be seen being drawn into this area from the stiller area on the left-hand side.

Figure 4.5 (c) shows the situation halfway through the intake stroke at 90 °CA ATDC. Air is still entering the cylinder at high velocity with most of the measurement area is showing flow over 30 m/s. At this point the intake valves are fully open and air can be seen entering the cylinder from right across the combustion chamber. This means that more flow is now entering via the top-side of the intake valves and entering the cylinder after following the roof of the combustion chamber. The area of slower air at the bottom centre of the map is still present.

Figure 4.5 (d) shows the airflow 30 °CA later at 120 °CA ATDC. The most striking change is the overall drop in velocity compared to the previous maps with a maximum velocity of around 15 m/s. This probably because the piston is now on the lower half of the intake stroke and is decelerating towards BDC. However, the intake flow now almost totally dominates the measurement area with most of the flow at approximately 45° to the cylinder head face.

With the piston 30 °CA from BDC of the intake stroke, Figure 4.5 (e) shows the flow field at 150 °CA ATDC. Here, flow is similar to that in the previous figure except, perhaps, a little slower and the lower central area has vectors that are more horizontal than before.

Figure 4.5 (f) shows the airflow at the end of the intake stroke and the earliest signs of vortex development, with the potential centre out of view below the measurement window. Flow from the topside of the intake valves, via the combustion chamber, is still strong while the lower right hand side is now dominated by flow from below. Maximum velocities are now less than 5m/s and the intake valves are beginning to close.

With the intake valves almost closed and the piston ascending into the compression stroke Figure 4.3 (g) shows the state of the inducted air at 150 °CA BTDC. The signs of a vortex are still present although the centre has been pushed towards the left of the cylinder with most of the vectors showing upward airflow with maximum velocity of less than 2 m/s. In a small region in the top right hand corner it appears some backflow into the intake port may be occurring with strong upward flow in the area.

Figure 4.5 (h) shows the flow field 60 °CA into the compression stroke at 120 °CA BTDC. Here the vortex has developed a little with the centre possibly a little higher than previously, while the strong backflow in the intake valve area has almost stopped. Maximum velocity has also fallen slightly from the previous measurement.

The state of the flow field at 100 °CA BTDC is shown in Figure 4.5 (i). The weak vortex still remains towards the left-hand side of the cylinder, while the upward flow on the right hand side is becoming stronger, presumably following the movement of the piston towards TDC. A small anomaly in the results can be seen towards the lower right hand side, the reasons for which are not clear.

With the piston halfway through the compression stroke Figure 4.5 (j) shows the airflow at 90° CA BTDC. The small vortex is still present on the left-hand side of the measurement region, with the centre now quite visible. Flow on the right hand side is now even stronger than before, with maximum velocities increasing again to over 5 m/s. All flow along the bottom of the measurement zone is now in an upward direction as a result of the rapidly approaching piston.

Figure 4.5 (k) shows the in-cylinder flow at 80 °CA BTDC. Here the flow map is very similar to previous crank angle, though the flow in the upward direction is stronger still.

With the piston now at the very bottom of the measurement area, Figure 4.5 (l) shows the flow at 70 °CA BTDC. Any sign of the vortex has now been destroyed and flow exceeding 5 m/s is present along the whole of the lower edge of the measurement region.

Figure 4.5 (m) shows the in-cylinder flow 10 °CA later at 60 °CA BTDC. Here the piston has encroached the measurement area and is producing very strong upward flow across much of the velocity map. Some flow across the cylinder towards the left-hand side is still present in the upper half of the map.

The map shown in Figure 4.5 (n) shows the flow at 50 °CA BTDC. Here almost all flow is in a strong upward direction though some horizontal flow is still present along the top edge.

The final map shown in Figure 4.5 (o) shows only strong upward flow, with no significant flow in any other direction.

Vertical Plane on Valve Centre-Line

Figure 4.6 shows the airflow PIV results obtained with a measurement plane below one exhaust and one intake valve. As with the central plane, the earliest result that could be achieved during the intake stroke was at 50 °CA ATDC and is shown in Figure 4.6 (a). Here the flow is markedly different to that seen at this point in the central plane shown in Figure 4.5 (a). There is a strong upward flow close to the intake valves, though it is not clear exactly where this is coming from since it does not appear to originate from the intake valves.

Figure 4.6 (b) shows how this flow develops and results in 2 weak vortices, one on the right hand side and one on the top edge of the measurement area. Comparing this result to that in the vertical plane, the strong flow from the intake valve shown in Figure 4.5 (b) is still absent and the peak flow velocities are approximately halved.

Halfway through the intake stroke at 90 °CA ATDC, Figure 4.6 (c) shows that although the right hand vortex has disappeared, the centre one has become more defined. It is likely that this vortex is formed by high-speed flow leaving the top side of the intake valve, passing along the cylinder head roof and entering the measurement region on the exhaust side.

Figure 4.6 (d) shows the state of the in-cylinder flow at 120°CA ATDC. Here the central vortex is still apparent, but the overall velocity of the flow has reduced, probably because the piston is now in the second half of the stroke and it decelerating towards BDC

In Figure 4.6 (e), taken at 150 °CA ATDC, the central vortex is still present though there is now a strong upward flow on the intake valve side of the cylinder. However, intake flow into the cylinder can be seen entering the field of view from above on the exhaust valve side, passing through the measurement region into the lower part of the cylinder.

As the intake stroke comes to an end, Figure 4.6 (f) shows that the vortex has now almost disappeared, while the upward flow on the intake side is still strong. However, the maximum flow velocity has reduced to around 3 m/s.

Figure 4.6 (g) shows the first set of results taken in the compression stroke at 150 °CA BTDC. Here the flow velocity on the exhaust valve side is very low, while on the intake side the upward flow has become stronger.

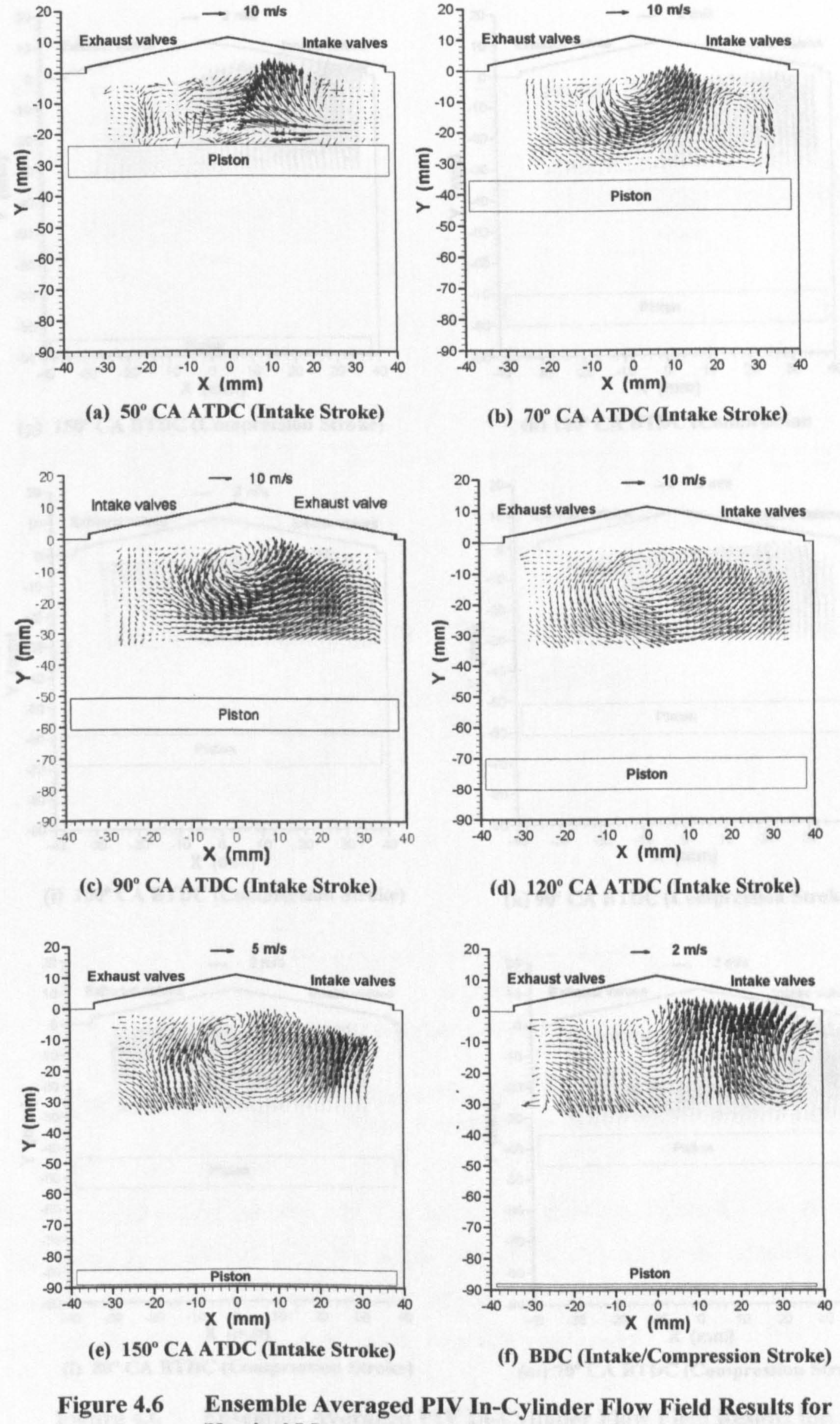

(a) 50° CA ATDC (Intake Stroke)

(b) 70° CA ATDC (Intake Stroke)

(c) 90° CA ATDC (Intake Stroke)

(d) 120° CA ATDC (Intake Stroke)

(e) 150° CA ATDC (Intake Stroke)

(f) BDC (Intake/Compression Stroke)

Figure 4.6 Ensemble Averaged PIV In-Cylinder Flow Field Results for Vertical Measurement Plane under Valves

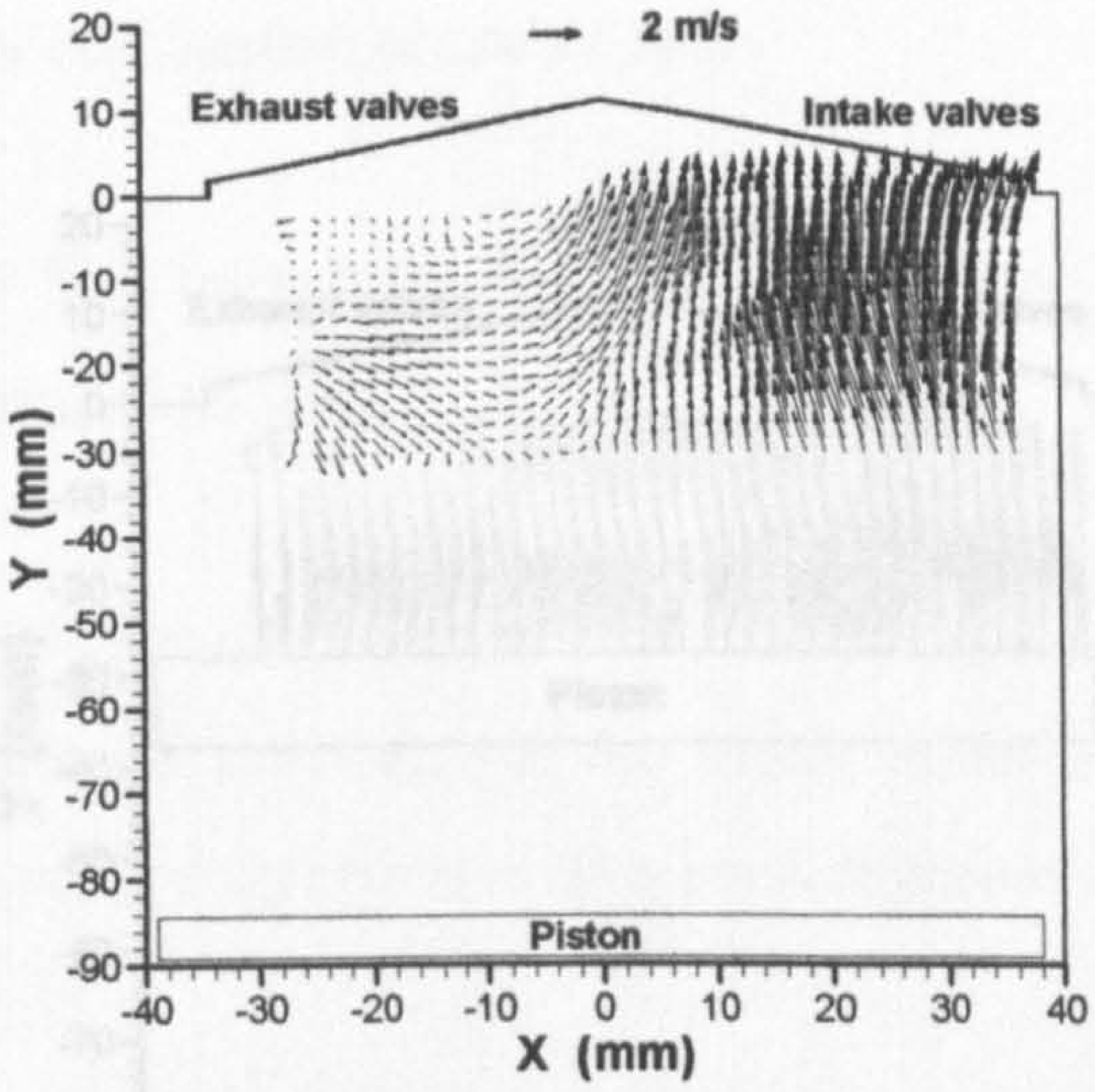

(g) 150° CA BTDC (Compression Stroke)

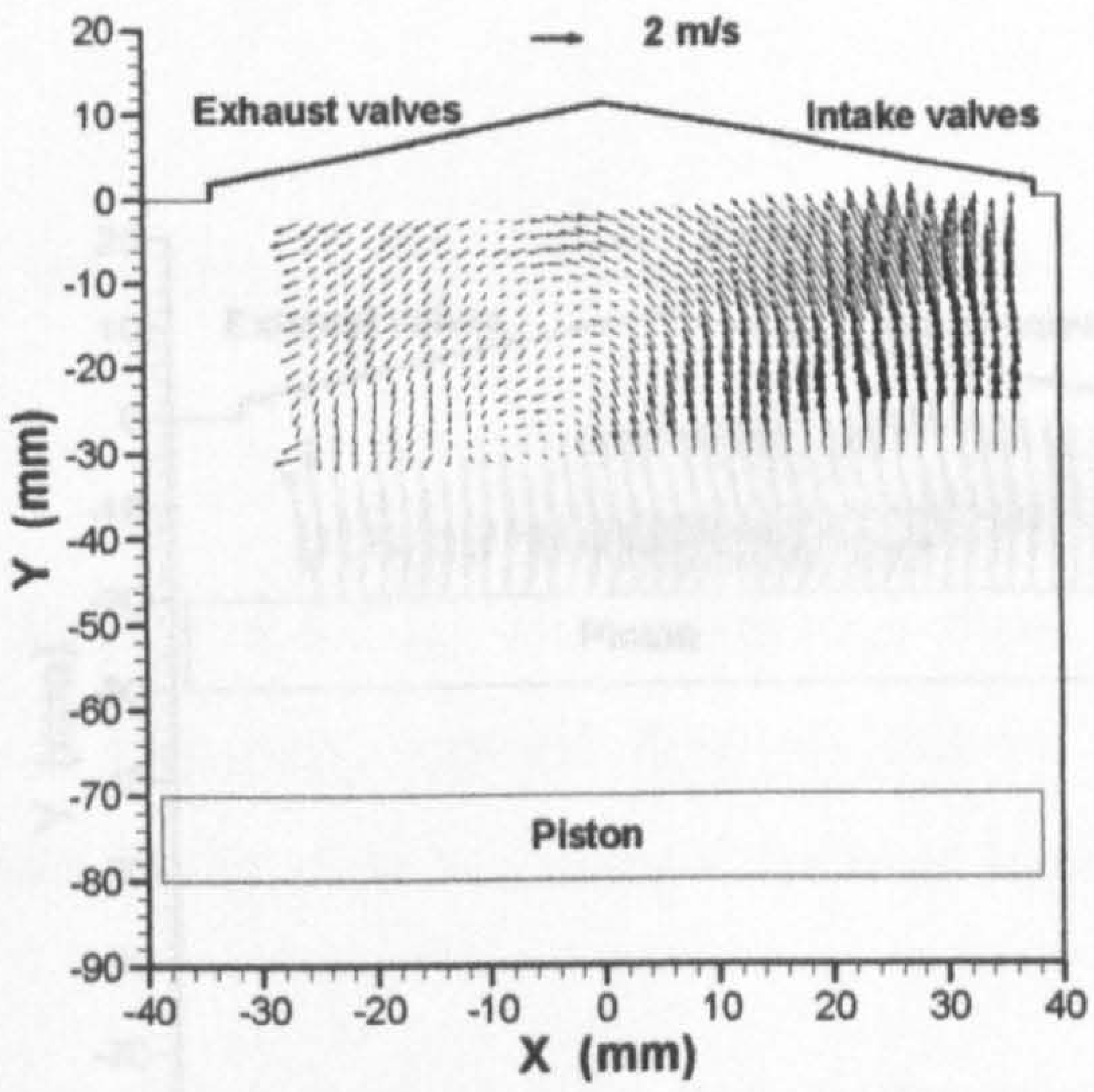

(h) 120° CA BTDC (Compression

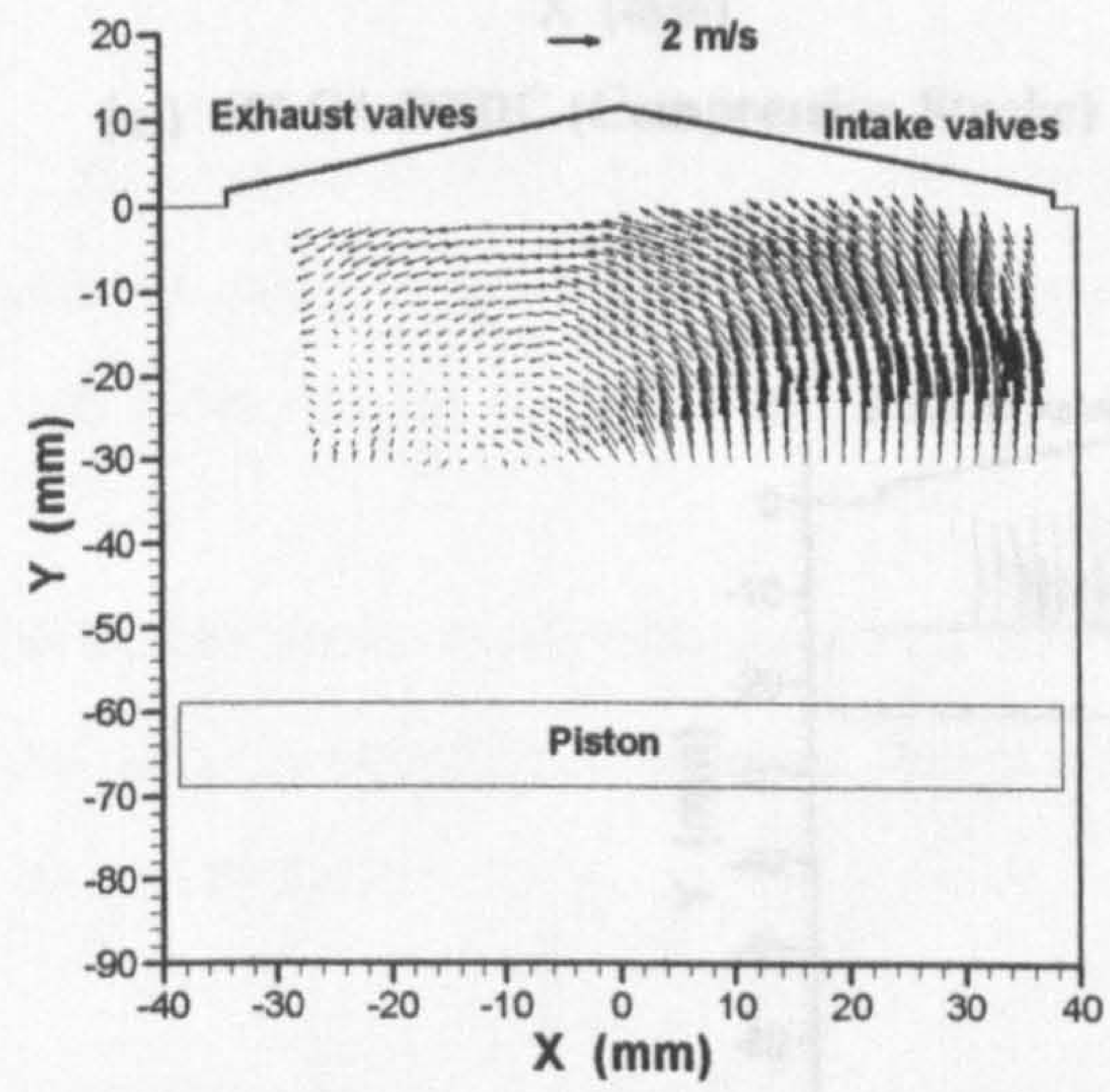

(i) 100° CA BTDC (Compression Stroke)

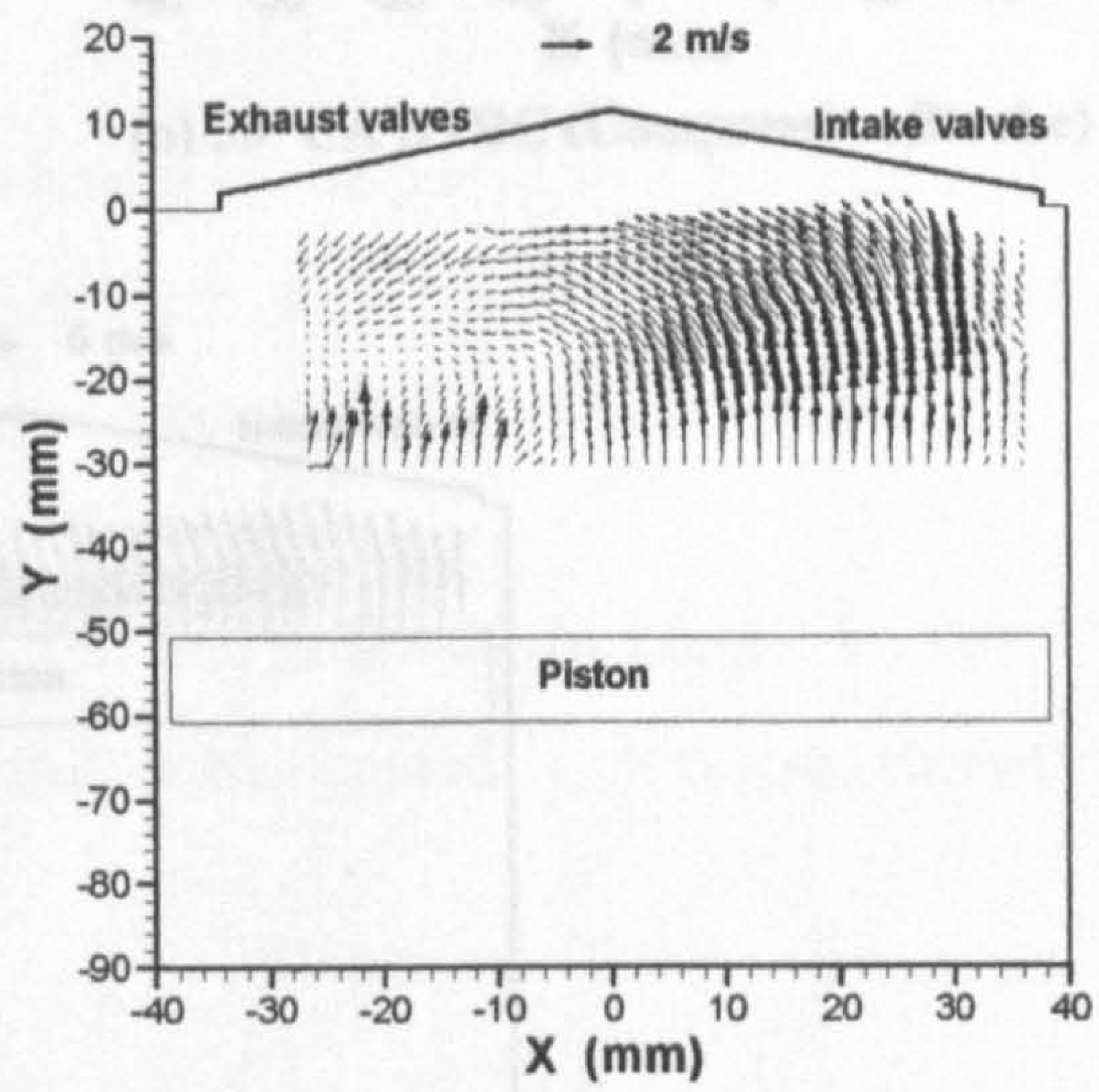

(k) 90° CA BTDC (Compression Stroke)

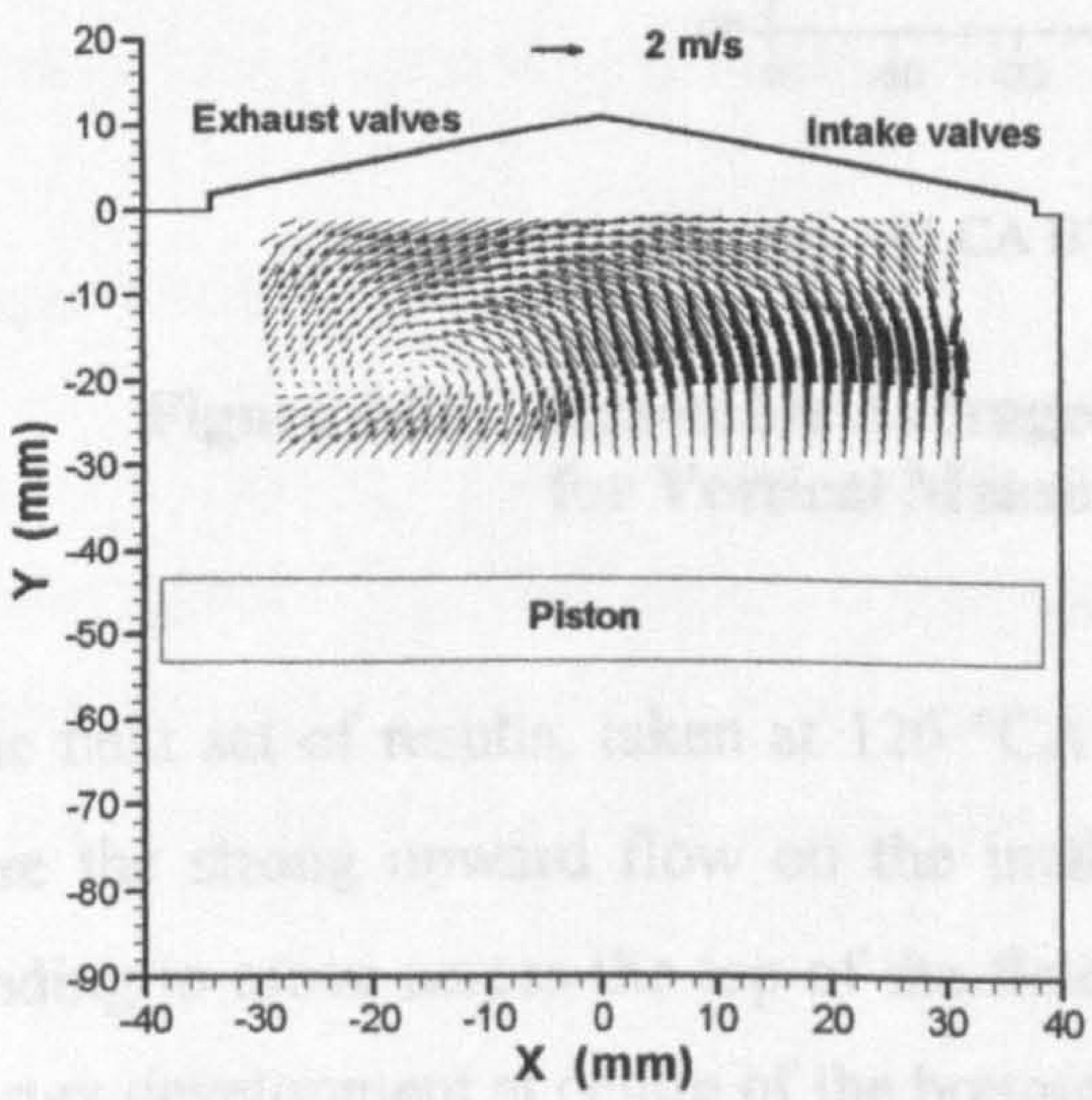

(l) 80° CA BTDC (Compression Stroke)

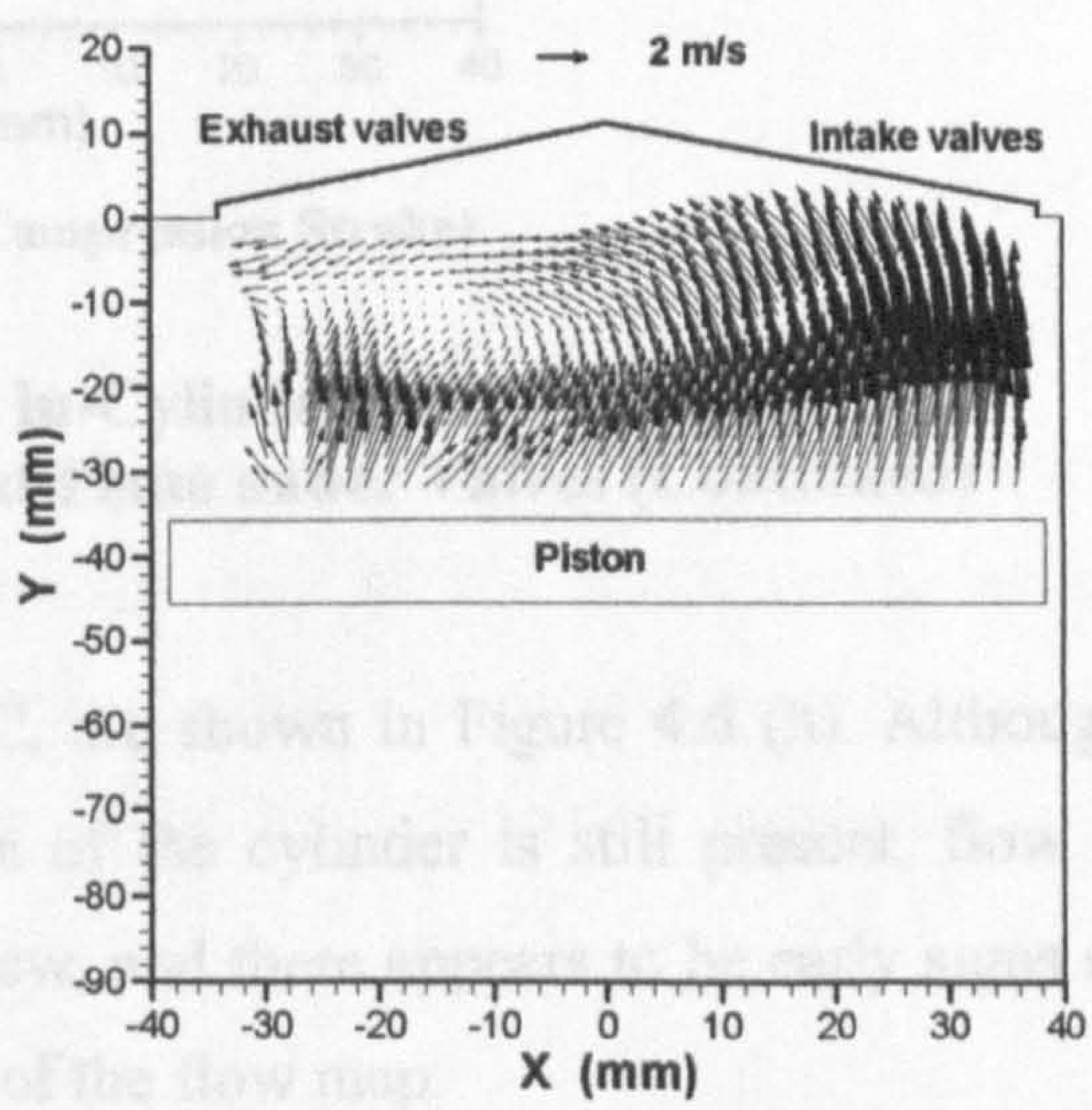

(m) 70° CA BTDC (Compression Stroke)

Figure 4.6 Ensemble Averaged PIV In-Cylinder Flow Field Results for Vertical Measurement Plane under Valves (Continued)

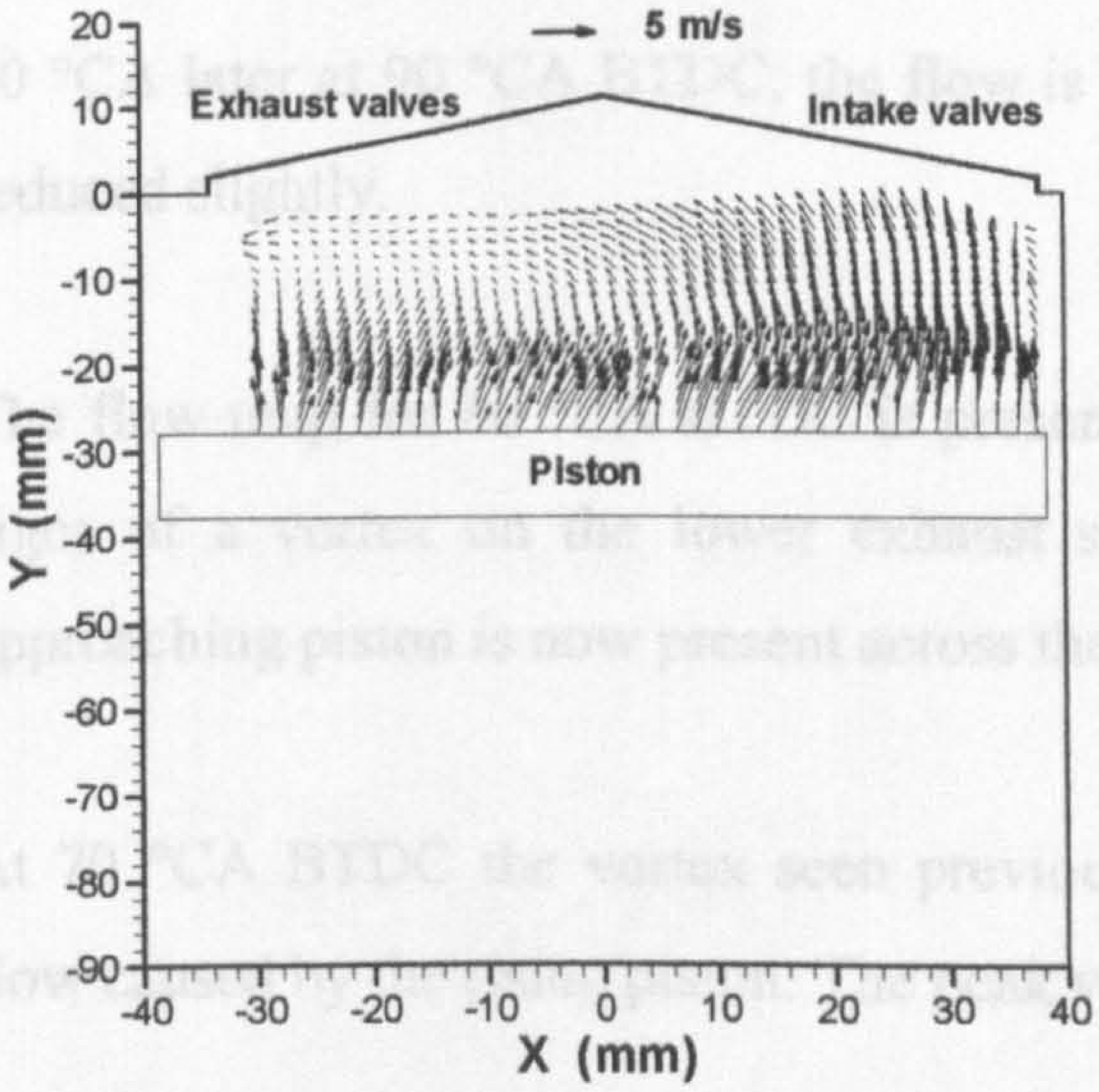

(m) 60° CA BTDC (Compression Stroke)

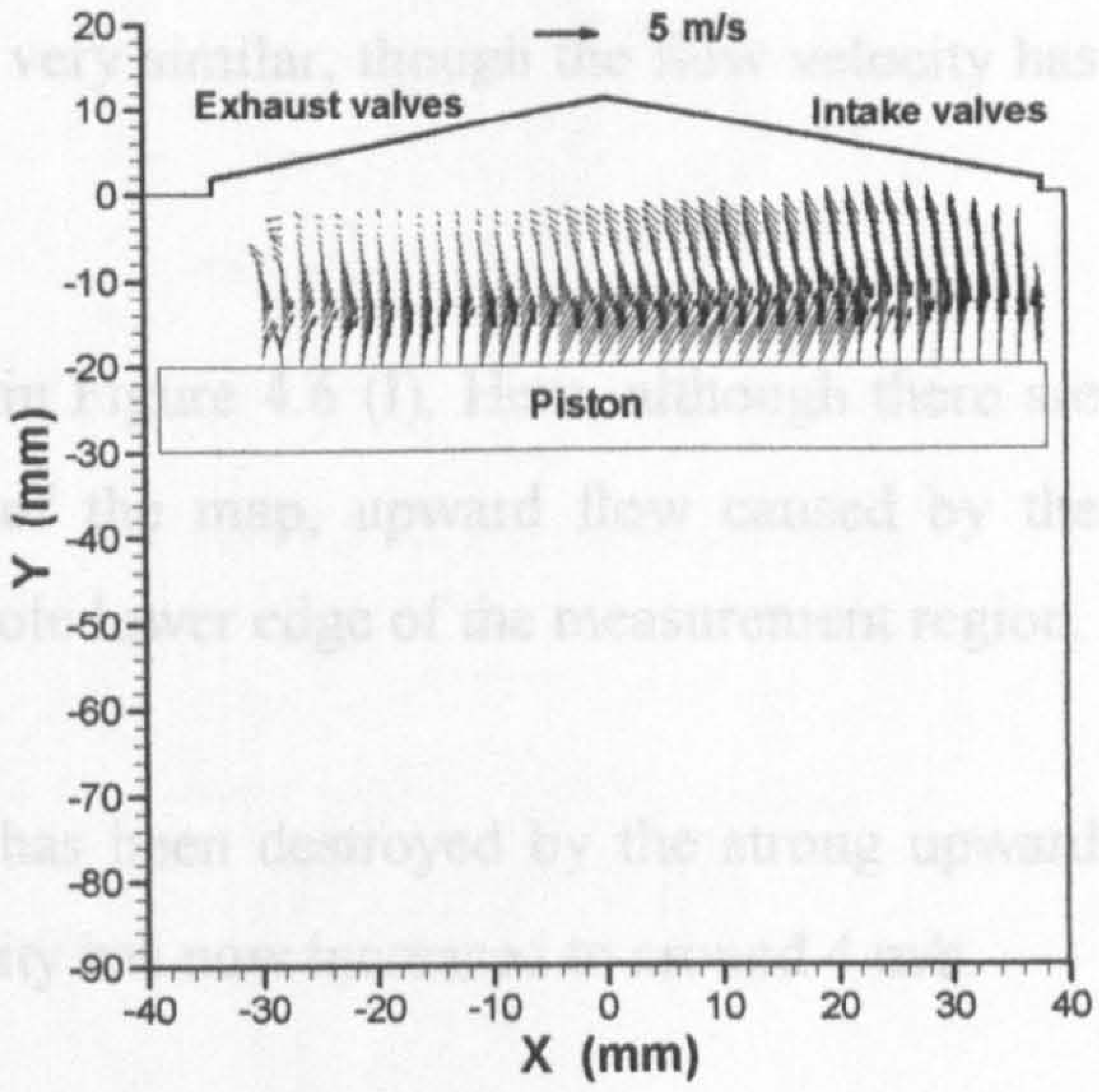

(o) 50° CA BTDC (Compression Stroke)

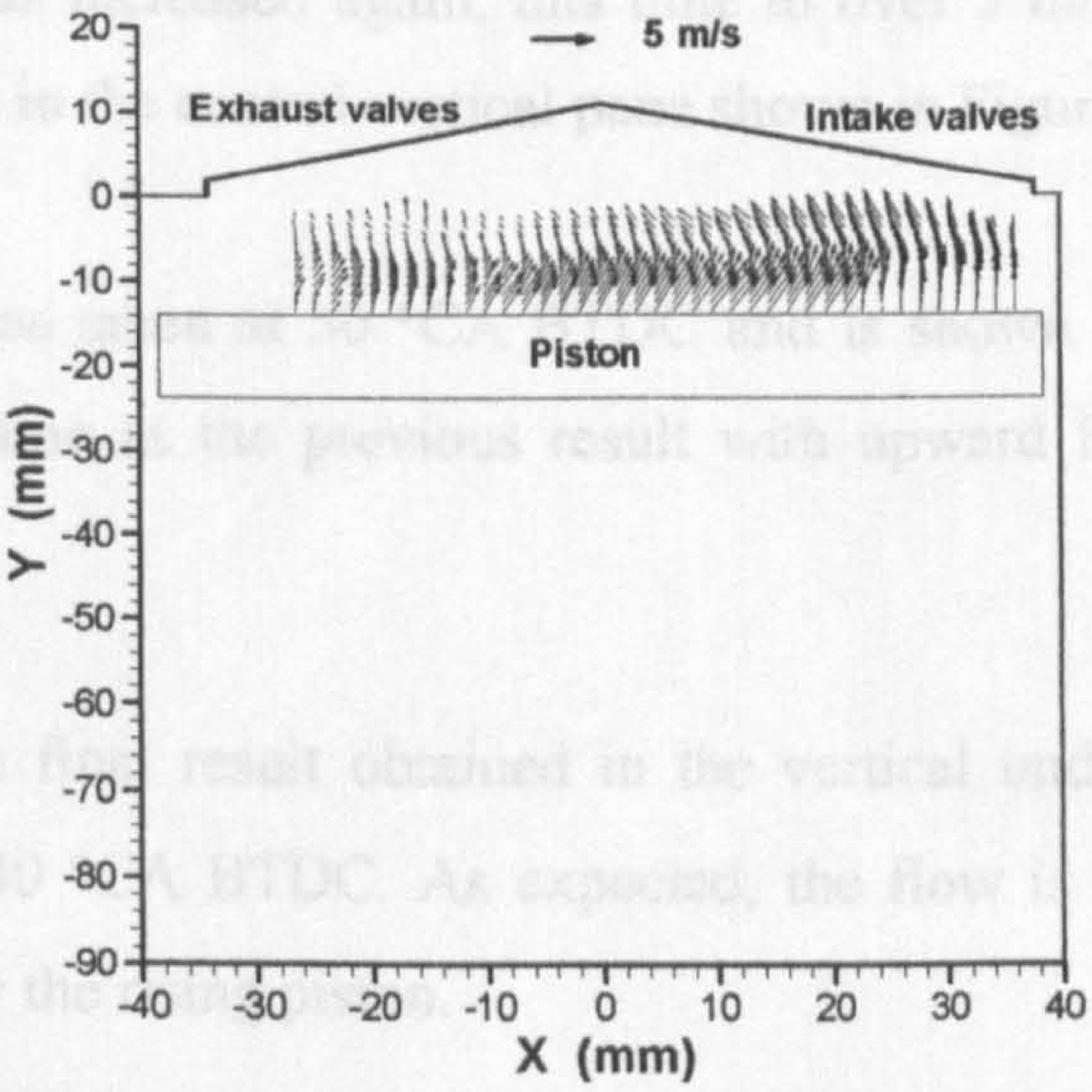

(p) 40° CA BTDC (Compression Stroke)

Figure 4.6 Ensemble Averaged PIV In-Cylinder Flow Field Results for Vertical Measurement Plane under Valves (Continued)

The next set of results, taken at 120 °CA BTDC, are shown in Figure 4.6 (h). Although here the strong upward flow on the intake side of the cylinder is still present, flow is tending to move across the top of the field of view, and there appears to be early signs of vortex development at centre of the bottom edge of the flow map.

Figure 4.6 (i) shows the in-cylinder flow conditions at 100 °CA BTDC in the compression stroke. The situation here is little different from that in the previous set of results, with the strong upward flow on the intake side tending to turn towards the exhaust side it reaches the combustion chamber roof.

10 °CA later at 90 °CA BTDC, the flow is still very similar, though the flow velocity has reduced slightly.

The flow map for 80 °CA BTDC is presented in Figure 4.6 (l). Here, although there are signs of a vortex on the lower exhaust side of the map, upward flow caused by the approaching piston is now present across the whole lower edge of the measurement region.

At 70 °CA BTDC the vortex seen previously has been destroyed by the strong upward flow caused by the rising piston. The peak velocity has now increased to around 4 m/s.

Figure 4.6 (m) at 60 °CA BTDC sees the encroachment of the piston into the field of view. Here the peak velocity has increased again, this time to over 5 m/s and the flow is now much more similar to that in the central vertical pane shown in Figure 4.5 (m).

The penultimate result was taken at 50 °CA BTDC and is shown in Figure 4.6 (o). The flow here is much the same as the previous result with upward flow across almost the whole flow field.

Figure 4.6 (p) shows the final result obtained in the vertical under valve measurement plane and was taken at 40 °CA BTDC. As expected, the flow is still dominated by the upward flow generated by the rising piston.

Upper Horizontal Plane

Figure 4.7 shows the airflow PIV results in the upper horizontal measurement plane. In this measurement field, good results could not be obtained until 90 °CA ATDC in the intake stroke. Attempts at obtaining measurements earlier in the induction process were prevented by the large out of plane motions present in the horizontal direction during this period.

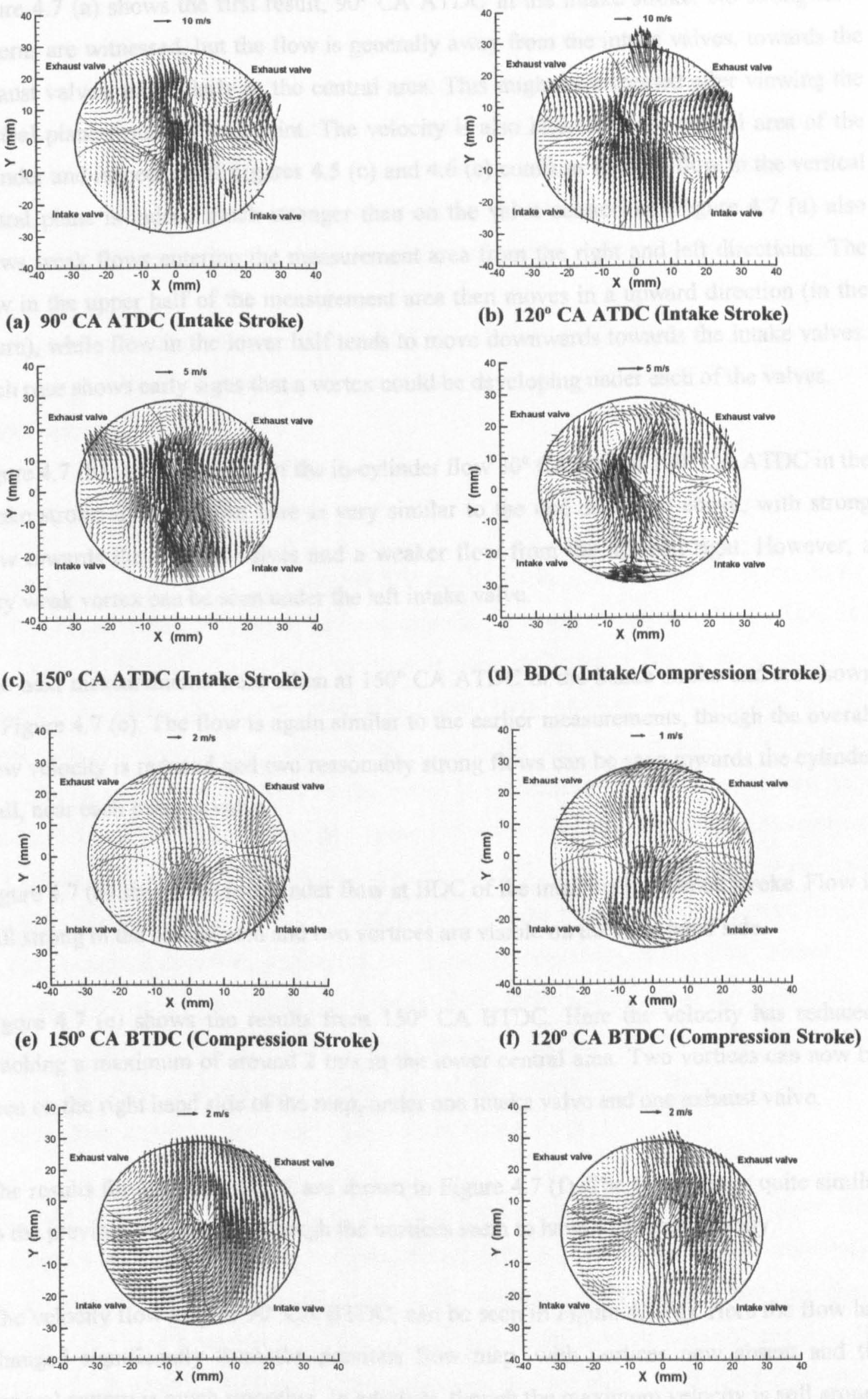

(a) 90° CA ATDC (Intake Stroke)

(b) 120° CA ATDC (Intake Stroke)

(c) 150° CA ATDC (Intake Stroke)

(d) BDC (Intake/Compression Stroke)

(e) 150° CA BTDC (Compression Stroke)

(f) 120° CA BTDC (Compression Stroke)

(g) 90° CA BTDC (Compression Stroke)

(h) 60° CA BTDC (Compression Stroke)

Figure 4.7 Ensemble Averaged PIV In-Cylinder Flow Field Results for Upper Horizontal Measurement Plane

Figure 4.7 (a) shows the first result, 90° CA ATDC in the intake stroke. No strong flow patterns are witnessed, but the flow is generally away from the intake valves, towards the exhaust valves, particularly in the central area. This might be expected after viewing the vertical plane results at this point. The velocity is also highest in the central area of the cylinder and inspection of Figures 4.5 (c) and 4.6 (c) confirms that the flow in the vertical central plane is indeed much stronger than on the valve centre line. Figure 4.7 (a) also shows weak flows entering the measurement area from the right and left directions. The flow in the upper half of the measurement area then moves in a upward direction (in the figure), while flow in the lower half tends to move downwards towards the intake valves. Each case shows early signs that a vortex could be developing under each of the valves.

Figure 4.7 (b) shows the state of the in-cylinder flow 30° CA later at 120° CA ATDC in the intake stroke. The situation here is very similar to the one discussed above, with strong flow towards the exhaust valves and a weaker flow from the left and right. However, a very weak vortex can be seen under the left intake valve.

The next measurements were taken at 150° CA ATDC in the intake stroke and are shown in Figure 4.7 (c). The flow is again similar to the earlier measurements, though the overall flow velocity is reduced and two reasonably strong flows can be seen towards the cylinder wall, near each exhaust valve.

Figure 4.7 (d) shows the in-cylinder flow at BDC of the intake/compression stroke. Flow is still strong in the central area and two vortices are visible on the right hand side.

Figure 4.7 (e) shows the results from 150° CA BTDC. Here the velocity has reduced, reaching a maximum of around 2 m/s in the lower central area. Two vortices can now be seen on the right hand side of the map, under one intake valve and one exhaust valve.

The results for 150° CA BTDC are shown in Figure 4.7 (f). The flow here is quite similar to the previous crank angle, though the vortices seem to have weakened slightly

The velocity flow map at 90° CA BTDC, can be seen in Figure 4.7 (g). Here the flow has changed significantly from the previous flow map, with vortices now absent and the general pattern is much smoother. In addition, though the maximum velocity is still around 2 m/s, the intensity is much more uniform across the flow field. Curiously, significant differences can be seen between each side of the velocity map since, while flow on the right hand side is mainly towards the exhaust valves, the left hand side and lower central area, has strong flow in the horizontal direction. This was not expected since the design of cylinder head is such that the flow should be symmetrical about the combustion chamber centre line between each pair of intake and exhaust valves. However, the non-symmetric nature of the flow would suggest that some geometric differences exist between the two intake ports. Since the cylinder head was made by machining from solid, rather than by casting, the ports are hand finished and therefore more variation than normal might exist.

The last set of results, taken at 60 °CA BTDC in the compression stroke, are shown in Figure 4.7 (h). The flow here is very similar to that found at 90 °CA BTDC, though the overall velocity has fallen.

Lower Horizontal Plane

Figure 4.8 shows the ensemble averaged PIV results for the lower horizontal plane. Again, the first set of results were taken half way through the intake stroke at 90 °CA ATDC and are shown in Figure 4.8 (a). Here the flow is quite different to that in the upper plane presented in Figure 4.7 (a). The strong flow in the central area is now absent, and the only continuous flow towards the intake valves exists in the area between the two valve pairs. The flow below each intake valve initially moves towards the exhaust side but then turns sharply towards the chamber wall and appears to show early signs of vortex development. Inspection of Figure 4.5 (c), which shows the central vertical plane at the same crank position, shows that area of the flow corresponding to the lower horizontal plane is largely in the downward direction, explaining the disappearance of the strong flow towards the exhaust valves seen in the upper plane. Meanwhile, at the same point in the vertical plane under the valves in Figure 4.6 (c), (which passes under the right hand set of valves in Figure 4.8), flow is towards the intake side of the cylinder head. This corresponds well with the flow measured in the right hand side of Figure 4.8 (a).

The flow map at 120 °CA ATDC in the intake stroke is presented in Figure 4.8 (b). Here the flow has changed from the previous result, with the development of a vortex below each intake valve. The flow is now much more symmetrical, with flow towards the exhaust valves in the centre section, and flow towards the intake side on the right and left. The general flow velocity has also reduced somewhat, peaking at less than 5 m/s. Comparing again with the central vertical plane at this point in Figure 4.5 (d), flow velocity is also much reduced. The vortex noted in the vertical under valve plane in Figure 4.6 (c) is still

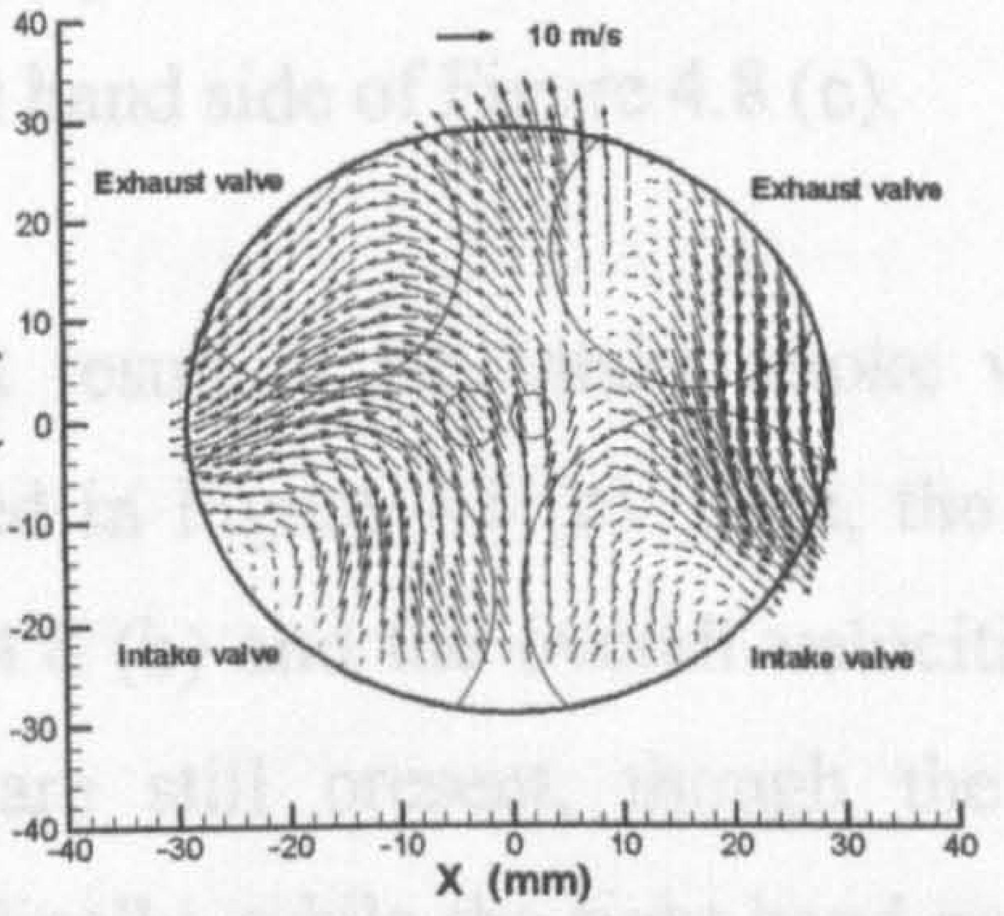

(a) 90° CA ATDC (Intake Stroke)

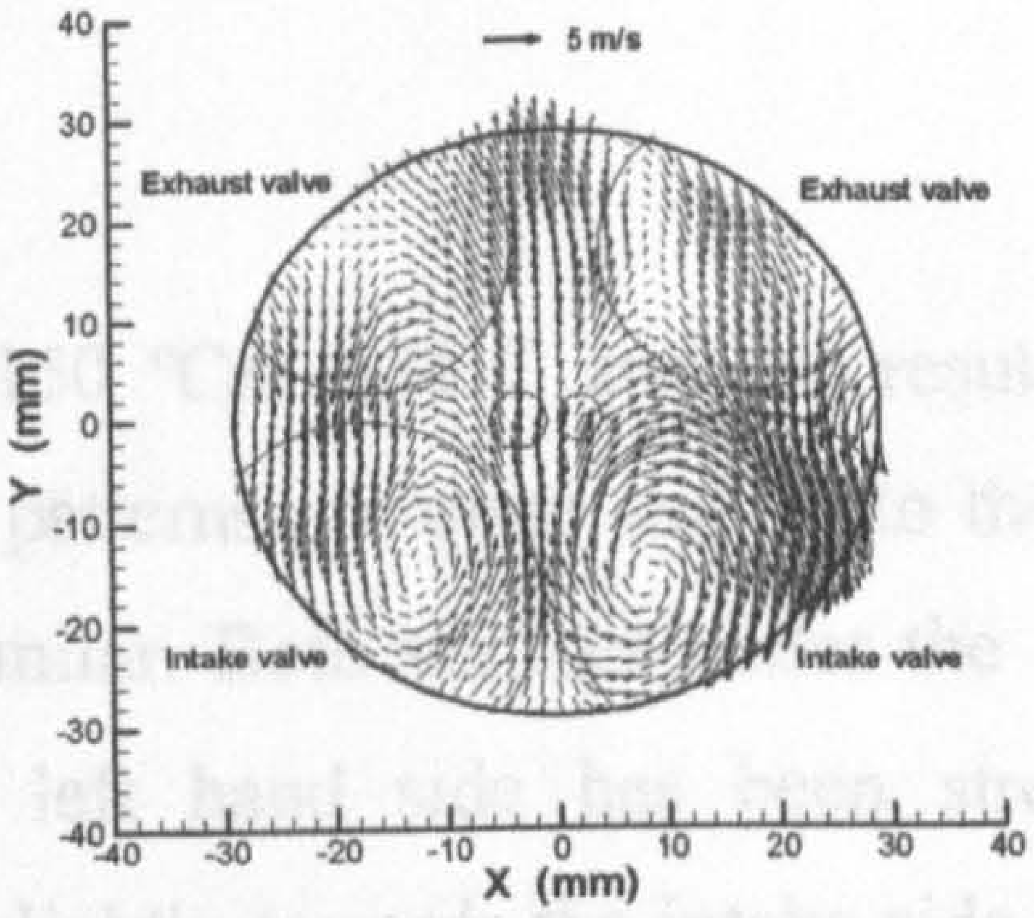

(b) 120° CA ATDC (Intake Stroke)

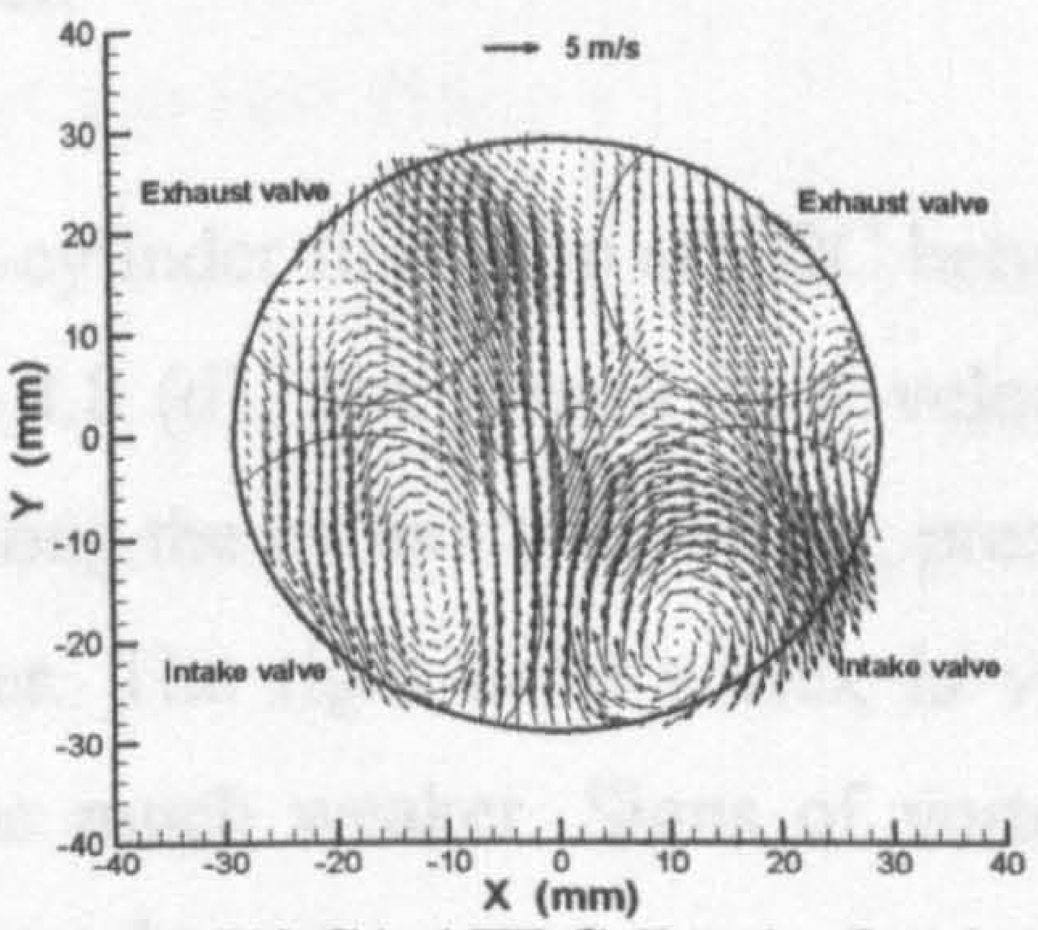

(c) 150° CA ATDC (Intake Stroke)

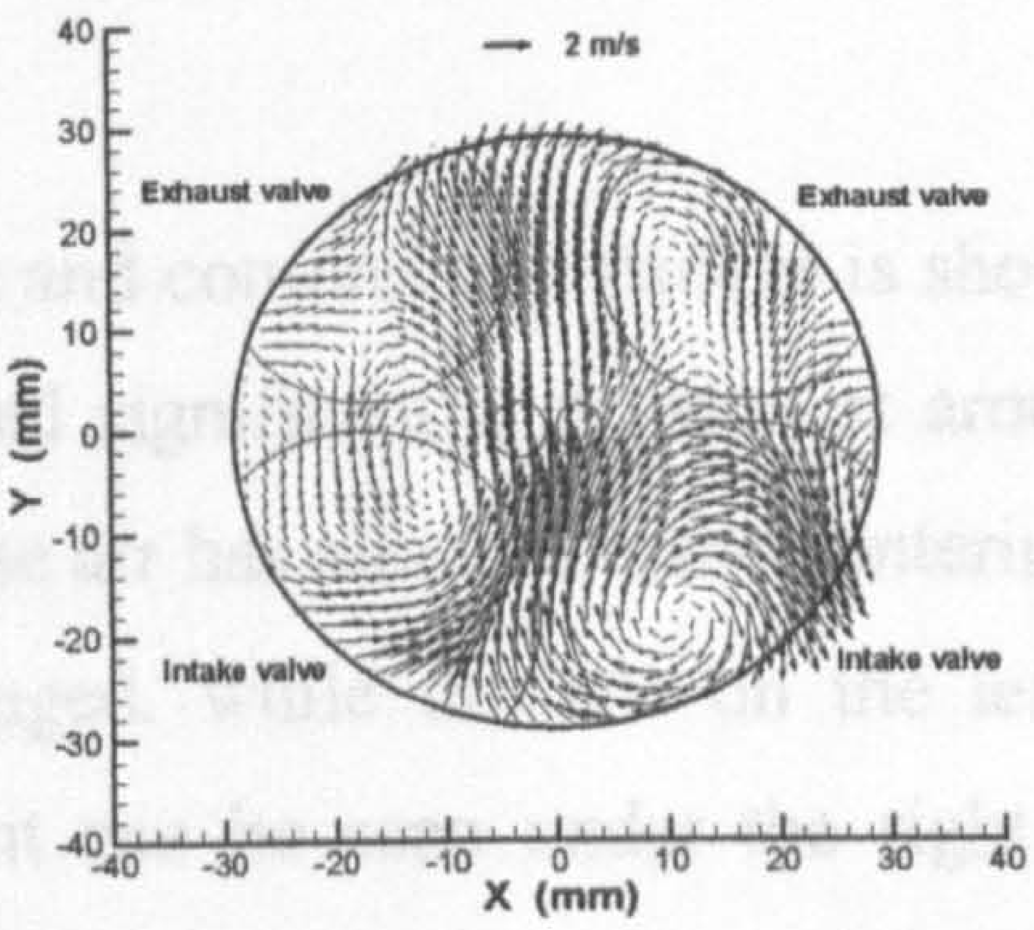

(d) BDC (Intake/Compression Stroke)

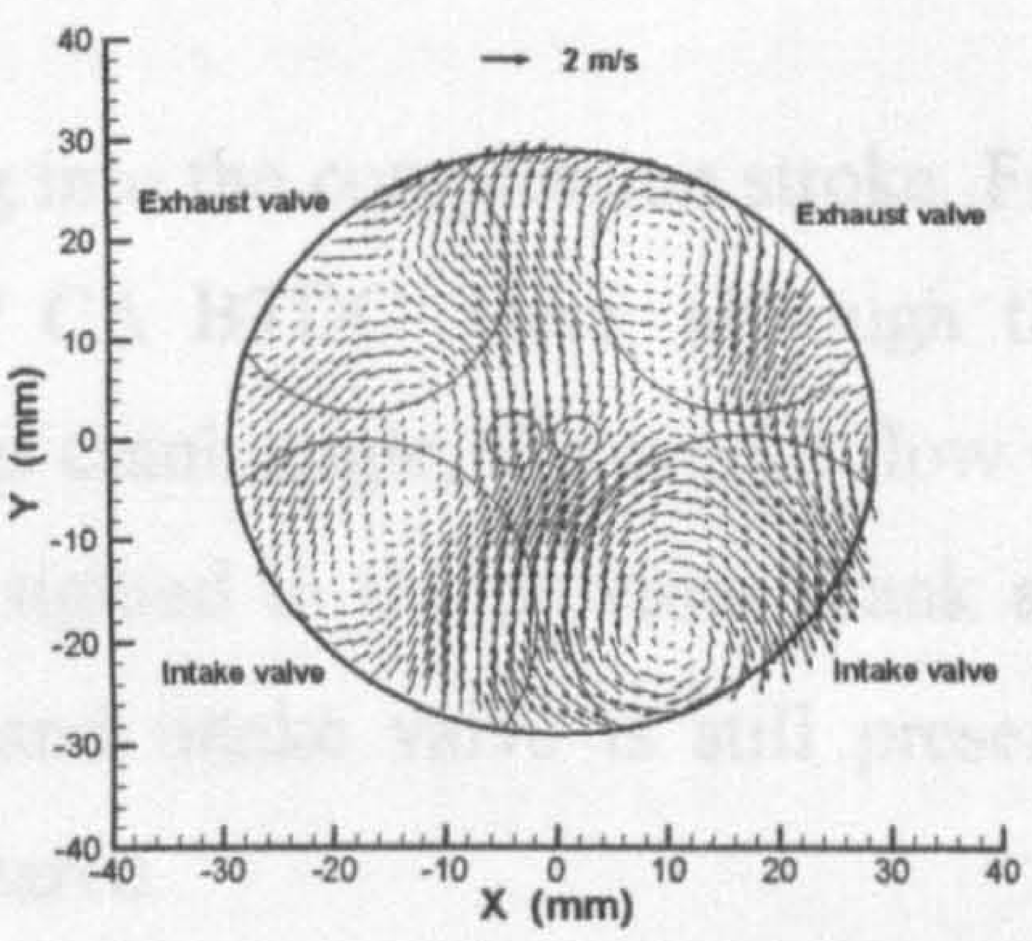

(e) 150° CA BTDC (Compression Stroke)

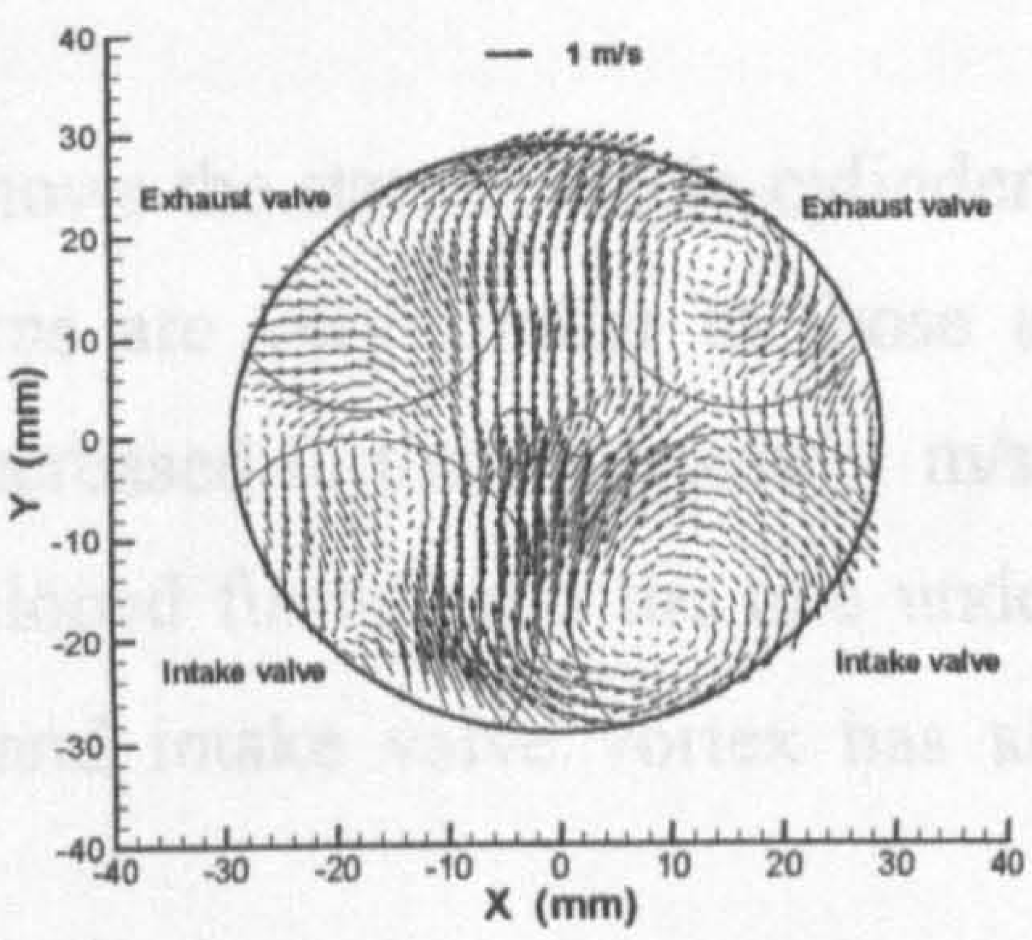

(f) 120° CA BTDC (Compression Stroke)

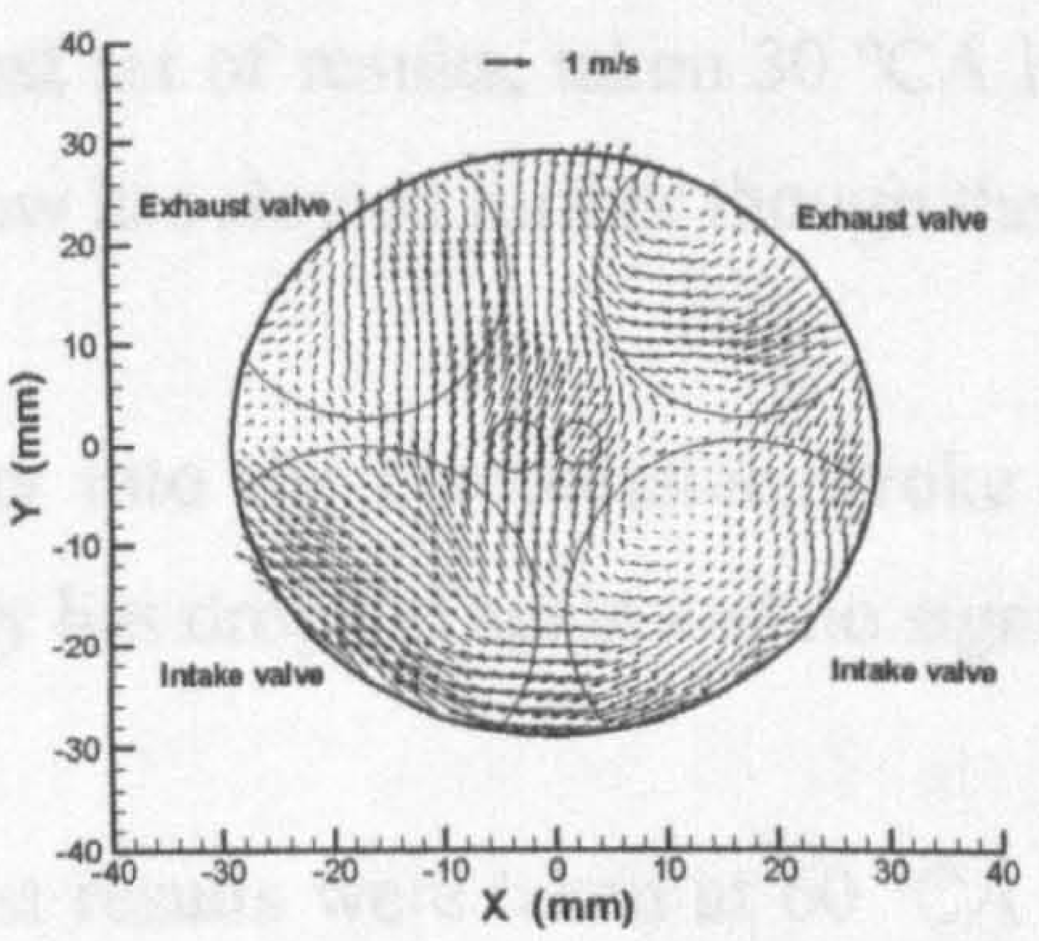

(g) 90° CA BTDC (Compression Stroke)

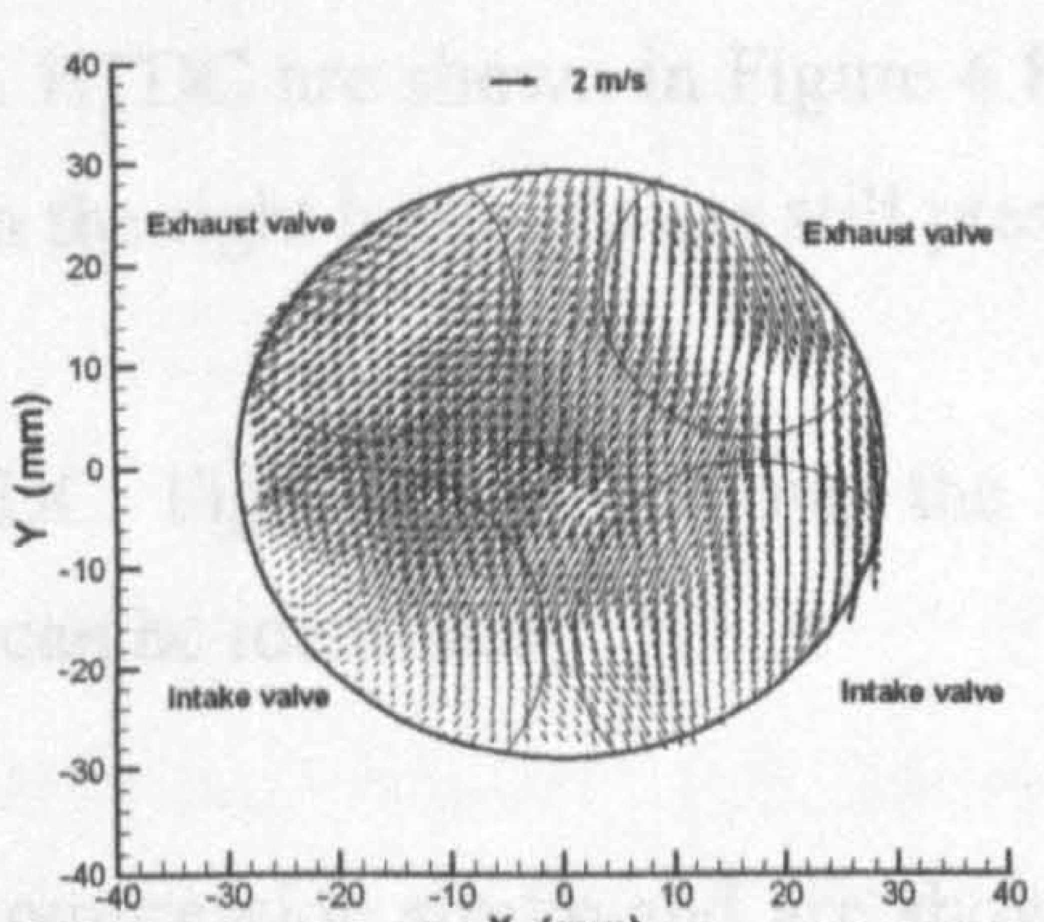

(h) 60° CA BTDC (Compression Stroke)

Figure 4.8 Ensemble Averaged PIV In-Cylinder Flow Field Results for Lower Horizontal Measurement Plane

there in Figure 4.6 (d) and therefore correlates well to the flow towards the intake side on the right hand side of Figure 4.8 (c).

The last result in the intake stroke was taken at 150 °CA ATDC and the results are presented in Figure 4.8 (c). Here, the general flow patterns are quite similar to those in Figure 4.8 (b) and the overall velocities are also similar. Both vortices under the intake valves are still present, though the one on the left hand side has been stretched longitudinally, while the right hand one has moved slightly towards the intake side of the chamber.

The in-cylinder flow map at BDC between the intake and compression strokes is shown in Figure 4.8 (d). The overall flow velocity has dropped significantly, peaking at around 2 m/s, along the cylinder centreline, presumably because air has almost finished entering the cylinder. The right hand vortex is virtually unchanged, while the one on the left has become much weaker. Signs of vortex development can be seen under the right hand exhaust valve.

Moving into the compression stroke, Figure 4.8 (e) shows the state of the in-cylinder flow at 150° CA BTDC. Here, although the flow patterns are very similar to those at the previous crank angle, the overall flow velocity has decreased further to around 1 m/s. The vortex sighted in the previous crank angle has developed further and the one under the right hand intake valve is still present. The left hand intake valve vortex has all but disappeared.

The next set of results, taken 30 °CA later at 120 °CA BTDC are shown in Figure 4.8 (f). The flow has slowed further though the two vortices on the right hand side are still present.

Midway into the compression stroke at 90 °CA BTDC, Figure 4.8 (g) shows the flow velocity has dropped again and no significant vortices can be identified.

The last results were taken at 60 °CA BTDC in the compression stroke and are shown in Figure 4.8 (h), with the piston crown only a few mm away from the measurement plane. Here the flow velocity has increased and most of the flow is moving diagonally across the cylinder, towards the left hand intake valve. Inspection of Figures 4.5 (m) and 4.6 (m) show that at, in the vertical plane, the corresponding area of the flow is almost exclusively moving in an upward direction as a result of the rapidly approaching piston. However the flow is also slightly towards the intake side, which confirms the results in Figure 4.8 (h).

4.8.1.2 Velocity Fluctuation

In order to help describe the large scale flow characteristics of the in-cylinder air motion the averaged RMS fluctuating velocity and averaged fluctuation kinetic energy were calculated over 80 cycles using Equations 4.15 and 4.16, as detailed in Section 4.7.2. It is important to note that these fluctuation fields include the bulk flow cycle to cycle variation

Central Vertical Plane

Figures 4.9 (a) and 4.9 (b) show the averaged RMS fluctuating velocity and averaged fluctuation kinetic energy in the central vertical plane during the intake and compression strokes. Beginning at 50° CA ATDC in the intake stroke, it can be seen that, after a modest initial increase, both the averaged RMS fluctuating velocity and averaged fluctuation kinetic energy fall rapidly throughout the intake stroke. The decline of the fluctuating velocity is less sharp that of the fluctuation kinetic energy, though both display an apparent increase at the end of intake stroke at 150° CA ATDC. The decline continues during the first half compression stroke, though at a much lower rate.

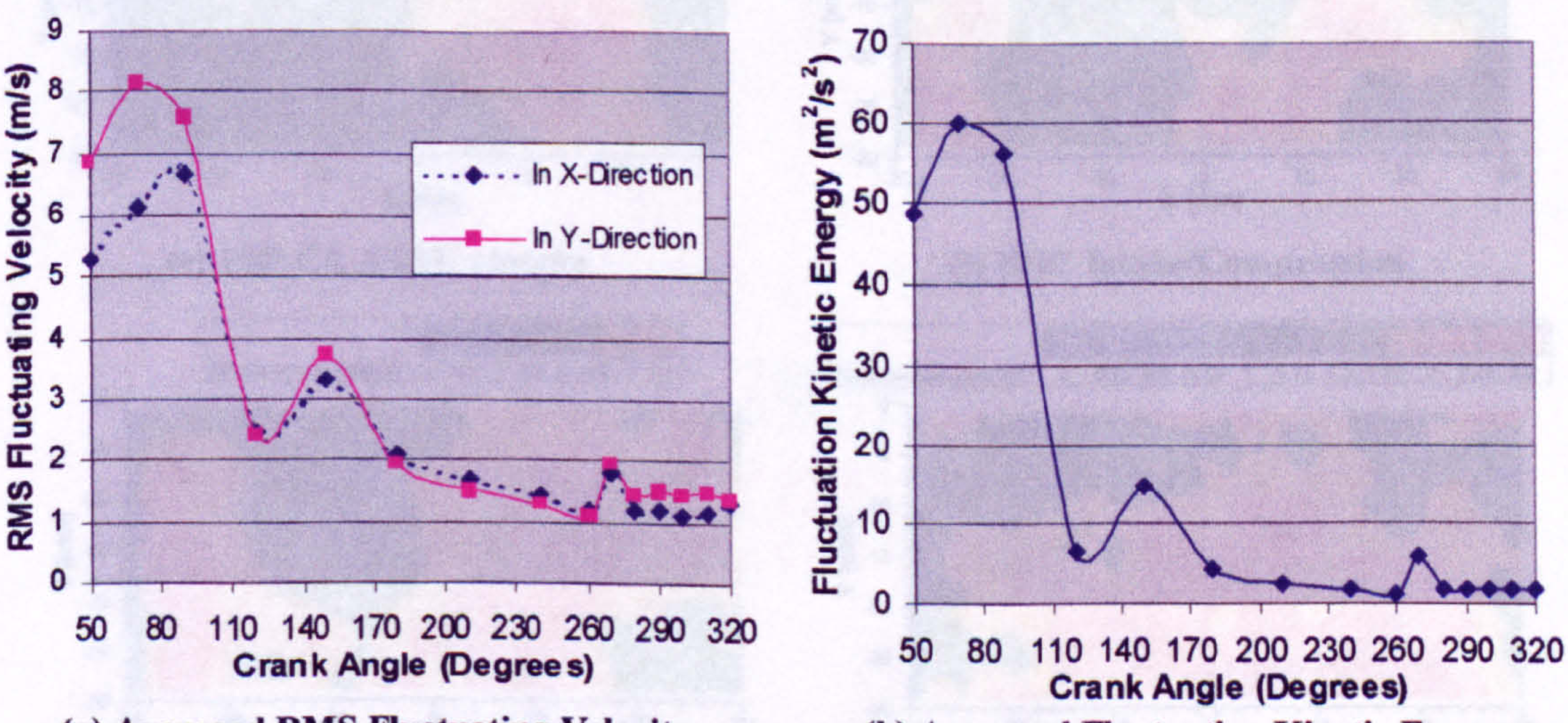

(a) Averaged RMS Fluctuating Velocity

(b) Averaged Fluctuation Kinetic Energy

Figure 4.9 Variation in Averaged RMS Fluctuating Velocity and Averaged Fluctuation Kinetic Energy during Intake and Compression Strokes (Central Vertical Plane)

In the second half of compression stroke, the fluctuation kinetic energy and fluctuating velocity in the in the X-direction appear to level off, while the fluctuating velocity in the Y- direction shows a very small increase. It is possible that this increase can be attributed to the breakdown of large scale flow structures at this point in the engine cycle, though

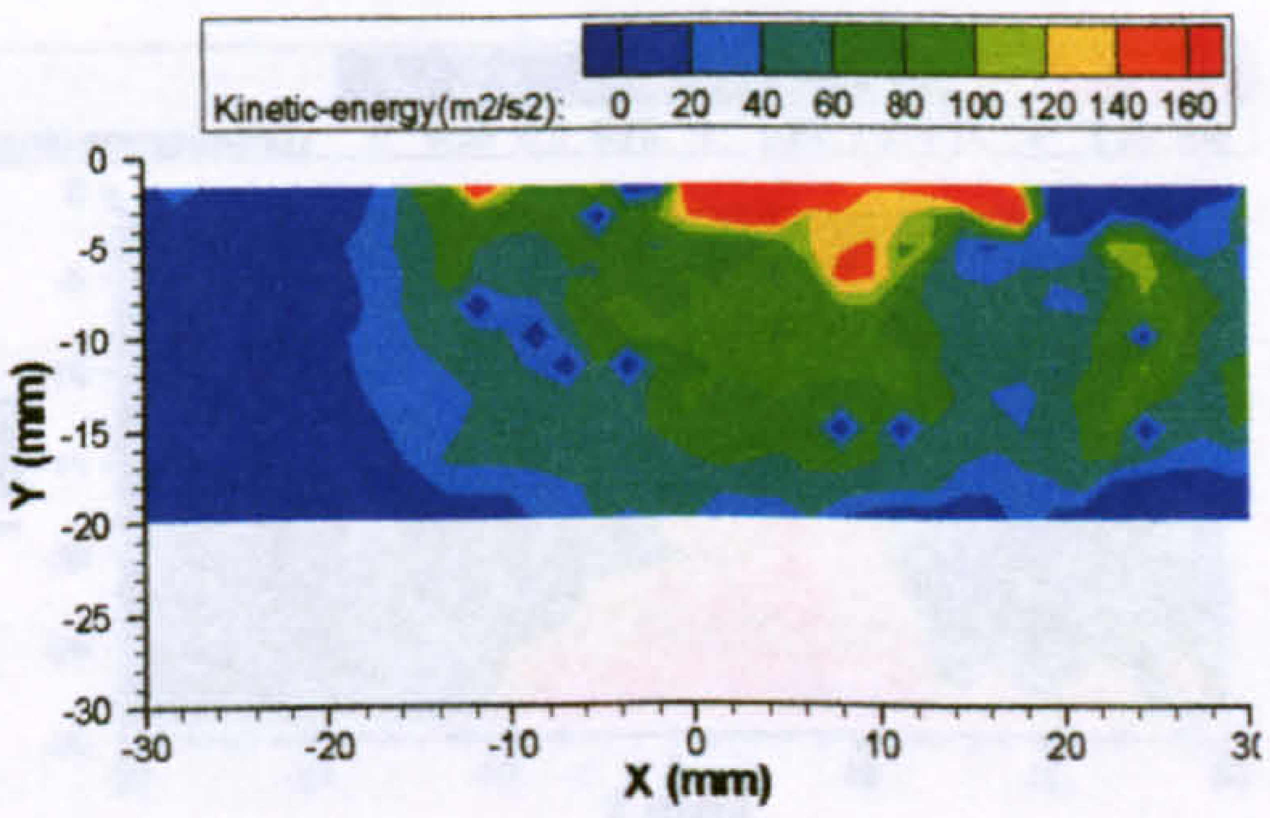

(a) 50° CA ATDC (Intake Stroke)

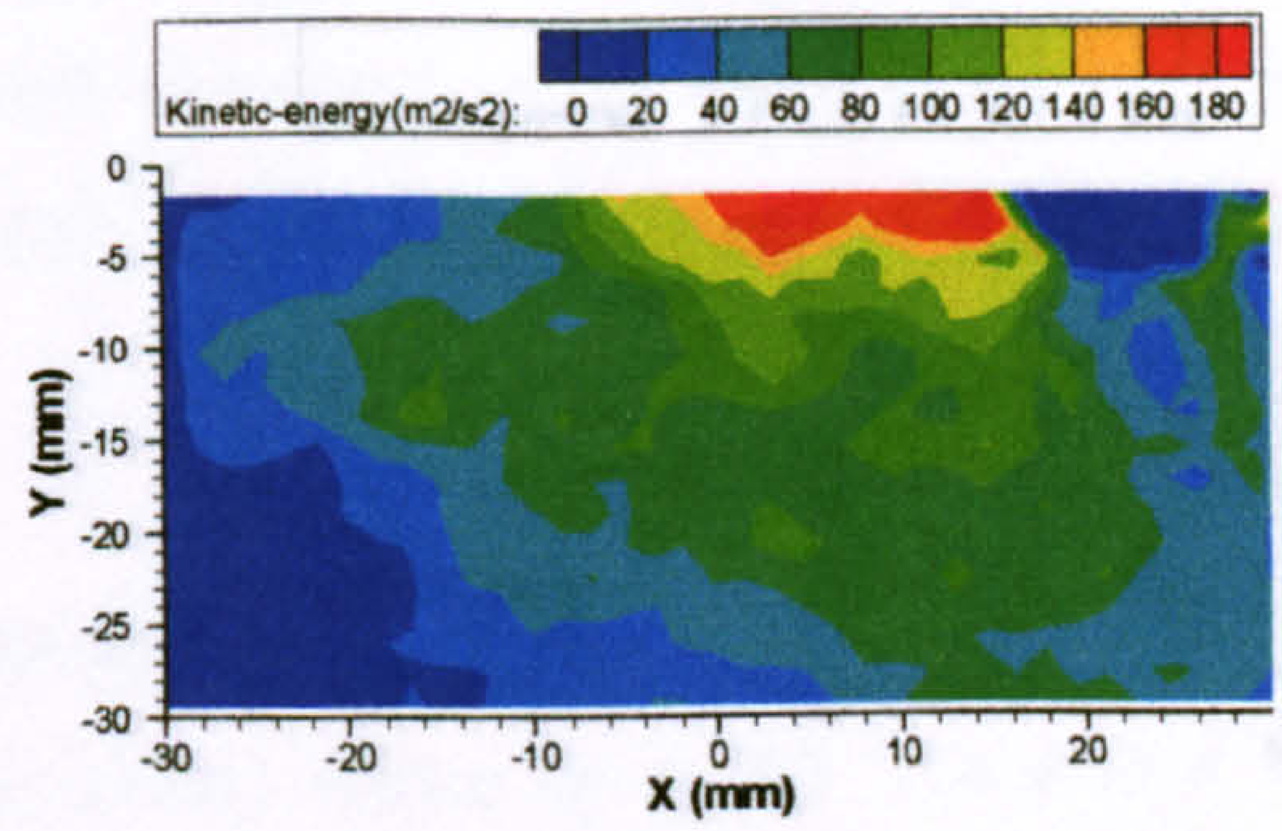

(b) 70° CA ATDC (Intake Stroke)

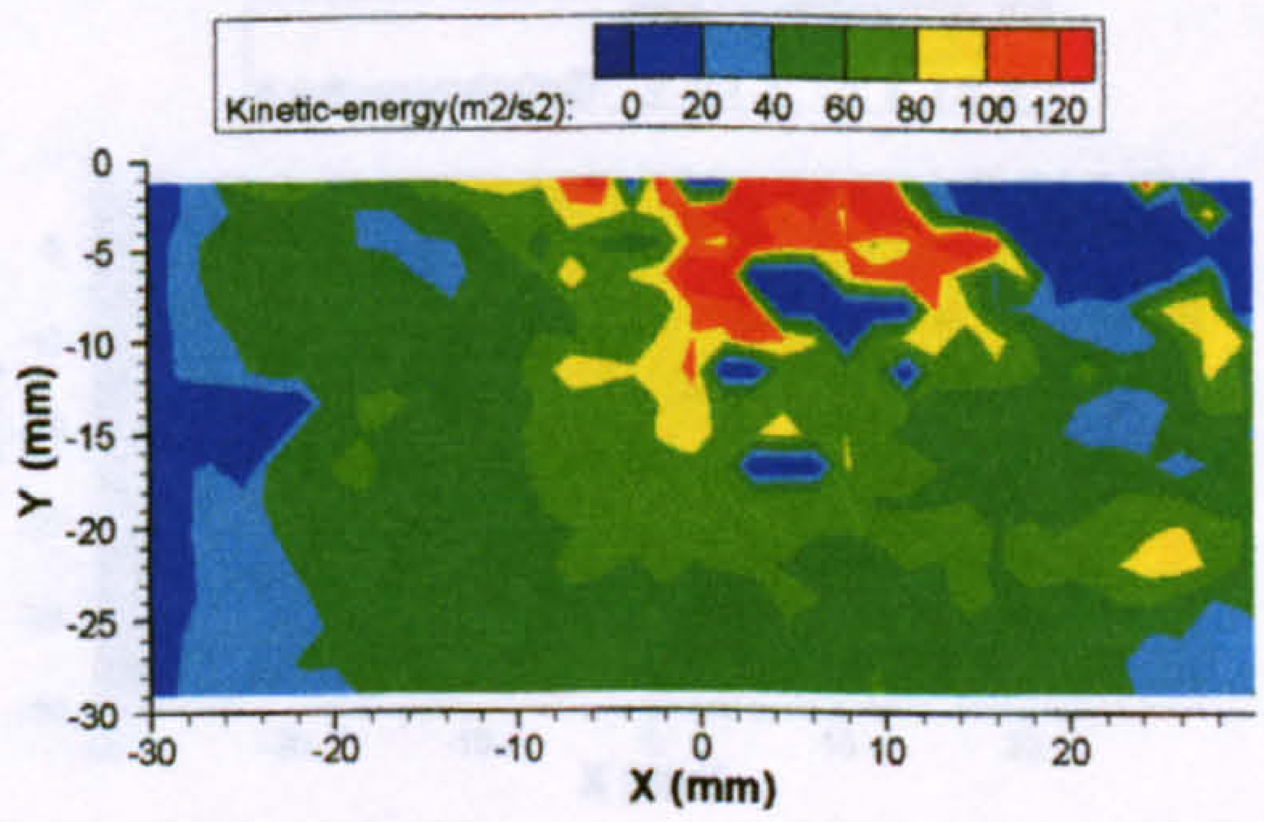

(c) 90° CA ATDC (Intake Stroke)

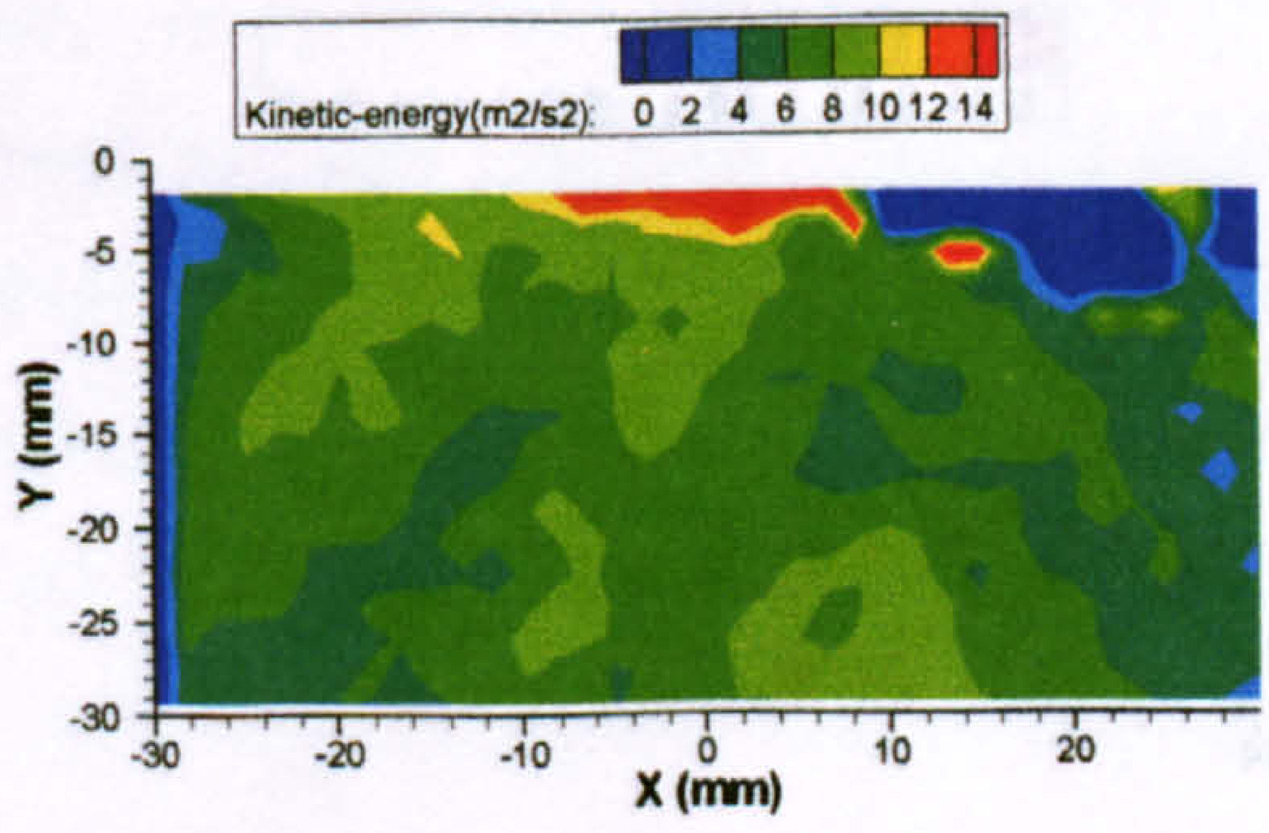

(d) 120° CA ATDC (Intake Stroke)

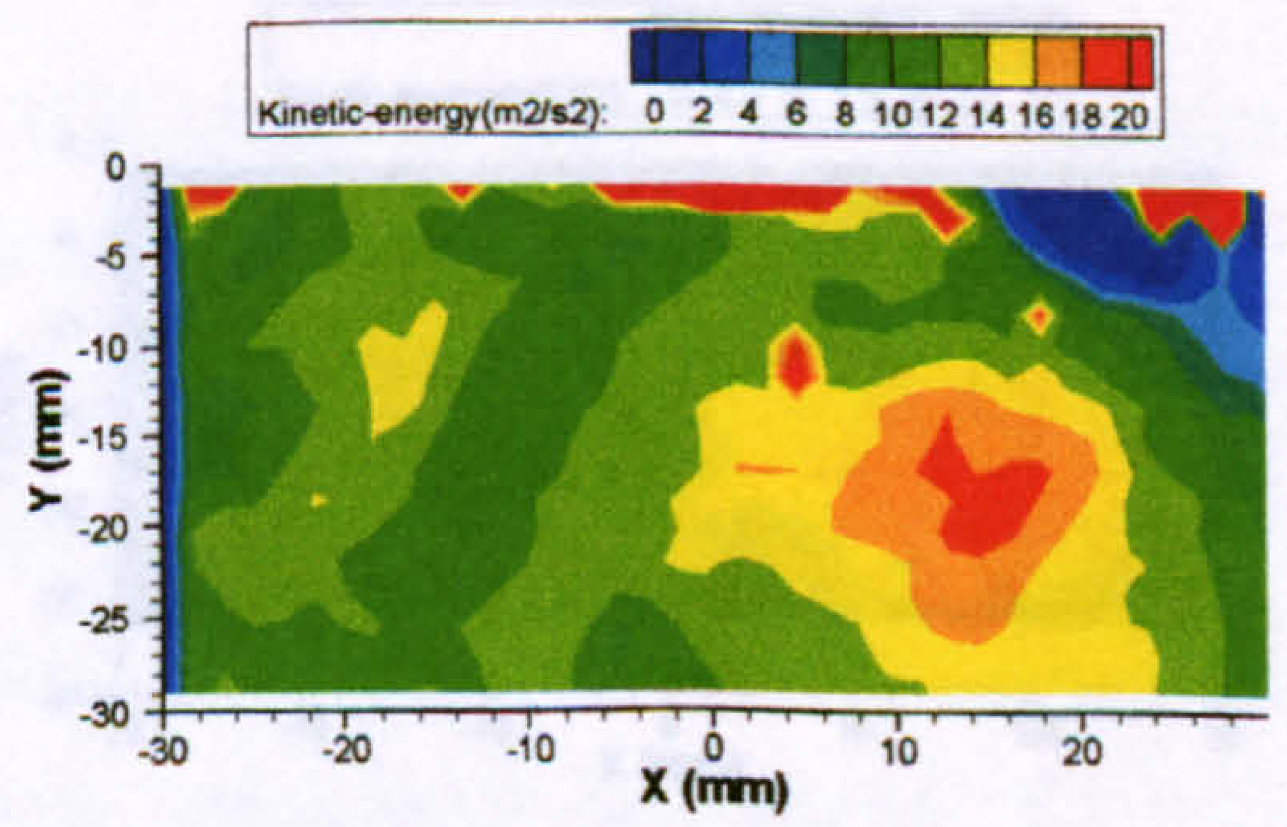

(e) 150° CA ATDC (Intake

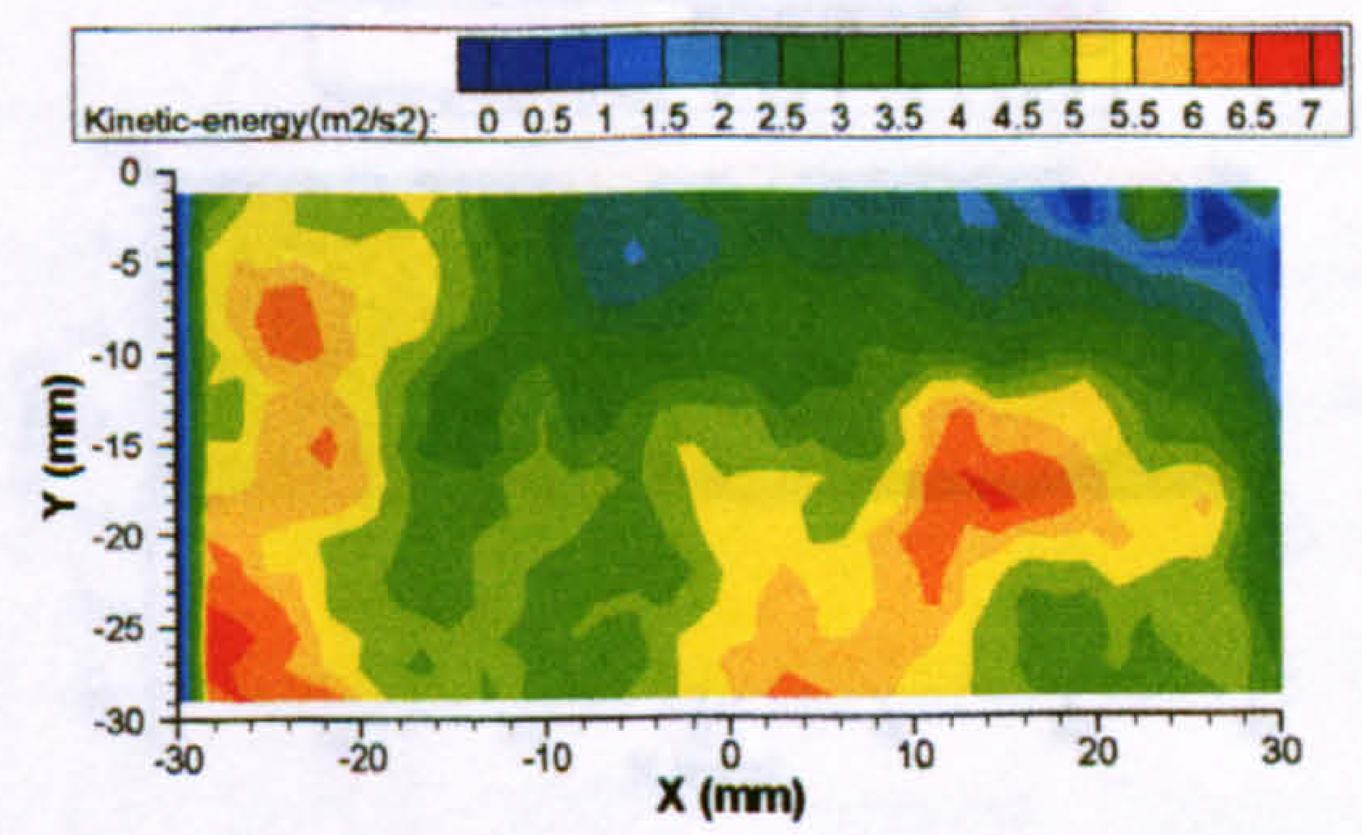

(f) BDC Intake/Compression

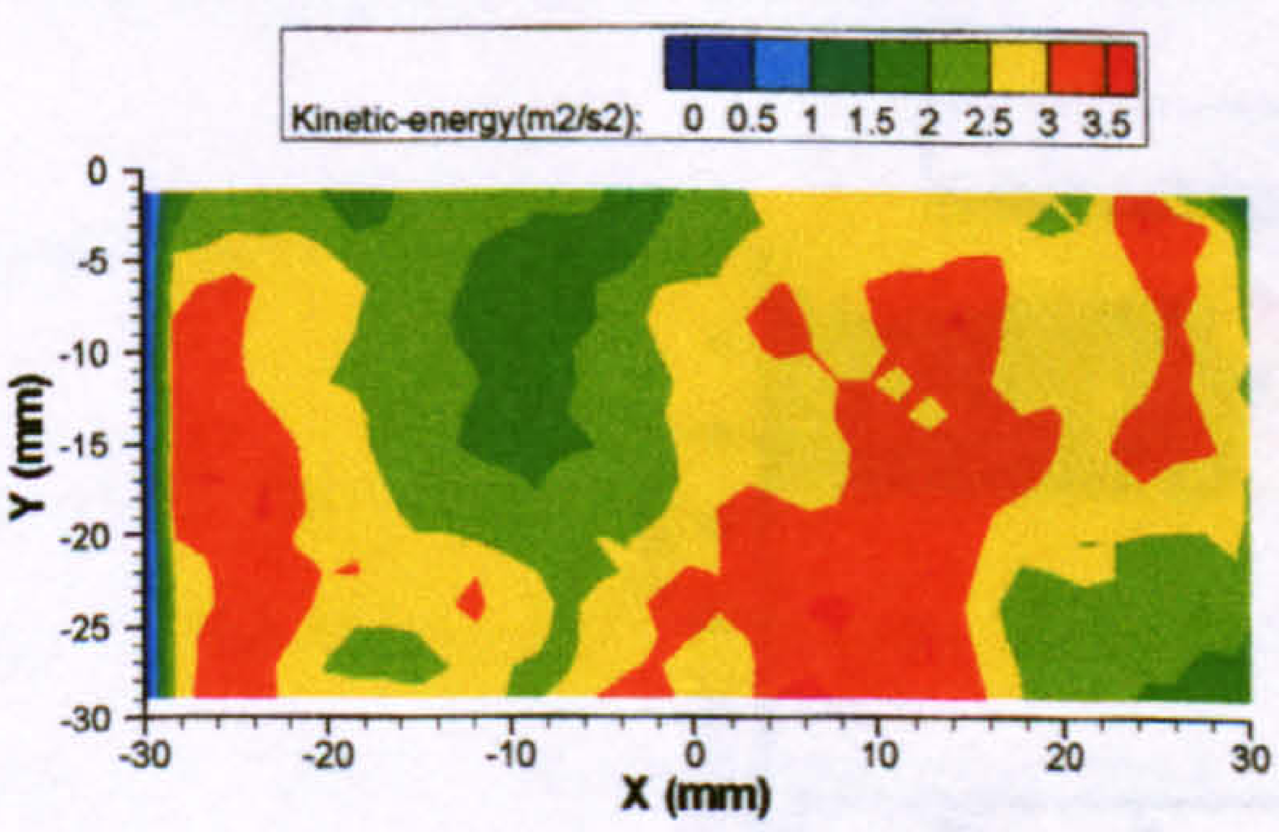

(g) 150° CA BTDC (Compression Stroke)

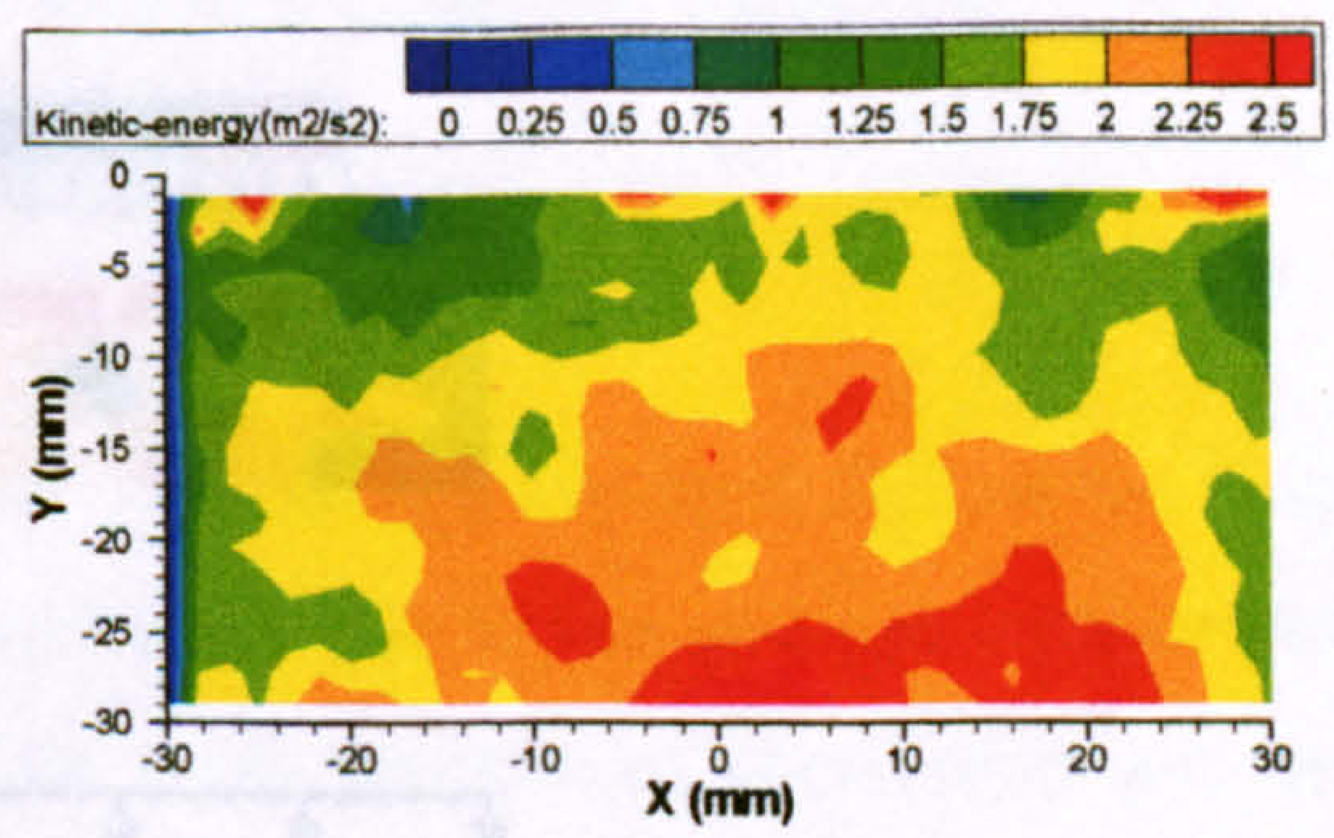

(h) 120° CA BTDC (Compression Stroke)

Figure 4.10 Averaged Fluctuation Kinetic Energy in the Central Vertical Measurement Plane

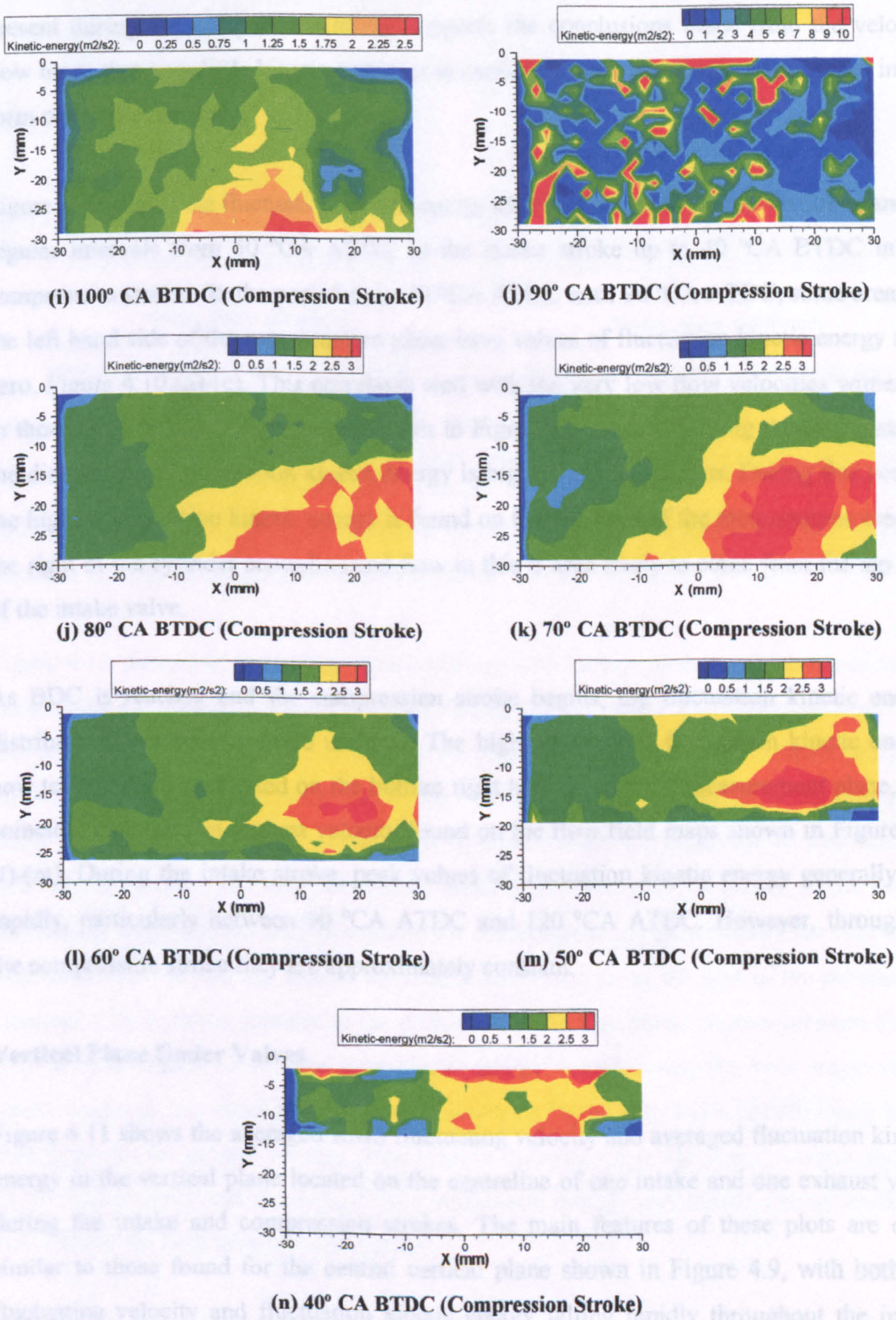

Figure 4.10 Averaged Fluctuation Kinetic Energy in the Central Vertical Measurement Plane (Continued)

the absence of coherent large scale flow structures in the velocity field maps in Figure 4.5 makes this debatable. In addition, the sharp decline in kinetic energy to the very low levels present during the compression stroke supports the conclusions made from the velocity flow maps that very little kinetic energy it is carried through the compression stroke in the form of tumble motion.

Figure 4.10 shows the fluctuation kinetic energy distribution in the central vertical plane, at regular intervals from 50 °CA ATDC in the intake stroke up to 40 °CA BTDC in the compression stroke. In the period from 50 °CA ATDC until 90 °CA ATDC, some areas on the left hand side of the measurement plane have values of fluctuation kinetic energy near zero, Figure 4.10 (a)-(c). This correlates well with the very low flow velocities witnessed in these areas in the velocity maps shown in Figure 4.5 (a)-(c). During the intake stroke the distribution of fluctuation kinetic energy is highly inhomogeneous. During this period, the highest fluctuation kinetic energy is found on the top edge of the measurement area, to the right of the cylinder centreline and flow in this is area likely to come from the top side of the intake valve.

As BDC is reached and the compression stroke begins, the fluctuation kinetic energy distribution becomes far more uniform. The highest levels of fluctuation kinetic energy now tend to be concentrated on the bottom right hand side of the measurement plane, and coincide with areas of highest velocity found on the flow field maps shown in Figure 4.5 (f)-(m). During the intake stroke, peak values of fluctuation kinetic energy generally fall rapidly, particularly between 90 °CA ATDC and 120 °CA ATDC. However, throughout the compression stroke they are approximately constant.

Vertical Plane Under Valves

Figure 4.11 shows the averaged RMS fluctuating velocity and averaged fluctuation kinetic energy in the vertical plane located on the centreline of one intake and one exhaust valve during the intake and compression strokes. The main features of these plots are quite similar to those found for the central vertical plane shown in Figure 4.9, with both the fluctuating velocity and fluctuation kinetic energy falling rapidly throughout the intake stroke and becoming reasonably stable during the compression stroke. However, the absolute levels witnessed during the intake stroke are significantly lower in the under valve plane, particularly in the case of fluctuation kinetic energy, though once stabilised in the compression stroke, both planes show comparable magnitudes for each parameter. In

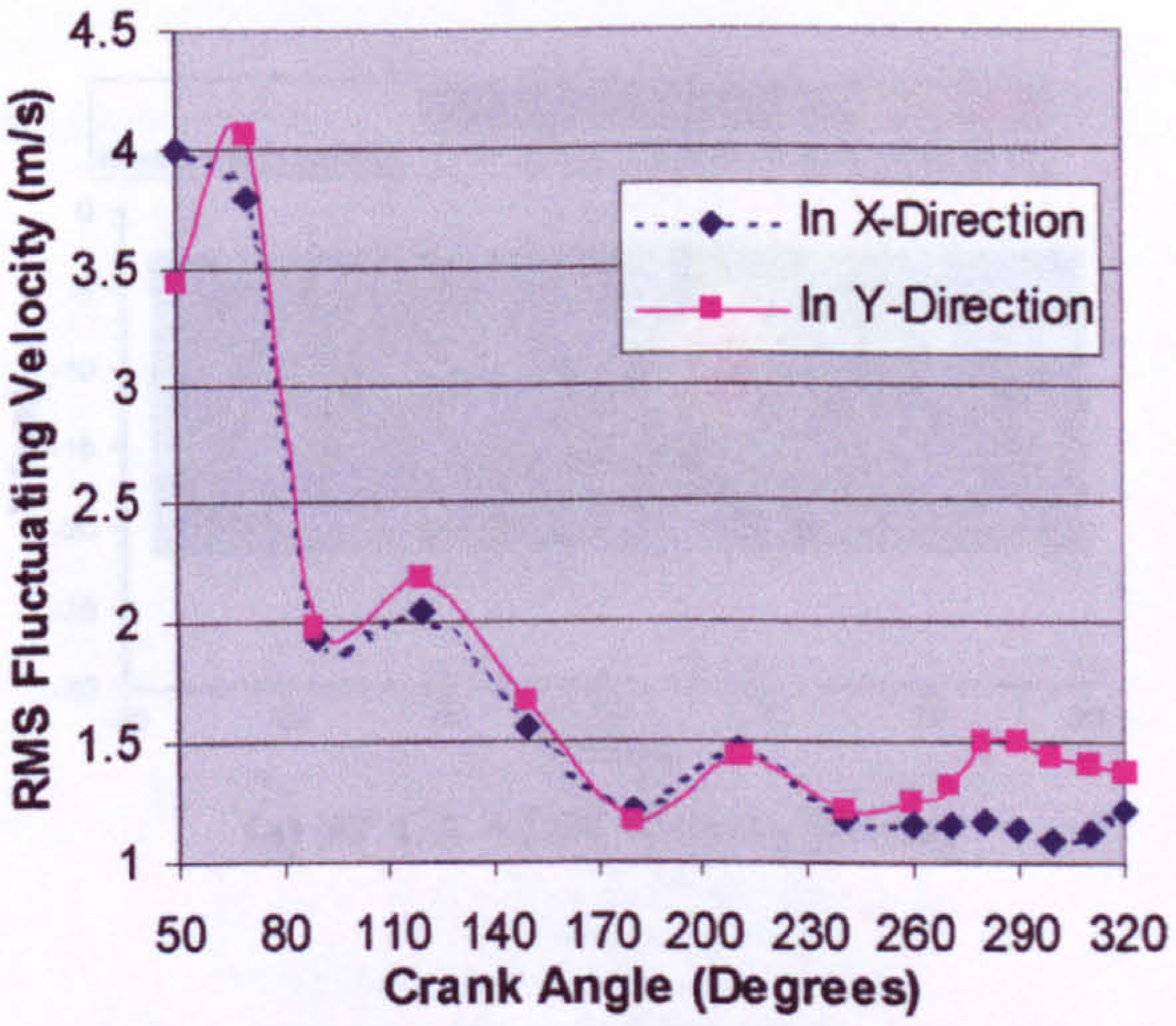

(a) Averaged RMS Fluctuating Velocity

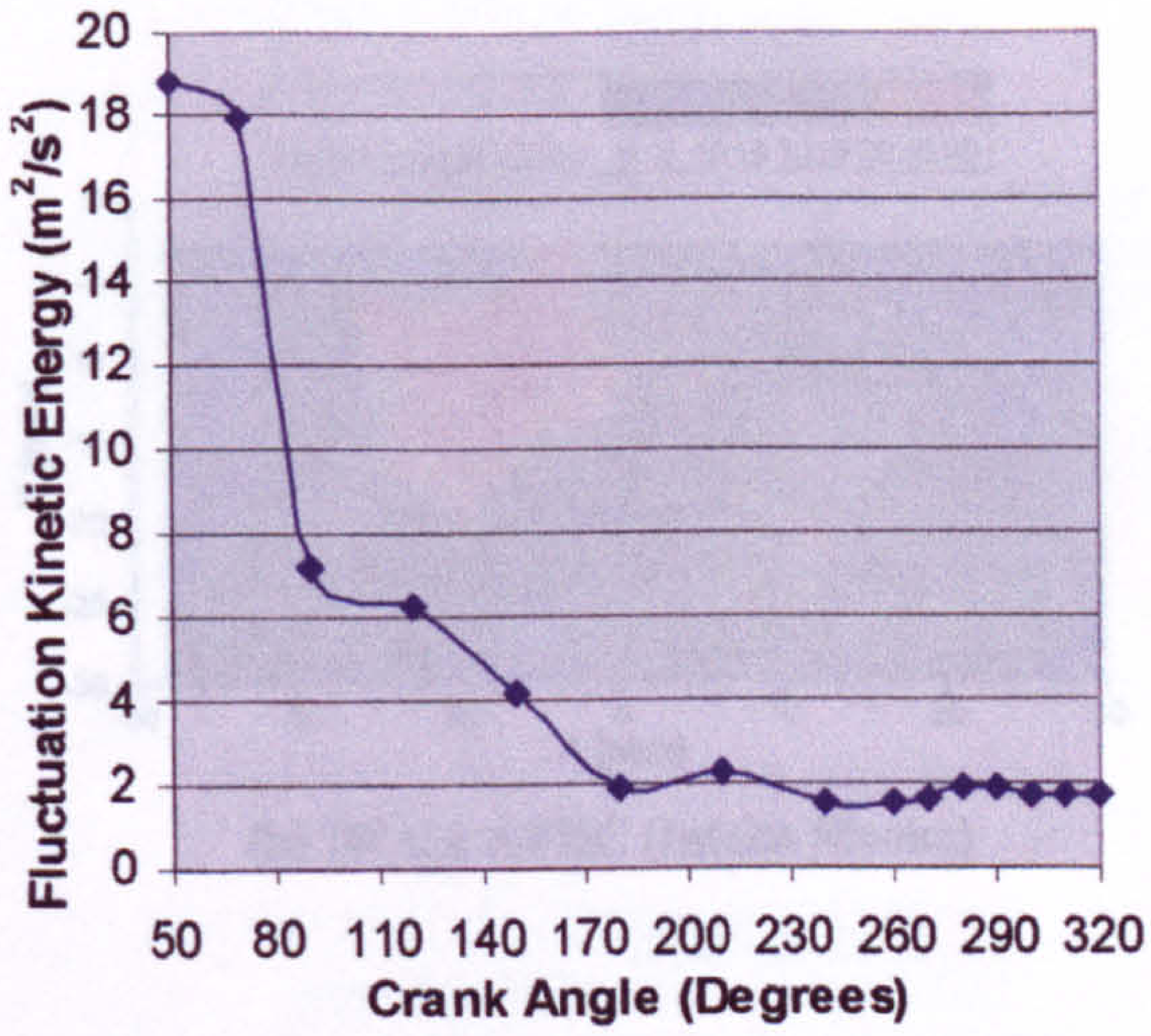

(b) Averaged Fluctuation Kinetic Energy

Figure 4.11 Variation in Averaged RMS Fluctuating Velocity and Averaged Fluctuation Kinetic Energy during Intake and Compression Strokes (Vertical Plane Under Valves)

addition, the fluctuating velocity increases slightly at the end of the compression stroke, in a similar manner to that seen in the central plane.

Figure 4.12 shows the fluctuation kinetic energy distribution in the vertical measurement plane under the valves at regular intervals during in intake and compression strokes. As in the vertical plane, (Figure 4.10), during the intake stroke the highest levels fluctuation kinetic energy are seen in the top half of the measurement area. However, in the case of the under valve plane, the kinetic energy peak is found on the left hand side of measurement area. This correlates well with the velocity maps shown in Figure 4.6 (a)-(e), where flow is particularly strong in this area throughout the intake stroke, as the air enters the cylinder at high velocity, from the top side of the intake valves and along the roof of the combustion chamber. In a similar manner to the difference in average values shown between Figure 4.11 (b) and Figure 4.9 (b), the peak kinetic energy values during the early stages of the intake stroke in the under valve plane as shown in Figure 4.12 (a) – (c) are much lower than those for the central vertical plane (Figure 4.10 (a) – (c)). However, towards the end of the intake stroke and throughout the compression stroke, peak kinetic energy levels are very similar for both measurement planes.

As with the central vertical plane, the peak fluctuation kinetic energy during the compression stroke in the under valve plane, shown in Figure 4.12 (f) – (n), was concentrated on the lower right hand side of the measurement area. This is likely to be a result of the strong upward flow in this area, shown in the velocity field maps of Figure 4.6 (f) – (n).

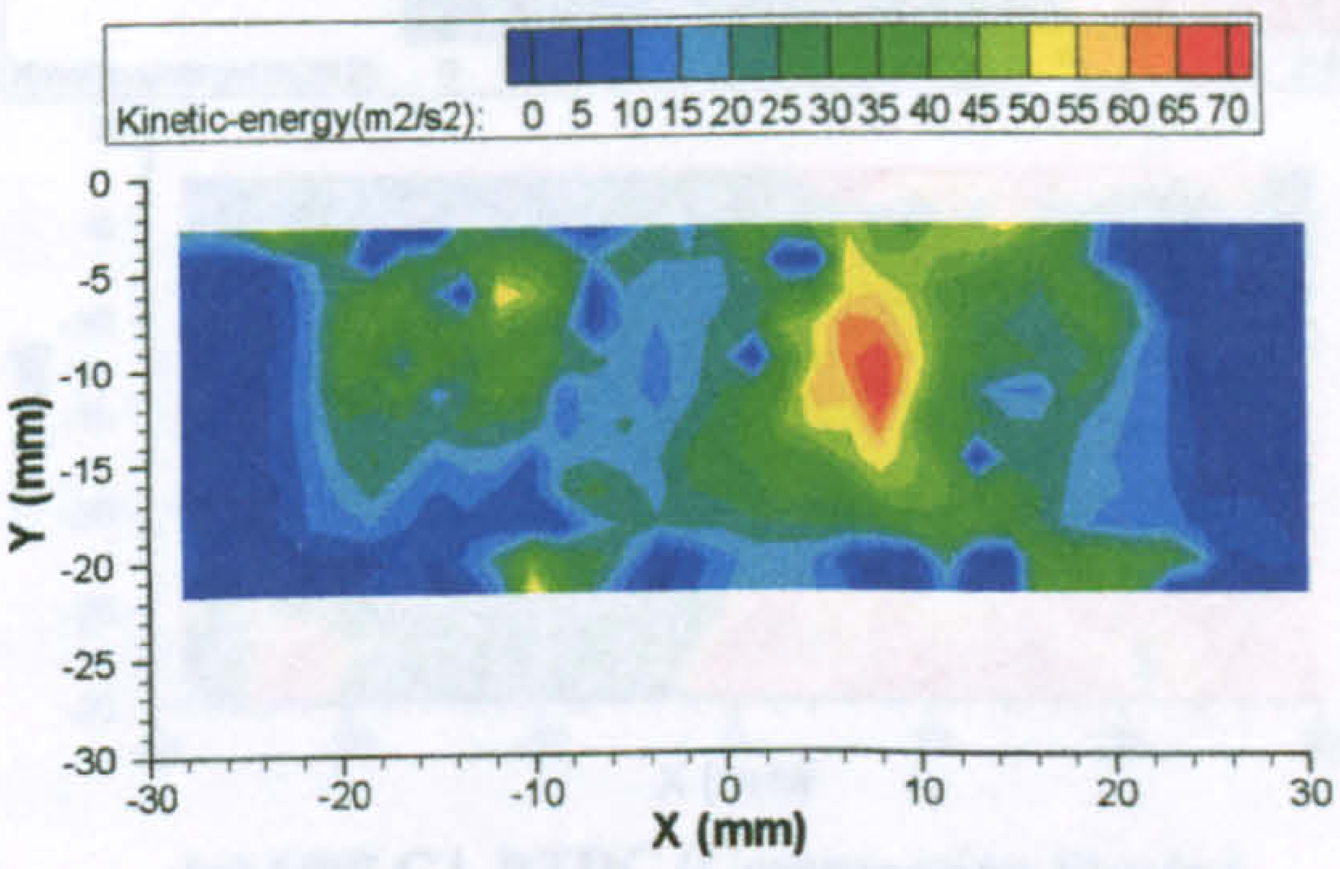

(a) 50° CA ATDC (Intake Stroke)

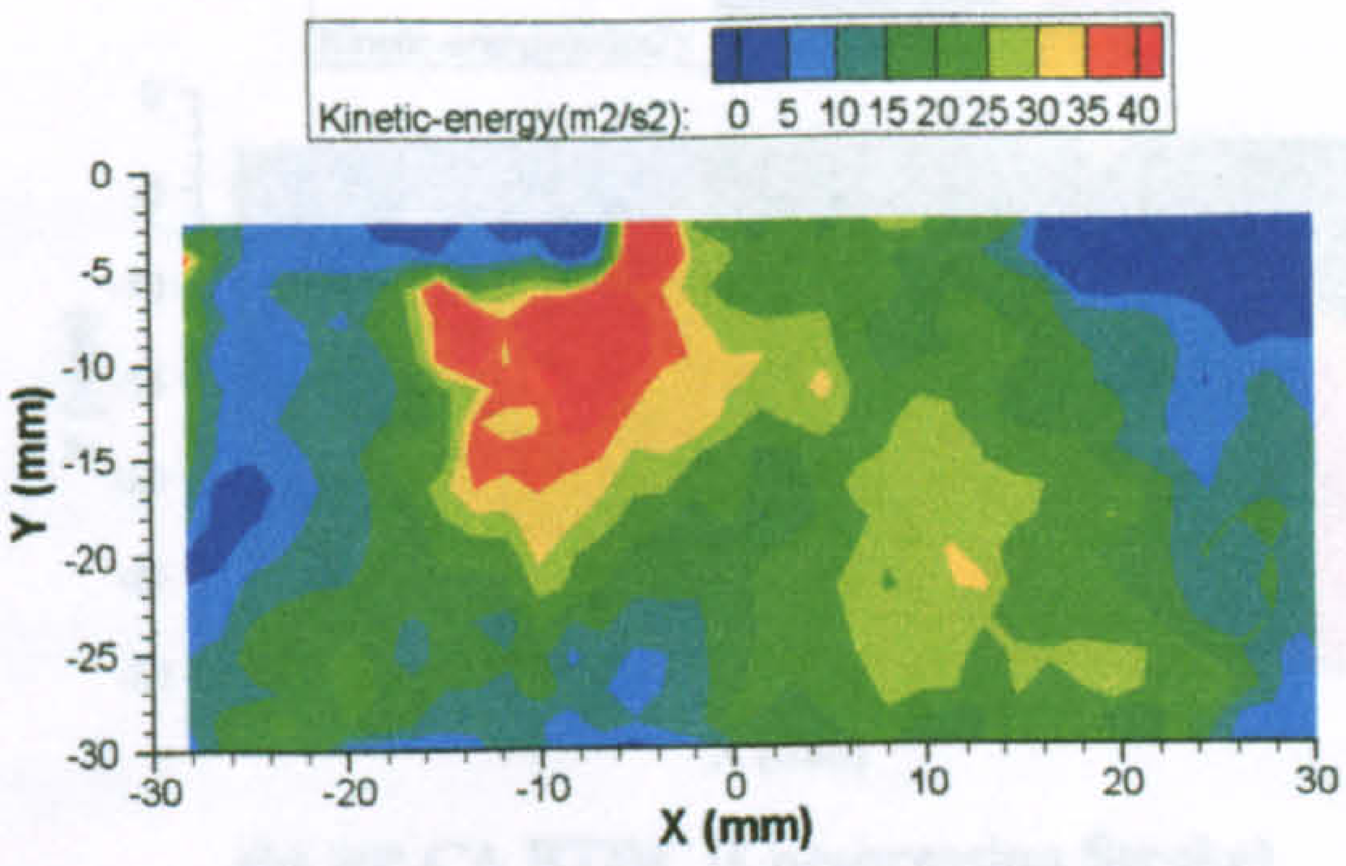

(b) 70° CA ATDC (Intake Stroke)

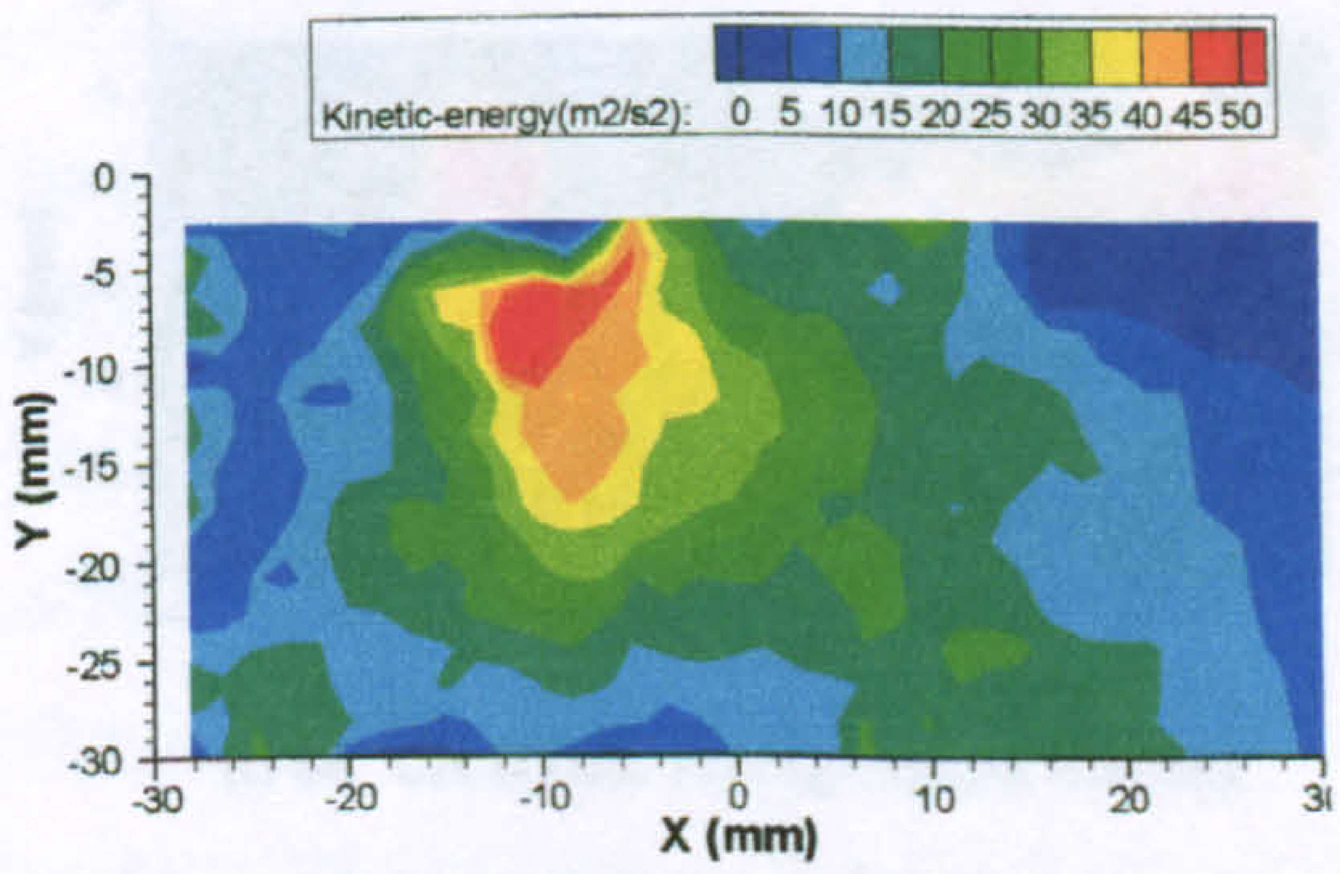

(c) 90° CA ATDC (Intake Stroke)

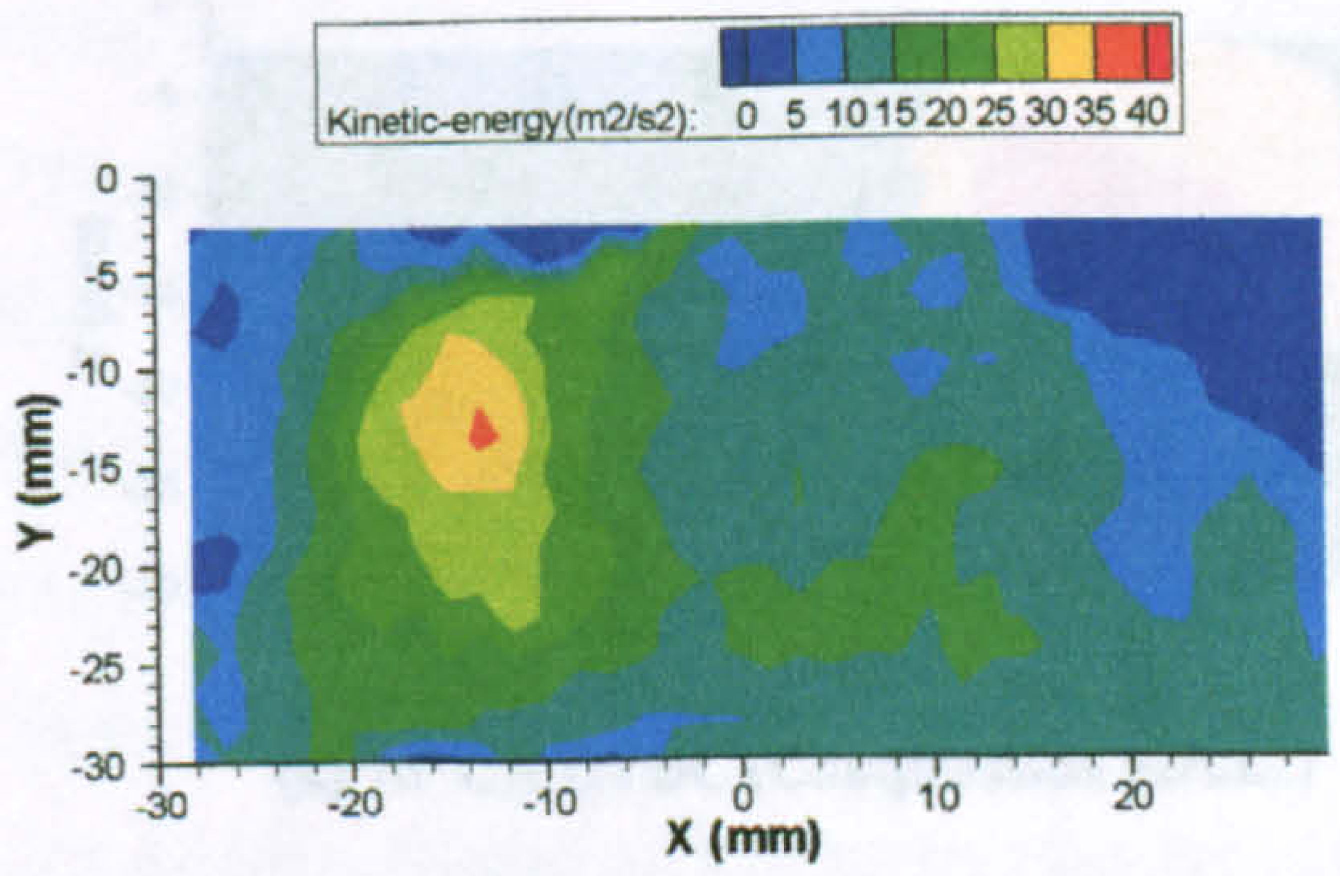

(d) 120° CA ATDC (Intake Stroke)

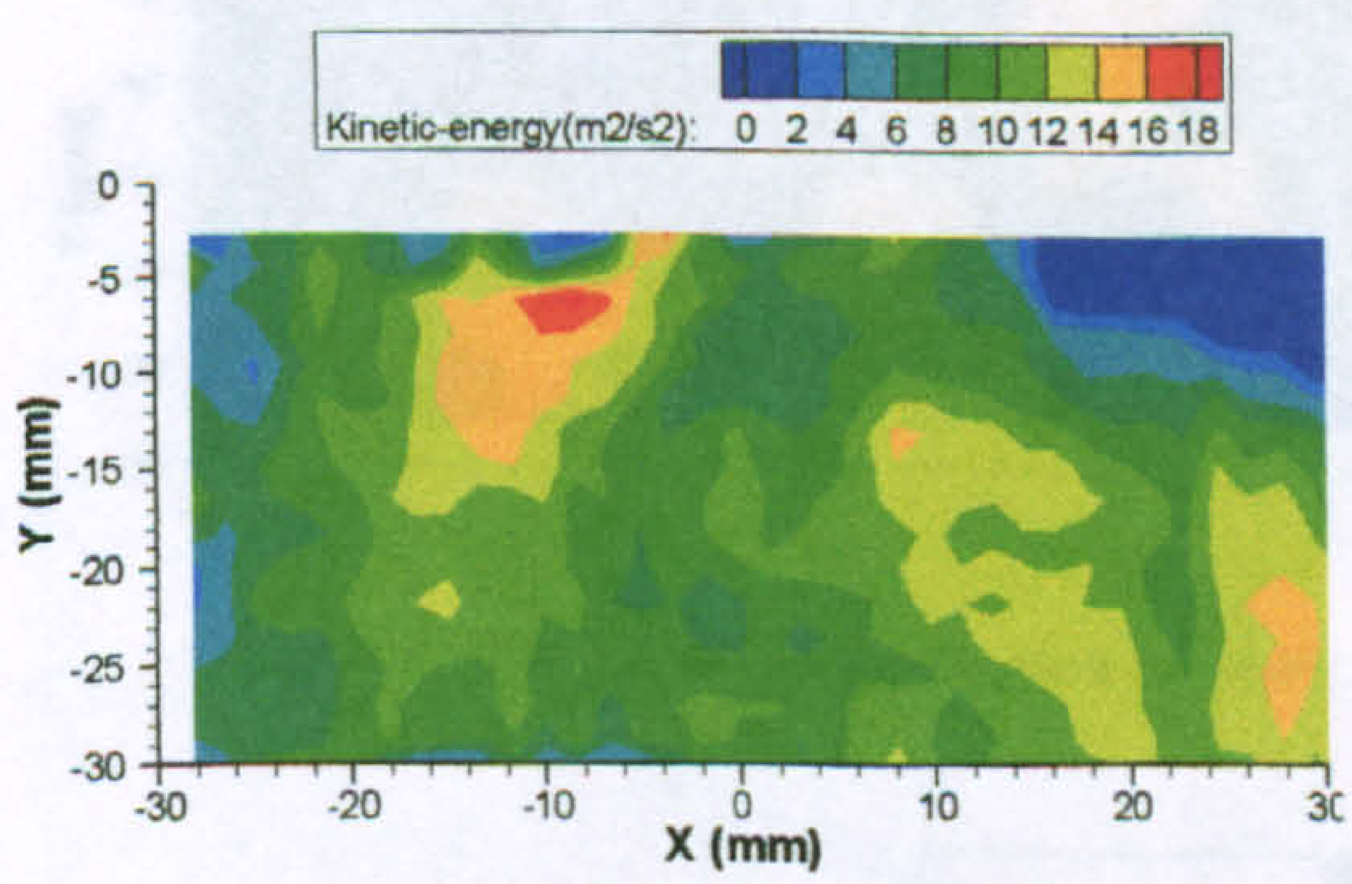

(e) 150° CA ATDC (Intake Stroke)

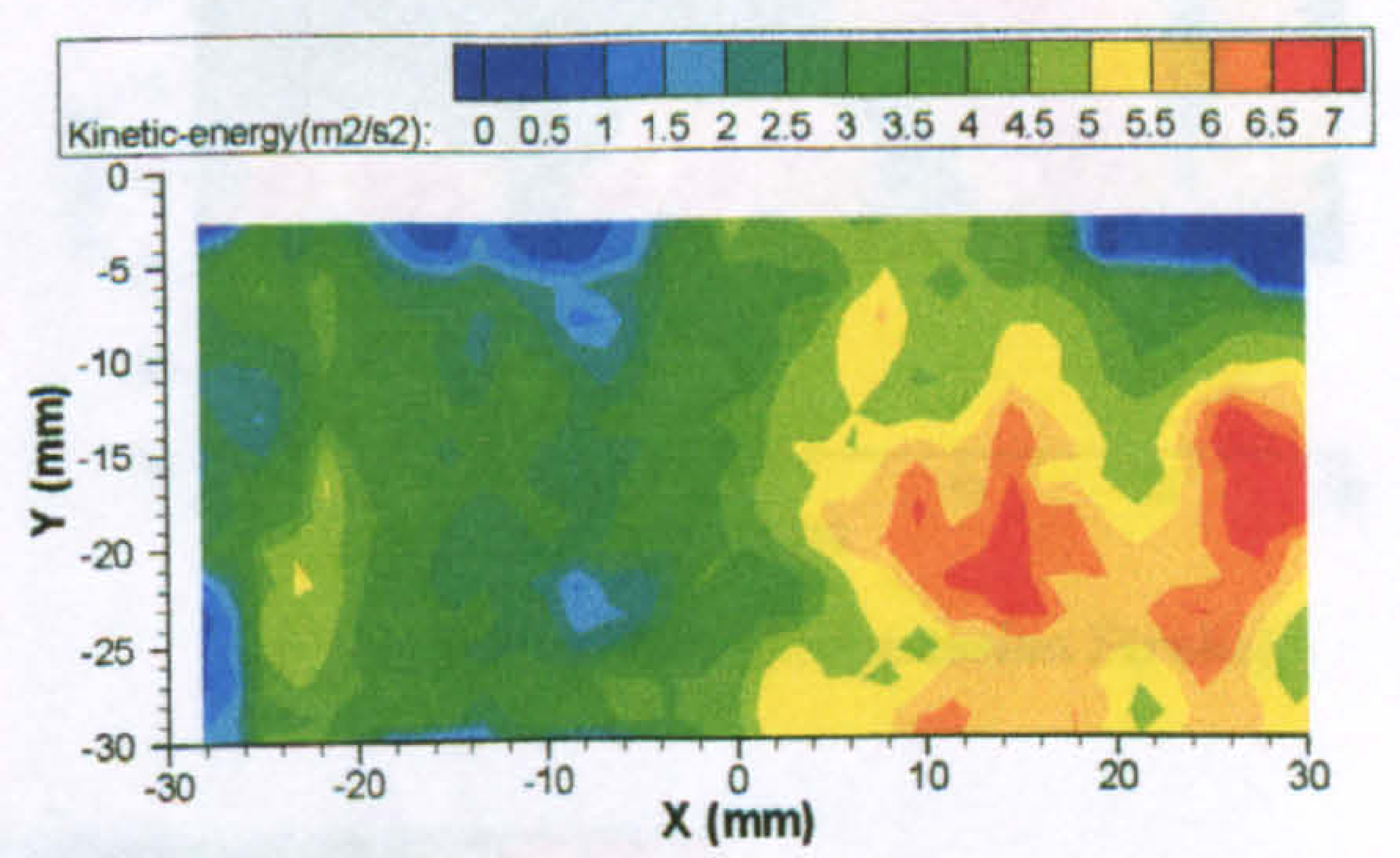

(f) BDC Intake/Compression Stroke

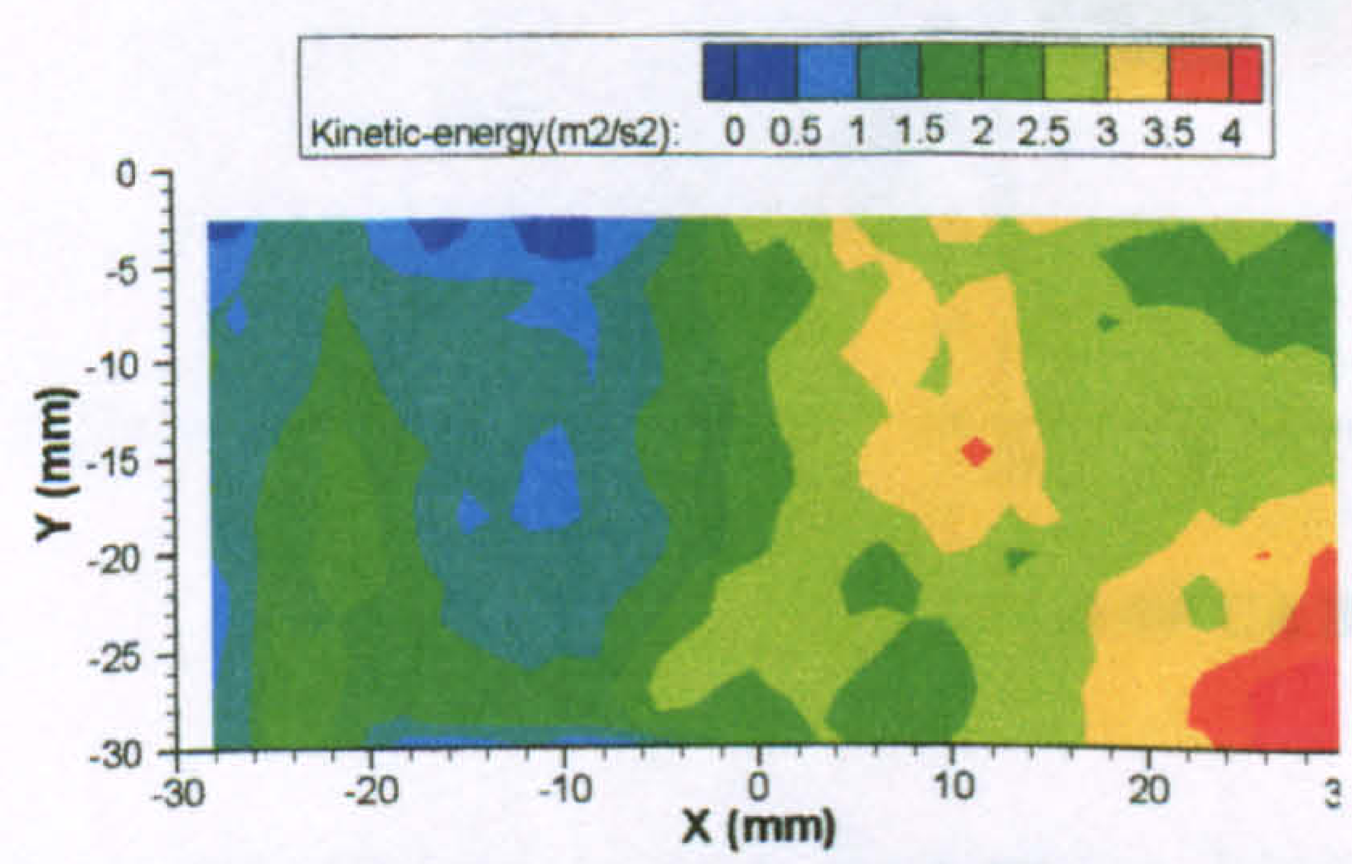

(f) 150° CA BTDC (Compression Stroke)

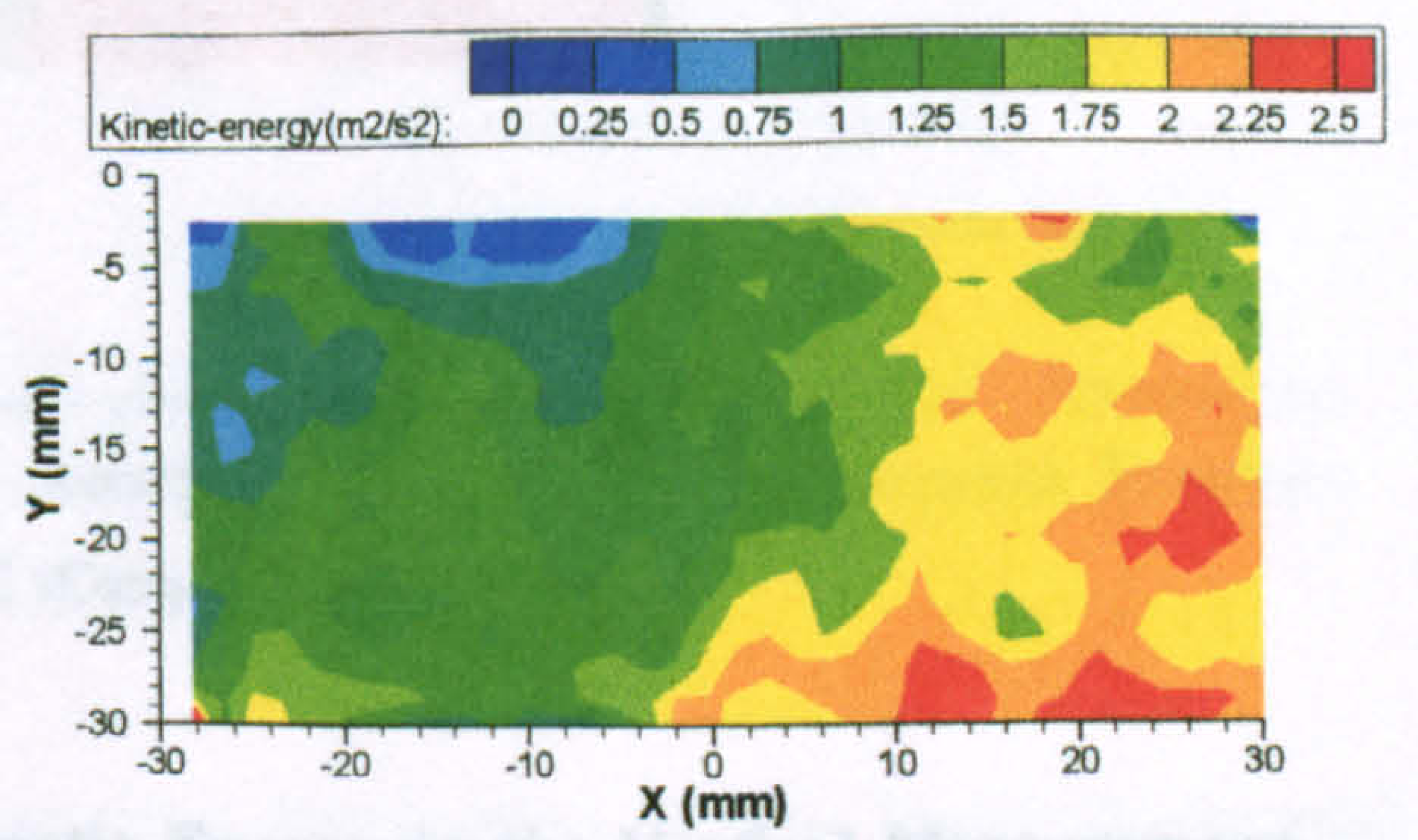

(e) 120° CA BTDC (Intake Stroke)

Figure 4.12 Averaged Fluctuation Kinetic Energy in the Vertical Measurement plane under one Intake and one Exhaust Valve

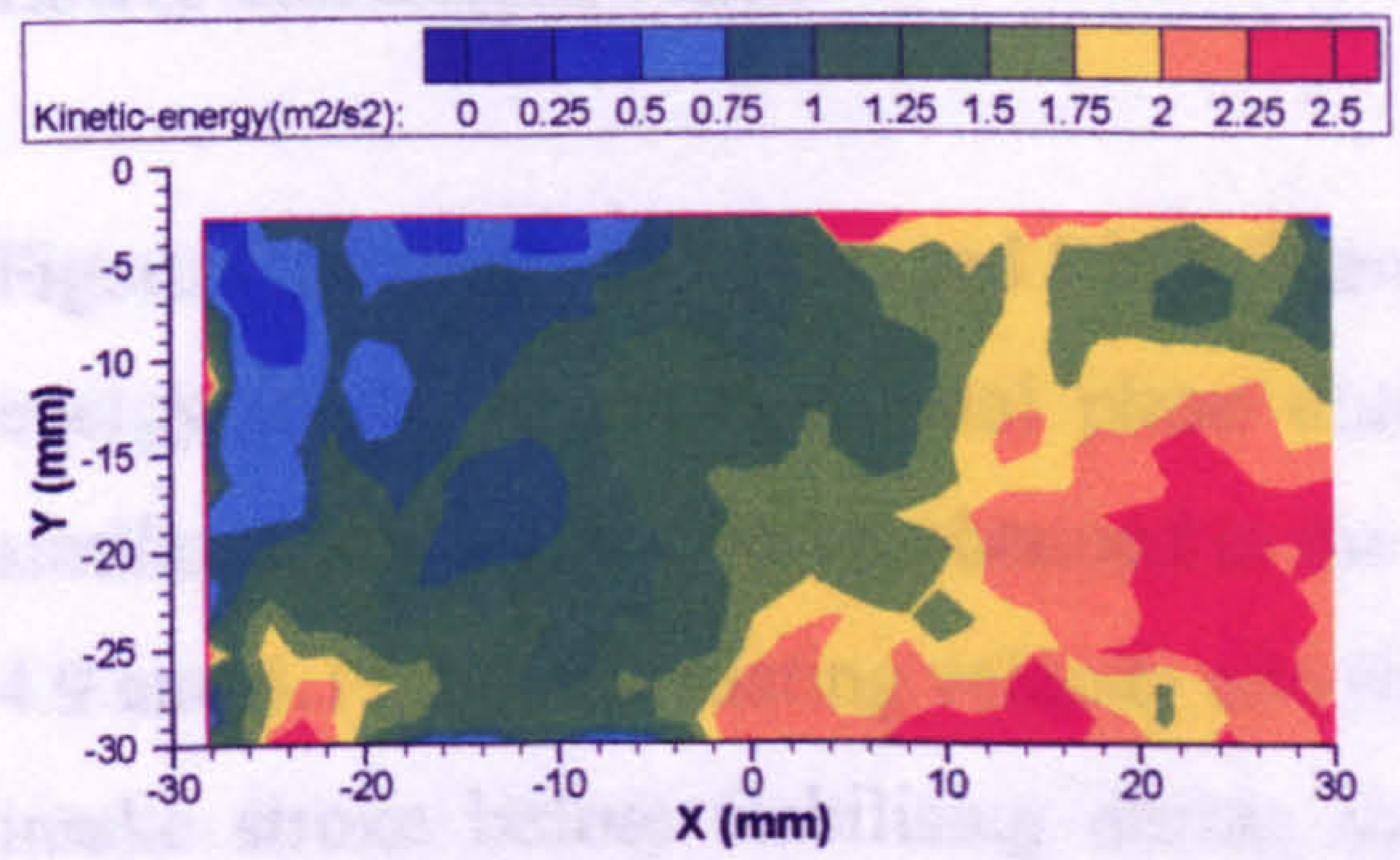

(g) 100° CA BTDC (Compression Stroke)

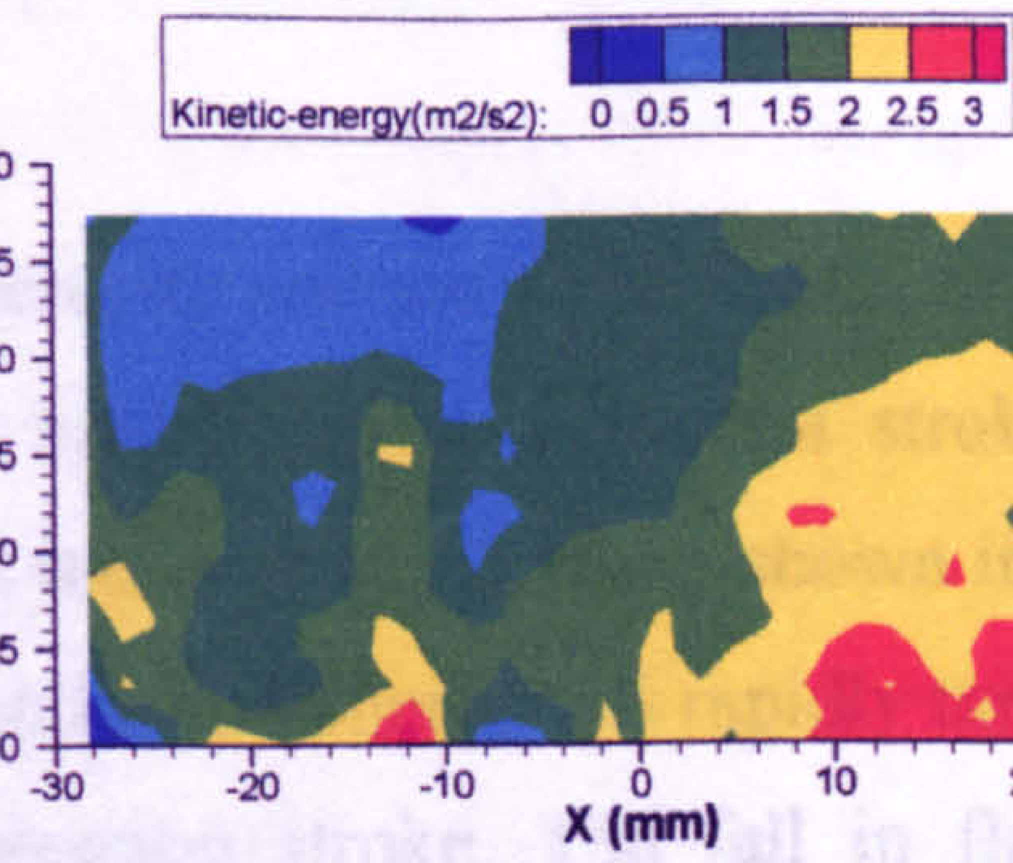

(h) 90° CA BTDC (Compression Stroke)

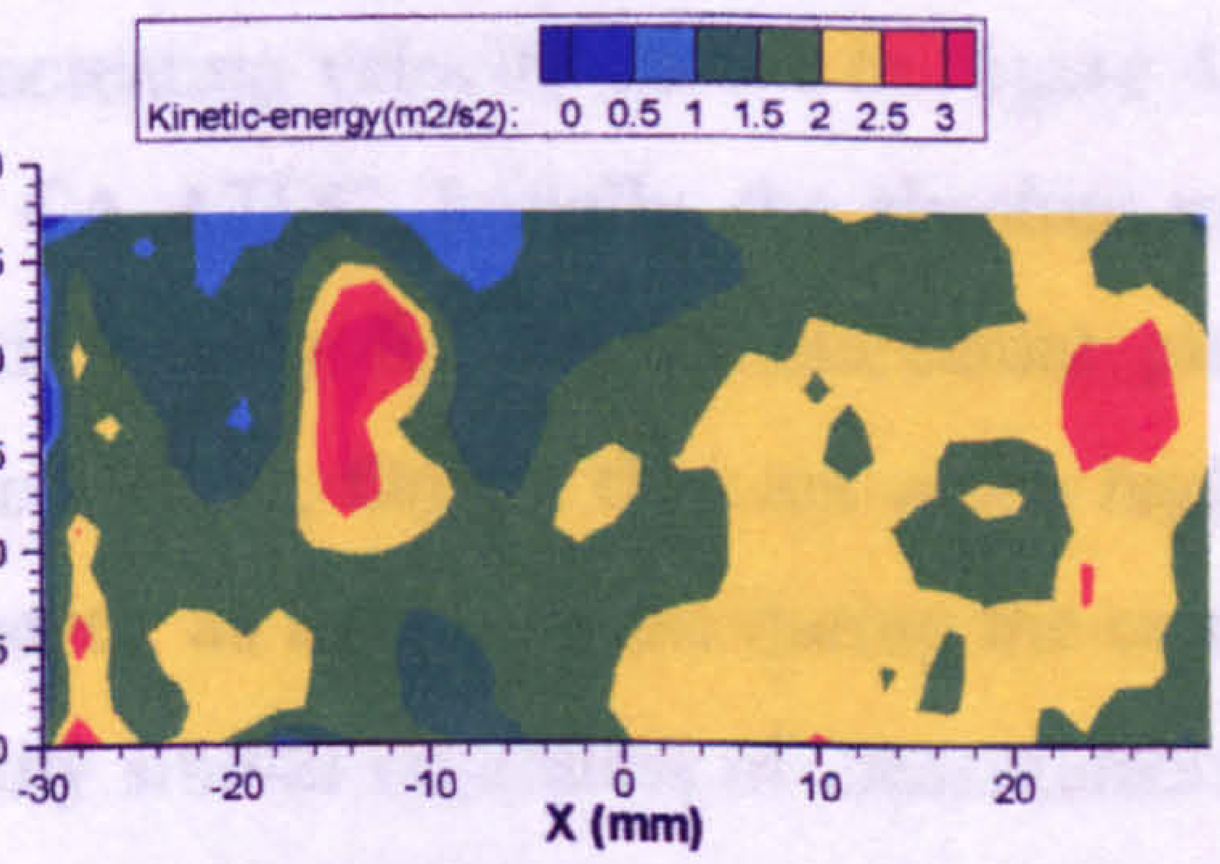

(i) 80° CA BTDC (Compression Stroke)

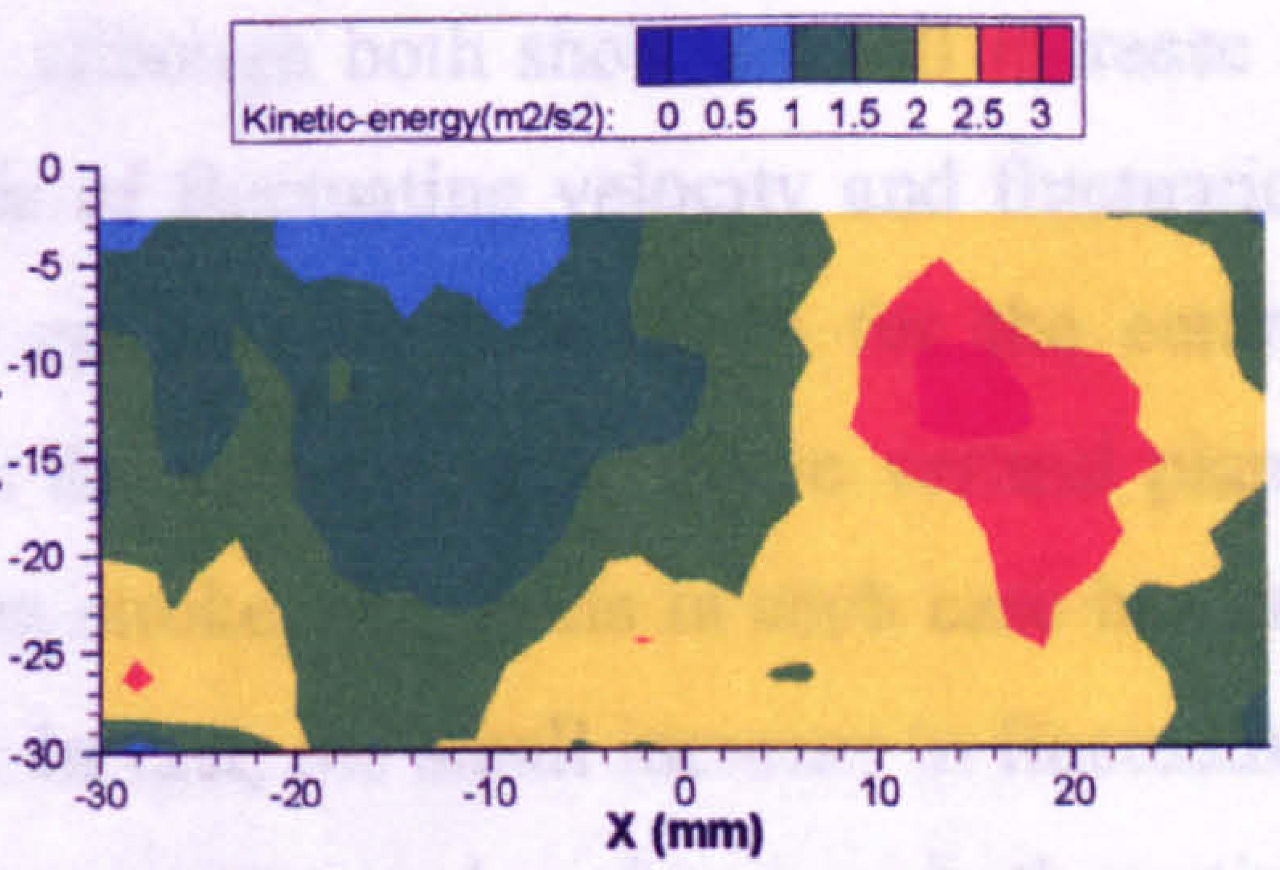

(k) 70° CA DTDC (Compression Stroke)

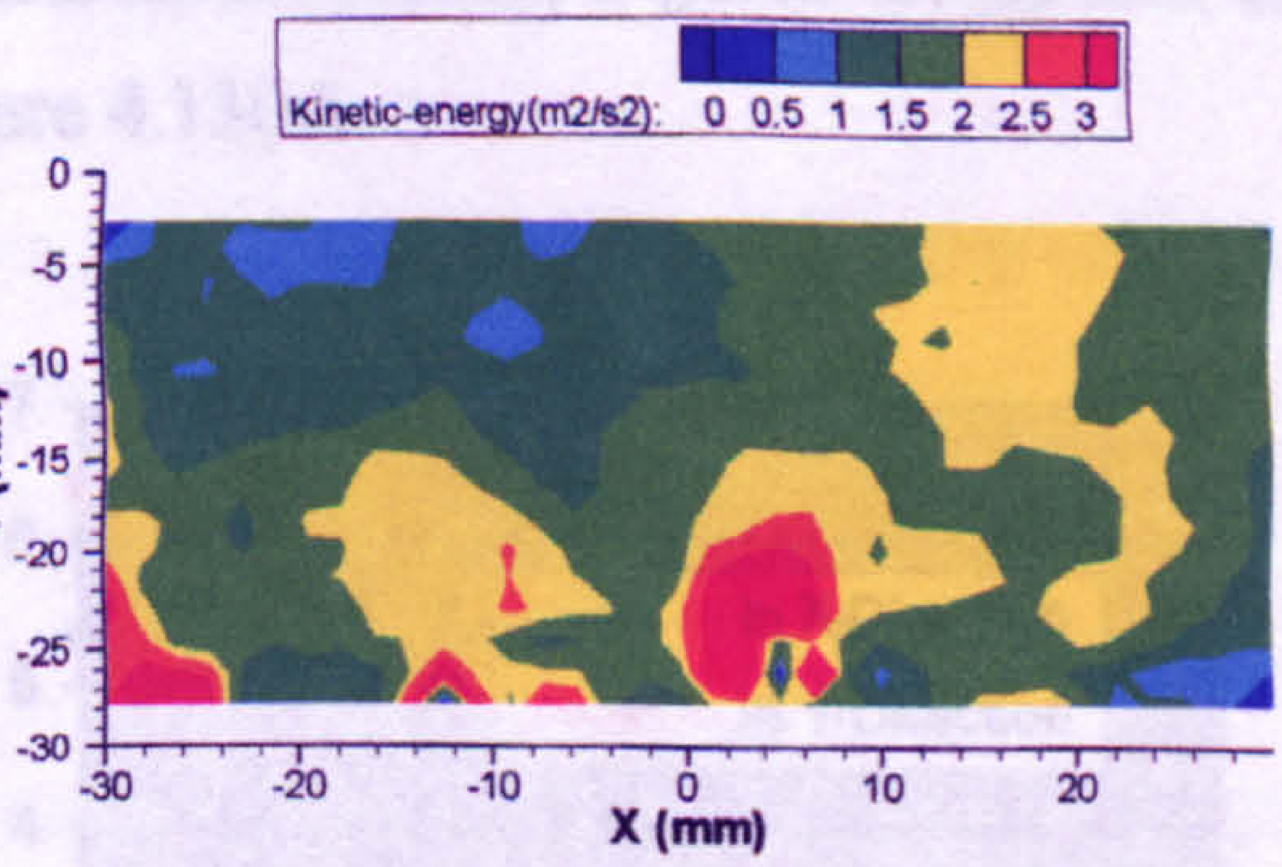

(l) 60° CA BTDC (Compression Stroke)

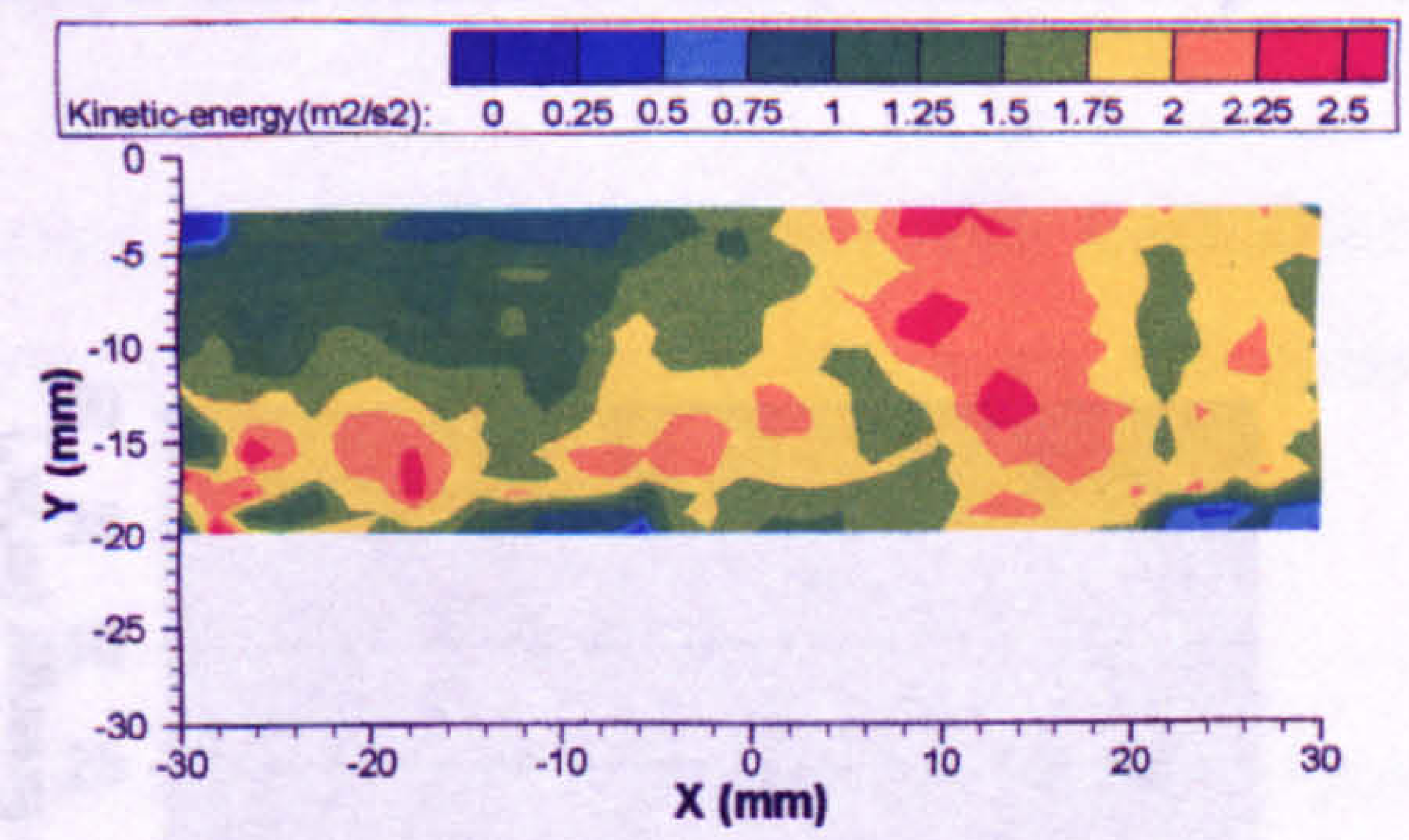

(m) 50° CA BTDC (Compression Stroke)

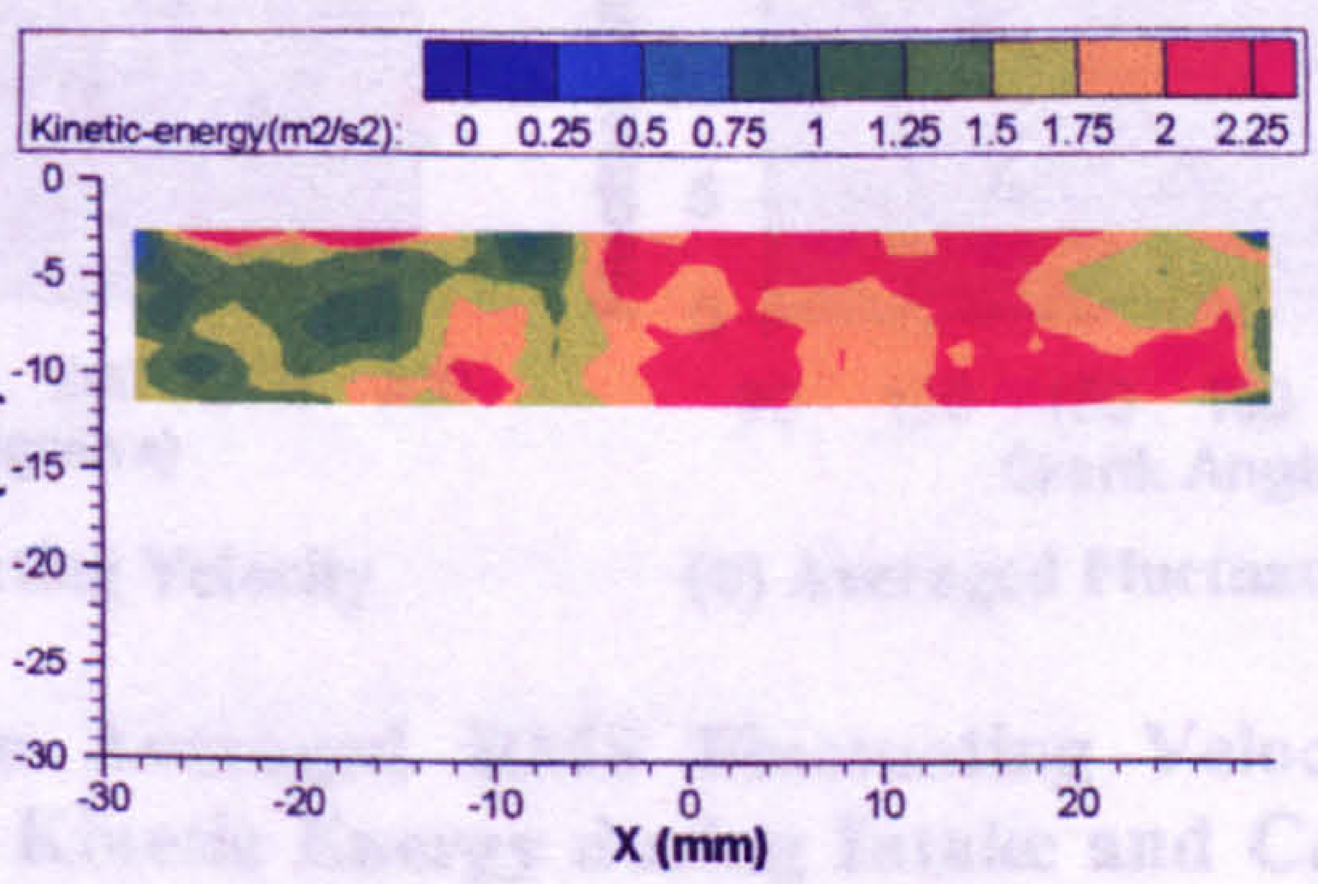

(n) 40° CA BTDC (Compression Stroke)

Figure 4.12 Averaged Fluctuation Kinetic Energy in the Vertical Measurement plane under one Intake and one Exhaust Valve (Continued)

Lower Horizontal Plane

Figure 4.13 shows the averaged RMS fluctuating velocity and averaged fluctuation kinetic energy in the lower horizontal plane during the intake and compression strokes. In a similar manner to the result obtained in the vertical measurement planes, shown in Figures 4.9 and 4.11, the fluctuating velocity and fluctuation kinetic energy fall rapidly through the intake stroke before stabilising during the compression stroke. The fall in fluctuating velocity during the intake stroke, as shown in Figure 4.13 (b), is much steeper than the fall in fluctuating velocity shown in Figure 4.13 (a), although both show a small increase at 150° CA ATDC. Initially, the absolute magnitude of fluctuating velocity and fluctuation kinetic energy for this measurement plane are comparable than those for the central vertical plane, though they are much higher than those in the under valve vertical plane. However, as they stabilise during the compression stroke, the levels in each case become broadly similar regardless of measurement plane. In fact, the small increase in fluctuating velocity in the Y-direction at the end of the compression stroke, shown in both vertical measurement planes, Figures 4.9(a) and 4.11(a), is also found in lower horizontal plane, Figure 4.13(a).

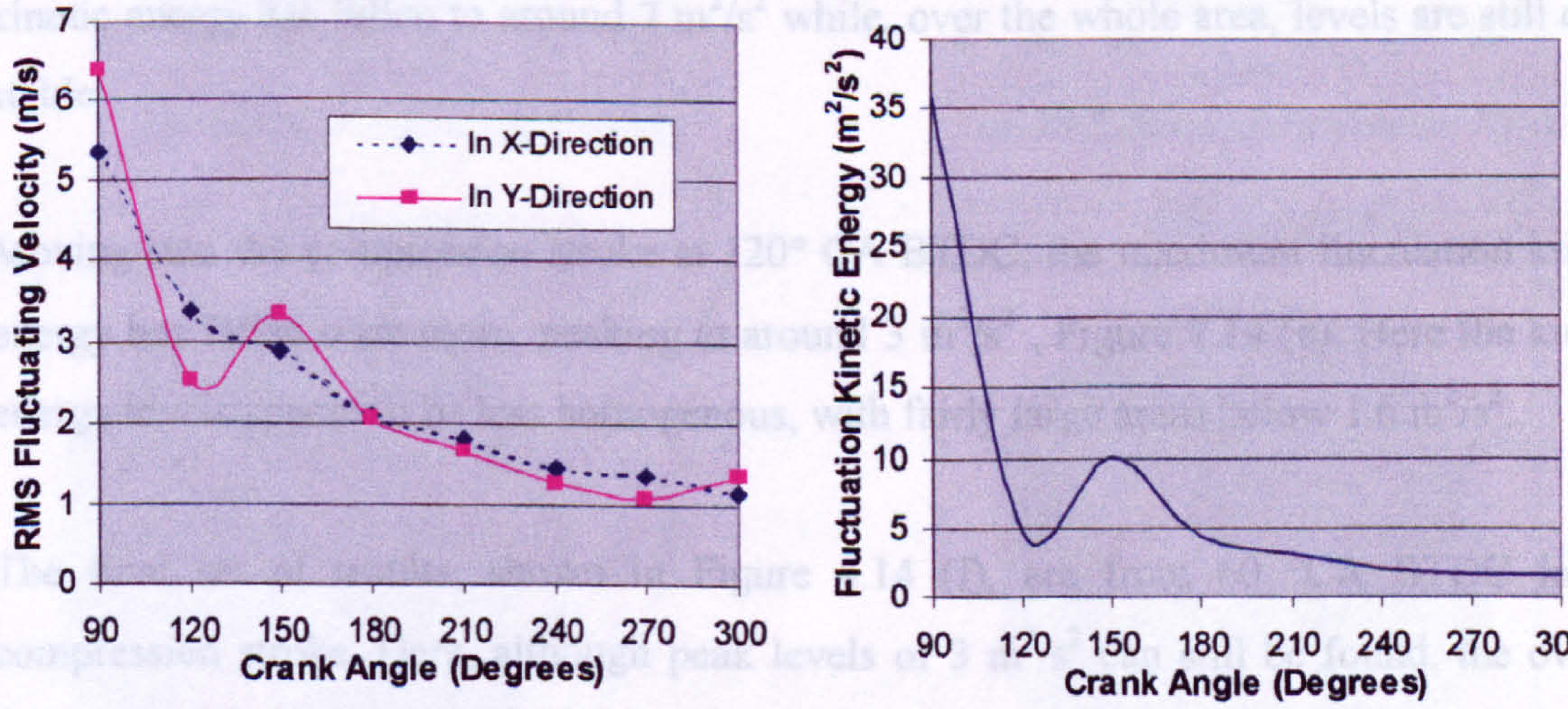

(a) Averaged RMS Fluctuating Velocity **(b) Averaged Fluctuation Kinetic Energy**

Figure 4.13 Variation in Averaged RMS Fluctuating Velocity and Averaged Fluctuation Kinetic Energy during Intake and Compression Strokes (Lower Horizontal Plane)

Figure 4.14 shows the fluctuation kinetic energy distribution in the lower horizontal measurement plane at regular intervals during in intake and compression strokes. Figure 4.14 (a) shows the fluctuation kinetic energy 90° CA ATDC in the intake stroke, which peaks at around 60 m^2/s^2, close to the centre of the cylinder. The level then generally falls towards the edge of the measurement area, apart from in one small region, also close to the centre. Here, there is an apparent 'hole' in the map, with less than 6 m^2/s^2 being recorded. However, inspection of the velocity map for this plane in Figure 4.8 shows that the velocity in this particular area is also very low.

Figure 4.14 (b) shows the situation 30 °CA later at 120 °CA ATDC. Here, the peak level of fluctuation kinetic energy has fallen to around 25 m^2/s^2 and is located on the right hand side of the diagram. An area with very low levels can still be seen very close to the centre of the map.

The level of fluctuation kinetic energy at 150 °CA ATDC is shown in Figure 4.14 (c). Here although the peak has reduced again to around 12 m^2/s^2, the level across the whole area is generally much more homogenous. Comparing Figure 4.14 (c) and Figure 4.13 (b), it can be seen that, although the peak level of fluctuating kinetic energy dropped here, the average level actually increased as a result of the increased homogeneity. Despite this, the very low level area seen in the previous maps is still present.

At BDC of the intake /compression strokes, Figure 4.14 (d) shows that the peak fluctuation kinetic energy has fallen to around 7 m^2/s^2 while, over the whole area, levels are still quite stable.

Moving into the compression stroke at 120° CA BTDC, the maximum fluctuation kinetic energy has fallen once more, peaking at around 3 m^2/s^2 , Figure 7.14 (e). Here the kinetic energy levels appear to be less homogenous, with fairly large areas below 1.6 m^2/s^2.

The final set of results, shown in Figure 4.14 (f), are from 60 °CA BTDC in the compression stroke. Here, although peak levels of 3 m^2/s^2 can still be found, the overall fluctuation kinetic energy is much more stable over the whole map, although, according to Figure 4.13 (b), the average level remains unchanged.

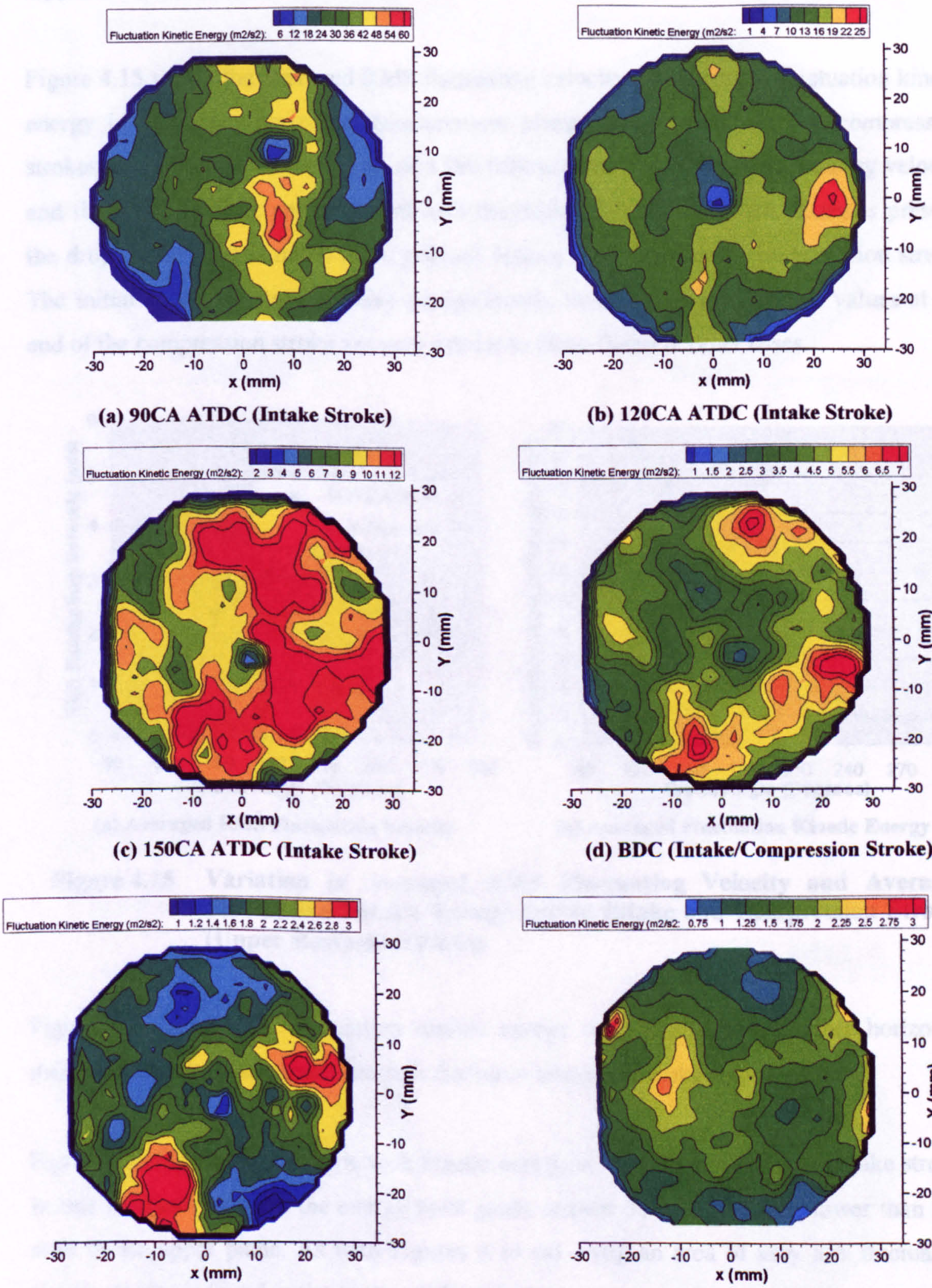

(a) 90CA ATDC (Intake Stroke)

(b) 120CA ATDC (Intake Stroke)

(c) 150CA ATDC (Intake Stroke)

(d) BDC (Intake/Compression Stroke)

Figure 4.14 Flow Field Kinetic Energy Fluctuation in Lower Horizontal Plane during Intake and Compression Strokes

Upper Horizontal Plane

Figure 4.15 shows the averaged RMS fluctuating velocity and averaged fluctuation kinetic energy in the upper horizontal measurement plane during the intake and compression strokes. Although the overall trend of a fall followed by a levelling of fluctuating velocity and fluctuation kinetic energy found with the three other measurement planes is present, the drop in this case is much more gradual, lasting half way into the compression stroke. The initial absolute values are also comparatively low, though the ultimate values at the end of the compression stroke are very similar to those found in other cases.

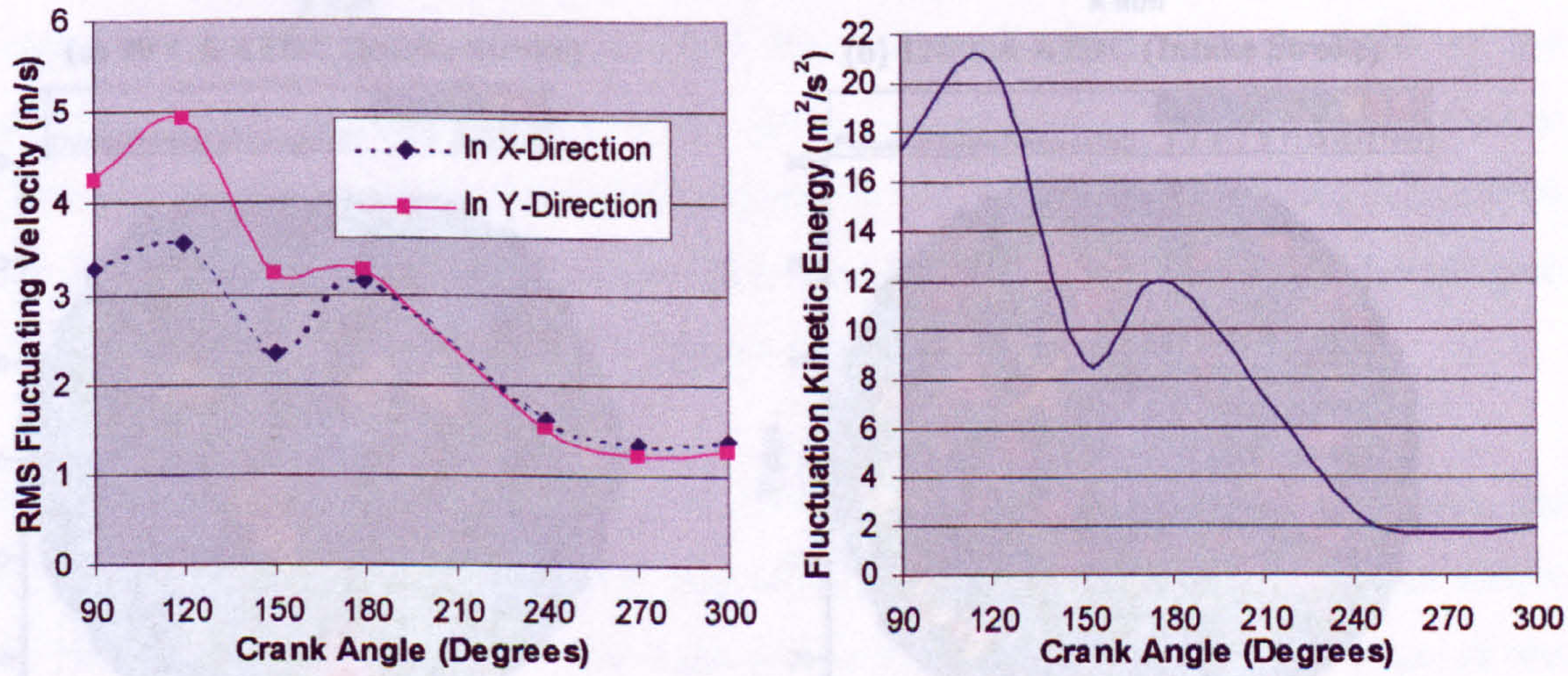

(a) Averaged RMS Fluctuating Velocity (b) Averaged Fluctuation Kinetic Energy

Figure 4.15 Variation in Averaged RMS Fluctuating Velocity and Averaged Fluctuation Kinetic Energy during Intake and Compression Strokes (Upper Horizontal Plane)

Figure 4.16 shows the fluctuation kinetic energy distribution in the upper horizontal measurement plane at regular intervals during in intake and compression strokes.

Figure 4.16 (a) shows the fluctuation kinetic energy at 90 °CA ATDC in the intake stroke. In this first set of results the energy level peaks at over 51 m^2/s^2, slightly lower than that seen in the upper plane. As with Figures 4.14 (a) – (c), an area of very low fluctuation kinetic energy is found in the centre of the cylinder.

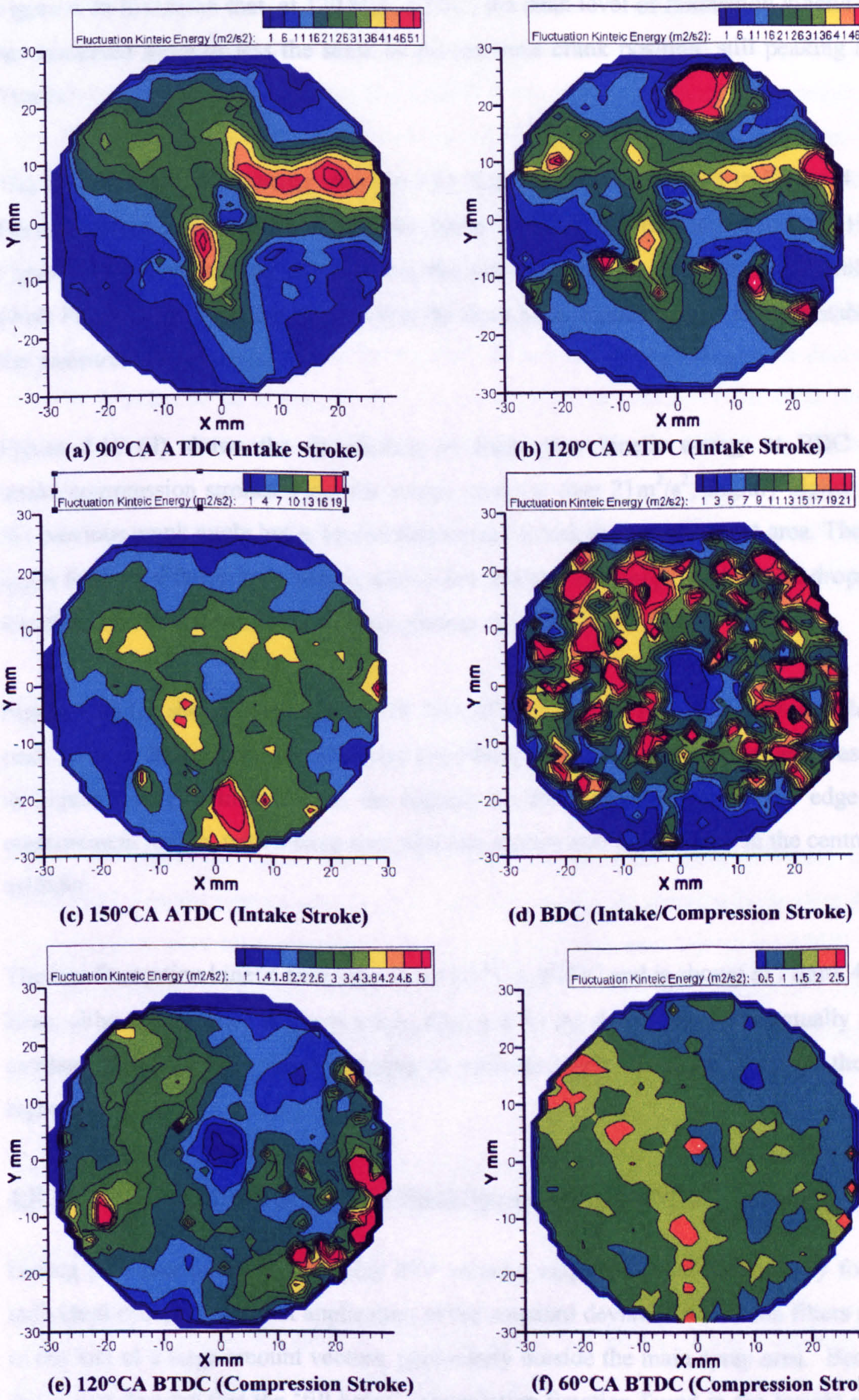

(a) 90°CA ATDC (Intake Stroke)

(b) 120°CA ATDC (Intake Stroke)

(c) 150°CA ATDC (Intake Stroke)

(d) BDC (Intake/Compression Stroke)

(e) 120°CA BTDC (Compression Stroke)

(f) 60°CA BTDC (Compression Stroke)

Figure 4.16 Flow Field Fluctuation Kinetic Energy in Lower Horizontal Plane during Intake and Compression Strokes

Figure 4.16 (b) shows that, at 120 °CA ATDC, the peak level of fluctuation kinetic energy has remained more or less the same as the previous crank position, still peaking at over $51m^2/s^2$.

The fluctuation kinetic energy map for 150 °CA ATDC is presented in Figure 4.16 (c). Here the Fluctuation kinetic energy has fallen significantly, peaking at around $19m^2/s^2$. Figure 4.15 (b) shows that, at this point, the average level has dropped significantly also. From Figure 4.16 (c) it also appears that the fluctuation kinetic energy is more stable over the measurement plane.

Figure 4.16 (d) shows the distribution of fluctuation kinetic energy at BDC of the intake/compression strokes. Here the energy peaks at over $21m^2/s^2$, slightly higher than at the previous crank angle but is less homogeneous across the measurement area. The centre again features a fairly large region with a low amount of energy, with levels dropping to less than $3m^2/s^2$ but is surrounded with patches of over $20m^2/s^2$.

Figure 4.16 (e) shows results from 120 °CA BTDC in the compression stroke. Here, the peak level of fluctuation kinetic energy has fallen, along with the average level, as shown in Figure 4.15 (b). In this case, the highest levels are found towards the edge of the measurement region, with a large area with low energy still being found in the centre of the cylinder.

The last fluctuation kinetic flow map is for 60 °CA BTDC and is shown in Figure 4.16 (f). Here, although the peak is much lower, Figure 4.15 (b) shows there was actually a slight increase in the average value, pointing to reduced levels of variation across the whole region.

4.8.2 Analysis of Liquid Fuel Spray Droplet Measurements

During post processing of the spray PIV velocity maps, the poor data quality found for individual cycles meant that application of the standard deviation and mean filters resulted in the loss of a large amount vectors, particularly outside the main spray area. Because of this it was decided that the 'fill holes' interpolation function found in the Insight software should not be used to replace the large amount of missing vectors, since this could result in an average result that was highly unrepresentative of the actual flow.

In addition, when averaging the individual cycles, some extra processing was undertaken in an attempt to improve the results. Firstly, it was assumed that the bulk spray would be travelling in a downward direction and therefore any odd vectors showing upward motion could be discarded. Secondly, since in most individual cycles apparently spurious vectors sometimes appeared in areas outside of the main spray area, a minimum data limit was applied during the averaging process. This meant that, for a particular vector to be retained in the average result, a vector had to be present in a certain number of individual cycles. Any point in the average field with less than the required amount data was assigned a velocity of zero. This limit was varied between 20% and 60% according to the data quality, and was selected so as to remove as many data points as possible from areas obviously beyond the main spray, while maintaining sufficient vectors in the main spray region.

Though this processing might be considered harsh and a little arbitrary, it was felt without this treatment the results would require large amounts in interpretation and would be less representative of the true flow.

4.8.2.1 General Description of Spray Characteristics

Late Injection Timing

Figure 4.17 shows the results from the PIV experiments on the liquid fuel spray from the air-assisted injector when using the late injection timing (as detailed in Section 4.7.1.2). Measurements were taken from the earliest point after the start injection (ASOI) when a good result could be obtained, in this case 6 °CA ASOI which corresponds to a crankshaft position of 64 °CA BTDC in the compression stroke. Results were then taken every 3° CA until a satisfactory result was no longer possible.

Figure 4.17 (a) shows the ensemble averaged result obtained at 64 °CA BTDC, 6 °CA ASOI. Here, the spray is entering the measurement region with velocities of up to approximately 10 m/s being recorded.

Figure 4.17 (b) shows the spray 3 °CA later at 61 °CA BTDC. Here it has reached the piston crown. Although it has spread a little, the spray is still fairly narrow.

Figures 4.17 (c) – (f) show plots of the results obtained through the rest of the injection from 58 °CA BTDC to 49 °CA BTDC. Here it appears that the spray is fully developed and, as a result, changes very little throughout this period.

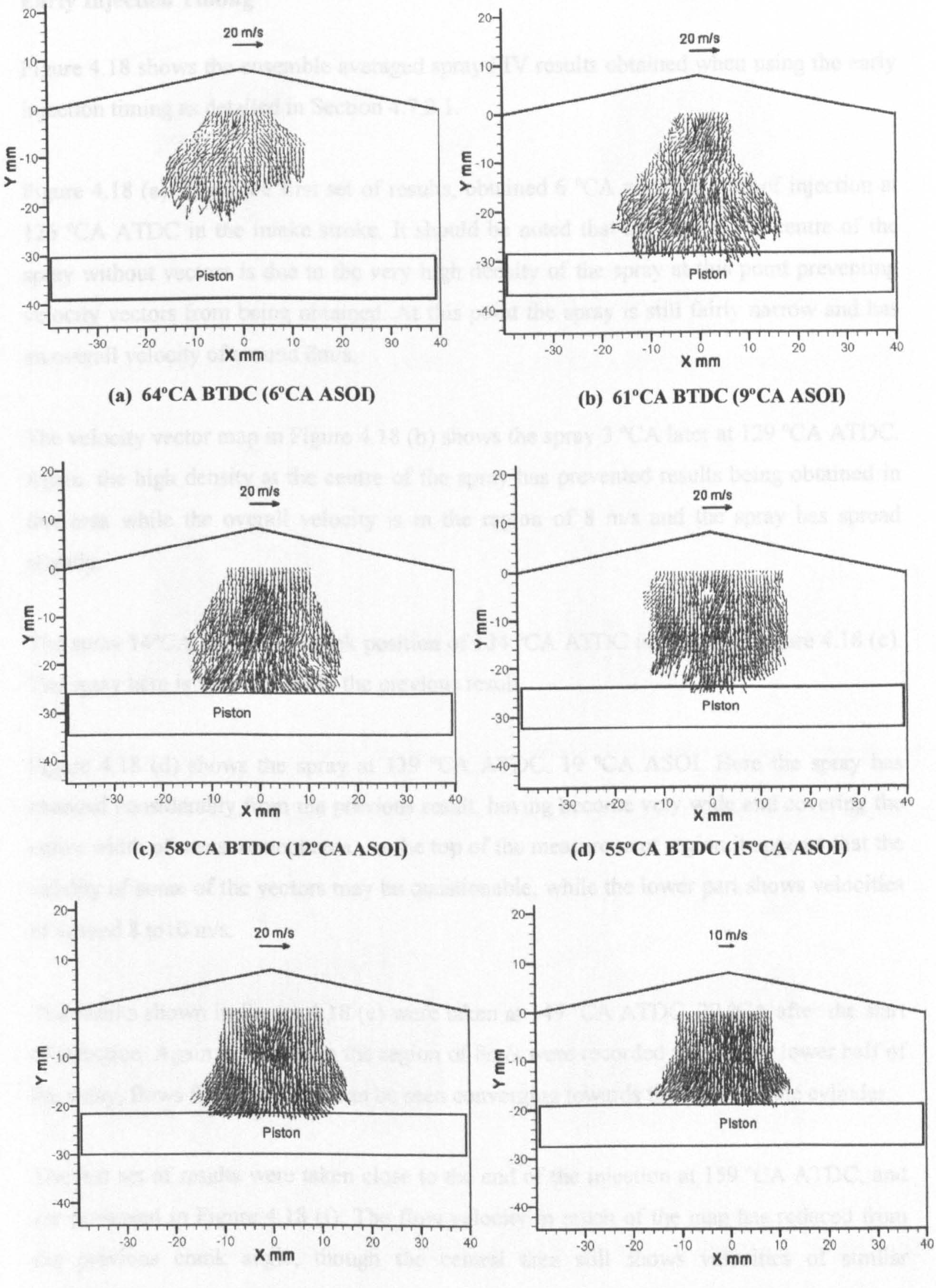

(a) 64°CA BTDC (6°CA ASOI)

(b) 61°CA BTDC (9°CA ASOI)

(c) 58°CA BTDC (12°CA ASOI)

(d) 55°CA BTDC (15°CA ASOI)

(e) 52°CA BTDC (18°CA ASOI)

(f) 49°CA BTDC (21°CA ASOI)

Figure 4.17 Ensemble Averaged PIV Fuel Spray Results with Late Injection Timing (SOI 70°CA BTDC, Intake Stroke)

Early Injection Timing

Figure 4.18 shows the ensemble averaged spray PIV results obtained when using the early injection timing as detailed in Section 4.7.2.1.

Figure 4.18 (a) shows the first set of results, obtained 6 °CA after the start of injection at 126 °CA ATDC in the intake stroke. It should be noted that the area in the centre of the spray without vectors is due to the very high density of the spray at this point preventing velocity vectors from being obtained. At this point the spray is still fairly narrow and has an overall velocity of around 8m/s.

The velocity vector map in Figure 4.18 (b) shows the spray 3 °CA later at 129 °CA ATDC. Again, the high density at the centre of the spray has prevented results being obtained in this area while the overall velocity is in the region of 8 m/s and the spray has spread slightly.

The spray 14°CA ASOI at a crank position of 134 °CA ATDC is shown in Figure 4.18 (c). The spray here is very similar to the previous result.

Figure 4.18 (d) shows the spray at 139 °CA ATDC, 19 °CA ASOI. Here the spray has changed considerably from the previous result, having become very wide and covering the entire width of measurement area. At the top of the measurement region it appears that the validity of some of the vectors may be questionable, while the lower part shows velocities of around 8 to10 m/s.

The results shown in Figure 4.18 (e) were taken at 149 °CA ATDC, 29 °CA after the start of injection. Again velocities in the region of 8m/s were recorded and, in the lower half of the spray, flows from each side can be seen converging towards the centre of the cylinder.

The last set of results were taken close to the end of the injection at 159 °CA ATDC, and are presented in Figure 4.18 (f). The flow velocity in much of the map has reduced from the previous crank angle, though the central area still shows velocities of similar magnitude.

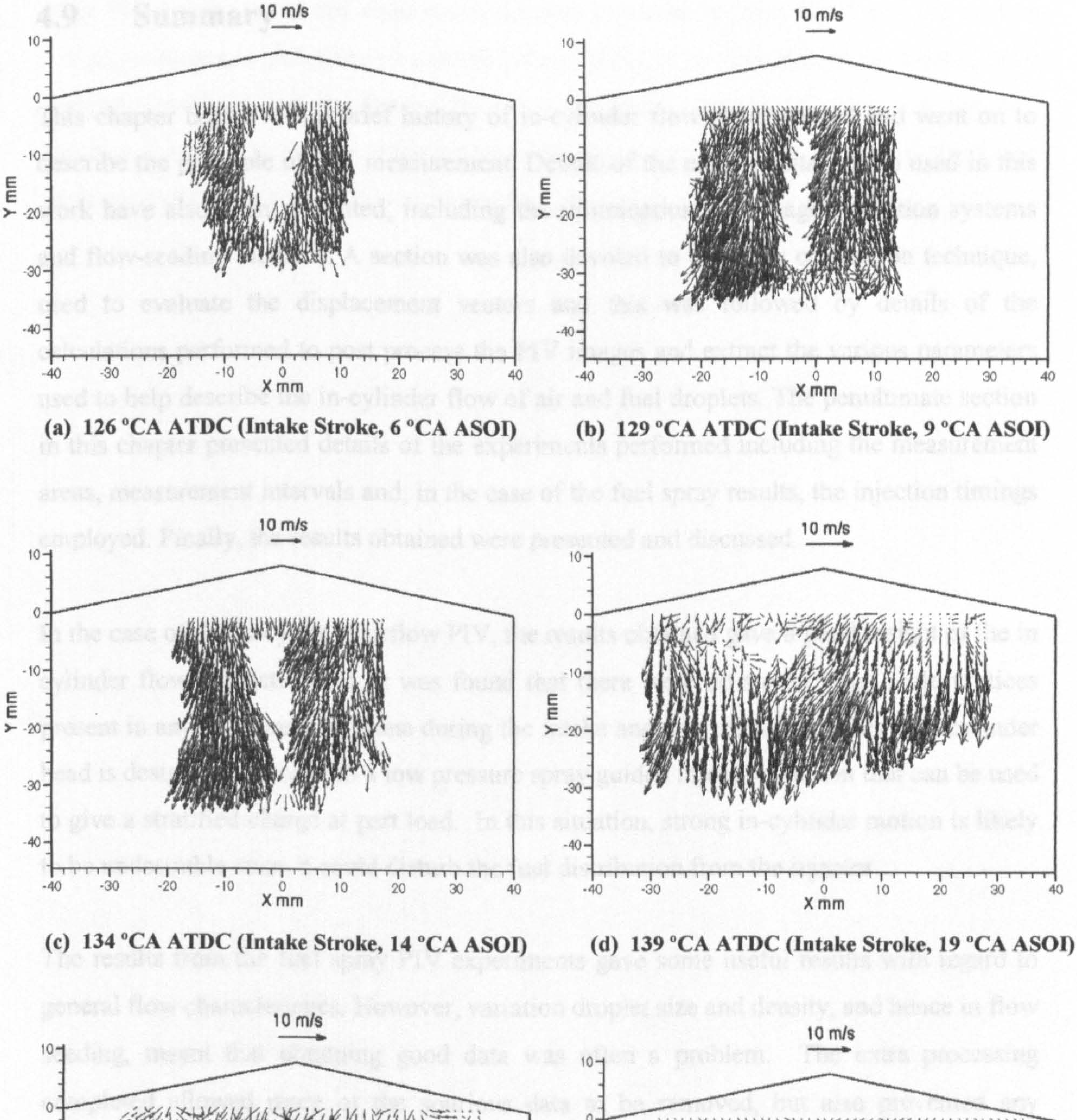

(a) 126 °CA ATDC (Intake Stroke, 6 °CA ASOI) **(b) 129 °CA ATDC (Intake Stroke, 9 °CA ASOI)**

(c) 134 °CA ATDC (Intake Stroke, 14 °CA ASOI) **(d) 139 °CA ATDC (Intake Stroke, 19 °CA ASOI)**

(e) 149 °CA ATDC (Intake Stroke, 29 °CA ASOI) **(f) 159 °CA ATDC (Intake Stroke, 39 °CA ASOI)**

Figure 4.18 Ensemble Averaged PIV Fuel Spray Results with Early Injection Timing (SOI 120°CA ATDC, Compression Stroke)

4.9 Summary

This chapter began with a brief history of in-cylinder flow measurement and went on to describe the principle of PIV measurement. Details of the experimental set-up used in this work have also been presented, including the illumination and image collection systems and flow-seeding medium. A section was also devoted to the cross correlation technique, used to evaluate the displacement vectors and this was followed by details of the calculations performed to post process the PIV images and extract the various parameters used to help describe the in-cylinder flow of air and fuel droplets. The penultimate section in this chapter presented details of the experiments performed including the measurement areas, measurement intervals and, in the case of the fuel spray results, the injection timings employed. Finally, the results obtained were presented and discussed.

In the case of the in-cylinder airflow PIV, the results obtained gave a good insight of the in cylinder flow characteristics. It was found that there were no strong large scale vortices present in any measurement plane during the intake and compression strokes. The cylinder head is designed for use with a low pressure spray guided injection system that can be used to give a stratified charge at part load. In this situation, strong in-cylinder motion is likely to be undesirable since it could disturb the fuel distribution from the injector.

The results from the fuel spray PIV experiments gave some useful results with regard to general flow characteristics. However, variation droplet size and density, and hence in flow seeding, meant that obtaining good data was often a problem. The extra processing completed allowed more of the spurious data to be removed, but also prevented any detailed analysis of the spray. When using the late injection strategy, the spray was found to be quite narrow, giving good stratification. However, when using early injection, although the spray was initially quite narrow, it quickly spread to give a very wide spray. This major difference in spray characteristics is caused by the changes in pressure difference across the injector in each case: with late injection the cylinder pressure is high which causes the spray to be contained into a tight pencil type spray. However, when injecting during the intake stroke the cylinder pressure is lower, allowing the wide spray to develop.

One of the objectives in this part of the study was to examine any interaction between the in-cylinder air motion and fuel spray. However, since the fuel spray does not appear to be particularly affected by the in-cylinder air motion, this was not possible. However, the fuel spray PIV results could not yield much detailed information spray itself and the airflow PIV experiments, which allowed a much better insight in the in-cylinder conditions, were completed without fuel injection. Therefore, in future research, the inclusion the fuel injection event in the airflow experiments might allow any intrusion of the fuel spray into the in-cylinder airflow to be better assessed.

Chapter 5

Characterisation of In-Cylinder Fuel Distribution using Laser Induced Exciplex Fluorescence

Chapter 5 Characterisation of In-Cylinder Fuel Distribution using Laser Induced Exciplex Fluorescence

5.1 Introduction to In-Cylinder Fuel Distribution Measurement

The fuel distribution and mixture formation process within an IC engine can greatly affect its ignition, combustion, pollutant formation processes and fuel consumption. This is particularly true for stratified charge direct injection gasoline (GDI) engines where the guiding of the charge to the vicinity of the spark plug at the time of ignition is vital for optimised operation.

In order to provide these in-cylinder conditions, the ability to measure the fuel concentration and air/fuel ratio distribution in the combustion chamber is almost essential. To this end, several non-intrusive laser based spectroscopic diagnostic techniques have been developed to allow in-cylinder fuel concentration measurement. These are based on three different light scattering processes, namely Rayleigh scattering, Raman scattering and laser induced fluorescence.

Laser Rayleigh scattering (LRS) is a simple, and easy to use, method for measuring gaseous species concentration. The light scattered by the Rayleigh method is the strongest of the techniques mentioned above and hence has the potential to facilitate 2D dimensional in-cylinder measurements. The main problem associated with the application of this technique to engines is the interference of the Rayleigh signal by Mie scattered light from both solid and liquid particles and the cylinder walls. Despite this, LRS has been successfully applied to the measurement of fuel vapour distribution with in the cylinder of motored IC engines. However, in this case, the desire to measure both the liquid and vapour phases of the fuel simultaneously renders this technique unsuitable.

The spontaneous Raman scattering (SRS) technique allows direct detection of in-cylinder air/fuel ratio via simultaneous multiple-species measurements of stable species such as N_2, O_2, CO_2, etc. Though this technique theoretically has potential to providing full and accurate spatially resolved information of the cylinder contents, the weak nature of the Raman signal often means it is limited to single point measurements.

Probably the most popular method of obtaining measurements of in-cylinder measurements at present is laser-induced fluorescence (LIF). Its popularity mainly stems from its ability to provide planar 2D images of fuel distribution with a good signal to noise ratio and, with careful calibration, the potential for quantitative air/fuel ratio measurements. However, while systems tend to be simple to set up and use, the selection of suitable dopants and compensation factors for phenomena that affect signal strength such as oxygen quenching and laser energy attenuation make the realisation of quantitative measurements very difficult. Another drawback of the classic planar LIF technique is that it is not suitable for use where fuel is present in both its liquid and vapour phases. This is because the range of signal levels between the very strong liquid phase emission and the weak vapour phase fluorescence is beyond the dynamic range of ICCD cameras currently available. Initially developed for application to diesel fuel sprays, but now also used in the study of GDI engines, laser induced exciplex fluorescence (LIEF) provides a solution to this problem [71-79]. In this technique the emission from the liquid phase is spectrally red shifted with respect to that of the of the vapour phase, allowing, with suitable filtering, the capture of each fuel phase separately. For these reasons, the LIEF technique was chosen for the study of the in-cylinder mixture distribution obtained from the Orbital air assisted GDI injection system.

5.2 Principle of Laser Induced Fluorescence

The emission of light from an atom or molecule that has been excited by a laser beam is known as laser induced fluorescence. The absorption of laser energy by the molecule moves it from a low energy level to high energy electronic states. It is essential that the wavelength of this excitation source is selected to match the absorption wavelength of the molecule to be excited. Since the higher electronic states are rarely populated by molecules at combustion temperatures, the initial lower state is normally the ground electronic level.

Figure 5.1 shows the five possible processes a molecule may experience following its excitation by a laser source. Firstly, the molecule can be returned to its ground state through laser induced stimulated emission, denoted in Figure 5.1 by $B_{12}I_0$. The second possibility is that the molecule absorbs an additional photon, exciting it to even higher states, potentially to ionised levels, denoted in Figure 5.1 as $B_{2i}I_0$. The third option is for rotational and vibrational energy transfers to be produced through in-elastic collisions with other molecules, shown as $Q_{vib,rot}$ in Figure 5.1. Alternatively, these collisions can result in electronic energy transfer, Q_{elec}, often termed quenching. Fourth, internal energy transfer and dissociation of the molecule can be produced by interactions between the individual atoms of the molecule. Lastly the molecule can return to its ground state by emission of a

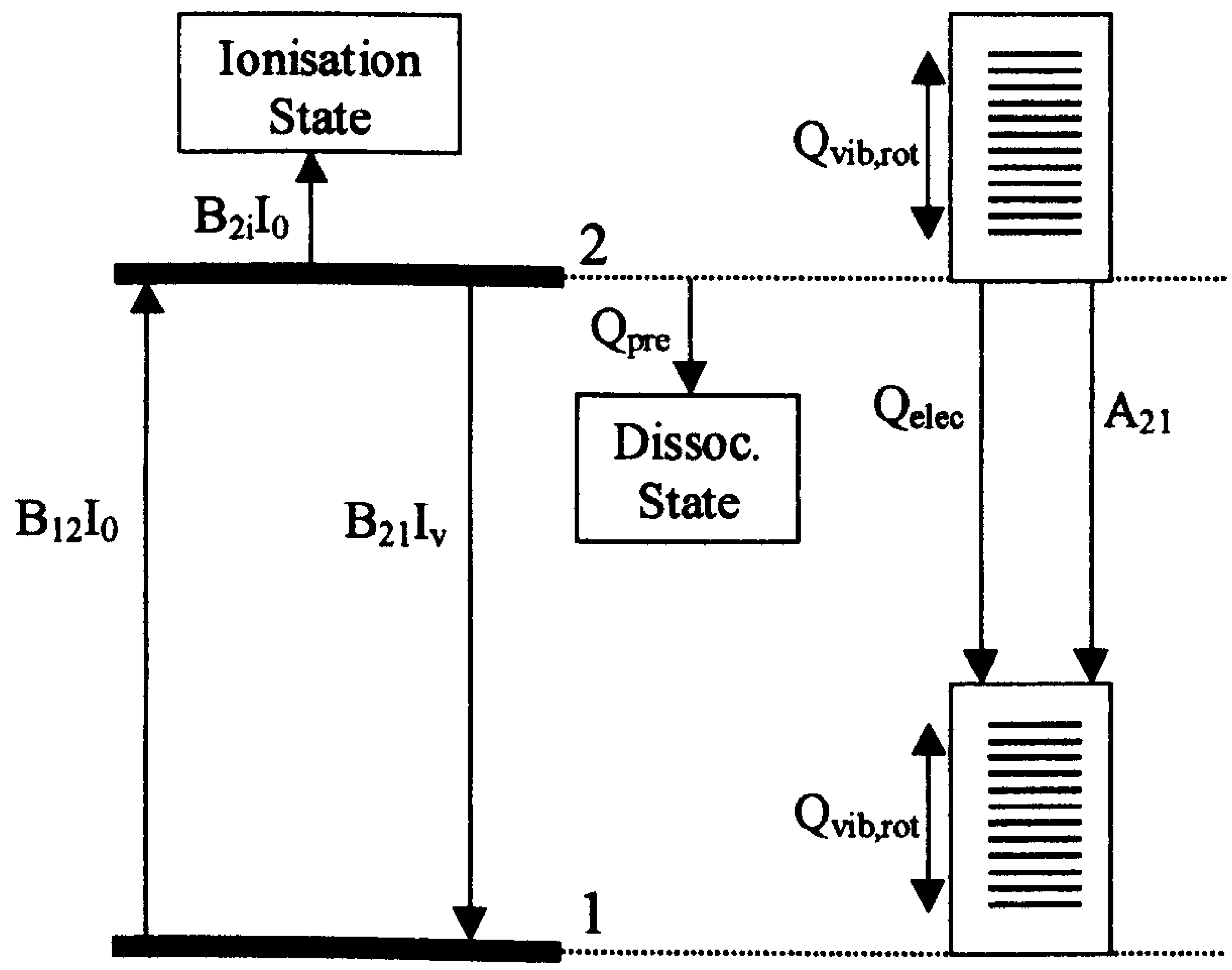

Figure 5.1 Main Energy Transfer Processes in LIF [90]

photon, producing the laser induced fluorescence. Since the fluorescence signal is a function of the population of molecules in the upper state, the concentration of the absorbing species can be determined by solution of the state-dependant population dynamics. Generally, analysis of LIF, particularly with regard to IC engines, is performed using a semi-classical rate equation developed by Piepmeier [91] rather than the quantum mechanical approach.

In actual data analysis, a two-level-energy model, such as that shown in Figure 5.2, is often used as a first approximation. Figure 5.2 also illustrates the essential properties of LIF. For this two-level-energy model, the rate equations for the lower and upper energy levels are:

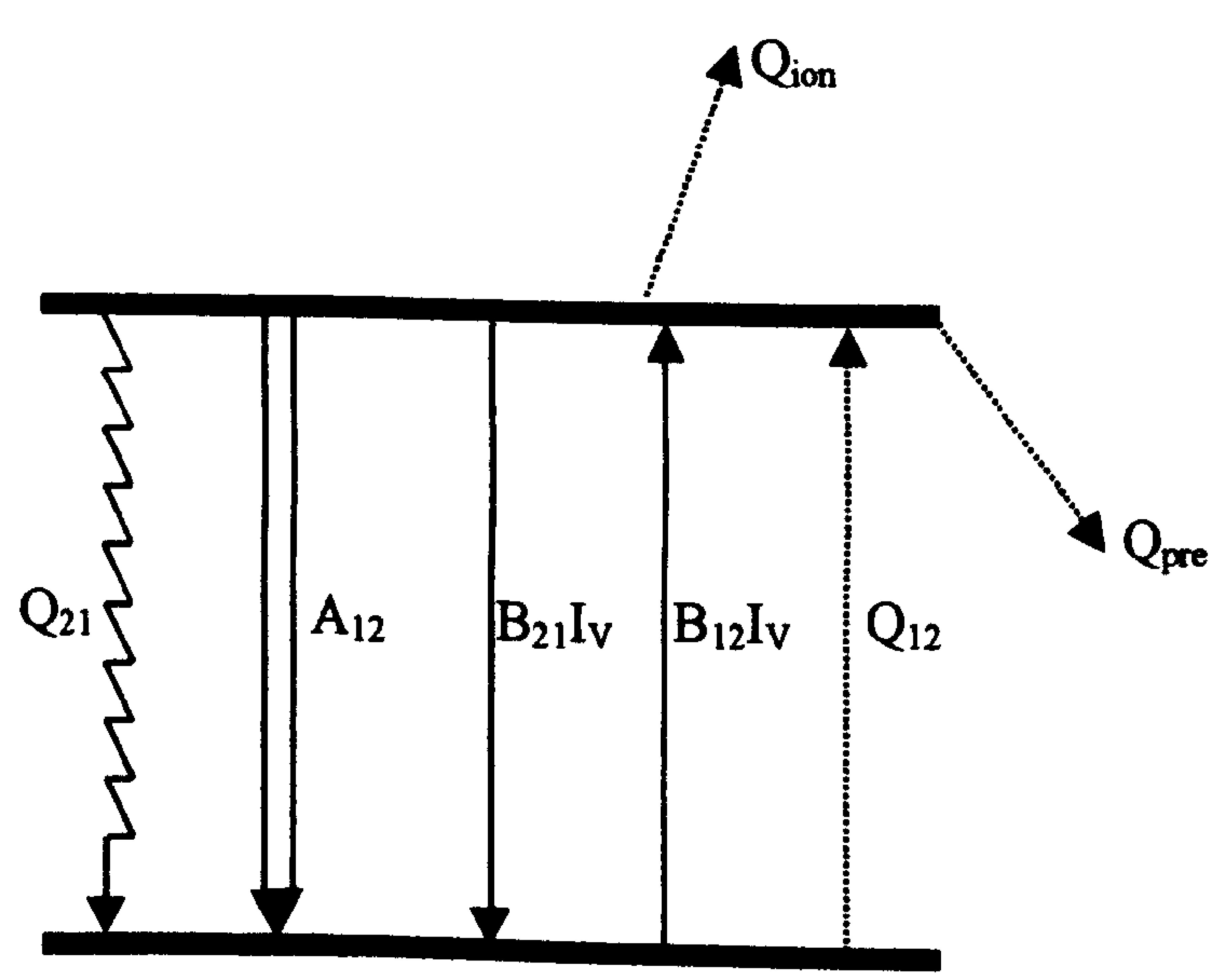

Figure 5.2 Simple Two-Energy-Level Diagram for LIF Modelling [90]

$$dN_1/dt = -N_1 (Q_{12} + B_{12}I_v) + N_2 (Q_{21} + A_{21} + B_{21}I_v) \quad (5.1)$$

$$dN_2/dt = N_1 (Q_{12} + B_{12}I_v) - N_2 (Q_{21} + A_{21} + B_{21}I_v + Q_{ion} + Q_{pre}) \quad (5.2)$$

Where B_{12} and B_{21} are the Einstein coefficients for stimulated absorption and emission, A_{21} is the Einstein coefficient for spontaneous emission, and I_v (Wcm^{-2} Hz^{-1}) is the laser spectral intensity. Since the separation of the two energy levels is normally only a few electron volts, for most measurements Q_{12} can be neglected. As most excited states are not pre-dissociative, unless specifically desired, photo-ionisation can often be omitted and Equations 5.1 and 5.2 can be rewritten as:

$$dN_1/dt = -N_1B_{12}I_v + N_2 (Q_{21} + A_{21} + B_{21}I_v) \quad (5.3)$$

$$dN_2/dt = N_1B_{12}I_v) - N_2 (Q_{21} + A_{21} + B_{21}I_v) \quad (5.4)$$

Since the upper state has a negligible population prior to excitation, the initial condition $N_2|_{t=0} = 0$ is applied to Equation 5.4. Also, since chemical reactions occur during the measurement it is necessary to conserve the population total, hence:

$$N_1 + N_2 = \text{constant} = N_1^0 \quad (5.5)$$

Where N_1^0 is the total population prior to excitation. The solution to the two level system is given by:

$$N_2 = N_1^0 B_{12}I_v \tau (1 - e^{-t/\tau}) \quad (5.6)$$

where the time constant τ is $(Q_{21} + A_{21} + B_{21}I_v + B_{12}I_v)^{-1}$. For laser pulses much longer than τ, the system reaches a steady state value of

$$N_2 = N_1^0 B_{12}I_v \tau \quad (5.7)$$

Which can be more conveniently written as:

$$N_2 = B_{12}I_v \frac{A_{21}}{Q_{21} + A_{21}} \frac{1}{1 + I_v / I_v^{sat}} \quad (5.8)$$

where the saturation intensity I_v^{sat} is defined as:

$$I_v^{sat} = \frac{A_{21} + Q_{21}}{B_{21} + B_{12}} \qquad (5.9)$$

Assuming the fluorescence is emitted equally into 4π steradians, the total number of photons N_p striking a photo-detector from a collection volume V_c is given by:

$$N_p = \eta \frac{\Omega}{4\pi} N_1^0 V_c B_{12} E_v \frac{A_{21}}{Q_{21} + A_{21}} \frac{1}{1 + I_v / I_v^{sat}} \qquad (5.10)$$

where η = transmission efficiency of the collection optics.

Ω = the collection angle, (sr),

E = the spectral fluence of the laser (J cm^{-2} Hz^{-1})

V_c= the sampling volume, defined by the cross-sectional area of the laser beam, A, and the axial extent along the beam, *l*, from which the fluorescence is detected

For a particular experiment the fluorescence signal can be expressed as

$$P_{flu} = \eta_c \Omega V_c f_l(T) \chi_m N I_v \frac{A_{21}}{Q_{21} + A_{21}} \frac{B_{12}}{1 + I_v / I_v^{sat}} \qquad (5.11)$$

where $f_l(T)$ = the fractional population of the lower electronic state

χ_m = the mole fraction of the absorbing species

N = the total gas number density

I_v = the spectral power of the incident laser light (W cm^{-2} Hz^{-1})

$f_l(T)$ represents the fraction of molecules of the absorbing species that are in the specific electronic-vibrational-rotational energy level excited by the laser, and is given by the Boltzmann distribution. Thus, the grouping $f_l(T)\, \chi_m$ N represents the number density of the absorbing species at ground state, N_1^0.

Further reduction of Equation 5.11 is possible if the limiting cases of high and low laser energy are applied. At low intensity with $I_v << I_v^{sat}$ Equation 5.11 can be written as

$$P_{flu} = \eta_c \Omega V_c f_l(T) \chi_m N I_v B_{12} \frac{A_{21}}{Q_{21} + A_{21}} \qquad (5.12)$$

In this regime fluorescence is directly proportional to the laser intensity and, for this reason, the relationship is termed the **linear fluorescence** equation. In this situation quantitative measurements are only possible after solving the quench rate constant for the species of interest. However, since the quenching rate is a function of temperature, pressure and composition it is very difficult to determine within the constantly changing environment of an IC engine.

Alternatively, if higher laser power is employed such that $I_v >> I_v^{sat}$ then Equation 5.11 becomes

$$P_{flu} = \eta_c V_c f_l(T) \chi_m N B_{12} \frac{A_{21}}{B_{21} + B_{12}} \tag{5.13}$$

Here, fluorescence has reached the saturation limit and the signal level is independent of both laser irradiance and quenching, negating the need to compensate for either of them. However, total saturation is difficult to achieve either due to the specific wavelength region of the absorption or the magnitude of the saturation intensity. Furthermore, saturation is not achieved at the outer edge of the laser beam or over the entire duration of the laser pulse due to temporal variation. It is especially difficult to achieve saturation when using a laser sheet to take planar fluorescence measurements, as is the case with most LIF experiments applied to IC engines.

5.3 Application of LIF to IC Engines

The application of LIF to IC engines is normally completed using a laser sheet to illuminate the desired measurement plane, with the fluorescence captured by a photo-detector positioned perpendicular to the measurement plane. This set-up is known as planar laser induced fluorescence (PLIF). As discussed in the previous section, the LIF system can operate in either linear or saturated regimes according to the laser light intensity used. When making 2D PLIF measurements within the high pressure and temperature environment of an IC engine cylinder it is rarely possible to fully saturate the absorbing molecules. For this reason, PLIF measurements in engines are almost universally completed in the linear regime. Returning again to Equation 5.12, the fluorescence signal is directly proportional to the species concentration χ_m, being measured. It must also be noted that, if quantitative measurements are to be taken, the quenching rate constant must also be evaluated. However, since the quenching rate is dependent upon temperature, pressure and composition it is very hard to achieve truly quantitative measurements within an IC engine.

Furthermore, if species concentration measurements are to be performed, several other requirements must be satisfied. Firstly, the molecules' absorption spectra must be known and accessible to a laser source. Secondly, the emission spectra must be known and be red shifted from the absorption wavelength to avoid interference from scattered laser light. Finally, the radioactive decay rate from the excited state must be known and losses from the excited state due to quenching, photo ionisation and pre-dissociation must be accounted for.

With regard to the fluorescing molecule used for fuel concentration measurements, one of three strategies can be employed; natural fluorescence from the fuel, fluorescence from a tracer molecule with properties comparable to the fuel or fluorescence from exciplex forming dopants. The first two methods have successfully been employed for measurements of fuels in either the gaseous or liquid phase. However, where the fuel is present in both phases simultaneously, for example in diesel and GDI engines, the exciplex method should be used.

5.4 Exciplex System and Dopant Selection

5.4.1 Exciplex System

When attempting to visualise an in-cylinder fuel distribution that has fuel in both liquid and vapour forms present, it is highly desirable to be able to spectrally separate the two phases. Unfortunately, this is not possible using a classic single fluorescing dopant LIF system since organic molecules have virtually the same absorption and emission spectra in both their vapour phase and liquid phase when dissolved into typical fuels.

Even if the desire to spectrally separate the phases is disregarded, visualisation of the two phases simultaneously is still virtually impossible when using of the single dopant system. This is because the fluorescence intensity from the liquid phase is many orders of magnitude greater than that of the vapour phase, meaning that with the limited dynamic range of available photo-detectors, it is very difficult to detect the presence of vapour when liquid fuel is present.

In order to overcome these problems, Melton and Verdieck [78] developed the laser induced exciplex fluorescence (LIEF) system. With this system, a second fluorescing species (M-G)* is formed by reacting the fluorescing molecule in the excited state M* with a suitable partner in the grounded state G.

$$M^*+G \Leftrightarrow (M\text{-}G)^*$$

This second fluorescing species (M-G)* is known as an exciplex, E*, and its fluorescence is always red shifted with respect to the excited monomer M*. This red shift occurs because exciplex formation is energy stabilising and thus E* has a lower energy than unbound M*.

The reaction to form (M-G)* from M* and G is reversible. With increasing concentration of G, the equilibrium of the reaction can be driven to the right (increasing exciplex) so that the (M-G)* dominates. Conversely, if the concentration of G is reduced below a certain level, the reaction will become unstable and the monomer M* becomes the dominant emitter. In some cases, careful adjustment of the species ratio of M* and G, can allow the exciplex (M-G)* to be the dominant emitter in the liquid phase, while in the vapour phase, due to the reduced density and higher temperature, the monomer emission dominates.

If the fluorescence from the exciplex and monomer are to be used as markers for the liquid and vapour phases respectively then it is important that they are sufficiently spectrally separated. This in turn allows the emissions to be isolated using appropriate filtering and collected with a photo-dector.

If the fuel within the measurement region is optically thin and the monomer M co-evaporates with the fuel then the emissions collected will relate directly to the amount of fuel in the liquid and vapour phases.

If quenching does not occur then the fluorescence intensity is directly proportional to the fuel concentration, allowing qualitative characterisation of the results or, with rigorous calibration, the potential for quantitative measurements.

Kim et al developed an exciplex fluorescence visualisation system suitable for gasoline engines [73]. This work investigated many different formulations and systems and found that 7% 1,4,6-trimethylnapthalene (TMN) and 5% N,N-dimethylaniline (DMA) in 88% iso-octane was the best for the LIEF technique when attempting to simulate gasoline fuels.

Unfortunately 1,4,6-trimethylnapthalene (TMN) is not generally available and extremely expensive, hence, naphthalene was used in this study. Figure 5.3 shows the main photo-physics features of the naphthalene / DMA exciplex system. When used, naphthalene fluoresces strongly and is suitable for use within the exciplex system. However, its biggest drawback is its boiling point of 218°C, beyond the 20 to 215°C boiling range of gasoline fuel. This means that it will underestimate the initial fuel evaporation rate. However, since in this case no attempt was being made to obtain quantitative results, coupled with the fact that the very small droplets produced by the air assisted injector have a fairly fast evaporation process, the use of naphthalene, along with DMA to form the exciplex was considered acceptable.

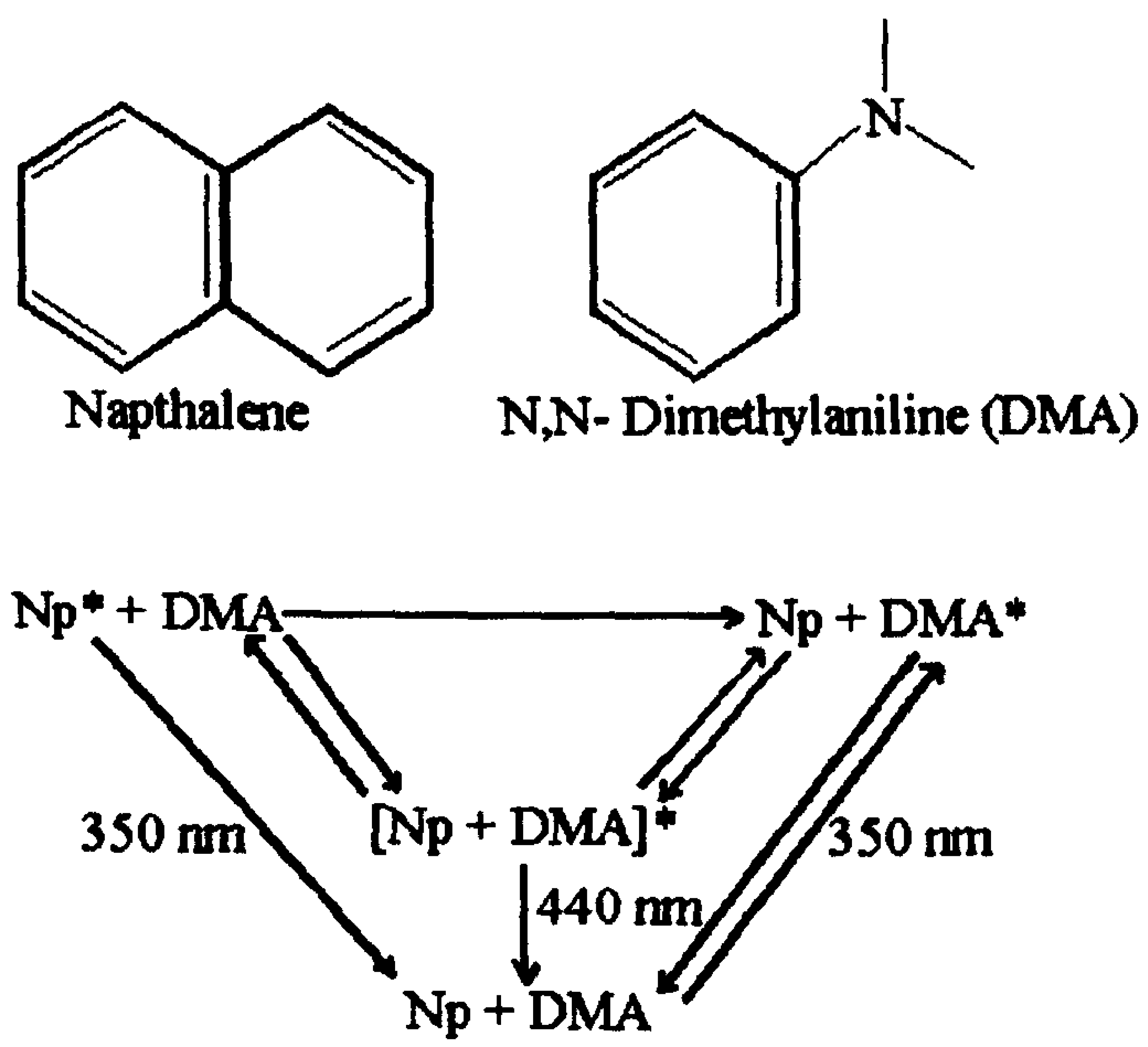

Figure 5.3 Naphthalene / DMA Exciplex System

5.4.2 Evaluation of Dopants

When choosing the dopants for use in the LIEF system, the following properties must be considered:

- Absorption and emission frequencies
- Satisfactory fluorescence yield
- Vulnerability to quenching
- Toxicity, stability and solubility in fuel
- Matching of vaporisation properties
- Availability of a partner to allow exciplex reaction

In order to check the suitability of the chosen dopants with regard to the above properties, tests were performed in a constant volume bomb prior to the engine experiments. The constant volume bomb was fitted with optical access windows on 3 sides. Excitation of the dopants was provided by a pulsed laser sheet from a XeCl Excimer laser. The emissions were then collected by an ICCD camera through a spectrograph unit from a direction perpendicular to the plane of the laser sheet. After calibration of the spectrograph system, tests were completed to assess the performance of the compounds in their vapour phase.

The following procedure was used in the constant volume bomb experiments: The combustion bomb was heated to 200°C and thoroughly purged with compressed air to remove any residuals that could affect the results. A small amount of the substitute fuel to be used, 7% naphthalene and 7% DMA in 86% iso-octane, was mixed. Once cool, one window of the bomb was removed and very small amount of the mixture was placed inside. The window was then replaced and the chamber resealed. The bomb was then reheated to 200°C, and the emissions observed with the spectrograph. In order to examine the compounds' sensitivity to oxygen quenching, the pressure of the bomb was then increased using compressed air. Whilst maintaining the temperature at 200°C the pressure was increased first to 4 bar and then 7 bar absolute, recording the fluorescence emissions at each stage. After depressurising and purging the bomb, the procedure was repeated but using nitrogen instead of compressed air. This was to allow any effects of pressure on the fluorescence emissions to be observed.

A second set of tests was then completed to allow emissions from the liquid phase to be observed. A small quantity of the substitute fuel was placed in a fluorimeter cuvet. The cuvet was then carefully positioned in the bomb so that the laser sheet could pass though the liquid and the emissions could be observed.

From the results it appeared that adequate signal strength could be obtained from the mixture in both liquid and vapour phases to complete successful engine tests. With regard to the vapour phase, oxygen quenching was found to be fairly severe but it was felt a reasonable signal could still be obtained without having to create an oxygen free environment within the engine, see Figure 5.4 (a). The results from the nitrogen tests showed that the vapour phase did not appear to be significantly affected by pressure. The results also confirmed that emission wavelengths of the 2 phases were as expected. The exciplex reaction appeared to work well with the liquid phase emission being sufficiently red shifted to allow easy separation of the 2 phases, see Figure 5.4 (b).

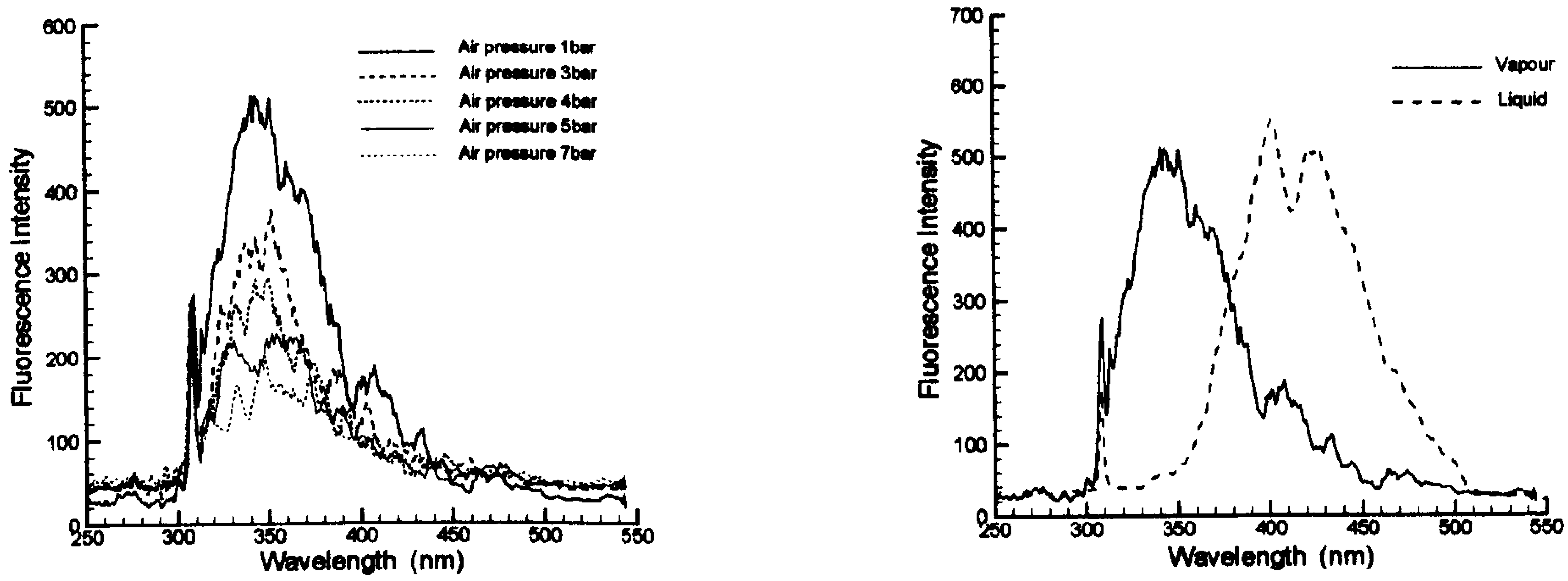

(a) Effect of Air Pressure on Vapour Phase Emission (b) Liquid and Vapour Phase separation

Figure 5.4 Emission Spectra of Mixed Compound (86% iso-octane + 7% DMA + 7% Naphthalene)

5.5 Experimental Set-up

This section will be used to describe the details of the optical set-up used specifically for the LIEF tests, including the illumination and image collection optics. The more general details of the engine, test bed and fuel systems have been dealt with previously in Chapter 3.

5.5.1 Illumination Optics

Figure 5.5 shows a schematic diagram of the optics and image capture set-up. The excitation source for fluorescence was provided by a XeCl Excimer laser with an output wavelength of 308nm and beam dimensions of approximately of 10mm x 25mm. The beam was passed to its required position via a series of mirrors. For the planar experiments a spherical lens with a focal length of 1000mm was used to loosely focus the beam. A laser sheet approximately 2mm thick was then created using a concave cylindrical lens with a focal length of -76mm, Figure 5.5. For the expanded beam experiments, a concave cylindrical lens with a focal length of 700mm was used to create a diverging expanded beam.

5.5.2 Image Capture Optics

The exciplex system required the capture of two images simultaneously. This was achieved by using an image doubler set-up to create a pair of images before capturing them with a single ICCD camera. The image doubler set-up consisted of a beam splitter plate and a mirror. The beam splitter was held at 45 degrees to both the area of interest and the camera. The mirror was located behind it at the same angle. The beam splitter reflected 30% of the fluorescence signal to the camera whilst transmitting the remainder on to the mirror, which then reflected the fluorescence signal to the camera. This produced a pair of images side by side on the camera.

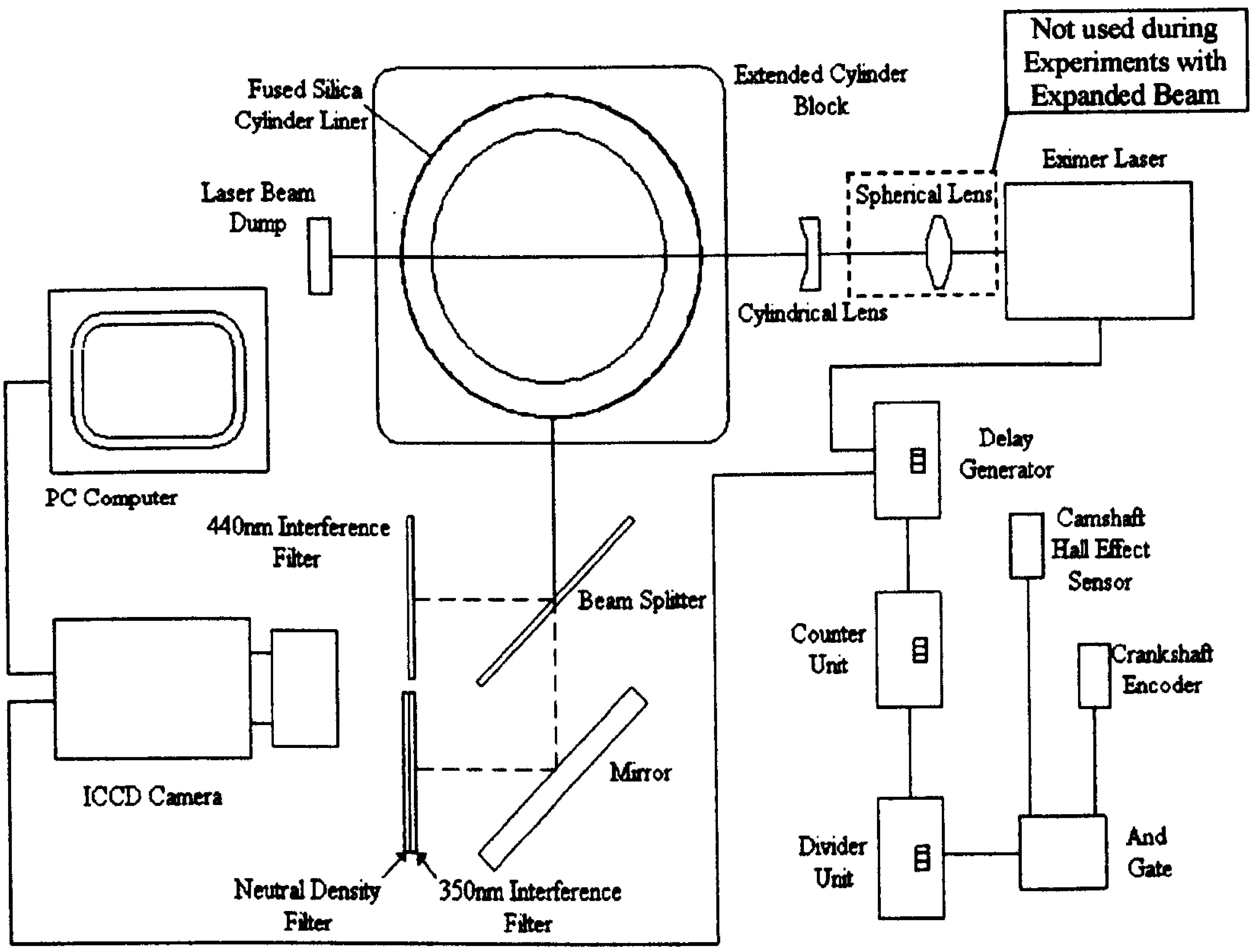

Figure 5.5 Optics and Image Capture Set-up for LIEF Experiments

Each image was then passed through a band pass filter. One of these filters was matched to the vapour phase fluorescence and had a central wavelength of 350nm and a bandwidth of 10nm FWHM. The other was matched to the liquid phase and had a central wavelength of 440nm and a bandwidth of 25nm FWHM. Since the liquid phase produced a much higher level of fluorescence intensity than the vapour phase, the beam splitter was selected to have a 30/70 reflectance/transmittance ratio and the filter for the vapour phase was arranged to receive its signal from the mirror side of the image doubler, see Figure 5.5. Because of the disparity in signal strengths between the two phases, the signal from the liquid phase was further attenuated to that of the vapour phase by use of neutral density filters. This allowed selection of the optimum light collection level i.e. camera gain and aperture settings.

Synchronisation of the camera and laser was achieved by the use of a delay generator. In order to determine the required settings for the delay generator, a photo diode connected to an oscilloscope was used to measure the time taken for the laser to produce a pulse of light after being sent the signal from the delay generator, along with the width of that pulse. Using these timings as a starting point, the optimum delay time and exposure time were found to be 1.9μs and 200ns respectively.

After being captured, the images were transferred from the camera to a PC for storage and processing. The image capture system used had a maximum capture frequency of around 0.2 Hz and hence, an image could only be captured every 50^{th} cycle at an engine speed of 1200 RPM.

In order to minimise the amount of fuel vapour exhausted from the engine and to reduce contamination of the optical access windows, it was important to ensure that fuel injection only took place on cycles when an image was to be captured. This was achieved by using a divider unit so that fuel injection and laser were activated only when the ICCD camera was ready.

5.6 Experiment

LIEF experiments were completed in several horizontal and vertical measurement planes. Two injection timings were used, simulating both homogenous and stratified injection strategies. Tests in the horizontal planes were illuminated with a laser sheet, while the vertical plane experiments were completed using both a laser sheet and an expanded laser beam. Since the images with the expanded beam appeared to show serious laser attenuation on the laser exit side, the tests were conducted with the laser beam entering the left, right and below and the results compared.

Images were taken at regular crank angle intervals, from the start of injection until the intrusion of the piston obscured the measurement area. At each crank angle, 20 spray images were recorded and subsequently ensemble averaged. In addition, at each crank angle tested, 5 'background' images (without injection but with the laser pulse) were taken.

These were also averaged before being subtracted from the spray images. This method proved very successful in removing reflections and ambient light from the images. In addition, for each laser configuration, calibration images were taken to determine the laser beam distribution. This involved supplying the engine with a homogenous mixture and taking a series of images in the same way as the main tests. A standard gasoline port fuel injector, positioned approximately 1 metre from the intake port, was used to supply a homogenous mixture to the engine. In order to ensure complete evaporation and avoid condensation of the fuel on route to the engine, the intake air was heated to 90°C. Any variation in the fluorescence of these images could then be attributed to the distribution of the laser energy within the beam or other anomalies with the optics system. If required, the images from the main tests could then be normalised to this distribution.

All the tests were completed with the engine oil and coolant at 80°C and at an engine speed of 1200 RPM. Even when using the divider unit to prevent injection on cycles that no image was taken, window fouling from fuel and lubricating oil was a problem, meaning the engine had to be stripped for cleaning at regular intervals throughout the tests. Since the fluorescing properties of the substitute fuel can degrade over time, a fresh batch was mixed prior to each day of testing. All testing was completed with the intake unthrottled and with the intake air at ambient temperature.

5.6.1 Measurement Planes

5.6.1.1 Measurements with Laser Sheet

As stated above, tests were initially illuminated with a laser sheet. These measurements were completed in the horizontal and vertical planes shown in Figure 5.6. In each case the laser entered through the ring window from the left-hand side when viewed from behind the camera. In the vertical plane case, shown in Figure 5.6 (a), the plane was located along the centreline of the cylinder bore, perpendicular to the crankshaft axis. The image was also collected via the ring window with the field of view positioned normal to the laser sheet. For the tests in the horizontal plane, two measurement planes were selected. The first, shown in Figure 5.6 (b) was 5mm from, and parallel to, the cylinder head face. The second plane was 5mm from the extended cylinder block (25mm from the cylinder head), parallel to the first, Figure 5.6 (c). In the field of view shown in Figure 5.6 (a) the injector was positioned vertically but the top was tilted away from camera at 5°.

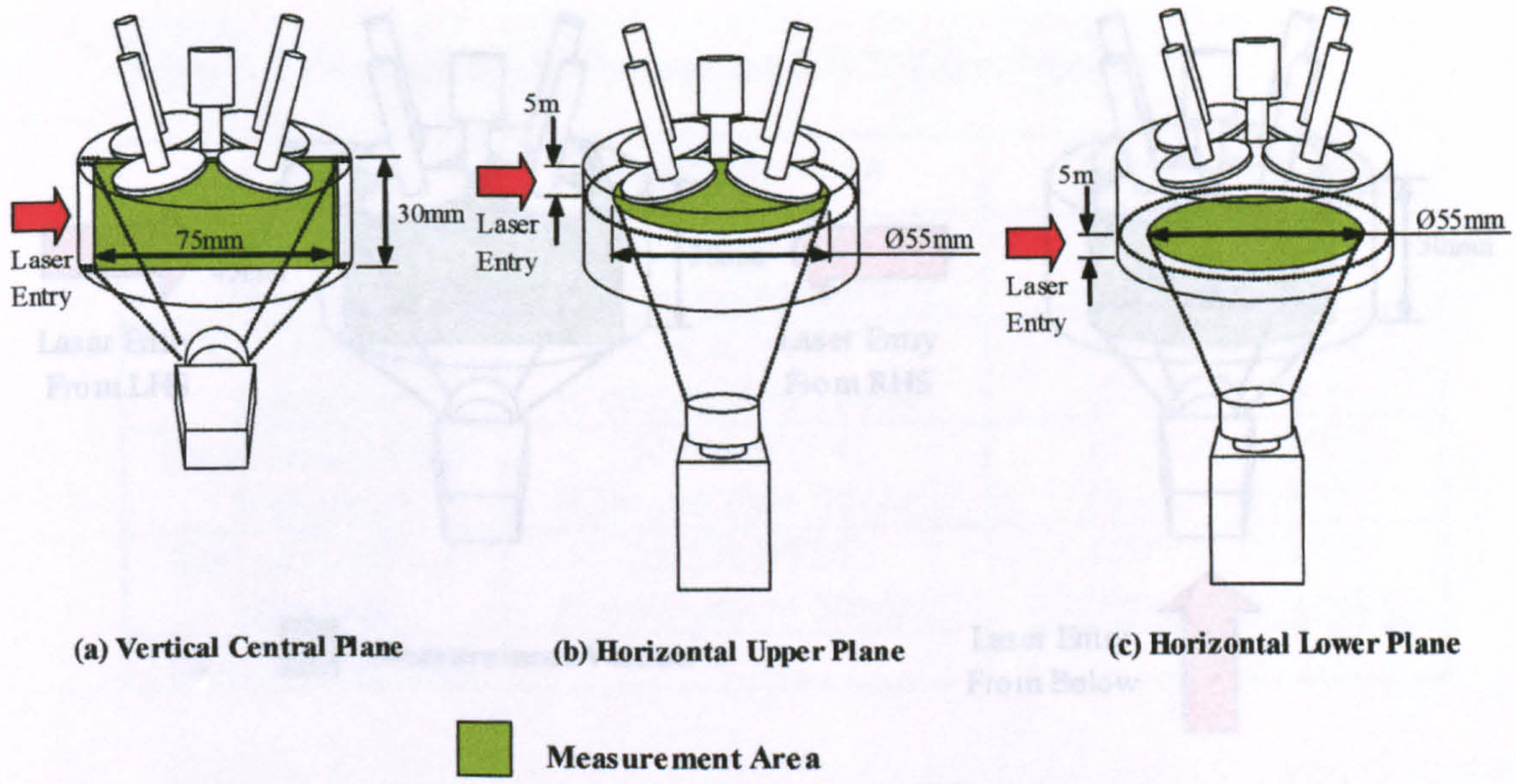

Figure 5.6 LIEF Measurement Planes when using Laser Sheet

5.6.1.2 Measurements with Expanded Laser Beam

The measurements in the vertical plane were then repeated using an expanded laser beam as the excitation source. In order to assess the effect of any attenuation of the laser beam by the fluorescing dopants, the experiment was completed with the laser entering from the left and right hand side of the image, via the ring window, and from below the image, via the transparent piston crown. This set-up is show in Figure 5.7. As with the laser sheet measurements in the vertical plane, the camera and image doubler were positioned to observe the fluorescence from the front of the engine, perpendicular to the crankshaft axis, via the transparent liner section.

When introducing the beam from the right and left, via the transparent cylinder liner, the original intention was to adjust the size of the expanded beam to match the height and width of the whole window area, allowing as much of the cylinder to be illuminated as possible. However, this set-up resulted in very serious internal reflections from the far side of the window making the system unusable. In order to overcome this problem, an adjustable aperture was introduced to progressively reduce the width of the beam until the level of reflection became tolerable. The maximum useable beam width was found to be 45mm. When introducing the beam from below, the beam was adjusted to fill the whole of the piston window, resulting in a beam of 55mm diameter entering the cylinder.

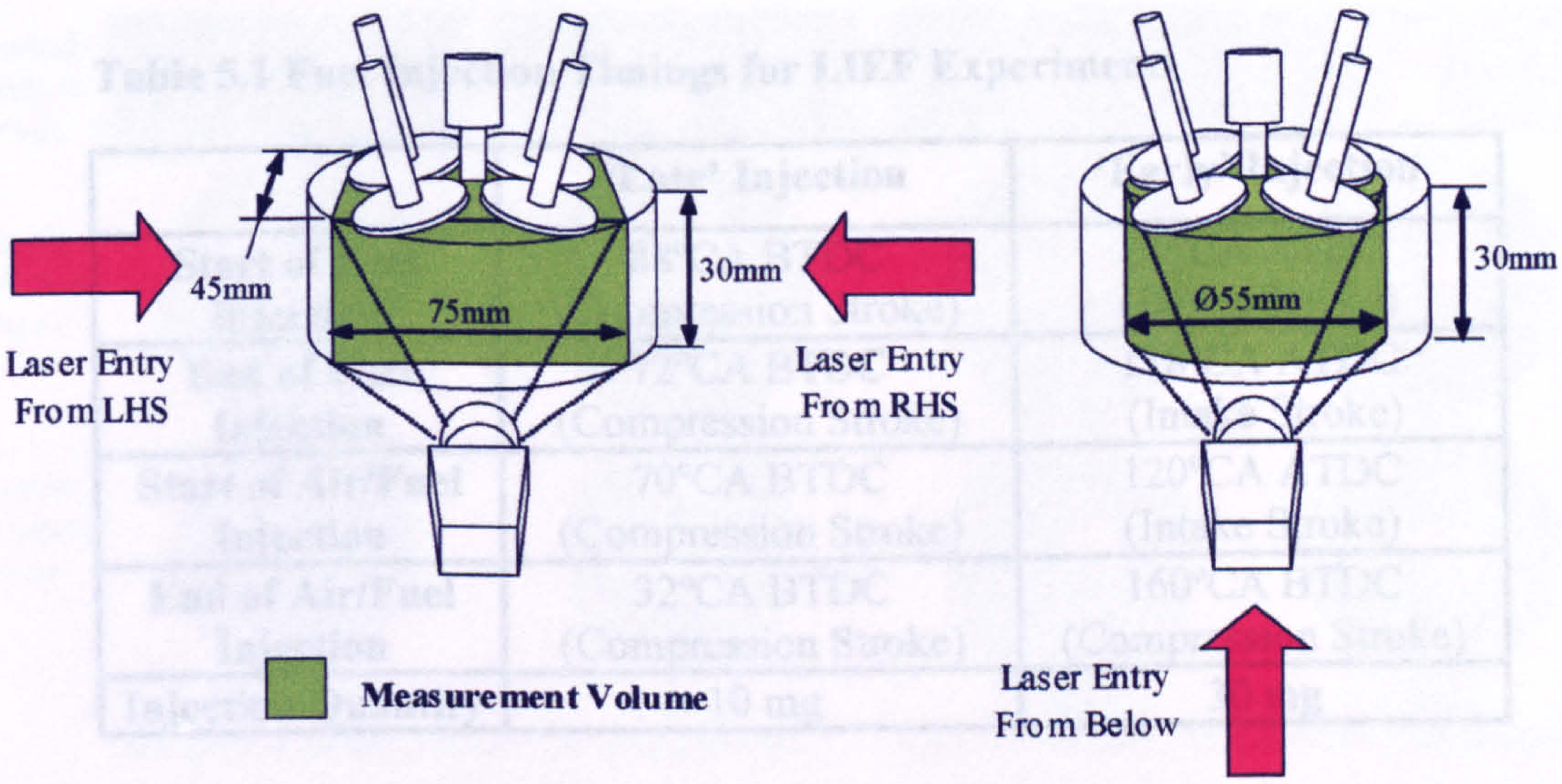

(a) **Measurements with Laser from LHS and RHS**

(b) **Measurements with Laser from Below**

Figure 5.7 LIEF Measurement Volumes and Laser Entry Directions when using Expanded Laser Beam

In order to observe any attenuation of the fluorescence signal caused by absorption of the laser energy by the dopants, the beam was introduced to the cylinder from 3 different directions. Initially the beam was introduced from the left via the transparent liner section, along the crankshaft axis. The experiment was then repeated with the beam entering from the right, again through the transparent liner section. Finally the beam was introduced from below, this time via the window in the extended piston.

5.6.2 Injection Timing

In order to explore the effect of injection timing on the fuel distribution, two different injection timing strategies were employed. The first was intended to represent a part load, late injection, 'stratified' operating point at 3 bar BMEP with an AFR of 40:1. In this condition, the injection into the cylinder was completed in the late stage of the compression stroke. The amount of fuel injected on each cycle was 10mg. The exact timings used can be seen in Table 5.1. The second set of injection timings, also shown in Table 5.1, attempted to simulate a homogenous charge, full load condition with injection taking place during the intake stroke and in this case 30mg of fuel was injected. Further details regarding the selection of these timings etc. have been discussed in Section 4.8.2.1.

Table 5.1 Fuel Injection Timings for LIEF Experiments

	'Late' Injection	'Early' Injection
Start of Fuel Injection	88°CA BTDC (Compression Stroke)	59°CA ATDC (Intake Stroke)
End of Fuel Injection	72°CA BTDC (Compression Stroke)	118°CA ATDC (Intake Stroke)
Start of Air/Fuel Injection	70°CA BTDC (Compression Stroke)	120°CA ATDC (Intake Stroke)
End of Air/Fuel Injection	32°CA BTDC (Compression Stroke)	160°CA BTDC (Compression Stroke)
Injection Quantity	10 mg	30 mg

5.7 Discussion of Results

5.7.1 Results with Laser Sheet

The sections below present and discuss the results obtained when using the laser sheet. In each case the laser entered the engine from the left-hand side when viewed from behind the camera. At each crank angle, 20 images were taken and subsequently ensemble averaged. In addition, for each set of 20 images, 5 'background' images (without injection but with the laser pulse) were recorded. These were also averaged before being subtracted from the spray images. As discussed in Section 5.6, images with a homogenous charge were taken in order to assess the energy distribution across the laser sheet. Since these calibration images were found to be quite uniform and normalisation made little difference to the results, normalisation was not performed on the images presented here.

5.7.1.1 Early injection Timing

Figure 5.8 shows the results obtained using the early injection timing when the tracer excitation was achieved with a laser sheet. For each crank angle at which measurements were taken, six images are presented. In each case, images in the left hand column represent the fluorescence intensity recorded from the liquid phase of the fuel while the right hand set of images correspond to emissions from the vapour phase. The top row of images were taken in the horizontal measurement plane (Figure 5.6 (a)), while the central and lower rows feature images from the horizontal upper and lower planes respectively, Figure 5.6 (b) and (c). In the later vertical plane images, the white area represents the piston encroaching into the measurement area.

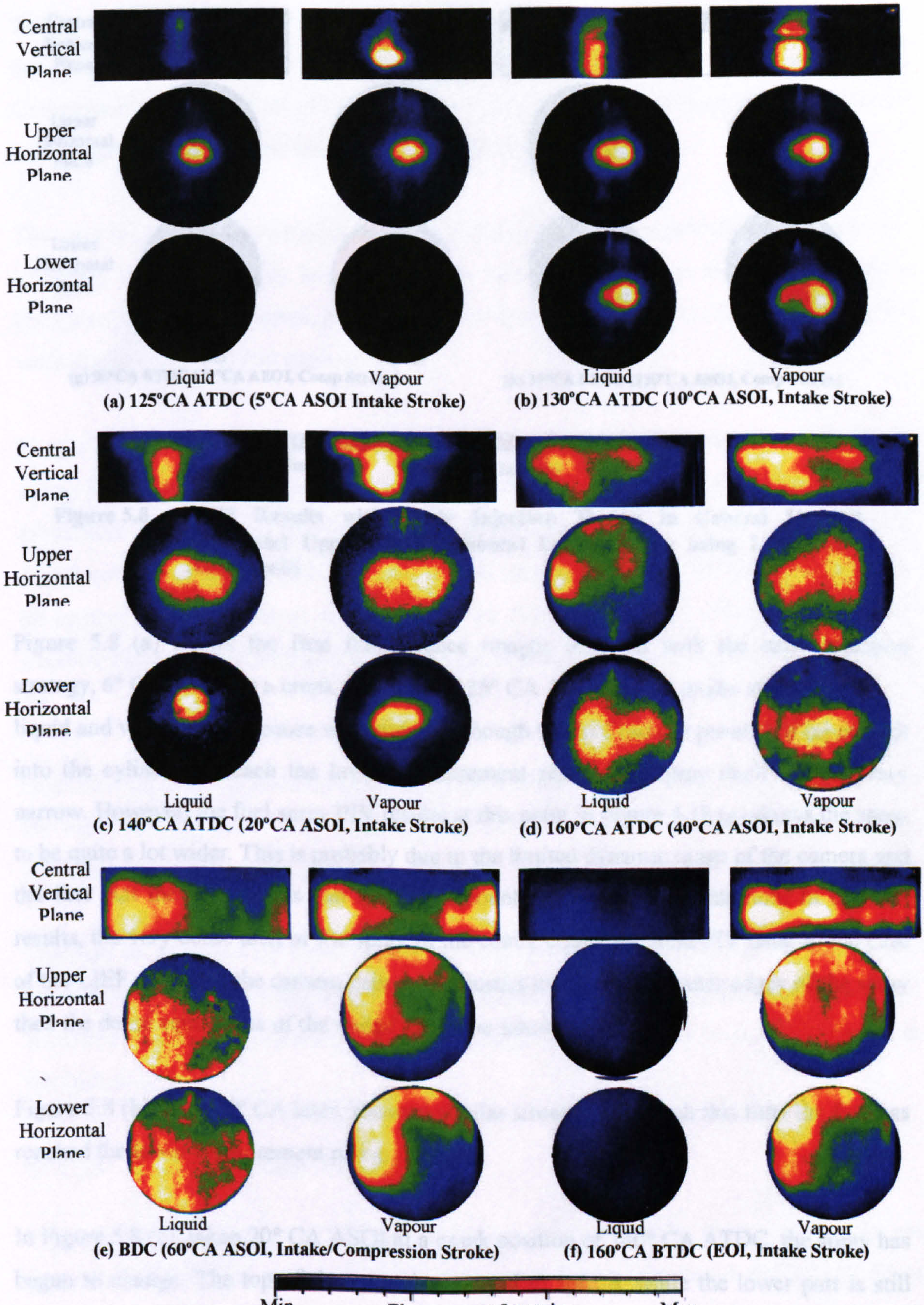

Figure 5.8 **LIEF Results with Early Injection Timing in Central Vertical, Horizontal Upper and Horizontal Lower Planes using Laser Sheet**

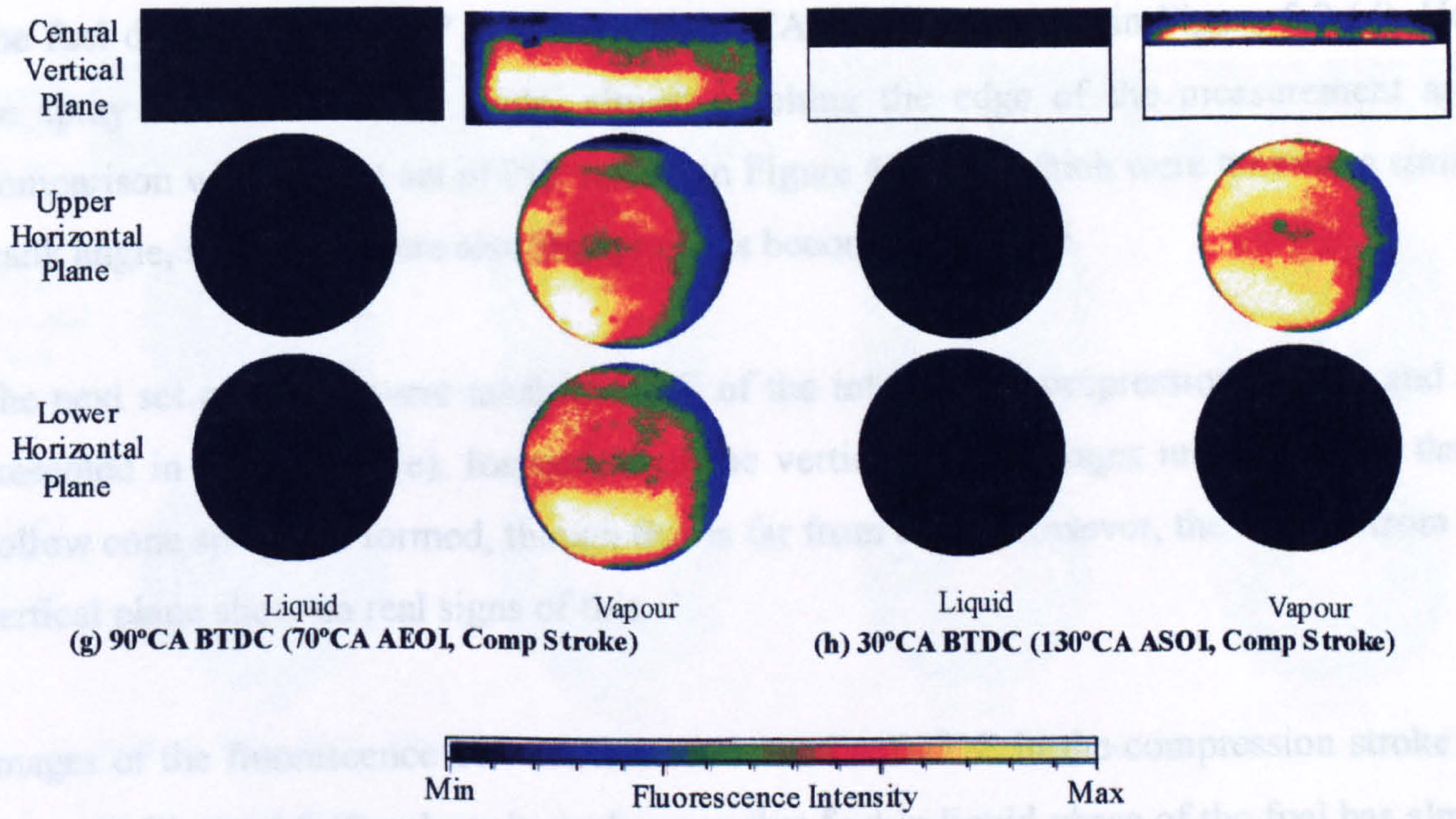

Figure 5.8 LIEF Results with Early Injection Timing in Central Vertical, Horizontal Upper and Horizontal Lower Planes using Laser Sheet (Continued)

Figure 5.8 (a) shows the first fluorescence images obtained with the early injection strategy, 6° CA ASOI, at a crank position of 125° CA ATDC in the intake stroke. Both liquid and vapour fluorescence was captured, though the fuel had not penetrated far enough into the cylinder to reach the lower measurement plane. The spray itself appears very narrow. However, the fuel spray PIV results at this point in Figure 4.18 (a) shows the spray to be quite a lot wider. This is probably due to the limited dynamic range of the camera and the fact that the PIV results can take no account of the fuel concentration. In the PIV results, the very dense area of the spray in the centre could not yield PIV data. In the case of the LIEF results, if the camera gain was adjusted to pick up the outer edges of the spray then the dense centre area of the image would be saturated.

Figure 5.8 (b), taken 5° CA later, shows a similar situation, although this time the fuel has reached the lower measurement plane.

In Figure 5.8 (c), taken 20° CA ASOI at a crank position of 140° CA ATDC, the spray has begun to change. The top of the spray has started to spread, while the lower part is still quite narrow. Comparison with the PIV results at the same position, presented in Figure 4.18 (d), show that here the spray has also widened significantly. However, both sets of results appear to show that the spray is solid, with no significant signs of a hollow central area.

The fuel distribution at 160° CA ATDC, 40° CA ASOI, is shown in Figure 5.8 (d). Here the spray has become very wide, almost reaching the edge of the measurement area. Comparison with the last set of PIV results in Figure 4.18 (f), which were taken at a similar crank angle, shows that here also the spray has become very wide.

The next set of results were taken at BDC of the intake and compression strokes and are presented in Figure 5.8 (e). Inspection of the vertical plane images might suggest that a hollow cone spray has formed, though this is far from clear. However, the images from the vertical plane show no real signs of this.

Images of the fluorescence 20° CA later at 160° CA BTDC in the compression stroke are shown in Figure 5.8 (f), where it can be seen that fuel in liquid phase of the fuel has almost evaporated. At this point the injection is just finishing, so it might be expected that a significant amount of liquid fuel should still be present. However, the peculiarities of the air-assisted injection system mean that all the fuel has probably already left the pre-chamber cavity and, for the previous few crank angles, the injector has been injecting only air.

Figure 5.8 (g) presents fluorescence images halfway through the compression stroke. Here the liquid fuel has totally evaporated, leaving a fairly homogenous mixture of vapour in the cylinder.

The final set of results are from 30° CA BTDC in the compression stroke. Here the piston has entered the measurement area, blocking the field of view in the lower horizontal plane. However, the other two views show that reasonably homogenous mixture of fuel vapour in the cylinder.

5.7.1.2 Late Injection Timing

Figure 5.9 presents the planar LIEF results taken with late injection timing. The results are presented in a similar manner to those in Figure 5.8, with the liquid and vapour phase images in the left and right columns respectively. As before, the top row features images from the vertical plane, while the middle and bottom present results from the two horizontal planes.

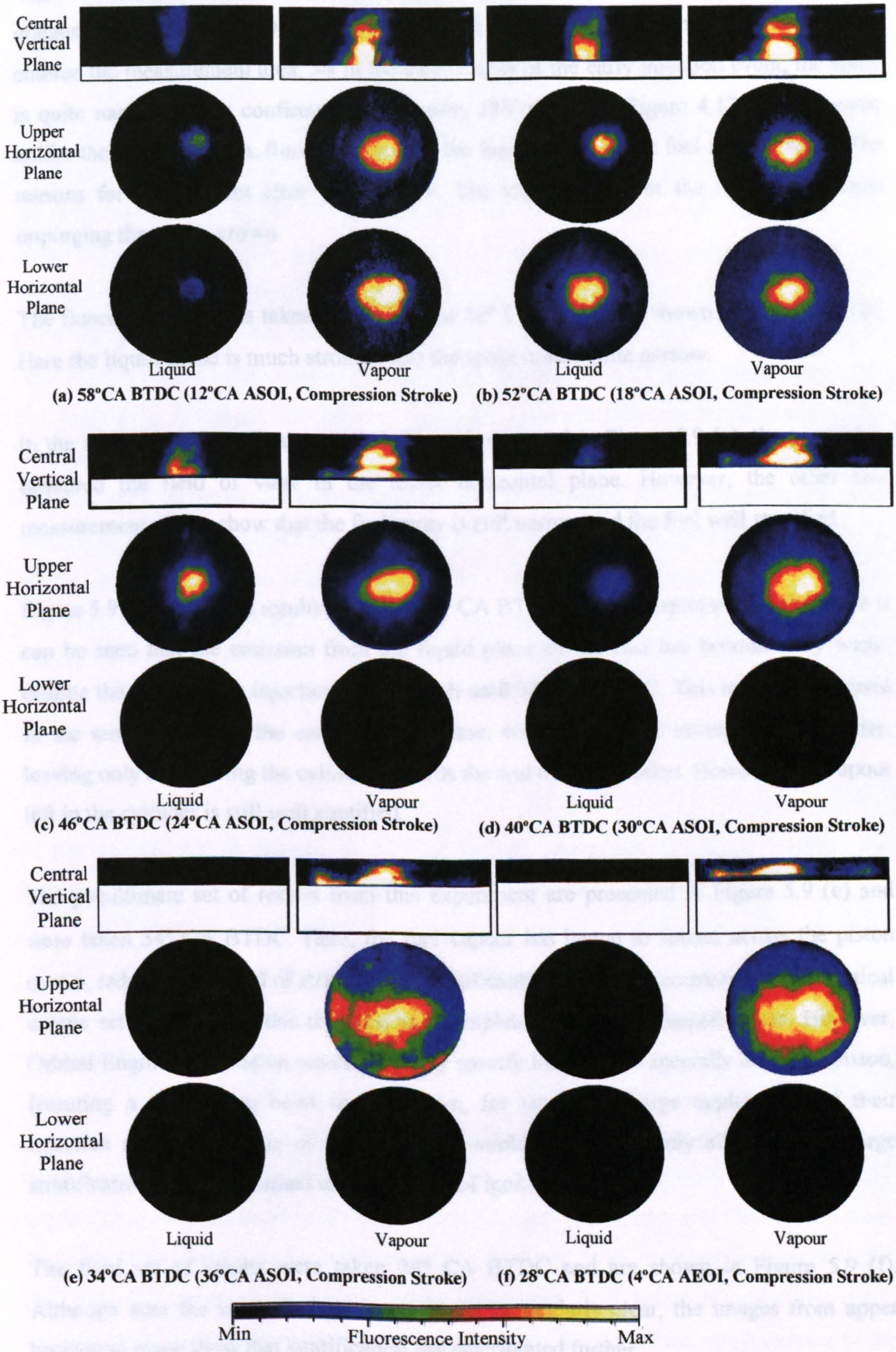

Figure 5.9 LIEF Results with Late Injection Timing in Central Vertical, Horizontal Upper and Horizontal Lower Planes using Laser Sheet

Figure 5.9 (a) presents the first set of results obtained with this injection timing. In these images, taken 12° CA ASOI (158° CA BTDC in the intake stroke), the piston has already entered the measurement area. As in the early stages of the early injection event, the spray is quite narrow, a fact confirmed by the spray PIV results in Figure 4.17 (a). However, unlike the early injection, fluorescence from the liquid phase of the fuel is quite weak. The reasons for this are not clear at this time. The vapour phase of the fuel can be seen impinging the piston crown.

The fluorescence images taken 6° CA later at 52° CA BTDC are shown in Figure 5.9 (b). Here the liquid phase is much stronger and the spray is still quite narrow.

In the next set of results, taken at 46° CA and presented in Figure 5.9 (c), the piston has obscured the field of view in the lower horizontal plane. However, the other two measurement planes show that the fuel spray is still narrow and the fuel well stratified.

Figure 5.9 (d) shows the results obtained 40° CA BTDC in the compression stroke. Here it can be seen that the emission from the liquid phase of the fuel has become very weak, despite the fact that the injection didn't finish until 32° CA BTDC. This may be explained in the same way as in the early injection case, with all the fuel having left the cavity, leaving only air entering the cylinder towards the end of the injection. However, the vapour left in the cylinder is still well stratified.

The penultimate set of results from this experiment are presented in Figure 5.9 (e) and were taken 34° CA BTDC. Here, the fuel vapour has begun to spread across the piston crown, reducing the level of stratification significantly. Due to the constraints of the optical engine set up available, this research was completed with a flat topped piston. However, Orbital Engine Corporation would normally specify the use of a specially designed piston, featuring a fairly deep bowl in the crown, for stratified charge applications of their injection system. The use of such a piston would almost certainly allow better charge stratification to be maintained until the point of ignition.

The final set of results were taken 28° CA BTDC and are shown in Figure 5.9 (f). Although here the vertical plane image is not particularly clear, the images from upper horizontal plane show that stratification has deteriorated further.

5.7.2 Results with Expanded Beam

5.7.2.1 Late Injection Timing

Figure 5.10 shows sets of ensemble averaged results at different crank angles. For each crank angle an average was taken over 20 cycles and in each case background light from the laser has been removed. The fuel injector was located in the centre just out of view along the top edge of the image. The area shown in the image represents the whole viewable area of the transparent liner section and measured 30mm x 75mm. The results cover the period from when the injected fuel first becomes visible (12° CA after the SOI) until 24° CA BTDC where intrusion of the piston prevents further images being taken.
For each set of 8 images, the top row shows fluorescence from the liquid phase of the dopants, while the bottom row shows fluorescence from the vapour phase. The first two columns show the results when illuminating from the left-hand side (LHS) and right hand side (RHS). The third column is an average of the LHS and RHS images while the column on the far right shows the results obtained when illumination was provided from below. The white area at the bottom of most images represents the intrusion of the piston into the field of view.

In Figure 5.10 (a), fuel can be seen entering the field of view from the top. Both liquid and vapour phases are present.

In the second set of images at 58° CA BTDC, presented in Figure 5.10(b), the encroachment of the piston into the field of view can be seen.

Figure 5.10 (c) shows the fluorescence images from 55° CA BTDC, 15° CA ASOI. In the image with illumination from below, the vapour phase can be seen beginning to impinge the piston crown.

In Figure 5.10 (d), taken at 52° CA BTDC, the impingement of the spray onto the piston crown can be seen in all images. It is also at this point that some attenuation of the signal appears to become apparent in the vapour phase images. The image with illumination from the left appears brighter on the left-hand side of the spray. With illumination from the right hand side the situation is reversed. When illuminated from below however, the spray appears to be much more symmetrical, and the upper section of the spray appears to be thinner than when illuminated from either side, suggesting laser attenuation is present here also. This attenuation of the fluorescence signal in areas away from the point of entry of

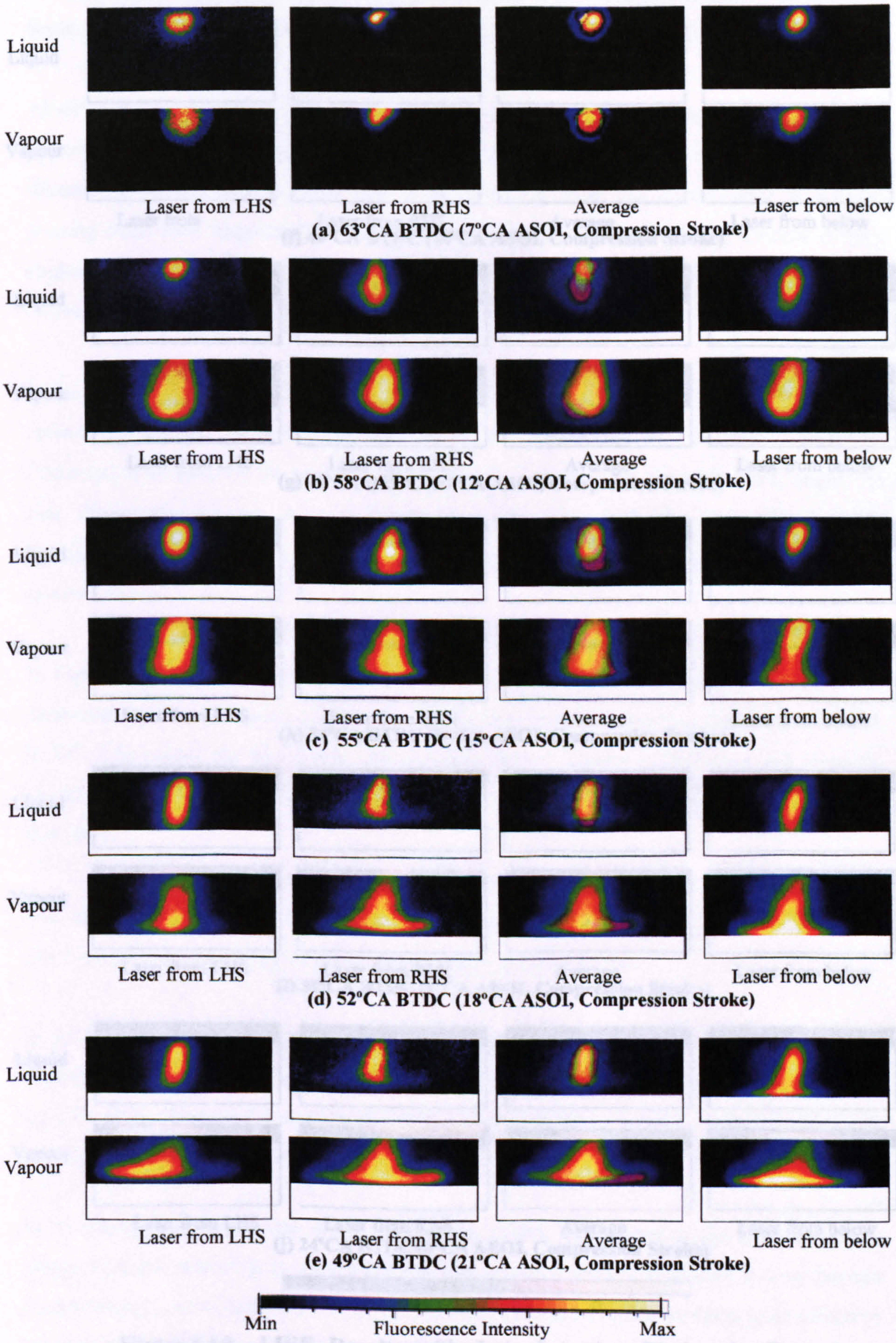

Figure 5.10 LIEF Results with Late Injection Timing in Central Vertical Plane using Expanded Laser Beam

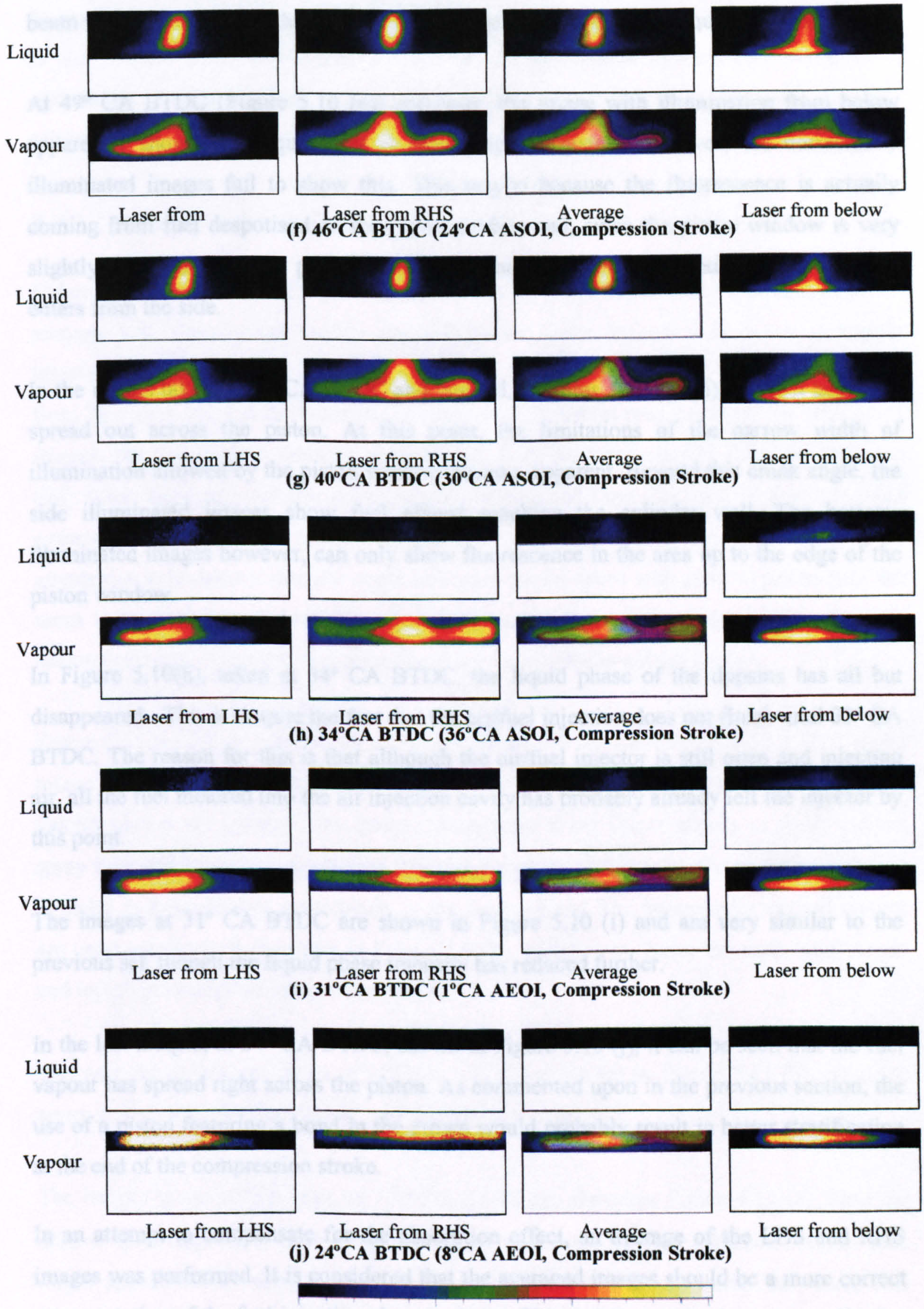

Figure 5.10 LIEF Results with Late Injection Timing in Central Vertical Plane using Expanded Laser Beam (Contimued)

the laser and behind dense areas of spray points to a problem of absorption of the laser beam as it passes through the spray. This can also be seen in all subsequent images.

At 49° CA BTDC (Figure 5.10 (e)) and later, the image with illumination from below apparently shows that liquid fuel is impinging the piston. However, the horizontally illuminated images fail to show this. This maybe because the fluorescence is actually coming from fuel despotised on the piston surface and, since the piston window is very slightly recessed from the piston crown, may not experience excitation when the laser enters from the side.

In the results taken at 46° CA BTDC and beyond, (Figures 5.10 (f)-(j)), the fuel begins to spread out across the piston. At this point, the limitations of the narrow width of illumination allowed by the piston window become apparent. Beyond this crank angle, the side illuminated images show fuel almost reaching the cylinder wall. The bottom-illuminated images however, can only show fluorescence in the area up to the edge of the piston window.

In Figure 5.10(h), taken at 34° CA BTDC, the liquid phase of the dopants has all but disappeared. This is despite the fact that the air/fuel injection does not finish until 32° CA BTDC. The reason for this is that although the air/fuel injector is still open and injecting air, all the fuel metered into the air injection cavity has probably already left the injector by this point.

The images at 31° CA BTDC are shown in Figure 5.10 (i) and are very similar to the previous set, though the liquid phase intensity has reduced further.

In the last images, at 24° CA BTDC, shown in Figure 5.10 (j), it can be seen that the fuel vapour has spread right across the piston. As commented upon in the previous section, the use of a piston featuring a bowl in the crown would probably result in better stratification at the end of the compression stroke.

In an attempt to compensate for the absorption effect, an average of the LHS and RHS images was performed. It is considered that the averaged images should be a more correct representation of the fuel injection characteristics. This technique is perhaps most effective when applied to the vapour phase during the later stages of the injection.

Examination of the last few image sets in Figure 5.10 shows that the attenuation appears to be caused by high densities of vaporised fuel rather than liquid, since here the liquid phase is not present. From inspection of the later images, it also appears that the level of attenuation increases as TDC is approached. This can be explained by the higher densities of fuel vapour present as a result of the reduction in cylinder volume.

5.7.2.2 Early Injection Timing

Figure 5.11 shows the LIEF fluorescence results obtained when using the early injection strategy with illumination via the expanded laser beam. Images were taken at regular intervals throughout the injection event. Again, at each crank angle, images were taken from 20 cycles and it is the ensemble average of these that is presented here. In each set of images, the first column features images taken with the laser entering from the left-hand side, while the centre column shows images illuminated from the right. In the right hand column the images were taken with the laser entering from below. Interestingly, the attenuation experienced with the expanded beam results taken with early injection does not seem to be a serious problem here due to the lower fuel vapour concentration. For this reason averaging of the left and right illuminated images was not performed.

Figure 5.11 (a) shows the first set of results, taken 10°CA ASOI at 130°CA ATDC in the intake stroke. Here the spray can be seen entering the cylinder and both the liquid and vapour phases are present. The images illuminated from below appear to show a fatter spray than the others do. In addition, the spray appears to have penetrated further into the cylinder in these images, particularly in the liquid phase. The horizontally excited images are quite similar with the those in Figure 5.9 (b), which were taken the same crank angle and injection timing but using a laser sheet.

The next set of images, taken at 140°CA ATDC are shown in Figure 5.11 (b). Here the spray is slightly wider than before, particularly at the top.

The images taken 10°CA later, at 150°CA ATDC are shown in Figure 5.11 (c). Here the narrow spray appears to have developed into a wide cone. At first glance the results here might appear a little confusing, since the expanded beam should excite the whole fuel spray, not just one plane as it appears here. However, as discussed in Section 5.6.1.2, serious internal reflections from laser meant that the beam width had to be reduced to 45mm. Scaling against the width of the measurement area gives an estimated spray width

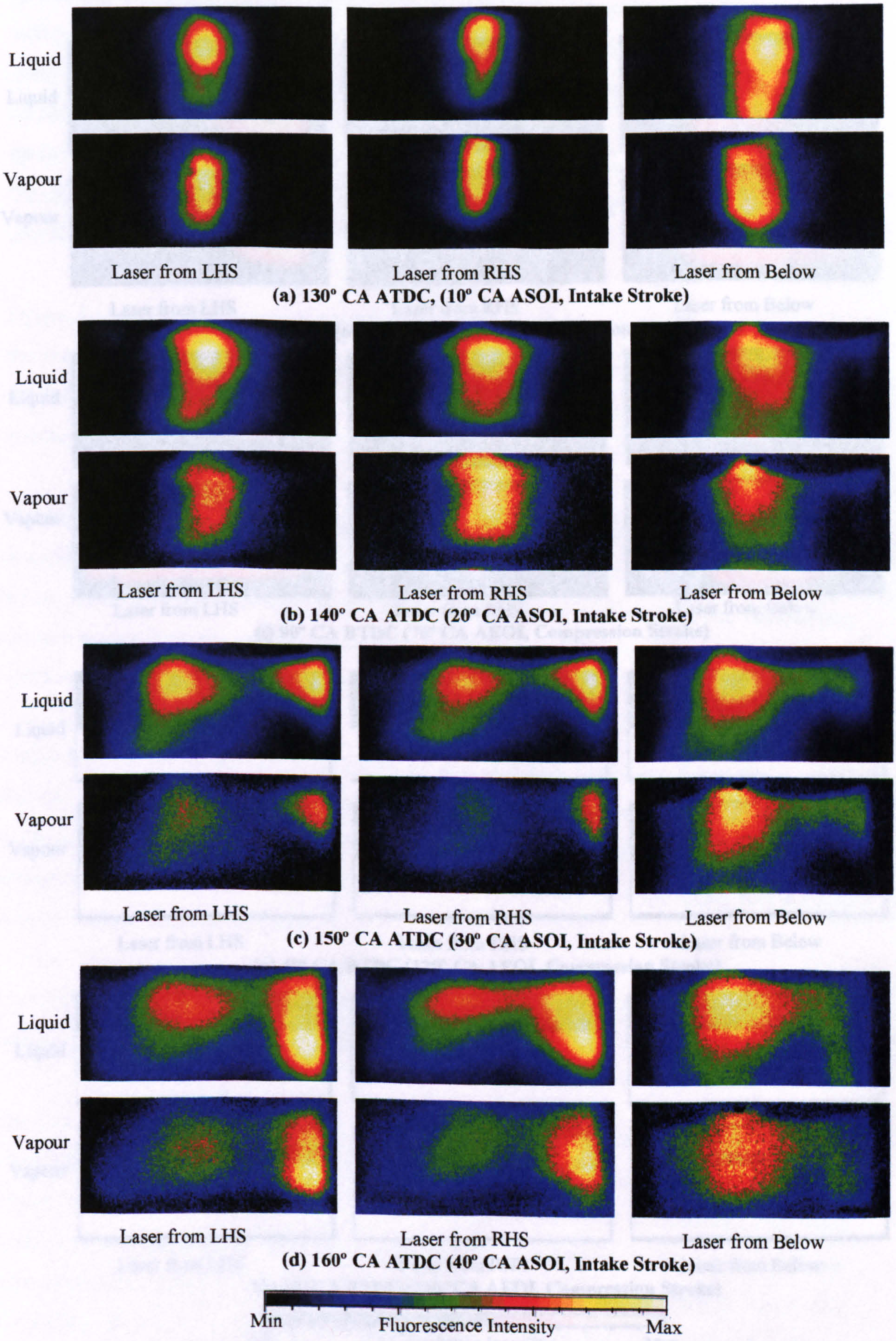

Figure 5.11 LIEF Results with Early Injection Timing in Central Vertical Plane using Expanded Laser Beam

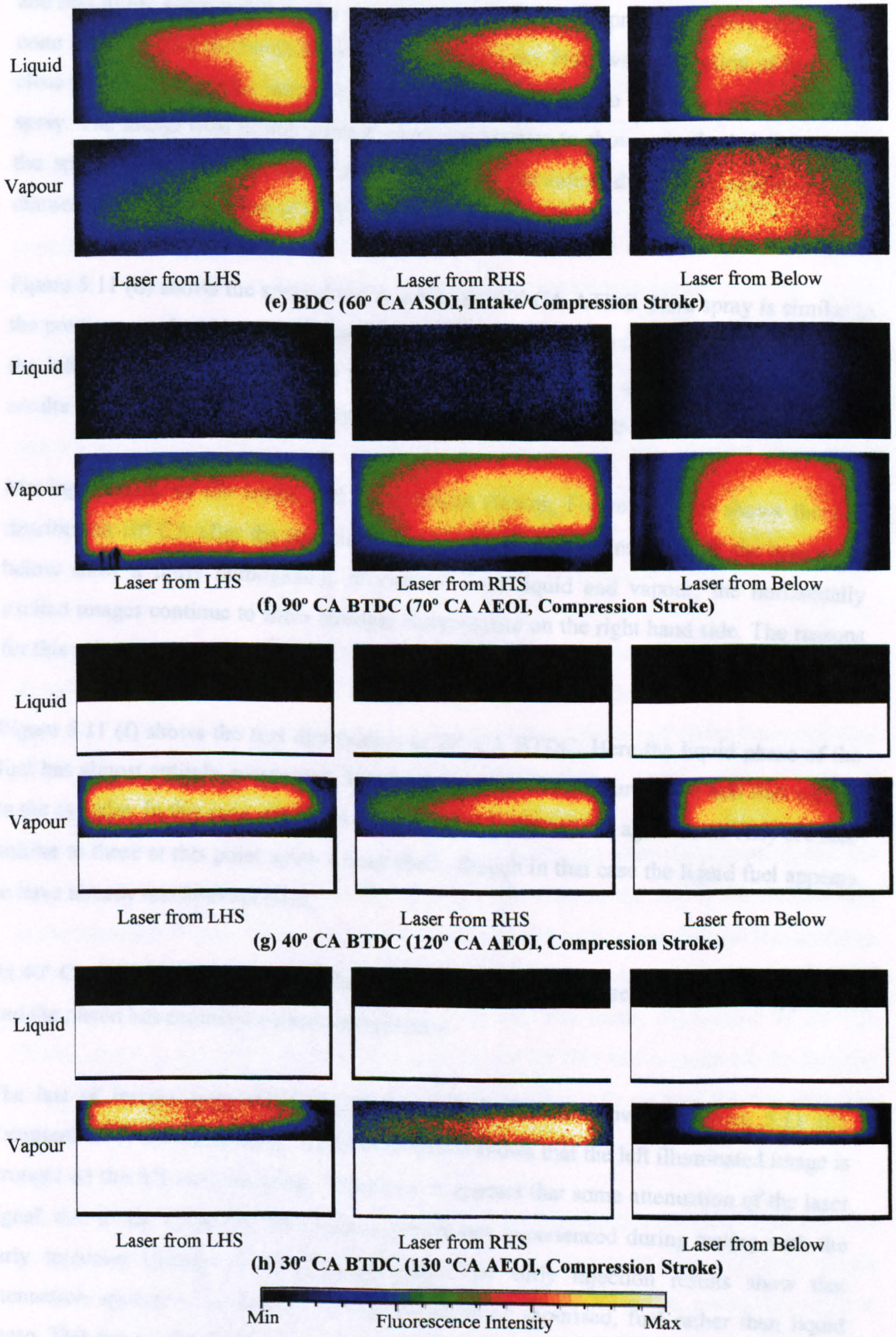

Figure 5.11 LIEF Results with Early Injection Timing in Central Vertical Plane using Expanded Laser Beam (Continued)

at this point of approximately 55mm. This would mean that some of the fuel at the front and rear of the spray might not be excited by the laser. If the spray was a very wide hollow cone this may give the result shown in Figure 5.11 (c). However, inspection of the results close to this point using a laser sheet in Figure 5.8 (d), show no sign of a hollow cone type spray. The image with illumination from below appears to show only the left-hand leg of the spray, while the right hand one has escaped excitation due to the restricted beam diameter caused by the size of the piston window.

Figure 5.11 (d) shows the spray 40° CA ASOI at 160° CA ATDC. Here spray is similar to the previous crank angle, though the right hand side of the spray is now much stronger than the left, suggesting that the spray is not symmetrical. Again, consulting the laser sheet results in Figure 5.8 (d) it is not easy to reconcile the 2 image sets.

Moving to BDC of the intake and compression strokes, Figure 5.11 (e) shows the fuel distribution 10° CA after the injection has finished. While the images with the laser from below show a fairly homogenous mixture of both liquid and vapour, the horizontally excited images continue to show stronger fluorescence on the right hand side. The reasons for this are not clear.

Figure 5.11 (f) shows the fuel distribution at 70° CA BTDC. Here the liquid phase of the fuel has almost entirely evaporated, leaving a homogenous mixture of air and fuel vapour in the cylinder. In this case, results from each set of images are in agreement. They are also similar to those at this point using a laser sheet, though in that case the liquid fuel appears to have already totally evaporated.

At 40° CA BTDC, Figure 5.11 (g) shows that that the liquid phase has totally disappeared and the piston has entered the measurement area.

The last of images were taken at 30° CA BTDC and are shown in Figure 5.11 (h). Examination of the horizontally illuminated results shows that the left illuminated image is stronger on the left and visa versa. Therefore, it appears that some attenuation of the laser signal, due to absorption by the dopants, which was experienced during testing with the early injection strategy is also present here. The early injection results show that attenuation appears to be caused by high densities of vaporised, fuel rather than liquid phase. This means that attenuation is most likely to occur near the end of the compression stroke, when the density of vaporised fuel, is highest as is found here.

5.8 Summary

A laser induced exciplex fluorescence system has been set up and used to examine the in-cylinder fuel distribution in a single cylinder optical engine with a prototype cylinder head fitted with an air assisted injection system. Using the LIEF system, images of injected fuel in both its liquid and vapour phases were obtained. Two means of illumination were assessed. Initially, the dopants were excited using a laser sheet to give images of a thin plane passing through the spray. However, in attempt to obtain images of the whole spray structure, illumination was then completed using an expanded laser beam.

In order to assess the performance of the fuel injector under different engine operating conditions, experiments were completed using two different injection timings: The first was intended to simulate part load condition with stratification with injection taking place in the late stages of the compression stroke. The second timing used was intended to represent a full load operating condition, with injection beginning in the intake stroke in order to provide a homogenous charge at the end of the compression stroke.

During the tests with the late injection timing and expanded laser beam, problems were encountered with attenuation of the laser light due to absorption by the fluorescing dopants. For this reason the experiment was carried out 3 times with laser beam entering the cylinder from a different direction on each occasion.

The results from the tests with the late injection timing and laser sheet showed that the spray was quite narrow throughout the injection. However, as the end of the compression stroke approached some of the stratification was lost although it was felt that this could be improved by using a piston with a bowl in the crown. The results from each measurement plane agreed quite well. The liquid phase of the fuel had totally evaporated by 34° CA BTDC, 2° CA before the injection had ended. It was felt this was because all the fuel had already left the injector pre-cavity by this point, meaning only air was flowing from the injector.

When using the early injection timing and laser sheet the results were quite different. The spray was initially quite narrow but quickly developed into a wide cone. However, details of the spray are not easy to extract from the results at this point, partly due to poor agreement between the results from each measurement plane, the cause of which has not been identified. As with the early injection case, most of the liquid fuel had evaporated by the end of the injection. The last set of images shows that a fairly homogenous charge is left at the end of the compression stroke.

As already discussed, when using the expanded beam and late injection timing, attenuation of the laser beam was experienced. This appeared to be as result of high densities of vapour fuel than liquid fuel as might be expected since it was at its worst towards the end of the compression stroke when no liquid fuel was present. For this reason, when using the expanded beam the experiments were completed 3 times with the beam entering from a different direction on each occasion. As with the early injection tests using the laser sheet, the fuel spray was quite narrow throughout the injection. However, the use of expanded beam yielded some fairly different results, particularly towards the end of the injection period. The main differences noted are the extra details as the spray begins to impinge the piston crown.

Averaging the left and right illuminated images appears effective means of approximating the true spray shape when severe laser attenuation is present. It offers the means to at least partially overcome the problem of laser absorption, without the need to supply the beam from both directions simultaneously, as it has been in previous studies [68-70]. The attenuation was only found to be a problem when using the expanded beam, since here the laser energy density is much lower than the laser sheet. However, when using the early injection timing in conjunction with the expanded beam, only very mild laser attenuation suffered at the end of the compression stroke. This was surprising, since these tests used 3 times more fuel than the early injection, meaning that density the of absorbing molecules should also be higher. However, when using the early timing, the charge was more homogenous, meaning that some of this fuel may have escaped excitation by the laser beam.

When using the expanded beam with illumination from below, the liquid image apparently shows that liquid fuel is impinging the piston, while the horizontally illuminated images fail to show this. This maybe because the fluorescence is actually coming from fuel despotised on the piston surface and, since the piston window is very slightly recessed from the piston crown, may not experience excitation when the laser enters from the side.

The phenomena of cross talking between the liquid and vapour phases must be considered when using the exciplex technique. Although the peak emissions from the two phases are sufficiently apart to allow their spectral separation, the distribution of the fluorescence signal from both phases either side of the peak is wide enough to cause them to overlap, see Figure 5.4 (a). The typical symptom of this problem is appearance of the much stronger liquid fluorescence signal on vapour side. The appearance of the vapour signal on the liquid side is highly unlikely because of the large amount of attenuation, in the form of neutral density filters, employed the liquid side. Inspection of results where the emission from the two phases is significantly different can show that cross talking is not occurring to any significant degree. Unfortunately, since during the injection, distinct areas of vapour are unlikely to appear away from liquid fuel, determining if cross talking is significantly affecting the results can be problematic. However, differences between the images of the two phases can be seen in many of the results, suggesting that cross talking is not a serious problem in this case.

As already discussed, when using the late injection strategy, the fuel spray maintains a narrow profile, helping facilitate good stratification at the point of ignition. However, when using the early injection timing, the spray quickly develops into a wide cone, providing a well-mixed, homogenous charge at the end of the compression stroke. This change of spray shape is a function of the cylinder pressure during the injection period.

During the analysis of the results, some anomalies were found to exist between the different measure planes and illumination methods the reasons for which are not clear. It is felt that the experiments would need to be repeated, while paying extra attention to these problems, to provide answers to this.

Chapter 6

Experimental set-up and Data Analysis for CAI and SI Engine Tests

Chapter 6 Experimental Set-up and Data Analysis for CAI and SI Engine Tests

6.1 Introduction

This chapter details the fired experimental tests completed with the engine in CAI and SI modes. The modifications made to the engine are discussed along with details of the extra equipment used and analytical data processing techniques employed.

SI engine tests were completed on the same engine across a similar load range to allow direct comparisons with CAI combustion to be made. Regardless of combustion mode, tests were completed at engine speeds of 1200 RPM and 2400 RPM while the air/fuel ratio was maintained at λ=1.0. Tests were completed with standard unleaded pump gasoline fuel of RON 95 (BS EN 228).

6.2 Engine Set-up

6.2.1 Introduction

All previous work for this project has been carried out with the engine in a configuration featuring optical accesses. Because of the limited mechanical strength of the engine in this form, it is not possible to fire the engine or run it at anything other than low speeds. For this reason all previous optical work was carried out with the engine under the motored condition only and at 1200 RPM. In order to carry out the CAI and spark ignition tests, the engine required substantial modification to allow it to be fired and run at higher speeds.

The work consisted of the removal of the extended cylinder block and piston and the design and fitment of a sandwich adapter plate to allow the cylinder head to be mounted directly to the lower cylinder block. In addition, it was necessary to design and manufacture a new cylinder liner, fit a new lower piston and manufacture and fit a modified little end bearing to the connecting rod. Modifications to the camshaft belt drive, oil and water connections and exhaust system were also required. A throttle and plenum chamber were also added to the intake during spark ignition operation.

6.2.2 Sandwich Adapter Plate

The mounting holes of the Orbital cylinder head did not align with those already in the cylinder block. In addition, the cylinder head mounting holes overlapped with the cylinder block holes so it was not possible to simply drill and tap the cylinder block to suit. It may have been possible to plug the existing holes in the cylinder block and re-drill and tap them with the required pattern but this would have meant that refitting of the extended cylinder block or other cylinder heads at a later date would be very difficult. Therefore, a sandwich adapter plate was designed and manufactured that would not require any detrimental modifications to be made to the cylinder block. Figure 6.1 shows a sectional view through the sandwich plate assembly (see Figure A3 in Appendix A for the detailed drawing). It consists of a steel plate approximately 20mm thick that is bolted to the cylinder block with counter-bored bolts. The holes for these bolts were drilled and tapped directly into the cylinder block and were located at positions towards its edge that would be unlikely to interfere with the mounting bolts of any cylinder head that may be fitted in the future. The mounting holes for the cylinder head itself were then drilled and tapped into the sandwich plate. A particularly useful feature of this method is that the fitting of alternative cylinder heads requires only the manufacture of a suitable adapter plate with the required mounting bolt pattern.

A water-cooling channel is incorporated in the sandwich plate to allow cooling of the top section of the cylinder liner. Coolant flows from the cylinder head into the sandwich plate and returns to the cooling system via an outlet located on one edge.

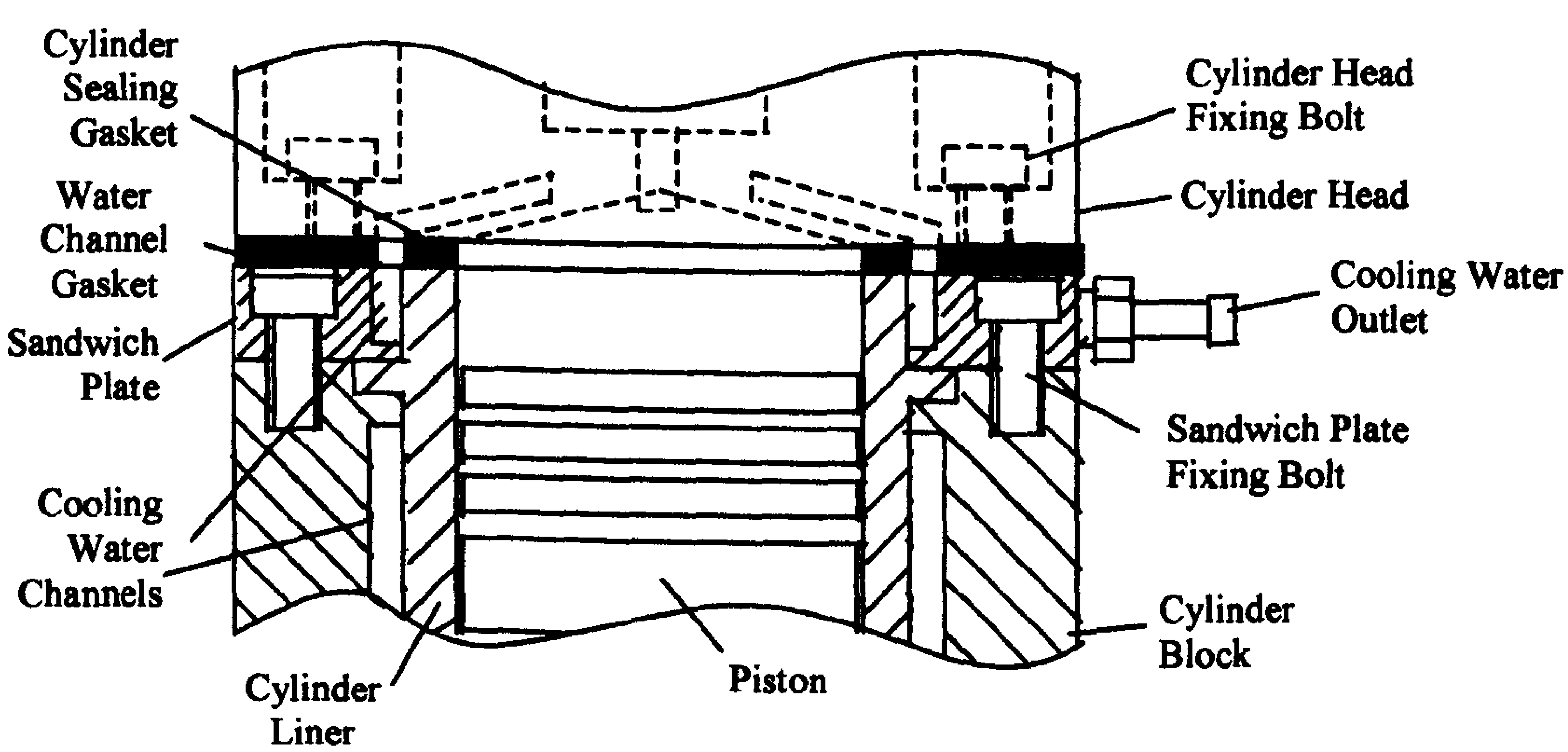

Figure 6.1 Sandwich Adapter Plate Arrangement

6.2.3 Cylinder Liner and Piston

The addition of the sandwich plate to the top of the cylinder block meant that the original cylinder liner and piston no longer reached the cylinder head deck surface. In order to rectify this, a longer cylinder liner was designed and manufactured and another more suitable piston sourced. Figure 6.1 shows a sectional view through the new assembly.

The original cylinder liner was located and fixed at its upper end by a step section that sat in a recess in the top of the cylinder block so that the top surfaces of both were flush. The liner was then held in its vertical direction by the clamping force of the cylinder head bolts. In the design of the new liner, this location method was retained but an extra section was added to the top of the liner to allow it to be flush with top surface of the sandwich plate. In the new configuration the vertical location of the liner is provided by the clamping force of the sandwich plate mounting bolts rather than the cylinder head bolts. The new liner was manufactured in the university workshops from a cast iron billet. Following the boring of the liner the running surface was honed using a 3-legged honing tool known as a 'glaze buster'. This removes the small ridges left by the boring tool and leaves a cross-hatched pattern on the surface that helps to retain oil on the cylinder wall, reducing cylinder leakage and wear.

In order to achieve the desired compression ratio, a new piston that reached the top of the new liner was sourced from Ricardo Consulting Engineers. The original cylinder block had an 86mm bore. The installation of the new liner reduced the cylinder bore to 80mm, which is the same as that of the extended cylinder block used in the previous optical engine experiments. The only modification required to the new piston was the removal of 3mm of material from the skirt to avoid contact with the main engine block around BDC. However, the gudgeon pin diameter of the new piston was smaller than the existing one. One option was to attempt to bore the piston to accept the existing gudgeon pin (and connecting rod). However, this could have proved to be very problematic due to the very high tolerances that have to be maintained between the piston and gudgeon pin. Instead, a new connecting rod bearing was manufactured and pressed into the connecting rod, allowing the gudgeon pin supplied with the new piston to be used.

6.2.4 Gasketing

Successful sealing of the cylinder head/sandwich plate joint proved to be a considerable challenge. The easiest and most obvious option was to use a section of head gasket from a multi-cylinder automotive engine with a similar bore size. However the relatively close bore centres of this type of engine meant that it was not possible to seal the water-cooling channel with this type of gasket. The silicon rubber gasket material used during the optical work could not be used due to the higher temperatures and pressures encountered within a fired engine. Initial attempts using high temperature Klingersil gasket material only lasted for a few fired cycles before being destroyed by the high temperature and pressure. Copper gaskets of various thicknesses were then manufactured and tested but proved to be insufficiently compressible to allow a seal to be made. The final solution was to cut the central 'cylinder sealing' section from an automotive gasket of the correct bore and use this to seal the cylinder and coolant channel junction. A second separate gasket made from a highly compressible high temperature gasket material slightly thicker than that of the 'head gasket' was then used to seal from the cooling channel to the outside.

The joint between the sandwich plate and cylinder block was sealed using Hermatite Instant Gasket sealing paste. The use of a conventional gasket at this point was not possible since its presence would interfere with the relationship between the height of the sandwich plate and the cylinder liner, making it very hard to achieve a good seal at the head gasket joint.

6.2.5 Fuel Supply System

Although the fuel and air injectors and control system used for the fired tests were the same as those used for the optical work, the method of supplying the fuel was different. For the fired tests, using regular gasoline, the use of a fuel pump was possible and much more convenient with respect to refuelling and control of fuel and air pressures. A schematic of the fuel system used for the fired tests is shown in Figure 6.2.

As with the optical work, the air injector was supplied from a compressed gas bottle, though in this case air rather than nitrogen was used. The compressed air supply was connected directly to the injector. The return from the injector was then connected to the regulator block. The supply pressure from the bottle was set just higher than the regulators' rated pressure so a small amount of air was continuously dumped to atmosphere.

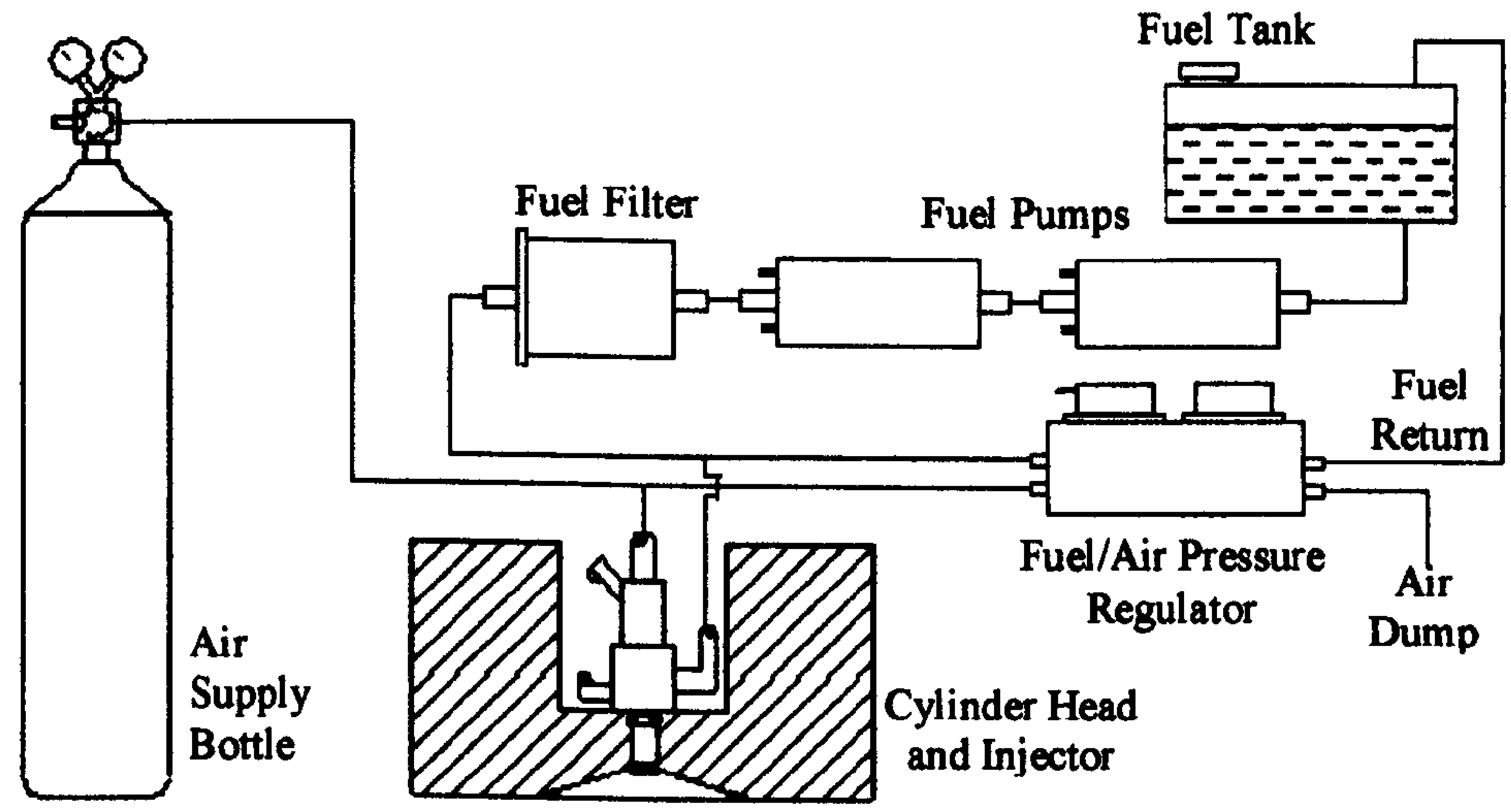

Figure 6.2 Schematic Diagram of the Fuel Supply System

However, care had to be taken to ensure that the supply pressure from the bottle was set correctly. If the supply pressure was set too high then the regulator may not have been able to dump sufficient air and the pressure at the injector would be too high. A permissible flow rate range for the amount of air dumped from the regulator was supplied by Orbital but equipment to measure this very low flow rate was not available. Instead, the supply pressure was set by monitoring the supply pressure to ensure that the regulator was always functioning within its operating range. As with the optical work, the air injector supply pressure (and hence injection pressure) was set to 6.5 bar.

The fuel pressure was set at 1.5 bar higher than the air pressure, the same as for the optical work meaning a supply pressure of over 8 bar was required. During the development of the fuel supply system it was found that a conventional PFI fuel pump was not capable of providing this supply pressure. Since no high-pressure pump was immediately available a second, identical pump was used in series with the first to boost the supply pressure to the required level. After leaving the pumps, the fuel passed to the injector via a filter. As with the air supply, the return from the injector was connected to the regulator block. However, unlike the air supply that takes it reference pressure from the atmosphere, the fuel regulator takes its reference pressure from the air supply pressure. In this way the fuel pressure is always controlled relative to the air pressure. The main reason for doing this is to ensure that the pressure across the fuel injector is always constant, thereby allowing it to be accurately calibrated. If for any reason the air pressure varies slightly the calibration will be preserved.

6.2.6 Injector Calibration

To allow the fuel consumption of the engine to be measured during the tests the fuel injector was calibrated using the following procedure:
The fuel injector was removed from the engine, leaving the air injector in place. The fuel system was then pressurised as normal but the 'air-side' of the system was left unpressurised. This ensured that pressure across the injector was the same as it would be during normal engine operation. The fuel injector was electrically connected to its driver as normal. In order to collect the injected fuel with minimum loss from either evaporation or splash back, the injector nozzle was then pushed into a hole that had been made in the lid of a small glass jar. The jar had been weighed previously and the scales tarred to this weight. With the injector duration set at the minimum setting that produced a visible injection (and the value noted) the engine was then run with the injector switched off until a stable speed of 1200 RPM was achieved. The injector was then switched on for 2 minutes and the injected fuel collected in the jar. The injector was then removed and the jar weighed to determine the mass of fuel injected.

The following calculation was then performed:

$$\text{Mass of fuel injected per engine cycle} = \frac{\text{Total mass of fuel collected}}{\text{20RPS x 120 seconds}}$$

The procedure was then repeated for different injector durations at regularly spaced intervals until a calibration line for the injector had been determined. This calibration curve can be found in Figure B1 in Appendix B

6.2.7 Engine Modifications for CAI Operation

Once the engine build was complete it was run briefly in spark ignition mode to test the various control and measurement systems. Once everything was working satisfactorily the engine was then dismantled again to prepare it for CAI operation.

The only modification needed to achieve CAI combustion was the fitment of short duration/low lift intake and exhaust camshafts. The special camshafts were produced by regrinding production items from a 1.6l Ford Zetec engine the required profile. Since these were originally intended for a four cylinder application, only the lobes for 'Cylinder No 1.' were modified and the superfluous portion of the camshaft, beyond the second bearing journal, was subsequently removed. Since the engine load would now primarily be controlled by the valve timing, the intake throttle was removed and replaced with a plain intake runner

6.3 Additional Measurement Systems for Fired Work

6.3.1 Introduction

During the experiments, measurements were taken to allow engine load, fuel consumption, exhaust emissions, air/fuel ratio, exhaust gas temperature and various combustion characteristics to be determined.

The equipment consisted of a cylinder pressure transducer and associated PC computer based data acquisition system, three exhaust gas analysers and a thermocouple located in the exhaust port. In addition a load cell integrated into the dynamometer was used to measure the brake torque output of the engine.

6.3.2 In-Cylinder Pressure Data Acquisition System

In-cylinder pressure measurement is a popular and powerful means of quantifying many operating characteristics of IC engines. This includes information on combustion phasing, such as ignition timing, burn duration and instantaneous burn rates. In addition it allows the identification of knocking combustion and misfires as well as providing insight into the gas exchange process. Analysis of pressures exerted as a result of combustion over a number of cycles can lead to accurate determination of engine load and cycle to cycle variation.

The real time in-cylinder pressure data acquisition system described below has proved to be an invaluable tool in the characterisation of the combustion process in this part of the project. In addition, it has proved to be a very useful diagnostic tool with respect to trouble shooting and development of the various control and measurement systems.

6.3.2.1 Pressure Transducer

A Kistler type 6055 piezo electric pressure located in the cylinder head was used to measure the in-cylinder pressure. It had a measurement range of 0-100 bar gauge and a sensitivity of –6 PC/bar. Normally when installing an in-cylinder pressure transducer in a production type engine a special tapping has to be made in the cylinder head. This retrofitment can sometimes prove less than straightforward due to lack of space in the combustion chamber and the presence of cooling channels and oilways. Since the Orbital cylinder head used was a prototype manufactured specifically for research, it already had a tapping made specifically for this purpose. The pressure transducer was mounted on the centreline on the pulley side of the cylinder head and entered the combustion chamber between the intake and exhaust valves. It was connected to a charge amplifier (Kistler Type 501) via a high impedance cable. The charge amplifier is used to convert the electric charge generated by the transducer into a voltage and amplify it so it can be used as an input to the data acquisition system.

The output of the charge amplifier must be calibrated so that it produces a known voltage for a predetermined pressure at the transducer and this was performed using a dead weight testing machine. This machine uses mass placed upon a piston to pressurise a hydraulic circuit. With the transducer connected to this circuit, mass producing a known pressure can be applied and the resulting voltage output from the charge amplifier measured with an oscilloscope. After applying a range of masses to determine the linearity of the transducer over its full measurement range a suitable calibration factor can be determined and applied to the charge amplifier. In this case the charge amplifier output was adjusted to correspond to 10 bar/V over a range of 0-100 bar and the time-constant was set to long during the calibration tests. Since, even in the most extreme cases, the in-cylinder pressure of an SI/CAI engine is unlikely exceed 60 bar, this calibration should prove suitable for all testing situations. In order to account for the rapid change in pressure, the time-constant of the charge amplifier was changed to short when in-cylinder measurements were carried out.

6.3.3 In-Cylinder Pressure and Heat Release Analysis

6.3.3.1 In-Cylinder Pressure Measurement

The data acquisition system is a PC based device that allows real-time display and recording of crank angle resolved in-cylinder pressure data. An input of in-cylinder pressure is taken from the charge amplifier and phasing information is provided by the clock and reference signals from the crankshaft encoder and camshaft position sensor. As discussed in Chapter 3, a crankshaft encoder and camshaft hall effect sensors and associated logic box are also used to provide clock and reference signals for the fuel injection, spark ignition, laser and camera systems. The clock signal provides the in-cylinder pressure sampling interval (in this case 1° CA) and the reference pulse is used to determine the phasing of that data with respect to the 4-stroke engine cycle.

The three signals are connected to the data acquisition card installed in the PC via a National Instruments BNC 2110 interface unit. The data acquisition card used is a National Instruments PCIMIO16-1 and is installed in a Pentium II PC running at 400 MHz.

The program used for the in-cylinder pressure display and logging was written by John Williams, formally of Brunel University, using National Instruments Labview software. In addition to recording pressure data the program is capable calculating and logging many other parameters such as IMEP, COVimep and heat release rate. It can also display p-V and p-CA diagrams in real time. However, in this case it was used only to collect and display crank angle and cylinder volume resolved in-cylinder pressure data, with subsequent processing being carried out manually in a Microsoft Excel spreadsheet.

A number of principles of its analytical operation are explained here.

Cylinder Volume Calculation

In order to allow cylinder volume resolved in-cylinder pressure data to be recorded it is necessary for the program to calculate the cylinder volume for each crank angle. This is calculated via the engine geometry, the details of which are entered into the program before testing, using the following formula:

$$V = V_c + \frac{\pi B^2}{4}(\,l + a\,2s\,) \qquad (6.1)$$

where V is cylinder volume, V_c is the clearance volume, B is the cylinder bore, l is the connecting rod length, a is the crank radius and s is the distance between the crank axis and the piston pin axis as defined as

$$s = a\cos\theta + \sqrt{(l^2 - a^2\sin^2\theta} \quad (6.2)$$

where θ is the crank angle relative to the vertical.

Determination of Absolute In-Cylinder Pressure

The pressure signal output from the charge amplifier represents a gauge pressure, i.e. it shows only a pressure difference relative to an arbitrary ground. Before accurate, useful information can be obtained from it the charge amplifier output must first be converted to absolute pressure. The relationship between the output voltage and the absolute pressure at any crank angle θ is defined by

$$E(\theta) = \frac{p(\theta)}{C} + E_b \quad (6.3)$$

where E_b is the bias voltage with zero pressure and C (bar/V) is the calibration factor of the charge amplifier [90].

Therefore, in order to determine absolute pressures, the charge amplifier output must be referenced (or "pegged") to a known pressure somewhere in the cycle. Pegging is possible by a variety of methods and nine of these are discussed by Randolph [93].

The most common method is to assume that the cylinder pressure at intake valve closure (IVC) is equal to the intake manifold absolute pressure (MAP). MAP can then be measured and the system pegged to this pressure at IVC. The absolute pressure at any crank angle can then be determined by

$$p(\theta) = C.(E(\theta) - E_{IVC}) + p_{IVC}$$

where E_{IVC} is the charge amplifier voltage at IVC.

During the CAI tests the in-cylinder pressure was pegged using this method. However, since engine load was controlled via the valve timing it was run unthrottled and no intake manifold was fitted, MAP was assumed to be equal to ambient pressure. Therefore ambient pressure, measured by the laboratory barometer was used as the IVC pegging pressure.

For the SI tests the intake was throttled in order to control engine load. In this case measurement of MAP would have been required to use pegging method described above. However, since the engine was single cylinder and had only a small plenum chamber fitted downstream of the throttle accurate measurement of the MAP was found to be problematic with the equipment available due to the pulsating flow through the throttle. Rather than fit a large plenum chamber, the system was pegged using the forced polytropic coefficient method.

This method is based on the fact that compression in most IC engines follows the polytropic equation, PV^n = constant, where the change in pressure between two points during compression can be determined from:

$$\Delta p = p_1\left[\left(\frac{V_1}{V_2}\right)^n 2 1\right] \tag{6.4}$$

The cylinder volume V at any crank angle θ can be found from Equations 6.1 and 6.2

Using Equation 6.3, the change in pressure between two points can be written as

$$E(\theta) = C\left[E(\theta_2) 2 E(\theta_1)\right] \tag{6.5}$$

Combining Equations 6.4 and 6.5 gives

$$E_b = E(\theta_1) \frac{E(\theta_2) 2 E(\theta_1)}{\left[\left(\frac{V_1}{V_2}\right)^n -1\right]} \tag{6.6}$$

So, for any θ_1 and θ_2, Equation 6.6 defines the bias voltage E_b. However, in order to increase accuracy, three values of θ_1 and θ_2 were chosen and the resulting bias voltages averaged to provide a more representative value. In order to use this method, the polytropic constant n must be evaluated and this was assumed to be approximately equal to the inverse of the gradient of the compression stroke section of the log(P)-log(V) diagram. Therefore the engine was run in spark ignition mode at wide-open throttle (where it was assumed that p_{IVC}= MAP = ambient pressure) and 50 cycles of pressure recorded. This was completed for the test speeds of 1200 RPM and 2400 RPM and the resulting data was then averaged and the log(P)-log(V) diagrams assessed to find a value of n for each speed.

6.3.3.2 Engine Combustion and Heat Release Analysis

Following the collection of in-cylinder pressure data, post-processing calculations were carried out to determine engine output and combustion characteristics. The calculations were performed within a Microsoft Excel spreadsheet.

Calculation of Engine Output

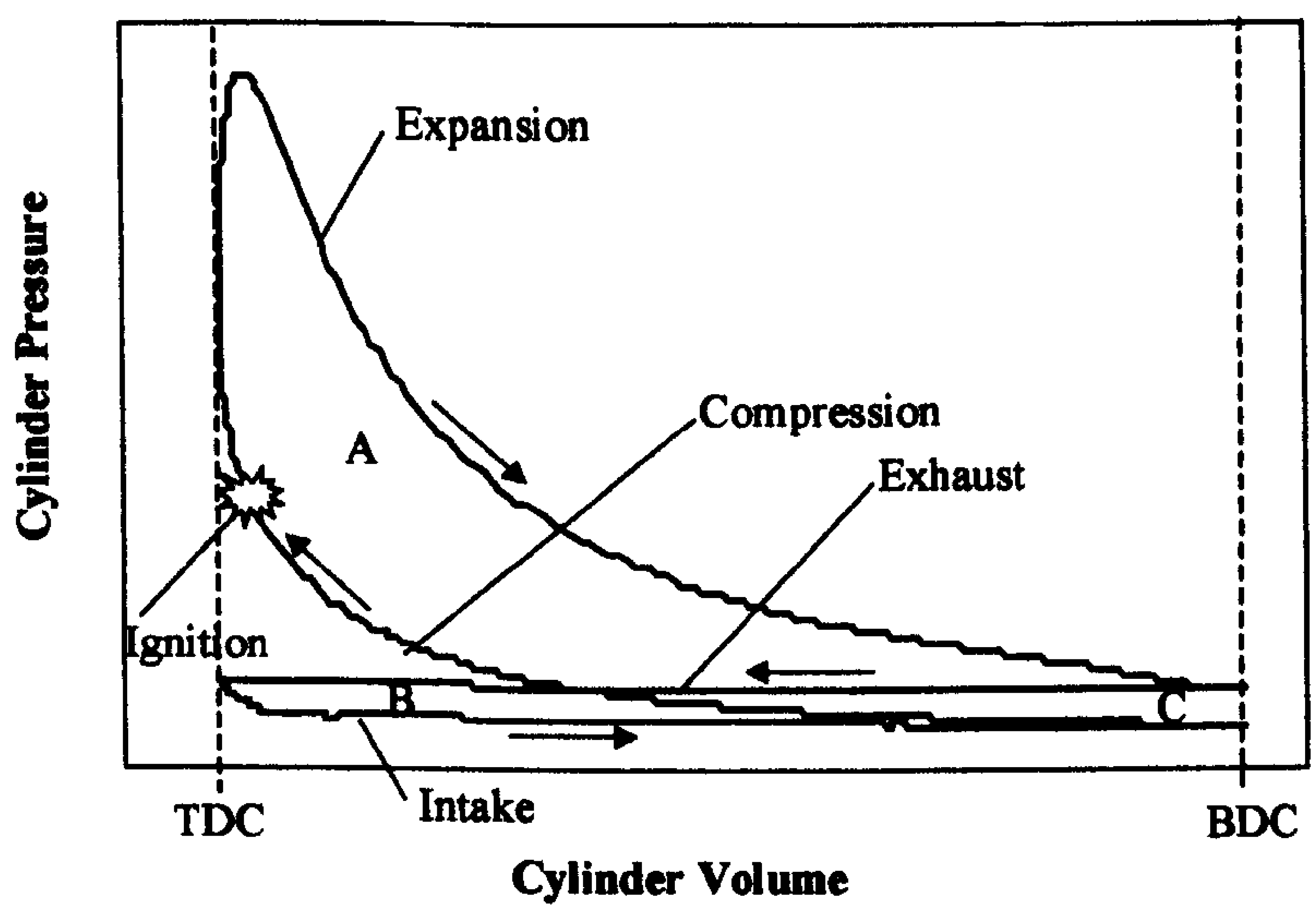

Figure 6.3 Example of a p–V Diagram for a SI Four-Stroke Engine at Part Load

Engine output can be determined from volume resolved in-cylinder pressure data. The resulting property is known as net indicated mean effective pressure (IMEP) and is equal to the area enclosed by the pressure/volume (p–V) diagram over the whole engine cycle. A typical p–V diagram for a four stroke, spark ignition engine running at part load is shown in Figure 6.3. In practical terms, net IMEP is evaluated through numerical integration of the p–V diagram, using a step interval equal to the cylinder pressure sampling interval, in this case 1°CA.

$$\text{Net IMEP} = \frac{1}{V_d} \oint p.dV \qquad (6.7)$$

From Figure 6.3 it can be seen that the p–V diagram has two main areas or 'loops'. The largest describes the pressure and volume changes during the compression and expansion strokes. Work delivered to the piston here is shown as area A + area C and defines the gross indicated work per cycle and is often termed gross IMEP. The smaller loop is made up of area B + area C and shows the work transfer between the piston and cylinder gases during the intake and exhaust strokes and is termed pumping work or pumping mean effective pressure (PMEP). Hence, net IMEP = gross IMEP + pumping work.

If IMEP is calculated for a number of consecutive cycles, a property describing its variability can be developed. This is known as the coefficient of variation of IMEP (COVimep).

$$COV_{imep} = \frac{x\sigma_{imep}}{\sum_{1}^{x} IMEP_i} \qquad (6.8)$$

where x is the total number of cycles for which IMEP values are calculated and σ_{imep} is the standard deviation in IMEP. Since any variation of IMEP corresponds directly to variations in combustion, it is a very useful means of evaluating both combustion stability and torque variation from cycle to cycle.

Heat Release Analysis

Heat release analysis is a very useful method for characterising various parameters related to the phasing of combustion in internal combustion engines. There are two main approaches in use. The Rassweiler and Withrow method estimates the mass fraction burned profile from cylinder pressure and volume data. Here, any increase in cylinder pressure is considered to be caused by the pressure rise due to volume change, Δp_v, and the pressure increase due to combustion, Δp_c

$$\Delta p = \Delta p_v + \Delta p_c \qquad (6.9)$$

However, though simple to use, this method has several limitations. The effect of heat transfer is not fully accounted for and the pressure rise due to combustion is proportional to the chemical energy released rather than the mass of fuel burned. This means that the mass fraction burned profile will always extend from zero at the point of ignition to unity at the end of combustion, regardless of the quality of pressure and fuel flow data or completeness of combustion.

The second method, and the one used in this work, is the one-zone net heat release rate analysis model. This method works by calculating the amount of heat that would need to be added to the cylinder to produce the recorded pressure change. This is achieved by the application of the first law of thermodynamics to the cylinder contents, which can be considered a closed system during combustion.

$$\delta Q_{ch} = \delta U_s + \delta W + \delta Q_{ht} \tag{6.10}$$

where δQ_{ch} is the chemical energy released by combustion, δU_s is the change in sensible energy. The term sensible is used since only changes in *u* or *h* that result from variation in temperature are included. Variation in *h* or *u* due to chemical reaction or phase change excluded. δQ_{ht} represents the heat transfer to the cylinder wall and δW is the work done on the piston by the system and is equal to $pd\mathrm{V}$.

As the combustion chamber is modelled as a single zone, the charge is assumed to be homogenous and of uniform temperature. In addition, the properties of reactants and products are considered to be identical. It can be assumed that

$$U_s = m.u(T) \tag{6.11}$$

where T is the charge temperature and m is the mass within the system. Therefore if crevice volume effects are ignored

$$\delta U_s = mc_v(T)dT \tag{6.12}$$

By substitution into Equation 6.10 and writing on an angle incremental basis

$$\frac{dQ_{ch}}{d\theta} = \frac{mc_v(T)dT}{d\theta} + \frac{pdV}{d\theta} + \frac{dQ_{ht}}{d\theta} \tag{6.13}$$

The first term, $dQ_{ch}/d\theta$ is the apparent heat release rate. Combined with the heat transfer term $dQ_{ht}/d\theta$ to give $dQ_{ch}/d\theta\ 2dQ_{ht}/d\theta$ it describes the net heat release rate, termed $dQ_n/d\theta$. This is the energy release rate due to combustion, minus the heat lost to the walls.

Introduction of the ideal gas law, $pV = mRT$, with R assumed constant, allows further simplification of Equation 6.12. The use of

$$\frac{dp}{p}+\frac{dV}{V}2\frac{dm}{m}=\frac{dT}{T} \qquad (6.14)$$

allows the elimination of T from Equation 6.12 to give

$$\frac{dQ_n}{d\theta}=\frac{\gamma}{\gamma 2 1}p\frac{dV}{d\theta}+\frac{1}{\gamma 2 1}V\frac{dp}{d\theta} \qquad (6.15)$$

where γ is the ratio of specific heats, C_p/C_v. In this way the net heat release rate can be calculated from the measured changes in cylinder volume and pressure but requires the assumption of a value for γ. The value of γ is almost always assumed to be constant with a value in the range 1.3 to 1.35. In reality this value changes throughout the engine cycle due to variations in gas composition and temperature.

The integration of equation 6.15 with respect to crank angle will yield a cumulative heat release function, from which the normalised mass fraction burned (MFB) curve can be obtained. The MFB curve can then be used to quantify a number of very useful parameters of combustion. Table 6.1 lists definitions commonly used to describe the various energy release stages in SI and CAI combustion in relation to MFB.

Table 6.1 Definitions of Energy Release Stages for SI and CAI Combustion

Mass Fraction Burned	Combustion stage	
	SI	CAI
0 2 10%	Flame development angle	2
10%	Start of rapid burn phase	Ignition
10 2 90%	Rapid-burning angle	Combustion duration
0 2 90%	Overall Burn Angle	2
90%	End of combustion	End of combustion

6.3.4 Calculation of Trapped Mass of Exhaust Products

The successful operation of the CAI combustion detailed in this work relies on the trapping of the correct proportion of residual gases within the cylinder using appropriate exhaust and intake valve timings. In order to enable a better understanding of the relationship between the amount of trapped residuals and combustion characteristics, in-cylinder residual rates were estimated.

The method used was employed by Zhao et al [33] on a multi-cylinder PFI engine, using high residual rates to achieve and control CAI combustion. The mass of trapped residuals m_r was estimated by applying the ideal gas law to the cylinder contents at EVC as follows,

$$pV = m_r R T \tag{6.16}$$

The burned gas temperature, T (K), at EVC was assumed to be equal to the temperature measured by the exhaust port thermocouple. The in-cylinder pressure at EVC, P, was measured from the in-cylinder pressure transducer and the cylinder volume at EVC was calculated from the engine geometry and EVC timing. The amount of residuals at EVC will be the total residual mass for the whole cycle since even if there is back flow into the intake ports under some conditions, during steady state operation this gas will subsequently be sucked back into the cylinder. To make the data more useful, the trapped residual mass was expressed as a percentage of the total charge in the cylinder at IVC

$$\text{Trapped residuals (\%)} = \frac{m_r}{m_{fc} + m_r} * 100 \tag{6.17}$$

where the mass of the fresh charge, m_{fc} was determined from the mass of fuel injected per cycle, m_f, and the AFR as follows.

$$m_{fc} = (m_f * \text{AFR}) + m_f \tag{6.18}$$

In the work by Zhao et al the estimated residual rates were compared with those predicted by a one-dimensional gas dynamic model and were found to be fairly similar. However, the residual rates estimated by the ideal gas law were found to correlate better with the other experimental data and hence this was chosen as the preferred method.

6.3.5 Exhaust Emissions

6.3.5.1 CO_2, CO, O_2 and Air/Fuel Ratio Measurement

Concentrations of CO_2, CO and O_2 in the exhaust gas stream were measured by a Horiba MEXA 554JE analyser. This analyser is of the type normally used for the annual mandatory UK Ministry of Transport tests for privately owned cars and light goods vehicles.

Cooled exhaust gas is drawn into the analyser by an integral vacuum pump, via a water trap and a particulate removal filter. Once inside, the gas is divided for analysis into an infrared absorption cell and a galvanic cell. Measurements of CO and CO_2 are performed by a nondispersive infrared (NDIR) absorption cell. It operates by measuring the level absorption of infrared radiation by these gases. The analyser is described as nondispersive since no diffraction of the light is performed and measurements are of total absorption over a given wavelength. Beer's law shows that the amount of radiation absorbed by a species is given by,

$$A_\lambda = 12\exp(2C_i Q_\lambda L) \tag{6.19}$$

Where C_I = the concentration of the species i

Q_λ = the absorption efficiency

L = the optical path length

Figure 6.4 shows the main components of an NIDR analyser. The infrared light source is provided by a heated filament that emits blackbody radiation over a broad band of wavelengths. The radiation first passes through a filter cell that removes any wavelengths that are no absorbed by the gas to be measured. These discrete wavelengths then pass through the sample cell containing the dried sample gas and on to the detector cell. The detector cells are filled with the gas to be measured so that they absorb the radiation in the absorption band of that gas.

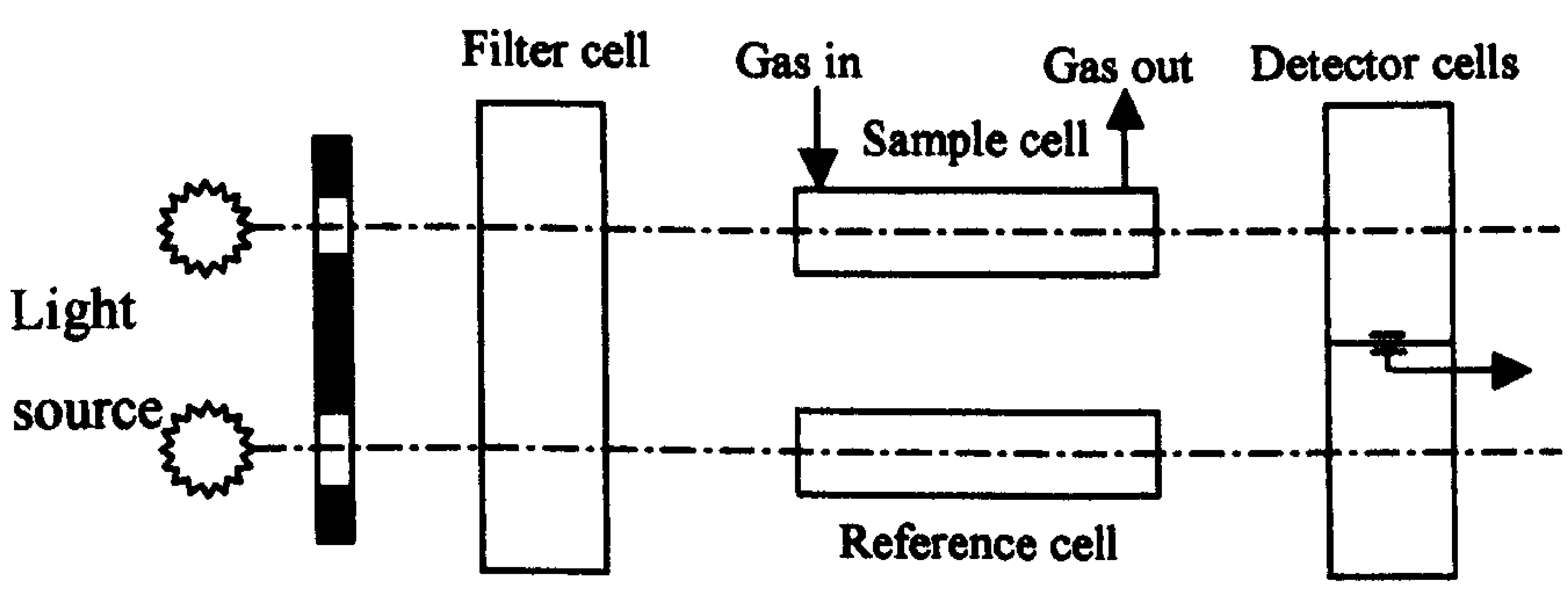

Figure 6.4 **NDIR Analysers with Differential Detectors**

The two halves of the cell are separated by a diaphragm that moves between two plates of a capacitor. Presence of the gas to be measured in the sample cell will result in absorption of the radiation and hence a reduction of the energy reaching the upper detector cell. The level of radiation reaching the detector cells via the sample cell is then compared with that which has passed through a reference cell containing a non-absorbing gas (nitrogen). Absorption of energy by either side of the detector cell causes the pressure in that side to rise. The attenuation of the radiation, and subsequent reduction of energy reaching the upper cell, causes the diaphragm to deflect in proportion to the difference in the energy absorption rates of each side of the cell. This deflection can be related directly to the gas concentration in the sample cell and the change in capacitance caused by deflection can be calibrated to read in units of concentration.

Since there is some overlap between the absorption wavelengths of CO and CO_2 the accurate measurement of one in the presence of the other is not possible. This problem is addressed by continually switching band pass filters in front of the light source according to the gas to be measured at the instant. For example, if CO is to be measured, a filter removing wavelengths absorbed by CO_2 will be employed.

It is also possible to measure the concentrations of unburned hydrocarbons in the exhaust gas using this method. However, since a variety of hydrocarbon species with a wide spectra of absorption are normally present, accurate measurements are difficult. For this reason the preferred method for determining the unburned hydrocarbon concentration is the flame ionised detector (FID) technique, detailed later in this chapter.

The oxygen content of the exhaust gas is used in the determination of the air/fuel ratio and in this case is found by the use of a galvanic cell. The galvanic cell consists of a gold plated PTFE diaphragm that serves as a cathode and a silver plated anode. These are immersed in an electrolyte of potassium chloride gel and a potential is placed across the electrodes. As the oxygen diffuses through the membrane, electrochemical reduction occurs and a current flows proportional to that of the partial pressure of the oxygen in the sample. This current can then be calibrated to read as oxygen content. The galvanic cell responds to other gases, including CO_2 which is far more abundant in the exhaust stream. However its sensitivity to other gases is low enough not to affect the results in practical terms. Although an accuracy of 60.1% is possible with this method, the majority of the error is caused during the 'zeroing' process that uses the oxygen content from ambient air. This can vary between 20.7% and 20.9% according to pollution and humidity. Using dry measured values of CO, CO_2, O_2, HC and a knowledge of the fuel composition the analyser calculates the air/fuel (A/F) ratio and lambda number.

6.3.5.2 NO_x Measurements

To measure exhaust gas emissions of NO_x a Signal 4000VM chemiluminescence analyser was used. The sample is drawn into the analyser by a separate vacuum pump via a heated sample line and particulate filter. The heated line is necessary to prevent water vapour in the sample from condensing. The chemiluminescence analyser measures the amount of light emitted by electrically excited molecules of nitrogen dioxide and uses this to determine the concentration of NO in the exhaust gas.

The exhaust gas stream can contain both nitric oxide (NO) and nitrogen oxide NO_2. The term NO_x is used to describe the sum of these gases. On entering the analyser any NO_2 in the sample is catalyliticaly converted to NO. Zero grade air is passed through an electrical discharge where some of the oxygen molecules are converted to ozone (O_3). The NO and air containing the ozone molecules are fed into a reaction chamber. Here reactions take place where the NO_2 and O_3 combine to form NO_2 in an excited state and O_2. The excited NO_2 can be returned to its ground state either by emission of a photon or by being quenched though molecular collision. These reactions are summarised below

$$NO + O_3 \Rightarrow \overset{*}{NO_2} + O_2 \Rightarrow NO_2 + O_2 + \text{photon} \qquad (6.20)$$

The amount of light produced is proportional to the combined content of NO_2 and NO in the exhaust gas. It is collected by a photomultiplier and amplified before being converted into NO concentration readings.

Frequent calibration of the analyser must be performed to ensure accurate measurements. The zero is set by comparison with zero grade nitrogen gas and the span is checked using a gas with 500ppm of NO with a balance of nitrogen. The analyser gives a fast response of around 2 seconds and can maintain an accuracy of 61% of the span gas.

6.3.5.3 Unburned Hydrocarbon Measurements

As mentioned above although the measurement of unburned hydrocarbons can be performed using the infrared absorption technique it is only really suitable for qualitative measurements.

The analyser used for the measurement of unburned hydrocarbons was a 'Signal 3000HM'. This analyser employs the flame ionised detector (FID) technique and although more complex and expensive, it can perform quantitative measurements to the accuracy required. The technique relies on the detection of ions that are formed when hydrocarbons are burned. The number of ions produced corresponds very closely to the number of carbon atoms present.

The sample is drawn into the analyser by an external vacuum pump via a sample line connected to the exhaust pipe. The line is heated to avoid condensation of any water vapour in the sample gas. It is then mixed with fuel and burned with a stoichiometric quantity of air in chamber containing an electrode system. A 40/60 hydrogen/helium mix fuel is used since a hydrocarbon fuel could cause ionisation, affecting the results. Similarly, high purity air is used to avoid the introduction of any hydrocarbon or other species that could impair the result. The presence of ions is detected by the flow of current between a high voltage electrode and a ground electrode. The current flow corresponds very closely to the number of ions present. The signal is then amplified and scaled to give a reading of concentration. Calibration is achieved in a similar manner to the NOx analyser described above, the main difference being the use of a span gas with a known hydrocarbon concentration with an inert balance, in this case 1500ppm propane in nitrogen.

Studies have shown the response of the detector can be affected slightly by species type and molecule size. Table 6.2 lists the relative responses of various molecular structures. Since the instrument response is related directly to the sample flow rate this must be carefully controlled. Similarly, the fuel flow rate must closely regulated since this will affect the flame temperature and therefore sensitivity.

Table 6.2 Typical responses of a flame ionisation detector to different molecular structures, normalised with respect to propane [92]

Molecular structure	Relative response
Alkanes	0.97 – 1.05
Aromatics	0.97 – 1.12
Alkynes	0.99 – 1.03
Alkenes	1.07
Carbonyl radical (CO-)	0
Oxygen in primary alcohol	0.23 – 0.68

A limitation of the FID technique is its inability to distinguish between different hydrocarbon species. Therefore, it is normal to describe measurements as parts per million carbon ($ppmC_1$) or parts per million methane ($ppmCH_3$).

6.3.5.4 Calculation of Specific Exhaust Emissions

Emissions data gathered by the exhaust gas analysers are on a volumetric basis (ppm, %). The volumetric flow through engines running at different speeds and loads and of varying size and type bears little relation to their respective power outputs. Because of this, comparisons of volumetric emissions data made in relation to engine output are of limited use. In order to allow meaningful universal comparisons to be made, the volumetric data must be expressed on an absolute basis. The most common way of achieving this is to normalise the emissions to the indicated - or brake output of the engine on a gravimetric basis.

The calculations were performed using a Microsoft Excel spreadsheet written by Oakley [26]. This uses the generic equation

$$\mathrm{IS}(x) = \frac{\mathrm{n}_P * \mathrm{vol}(x) * m_{(x)}}{\mathrm{n}_R\, a(\mathrm{m}_C + b m_H + c m_O)} * \mathrm{ISFC}$$

where x is the emission concerned, $\mathrm{vol}(x)$ is the mole fraction quantity of that emission and $m_{(x)}$ is its molecular mass. n_P and n_R are the number of moles of products and reactants respectively and a is the wet molar fraction of the fuel. b and c are the H/C and O/C ratios of the fuel respectively and m_C ,m_H and m_O are the relative atomic weights of carbon, hydrogen and oxygen.

6.3.6 Temperature Measurements

Thermocouples were installed on the engine and test bed to measure exhaust gas, coolant and oil temperatures. The coolant and oil temperature thermocouples and displays were integrated within the engine test bed and formed part of the closed loop temperature control system described in Chapter 3. The coolant and oil thermocouples were both located near the entrances of their respective heat exchangers. A 'K' type thermocouple mounted in the exhaust pipe, located very close to the exhaust port, was used to measure the exhaust gas temperature (EGT). The resulting reading was displayed on LCD display connected directly to the thermocouple.

6.4 Summary

Modifications the experimental set-up for the fired work have mainly been concerned with the preparation of the engine to sustain operation with combustion and has included design and manufacture of a new piston and cylinder assembly. This chapter has also detailed the sandwich adapter plate and the gaskets required to fit these new components while modifications to the camshafts and fuel supply system have also been covered. A discussion of the various additional measurement systems used during the combustion work has also been included.

Chapter 7

Engine Experiments with CAI Combustion

Chapter 7 Engine Experiments with CAI Combustion

7.1 Introduction

The reasons for the continued interest in CAI combustion along with the various methods of achieving it have been detailed in Chapter 2. The method chosen for initiating and controlling CAI combustion in this work is the retention of large amounts of burned gas in the cylinder. This provides both the thermal energy to allow the fuel to auto-ignite and the dilution necessary to control the subsequent heat release rate. The residual gases are trapped by closing the exhaust valves early and has been achieved by the use of camshafts with very short duration.

The aims of this work are to assess the merits of CAI combustion compared to conventional SI engines in terms of fuel consumption, exhaust emissions and operating region. In addition, cylinder pressure data are recorded and used to investigate various characteristics of CAI combustion including ignition timing, burn duration, combustion stability and combustion temperature. The effects of injection timing and exhaust and intake valve timing on CAI combustion will also be examined.

7.2 Valve Timing Strategy for CAI Combustion

As detailed in Chapter 2, the method selected to initiate CAI combustion and to control the subsequent heat release rate was the trapping of large amounts of residual gases in the cylinder. This method, often referred as internal exhaust gas recirculation (IEGR) was achieved by closing the exhaust valves early. As a consequence, the opening of the intake valves must be delayed accordingly to prevent unwanted back-flow of the residual gases into the intake port. However, it is not practical to achieve the required valve events by simply advancing and retarding the original exhaust and intake camshafts respectively. Since the original camshafts had a standard duration for an engine of this type, radical departure from the intended phasing as described above would result in exhaust and intake valves opening unacceptably early and late respectively. To overcome this, a pair of short duration camshafts were produced by reprofiling a set of spare production camshafts. The cam profiles used had successfully been employed in a similar manner by Zhao et al [1] at Brunel University and are as described by Duret and Lavy [3].

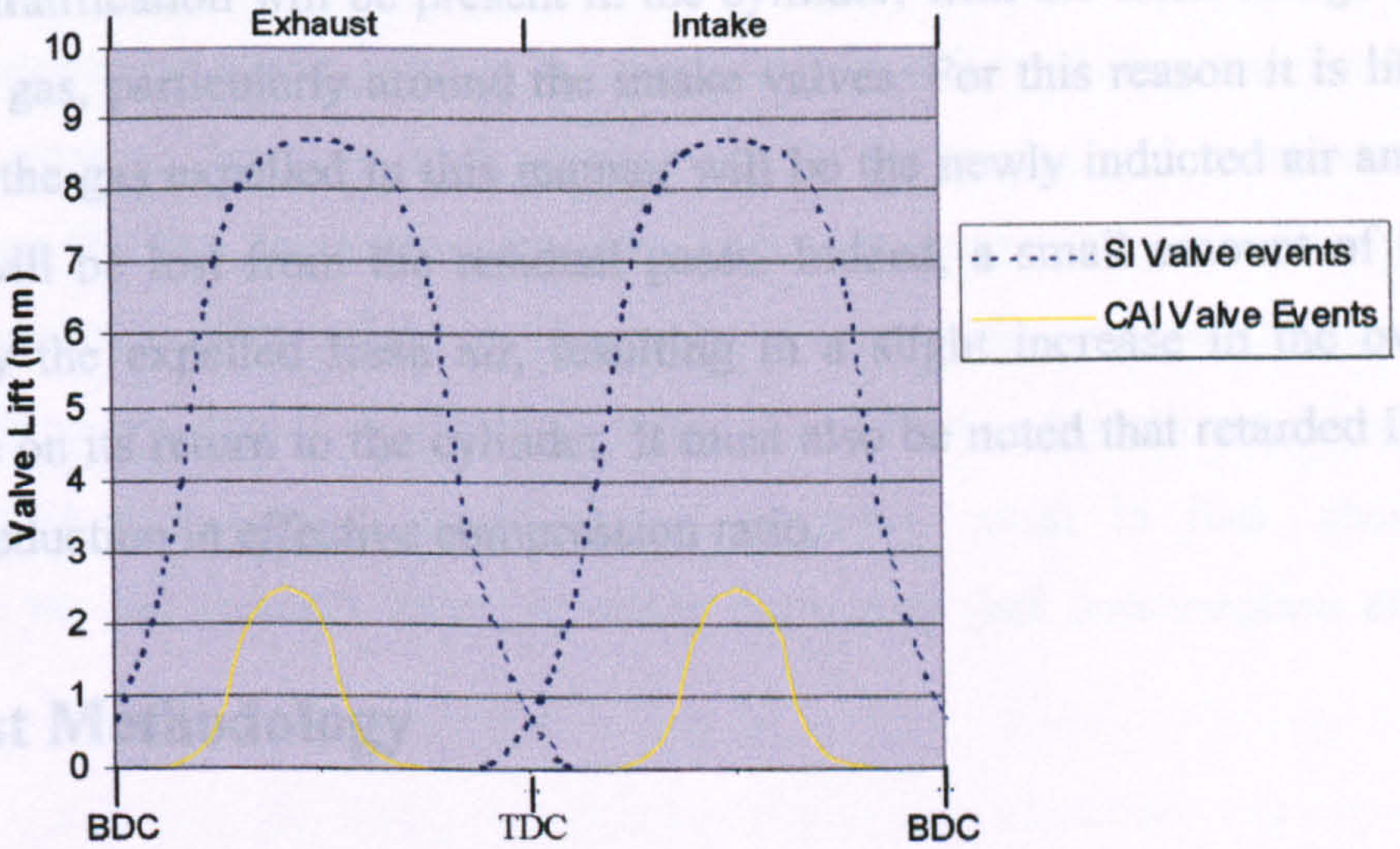

Figure 7.1 Typical CAI and SI Valve Timing Diagram

The exhaust and intake camshafts used had duration's of 110° CA and 120° CA respectively, measured at 0.1mm lift. It is common to describe the opening and closing points of a camshaft at a small, defined, amount of lift. During the first and last few degrees of the camshaft duration the rate of change of lift is very small. As a result it is hard to accurately define the camshaft duration and or timing at zero lift. It is estimated that in this case approximately 10° CA of rotation is required to generate the first (and last) 0.1mm of valve lift. The reprofiling of production camshafts to achieve the desired duration resulted in a reduction in maximum valve lift from 8.8mm to 2.5mm.

Since no intake throttling was used for the CAI tests, the engine load was controlled primarily by the camshaft phasing. As already described, the early closure of the exhaust valves dictates that the opening of the intake valves should be delayed to prevent excessive back-flow of trapped residuals. However, as discussed by Zhao et al [1], the phasing of IVO relative to EVC can be used to control the mixing of fresh and residual gases and, to a certain extent, the final charge temperature and ignition timing. If the intake valves are opened early, when the cylinder pressure is higher than the intake manifold pressure, back flow of the trapped residual gases into the manifold will occur. However, as the piston moves downward the backflow gas, along with fresh charge air, will be pulled back into the cylinder. Some heat from the back flow gas will be lost to the manifold walls. This is termed early back flow. If the intake valves are opened late, when the cylinder pressure has fallen below the manifold pressure, there will be no back flow at IVO. However, the late IVO will result in a late IVC, causing some of the in-cylinder gas to be expelled into the intake manifold as the piston begins to rise. This gas will then dwell in the manifold until it is returned to the cylinder at IVO of the next cycle and is termed late back flow. It is quite likely that during the intake and early compression strokes some degree of horizontal stratification will be present in the cylinder, with the fresh charge sitting above the residual gas, particularly around the intake valves. For this reason it is likely that the majority of the gas expelled in this manner will be the newly inducted air and as a result little heat will be lost from the residual gases. Indeed, a small amount of heat may be absorbed by the expelled fresh air, resulting in a slight increase in the overall charge temperature on its return to the cylinder. It must also be noted that retarded IVC will also result in a reduction in effective compression ratio.

7.3 Test Methodology

7.3.1 Introduction

As already established in Section 7.2, the primary means adopted for promoting and controlling CAI combustion during this work is the trapping of large amounts of residual gasses in the cylinder, which is achieved by early exhaust valve closure. Since the amount of trapped gas has such a profound effect on the subsequent combustion, particularly in terms of engine load, EVC was chosen as the primary test variable.

Section 7.2 also introduces IVO timing as a means of influencing the mixing of fresh and residual charges. In order to explore the effects of early and late backflow on combustion three IVO timings were chosen for each EVC timing. One was set to be symmetrical about TDC to the EVC timing, one 10° CA advanced from this (in an attempt to increase early back flow) and another 10° CA retarded (attempting to cause more late back flow).

For each valve timing configuration, two engine test speeds were chosen. The low speed point was selected as 1200 RPM since this corresponds to the test speed of the optical work described earlier in this work. The high speed point selected was 2400 RPM.

Although the effect of A/F ratio on the CAI combustion and subsequent emissions is of potential interest, time constraints prevented this variable from being investigated. Throughout testing, the A/F ratio was maintained at $\lambda = 1$. This A/F ratio was selected since it allowed easy comparison with other CAI work completed at Brunel University [1] that was also completed at $\lambda = 1$.

7.3.2 Selection of Injection Timings

One of the objectives of this work is to investigate the effect of injection timing on the CAI combustion process. Because of the time available for testing and subsequent analysis of the data it was felt that the number of injection timings tested should be limited to three. To allow the maximum effect of the timings to be observed, the range of timings were chosen to be as wide as practicable. In practical terms the earliest an injection can begin is at EVC, since injecting any sooner would almost certainly result in fuel 'short circuiting' combustion via the exhaust valve, severely damaging fuel consumption and increasing emissions.

However, with this configuration of low-pressure injection system and extreme valve timings, there is another factor to consider. The Orbital air-assisted injection system has an in-cylinder injection pressure of only 6.5 bar. During periods where the cylinder pressure approaches this level, injection is not possible. As a consequence of the early EVC and late IVO used for CAI operation a second in-cylinder pressure rise, known as recompression, is introduced around TDC of the exhaust/intake strokes, as shown in Figure 7.2. Depending on EVC and IVO timings employed, the recompression phase has a peak cylinder pressure ranging from 8 to 15 bar and a duration of between 30° CA and 70° CA. The practicalities of an injection event around EVC therefore require further investigation. At the higher test speed of 2400 RPM an injection duration of 3 ms corresponds to an injection period of 22° CA. Therefore, a window where the cylinder pressure is below 6.5 bar for at least 22° CA is required for a full injection to take place.

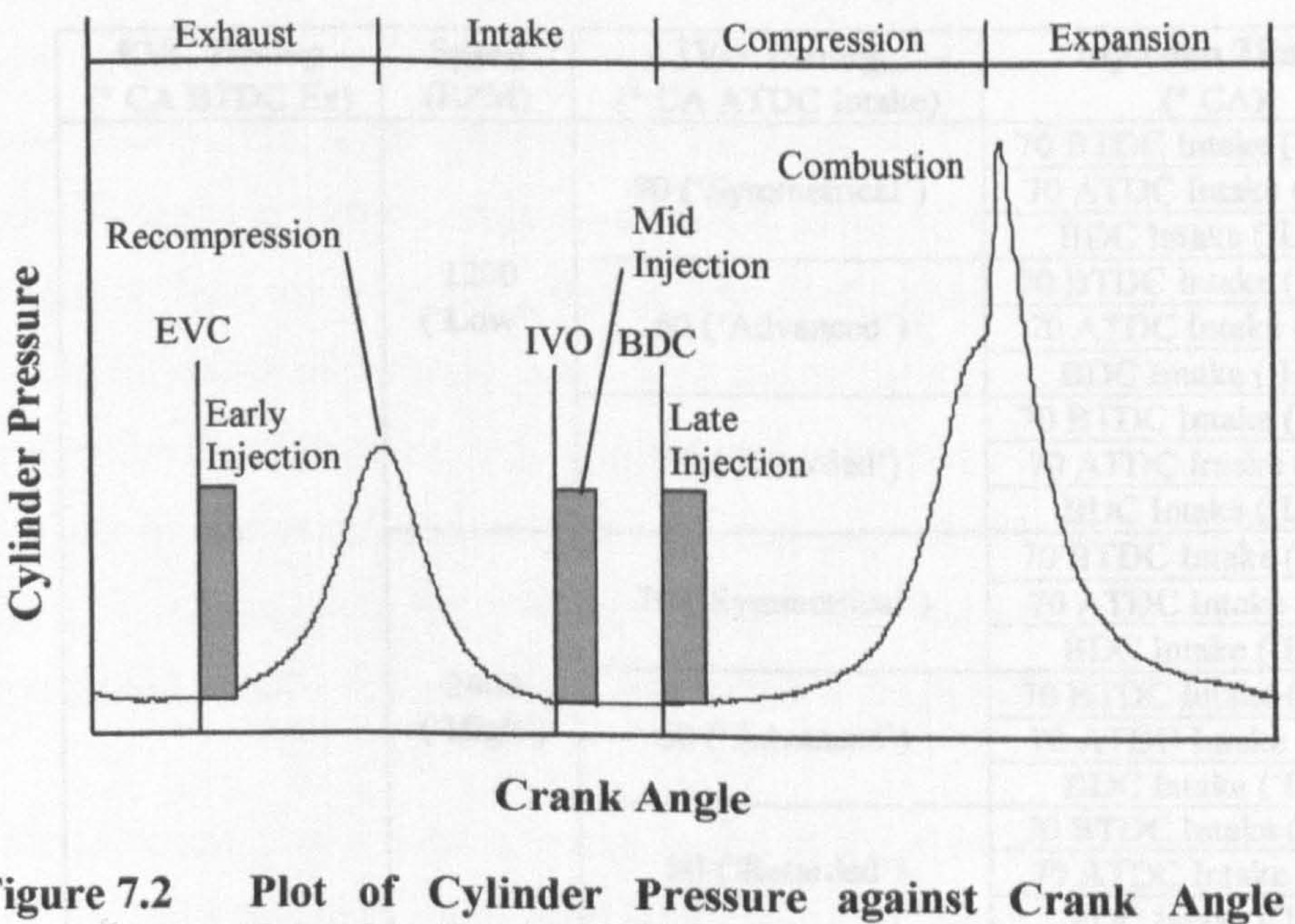

Figure 7.2 Plot of Cylinder Pressure against Crank Angle showing Injection Timing Windows (2400 RPM, EVC 100° CA BTDC, IVO 100° CA ATDC)

Figure 7.2 shows a plot of CAI cylinder pressure against crank angle for EVC and IVO timings of 100° CA BTDC and 110° CA BTDC at 2400 RPM. With these valve timings, the engine operates at the lowest load condition tested and hence the most trapped residuals and largest recompression. They therefore represent the 'worst case' situation in which to perform an injection event at EVC. Overlaid on the pressure trace is a 6.5 bar injection event beginning at EVC. It can be seen that there is sufficient time to perform the injection before the in-cylinder gas pressure approaches the injection pressure. As a result, the earliest injection timing will be set equal to EVC. This obviously means that it has no fixed value but must be varied according to the EVC timing used.

With regard to the selection of the second or 'middle' injection timing the in-cylinder pressure exerts a similar constraint, though this time the injection event must be delayed until the cylinder pressure has fallen sufficiently following the recompression. Since the recompression event is roughly symmetrical around TDC it was decided to phase the second injection to take place at a crank angle ATDC symmetrical about TDC to the EVC timing, see Figure 7.2.

From previous experience with the Orbital air-assisted injection system and from the LIEF data presented in Chapter 5 it was felt that the latest practical injection timing that would give a reliable homogenous charge would be around BDC of the intake stroke. For this reason the 'late' injection timing was fixed here.

Table 7.1 shows a summary of the test variables for an EVC timing of 70° CA BTDC.

Table 7.1 Example set of test variables at 70° CA BTDC EVC

EVC Timing (° CA BTDC Ex)	**Speed** (RPM)	**IVO Timing** (° CA ATDC Intake)	**Injection Timing** (° CA)
70	1200 ('Low')	70 ('Symmetrical')	70 BTDC Intake ('Early')
			70 ATDC Intake ('Mid')
			BDC Intake ('Late')
		60 ('Advanced')	70 BTDC Intake ('Early')
			70 ATDC Intake ('Mid')
			BDC Intake ('Late')
		80 ('Retarded')	70 BTDC Intake ('Early')
			70 ATDC Intake ('Mid')
			BDC Intake ('Late')
	2400 ('High')	70 ('Symmetrical')	70 BTDC Intake ('Early')
			70 ATDC Intake ('Mid')
			BDC Intake ('Late')
		60 ('Advanced')	70 BTDC Intake ('Early')
			70 ATDC Intake ('Mid')
			BDC Intake ('Late')
		80 ('Retarded')	70 BTDC Intake ('Early')
			70 ATDC Intake ('Mid')
			BDC Intake ('Late')

7.3.3 Experimental Procedure

Successful CAI operation requires a certain in-cylinder charge temperature to be attained before auto-ignition can take place. It also requires a high level of charge dilution to control heat release rates. It this case, both these requirements are met by the presence of hot residual gases. For this reason it will difficult to run the engine in CAI mode from cold start conditions and hence the engine should first be run in SI mode until sufficient heat is available to initiate CAI. In addition, all the experiments were performed after the engine had fully warmed up in order to obtain repeatable results. The extension of CAI to cold engine operation will be an interesting area of future research.

With all the required lab equipment on and the exhaust gas analysers warmed up and calibrated, the engine was motored at a speed of 800 RPM and the spark and fuel systems switched on. Following a sweep of fuel injection duration the engine begins to fire and the AFR is adjusted to lambda 1.0. As the coolant temperature reaches 50°C, some cycles of CAI combustion begin to appear. CAI combustion can be observed as a very fast pressure rise during combustion on the real-time pressure/crank angle display on the DAQ PC monitor. As the coolant temperature reaches its normal operating point 80°C, the engine speed is increased to 1200 RPM and CAI combustion becomes stable.

After some preliminary engine tests, the EVC and IVO timings were set 70° CA BTDC and ATDC respectively since this was found to be approximately the centre of the CAI operating range. The injection was set to occur at the early timing and the engine was run at the lower engine speed until the coolant temperature reached 80°C and the AFR was stabilised at lambda =1.0. Once CAI combustion was stable, as observed from the DAQ real-time display, the spark system was switched off. Some time was allowed for the analysers to settle before readings were taken along with exhaust gas temperatures and torque output from the load cell display. The DAQ system was then switched to 'save' mode and 100 cycles of pressure data were recorded and saved to the PC hard drive. Once all the data for that test point had been collected the injection timing was adjusted to the middle, post re-compression timing and the fuel amount adjusted as required to maintain lambda = 1.0. Again, once the analysers had settled, data was collected and 100 pressure cycles recorded. Finally the procedure was repeated for the late BDC injection timing.

Next the injection timing was returned to the early position and the speed increased to 2400 RPM. With the AFR readjusted to lambda 1.0, the combustion as confirmed stable and the analysers settled, the next data set was recorded. Once this had been repeated for the other injection timings the fuel injector was turned off and the engine stopped.

The intake valve timing was then advanced by 10° CA and the above procedure repeated. The intake valve timing was then retarded by 10° CA from its original position and the test repeated once more. Following this, the exhaust valve timing was retarded by 10° CA and the tests repeated for all the required speeds, IVO and injection timings. The EVC timing was then retarded further in 10° CA increments and the tests repeated until stable CAI operation was no longer possible. Once the most retarded practical EVC timing for CAI had been found, the EVC timing was advanced to 10° CA beyond its original position and the tests repeated. The EVC timing was then advanced in 10° CA increments and data recorded until CAI combustion was no longer stable.

7.4 Discussion of Results

7.4.1 CAI Operation Performance

7.4.1.1 General / Overall Performance

Figure 7.3 shows the attainable operating range for CAI combustion for each combination of engine speed and EVC, IVO and injection timing. In each case the minimum load was limited by misfire. At this point the amount of residual gases retained was high but the overall charge temperature was too low to allow auto-ignition. Maximum load was also limited by misfire but here, although the temperature of the trapped gas was high, their mass in relation to the amount of fresh charge was insufficient to initiate CAI combustion. Other researchers investigating CAI initiated by large amounts of trapped exhaust gas have found that in some situations maximum load is limited by knocking combustion, suffered when the rate of cylinder pressure rise becomes too great [9] rather than misfire. In these cases the amount of residual gas is very low and, although in-cylinder temperatures are still high enough to initiate CAI combustion, the charge is not diluted enough to prevent excessive rates of pressure rise. However, in this work knocking combustion during CAI operation was not encountered. It is felt that this is probably due to the relatively low compression ratio of 9:1 used when compared to the other studies e.g. 15:1 [9]

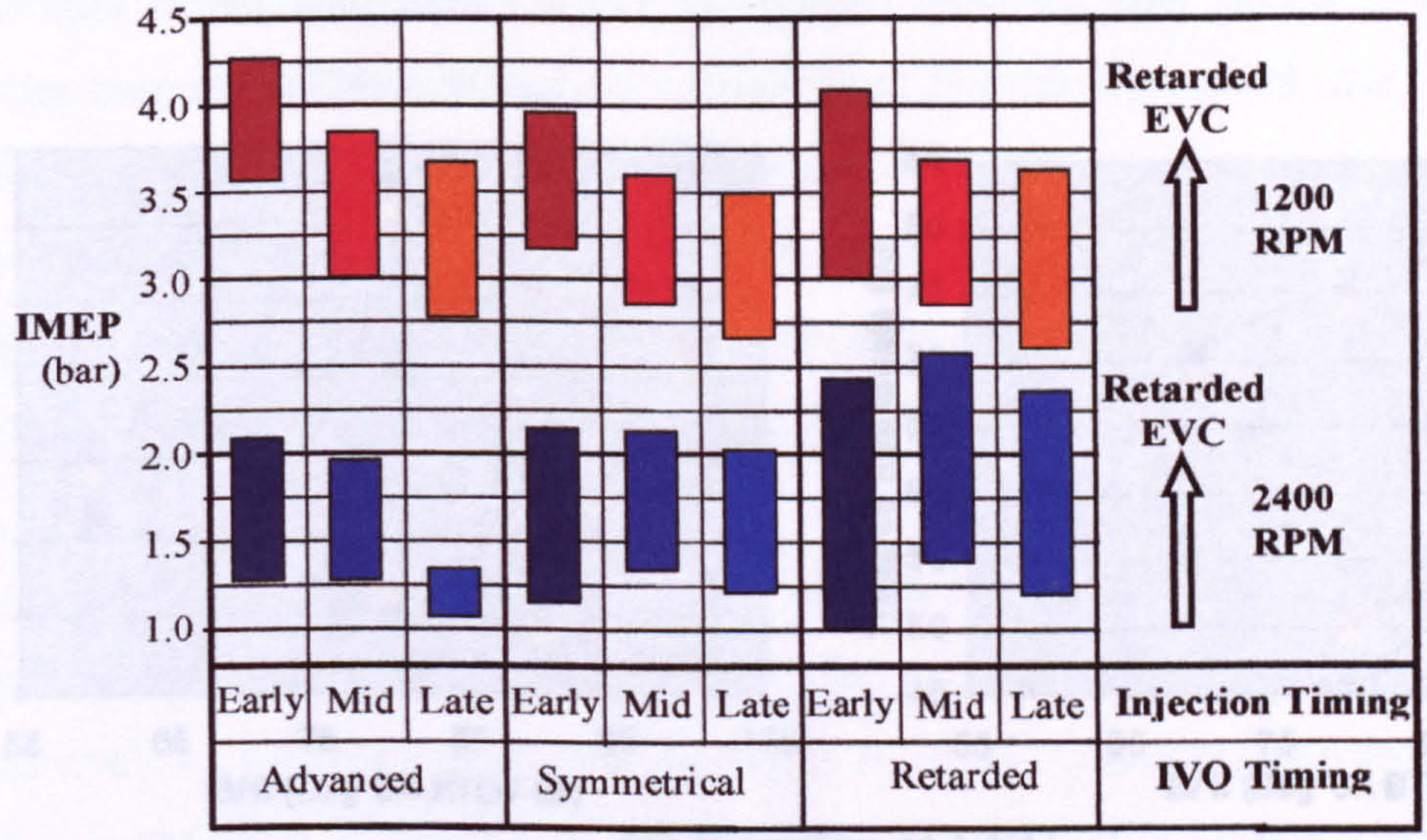

Figure 7.3 Operating Range with CAI Combustion

7.4.1.2 Effect of Valve Timing

Each test variable had a significant effect on engine output. However, as expected, the biggest variations were caused by changes in the EVC timing. In this case, the change in engine output was caused primarily by the amount of residuals trapped in the cylinder. Essentially, more residuals retained in the cylinder means less space is available for the incoming fresh charge.

Figure 7.4 shows how the IMEP and amount of trapped residuals, as a percentage of the total charge, change with IVO timing across the range of EVC timings with injection at EVC, IVO and BDC of the intake stroke. For the lower test speed of 1200 RPM the amount of trapped residuals ranges from approximately 45% to 65% for EVC timings of 80 and 100°CA BTDC respectively. At the higher speed of 2400 RPM a range of 65% to 80% is found for timings of 60 to 100°CA BTDC. The higher test speed resulted in a much higher percentage of trapped residuals since less time was available for the gas exchange process to take place. This corresponds to operating ranges of approximately 1 to 2.5 bar IMEP for high speed and 2.5 to 4 bar IMEP for low speed.

Figure 7.4 also shows the effect of IVO timing on net IMEP. It can be seen that, at low speed, the IVO timing has a noticeable effect on engine output. The highest output for most of the operating range was achieved using advanced IVO timing, while the lowest was produced with the symmetrical timing. The retarded timing produced the highest load in the centre of the operating range.

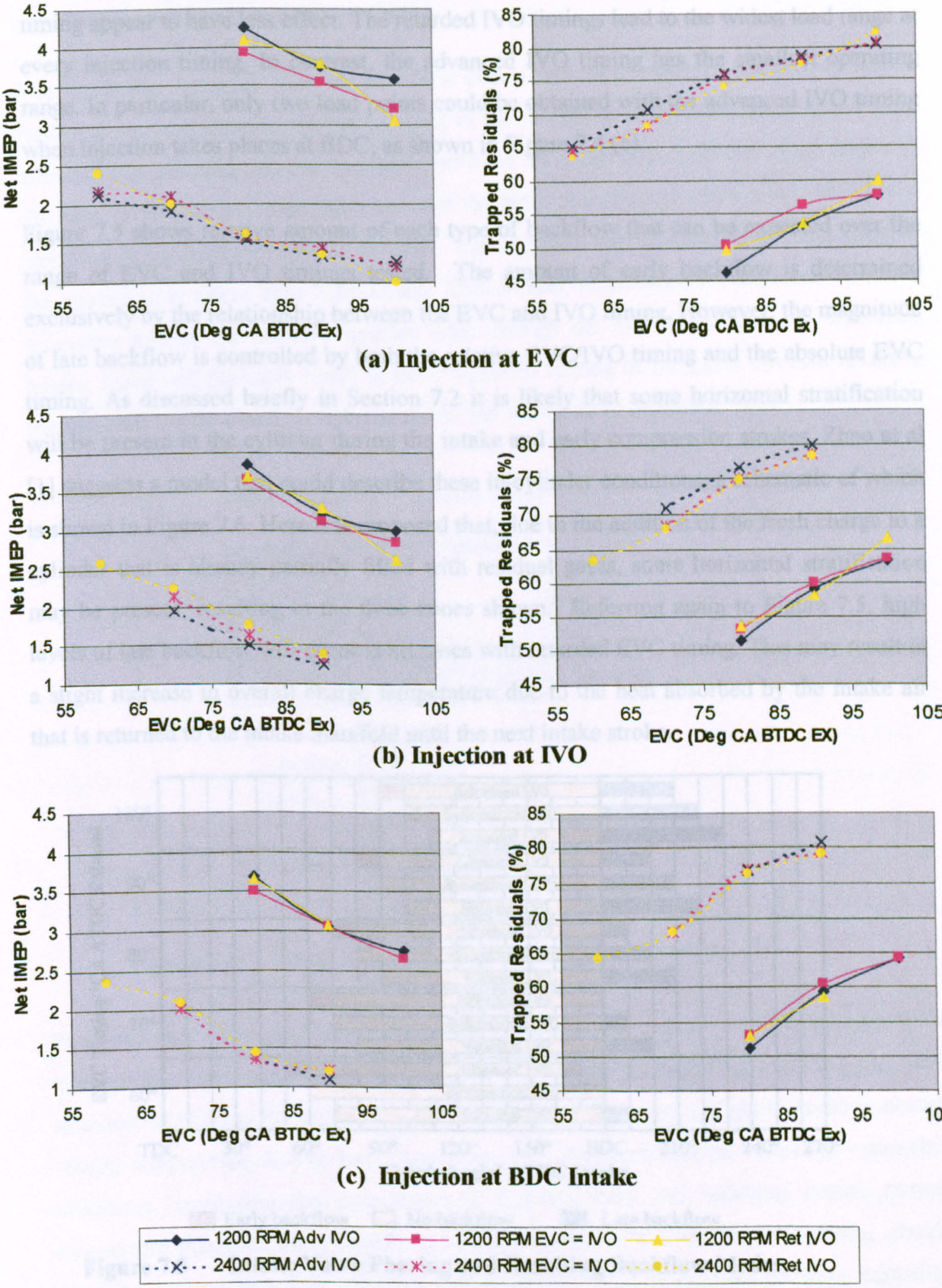

Figure 7.4 Variation in IMEP and Trapped Residuals with Valve Timing

This data agrees well with the plot of trapped residuals also shown in Figure 7.4 with greater trapped residuals producing a lower load. For the high speed case, changes in IVO timing appear to have less effect. The retarded IVO timings lead to the widest load range at every injection timing. In contrast, the advanced IVO timing has the smallest operating range. In particular, only two load points could be obtained with the advanced IVO timing when injection takes places at BDC, as shown in Figure 7.4 (c).

Figure 7.5 shows relative amount of each type of backflow that can be expected over the range of EVC and IVO timings tested. The amount of early backflow is determined exclusively by the relationship between the EVC and IVO timing. However, the magnitude of late backflow is controlled by both the relative EVC/IVO timing and the absolute EVC timing. As discussed briefly in Section 7.2 it is likely that some horizontal stratification will be present in the cylinder during the intake and early compression strokes. Zhao et al [1] suggests a model that could describe these in-cylinder conditions, a schematic of which is shown in Figure 7.6. Here it is proposed that, due to the addition of the fresh charge to a cylinder that is already partially filled with residual gases, some horizontal stratification may be present, resulting in the three zones shown. Referring again to Figure 7.5, high levels of late backflow will occur at all cases with retarded EVC timing. This may result in a slight increase in overall charge temperature due to the heat absorbed by the intake air that is returned to the intake manifold until the next intake stroke.

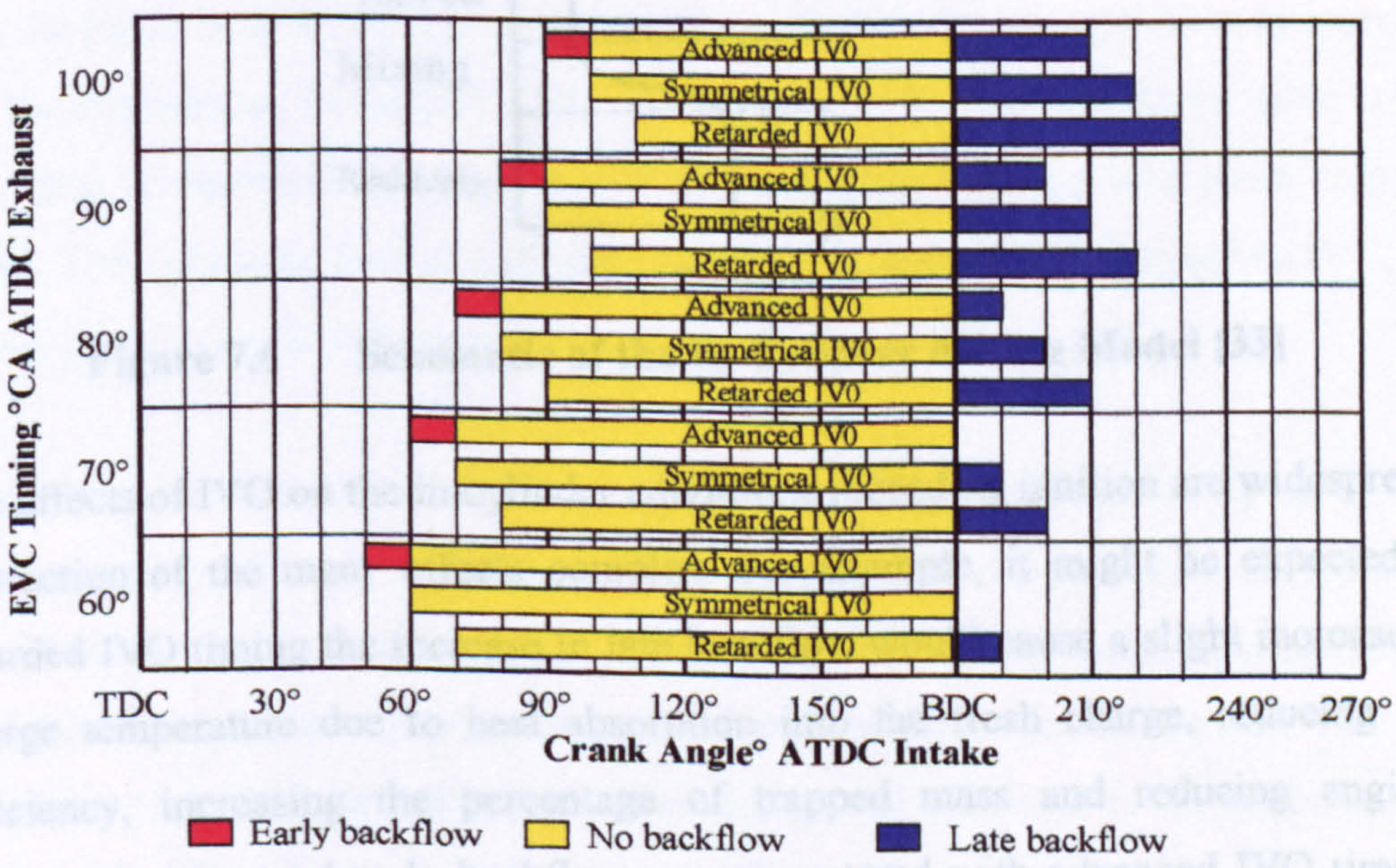

Figure 7.5 Intake Valve Phasing and Resulting Backflow Modes

An important consequence of the very late IVC timing that arises from early EVC timing is the reduction in effective compression ratio and resulting decrease in cycle efficiency.

With an IVC timing of 230° ATDC a reduction in effective compression ratio from 9:1 to 8:1 would occur when compared to IVC at TDC. This would result in a reduction in overall efficiency of approximately 4% [5].

It is likely that the early and late backflow events will also influence the mixing of the fresh and residual charges. Referring again to the in-cylinder model shown in Figure 7.6, although it is probable that the distinction between the zones is exaggerated in the diagram, the large difference in temperature between the fresh and residual gases would result in a temperature gradient through the cylinder. Auto-ignition will commence at some point in the mixing zone where both fresh charge fraction and temperature are sufficient and then propagate rapidly via multiple ignition sites through the fuel air mixture [6]. Increased engine speed will probably result in more vigorous mixing of the gases but heat losses to the manifold walls should be reduced due to the shorter time available.

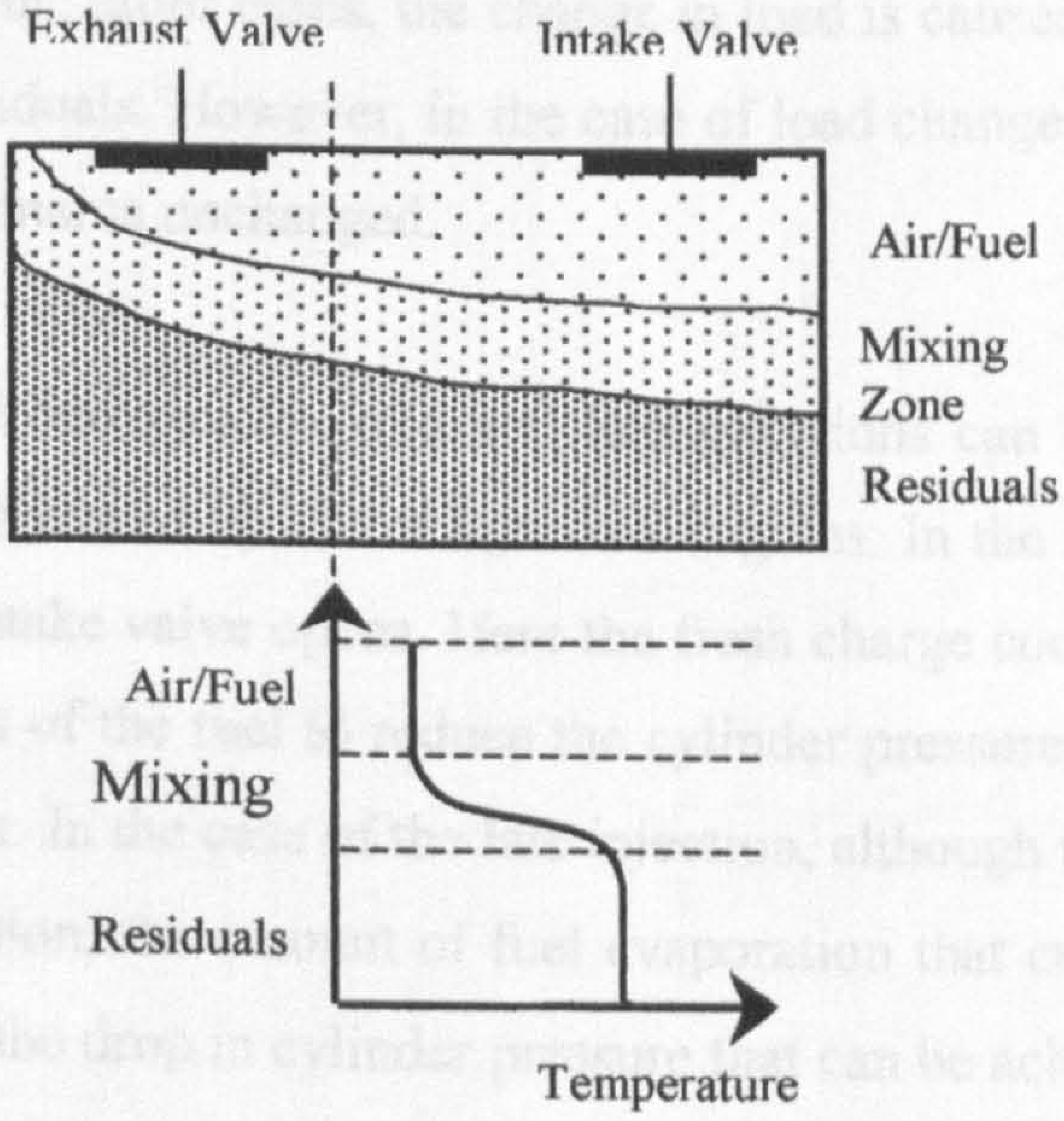

Figure 7.6 Schematic of the In-Cylinder Mixing Model [33]

The effects of IVO on the in-cylinder conditions preceding ignition are widespread and the interaction of the many effects complex. For example, it might be expected that with retarded IVO timing the increase in late backflow would cause a slight increase in overall charge temperature due to heat absorption into the fresh charge, reducing volumetric efficiency, increasing the percentage of trapped mass and reducing engine output. Conversely increased early backflow, as encountered with advanced IVO timing, should resulting in some heat loss from the residual gases, reducing cylinder pressure, admitting more fresh charge and increasing engine output. However, Figure 7.4 only shows this to be the case in a few low speed cases with the high-speed data showing the opposite trend. It is therefore likely that the gas dynamics cannot be predicted using this simplified model. In addition, changes in the temperature and spacial composition of the charge will affect combustion phasing, impacting load, fuel consumption and exhaust emissions. A much more rigorous treatment of the gas exchange process could therefore provide a large and rewarding area for future research.

7.4.1.3 Effect of Injection Timing

Figure 7.7 shows the variation in IMEP and trapped residuals across the range of EVC timings and also illustrates how they change with injection timing for advanced, symmetrical and retarded IVO timings. Though the operating range and levels of trapped mass are similar to Figure 7.4 it is clear that the variation of injection timing had a far greater effect than changes in IVO timing. It can be seen that the earlier injection takes place, the greater the engine load. The way by which engine load is affected by changes in injection timing is subtly different to that of those brought about by changes in EVC timing or engine speed. In the latter cases, the change in load is caused directly by a change in the mass of trapped residuals. However, in the case of load changes due to injection timing the mass of residuals remains unchanged.

The change in load between the mid and late injections can be explained by the charge cooling effects experienced by direct injection engines. In the mid injection case injection takes place as the intake valve opens. Here the fresh charge cooling effect can be exploited using the latent heat of the fuel to reduce the cylinder pressure and draw in more fresh air from the atmosphere. In the case of the late injection, although the intake valve is still open at the time of injection, the amount of fuel evaporation that can take place before IVC is limited. This limits the drop in cylinder pressure that can be achieved before IVC, reducing the amount of extra air inducted.

Perhaps more interesting is the increase in engine output achieved by using the early injection strategy. In this case the injection takes place at EVC, before the recompression of the residual gases, see Figure 7.2. Injection into the residual gases causes a reduction of in-cylinder temperature and pressure, again due to the latent heat of the fuel. This reduction in cylinder pressure means that more fresh air can be admitted to the cylinder during the intake stroke. The charge cooling effect on the residual gases is greater than that on the fresh air because the greater temperature difference between fuel and exhaust gases is likely to result in complete evaporation of the fuel. In the early injection case, all the fuel is almost certainly evaporated by the injection into the hot exhaust gas. However, with mid and late injection it is likely that liquid fuel is still present beyond IVC, preventing the full

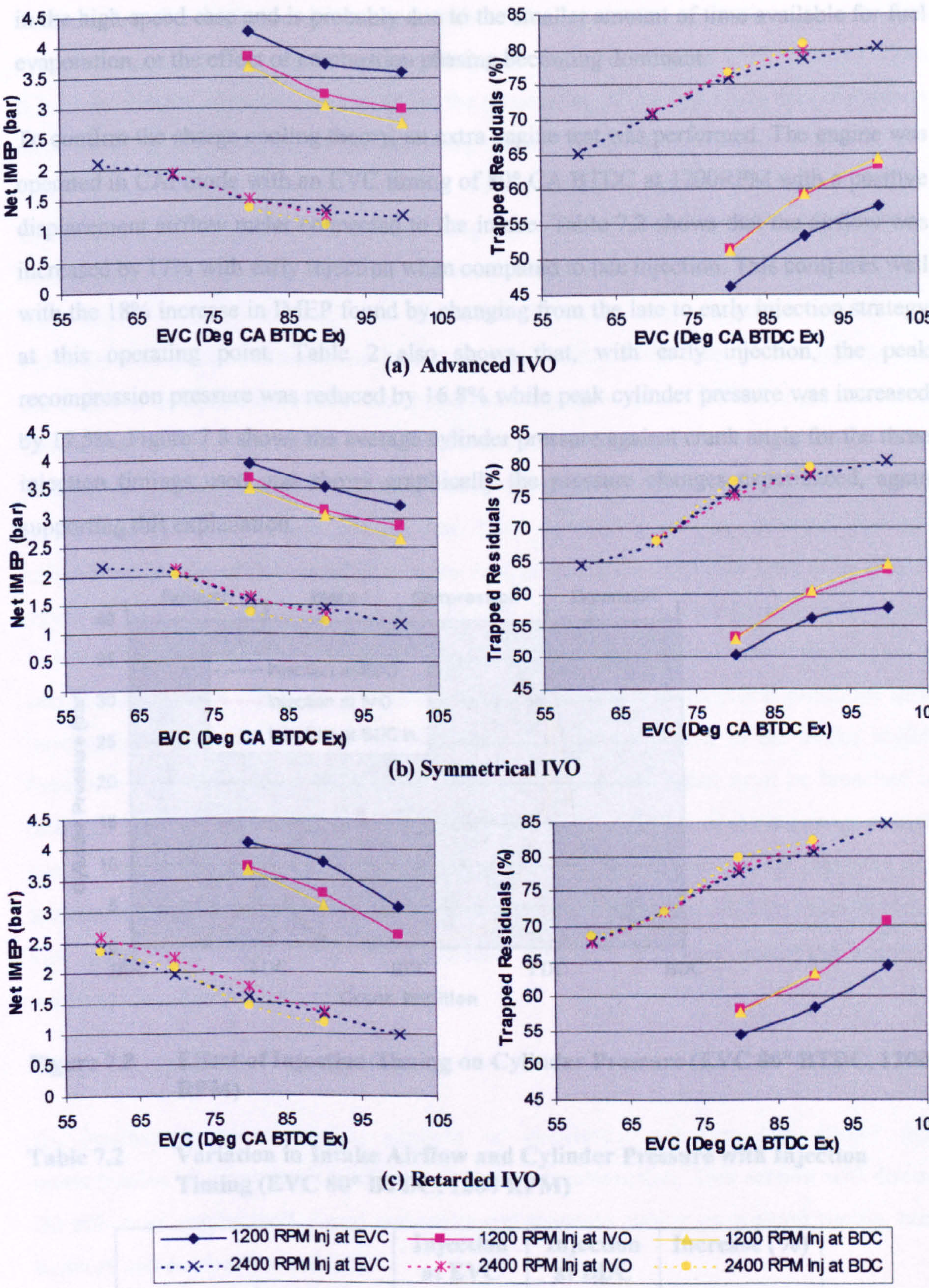

Figure 7.7 Variation in IMEP and Trapped Residuals with Injection Timing

charge cooling effect from being utilized. This phenomenon is present to a far lesser extent in the high-speed case and is probably due to the smaller amount of time available for fuel evaporation, or the effect of combustion phasing becoming dominant.

To confirm the charge cooling theory, an extra engine test was performed. The engine was operated in CAI mode with an EVC timing of 80° CA BTDC at 1200RPM with a positive displacement airflow meter connected to the intake. Table 7.2 shows that the airflow was increased by 17% with early injection when compared to late injection. This compares well with the 18% increase in IMEP found by changing from the late to early injection strategy at this operating point. Table 2 also shows that, with early injection, the peak recompression pressure was reduced by 16.8% while peak cylinder pressure was increased by 17.5%. Figure 7.8 shows the average cylinder pressure against crank angle for the three injection timings used and shows graphically the pressure changes experienced, again supporting this explanation.

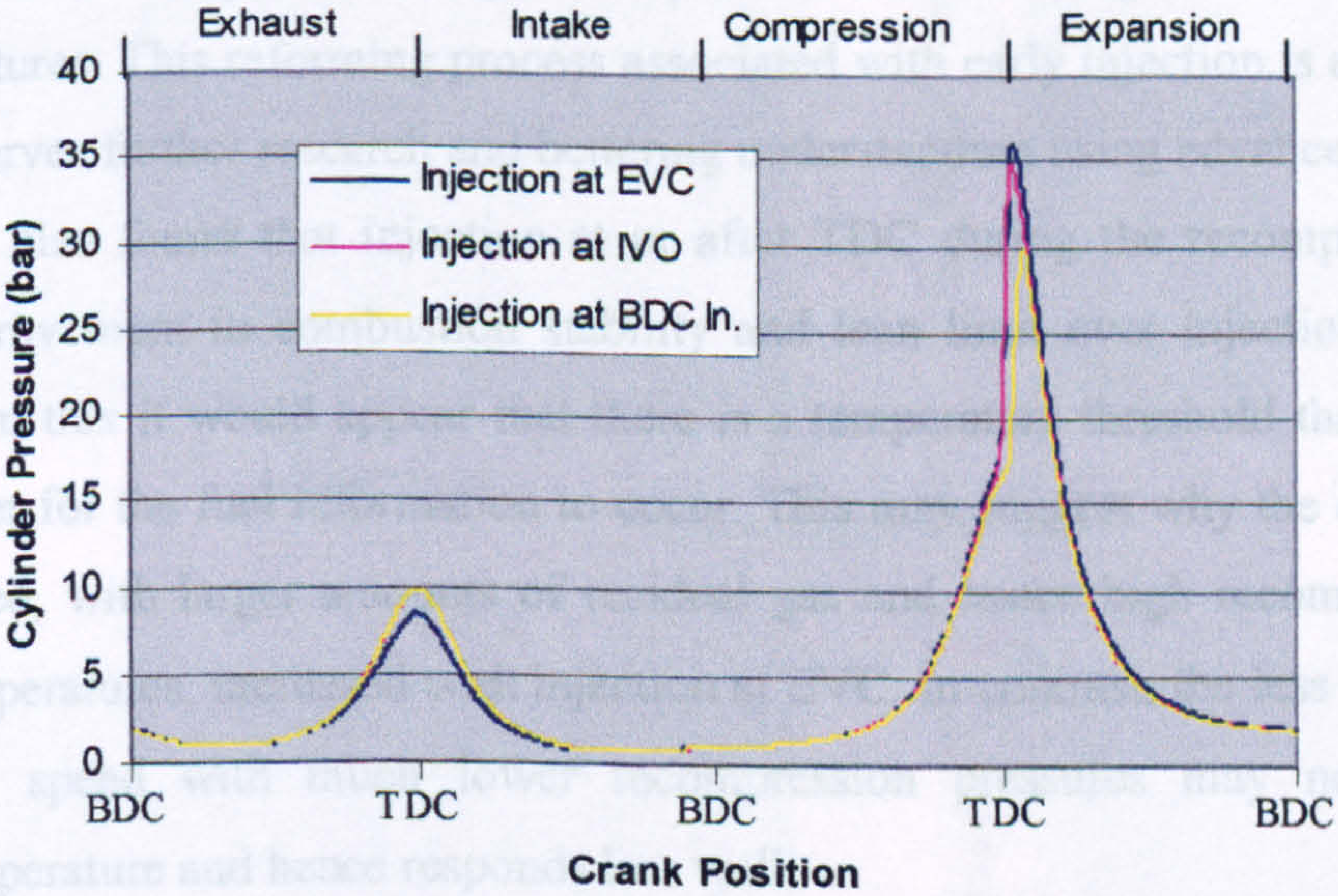

Figure 7.8 **Effect of Injection Timing on Cylinder Pressure (EVC 80° BTDC, 1200 RPM)**

Table 7.2 **Variation in Intake Airflow and Cylinder Pressure with Injection Timing (EVC 80° BTDC, 1200 RPM)**

	Injection at EVC	Injection at BDC Intake	Increase (%)
Intake Air Mass Flow (g/sec)	1.71	1.42	17%
Max Recompression Cylinder Pressure (bar)	8.36	9.77	-16.8%
Max Combustion Cylinder Pressure (bar)	36.13	29.79	17.5%

Figure 7.7 also shows that, at 1200 RPM, the operating ranges for all injection timings were similar. For high speed however, earlier injection tended to produce an extended operating range (i.e. was capable of operating over a greater range of EVC timings). Here it is likely that the extra time available for the preparation of the fuel made the combustion more robust in the extremes of the operating range. The effect is less pronounced at low speed since there is sufficient time for fuel preparation, even with late injection. Urushihara et al [9] also found that injecting near EVC in a GDI engine using IEGR to initiate CAI combustion increased the attainable output range and combustion stability. In their study, where the load was controlled by AFR only, injection during the recompression phase increased the lean limit significantly when compared to injection in the intake or compression stroke. The paper cites the main reason for the improvement in combustion as the reformation of the fuel, caused by exposure to the high in-cylinder temperatures during the early part of recompression phase. Though no detailed chemical analysis of this reformation process has been completed, it was assumed that the reformation improved the ignitability of the fuel, allowing CAI to occur with more diluted mixtures. This reforming process associated with early injection is an interesting topic that deserves further research and bettering understanding using advanced optical techniques. It was also found that injection at or after TDC during the recompression produced little improvement in combustion stability and lean limit over injection in the intake stroke. From this it would appear that there is a temperature threshold that must be breached in order for the fuel reformation to occur. This may suggest why the operating range at high speed, with larger amounts of residual gas and hence high recompression pressures and temperatures, increased with injection at EVC. In contrast, the less dilute mixture found at low speed with much lower recompression pressures may not reach the requisite temperature and hence responds less well.

7.4.2 Combustion Characteristics

As detailed in Section 6.3.3, analysis of in-cylinder pressure data allows easy quantification of many important characteristics of combustion. This section will discuss the effects of engine load, speed and valve and injection timing on ignition timing, burn duration and combustion stability.

7.4.2.1 Ignition Timing

Ignition timing for CAI combustion is defined as the crank angle at which 10% of the charge mass has been burned, as determined from the cumulative heat release profile. 10% MFB is chosen to define the point of ignition since the rate of heat release prior to this

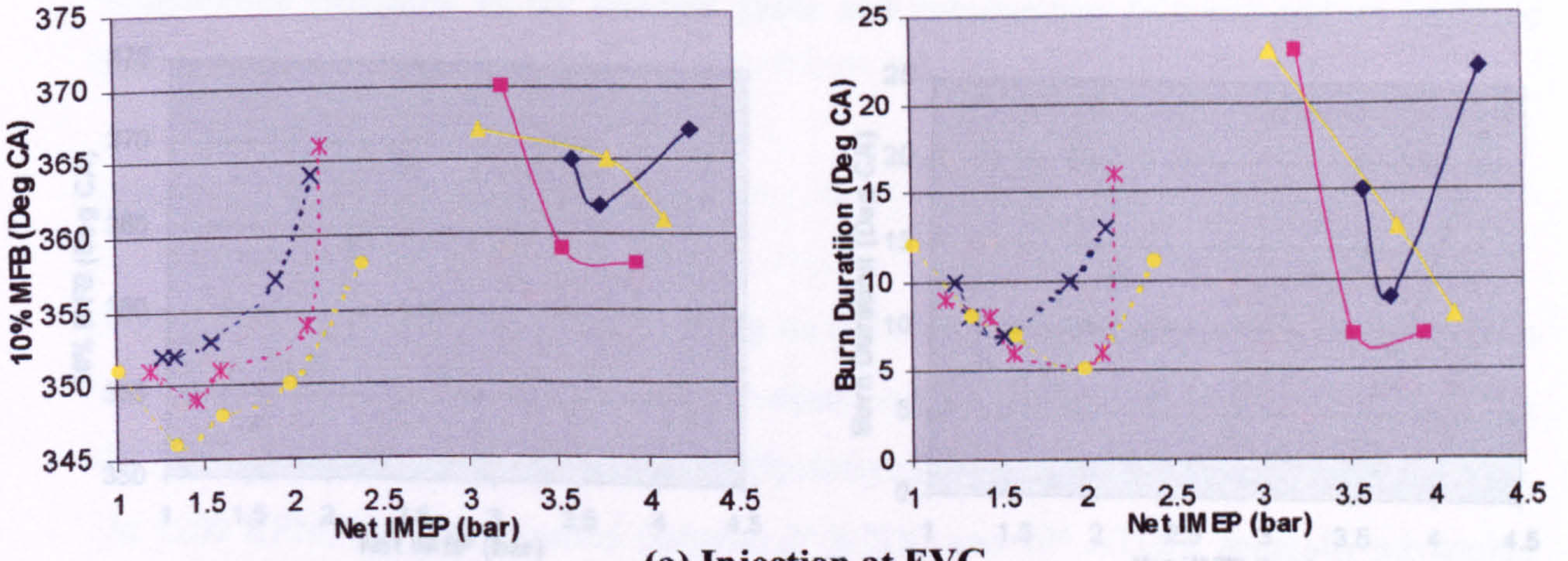

(a) Injection at EVC

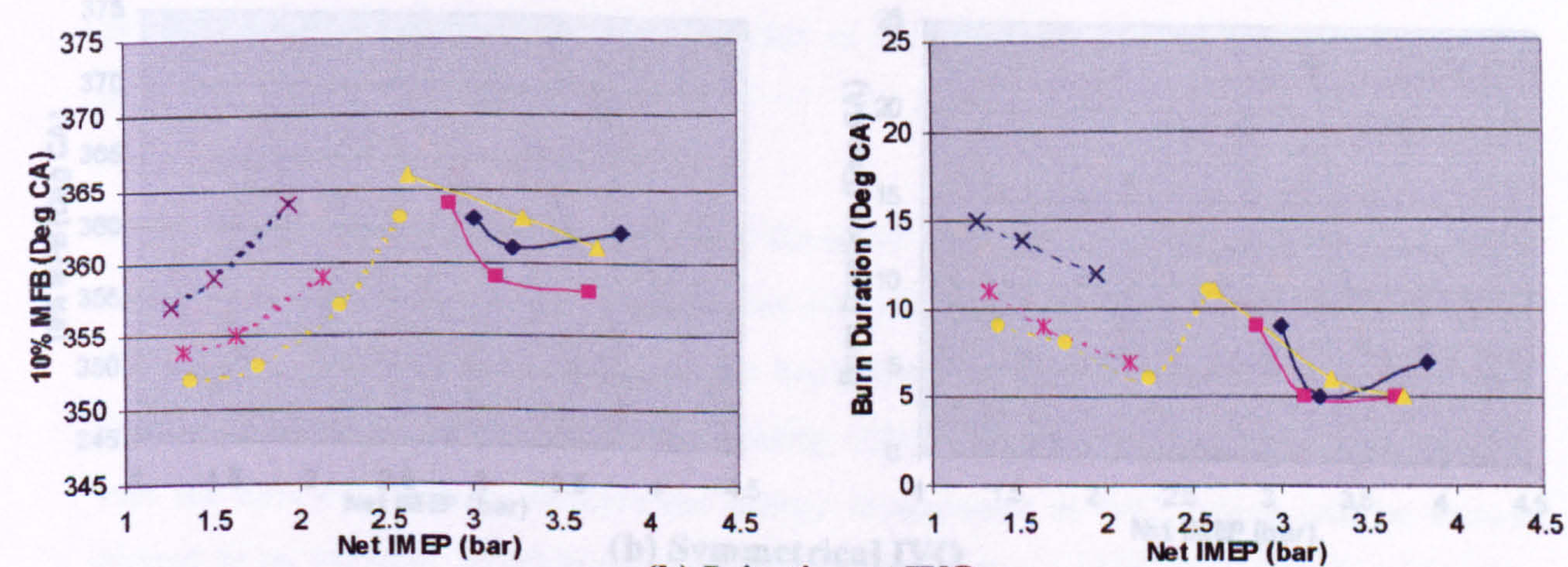

(b) Injection at IVO

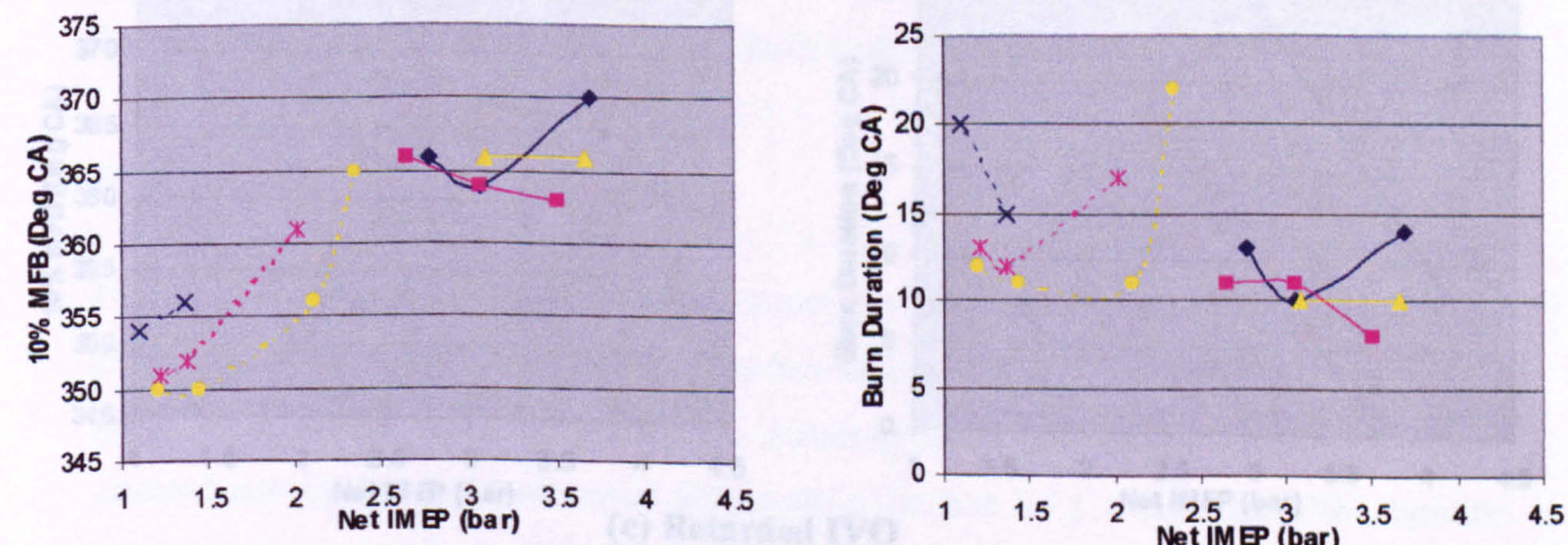

(c) Injection at BDC Intake

Figure 7.9 Variation in 10% MFB and Burn Duration with IVO Timing

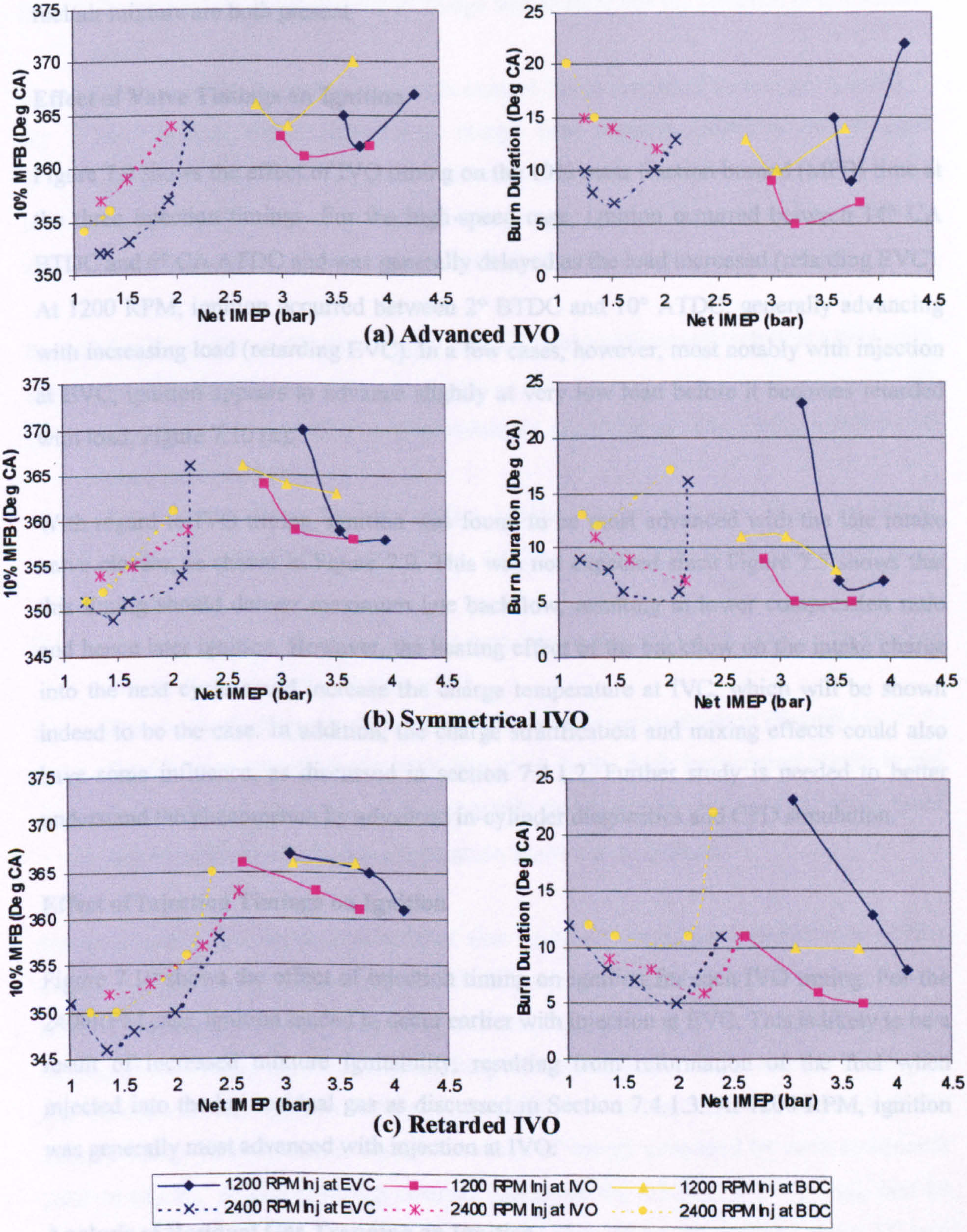

Figure 7.10 Variation in 10% MFB and Burn Duration with Injection Timing

point is generally very slow and making accurate assessment of ignition timing in this area very difficult. As discussed in Section 7.2 auto ignition will take place where sufficient temperature (supplied by the residual gases and compression process) and an ignitable fuel/air mixture are both present.

Effect of Valve Timings on Ignition

Figure 7.9 shows the effect of IVO timing on the 10% mass fraction burned (MFB) time at the three injection timings. For the high-speed case, ignition occurred between 14° CA BTDC and 6° CA ATDC and was generally delayed as the load increased (retarding EVC). At 1200 RPM, ignition occurred between 2° BTDC and 10° ATDC, generally advancing with increasing load (retarding EVC). In a few cases, however, most notably with injection at EVC, ignition appears to advance slightly at very low load before it becomes retarded with load, Figure 7.10 (a).

With regard to IVO timing, ignition was found to be most advanced with the late intake valve closure, as shown in Figure 7.9. This was not expected since Figure 7.5 shows that this timing should deliver maximum late backflow, resulting in lower compression ratio and hence later ignition. However, the heating effect of the backflow on the intake charge into the next cycle could increase the charge temperature at IVC, which will be shown indeed to be the case. In addition, the charge stratification and mixing effects could also have some influence, as discussed in section 7.4.1.2. Further study is needed to better understand the phenomenon by advanced in-cylinder diagnostics and CFD simulation.

Effect of Injection Timings on Ignition

Figure 7.10 shows the effect of injection timing on ignition for each IVO timing. For the 2400RPM case, ignition tended to occur earlier with injection at EVC. This is likely to be a result of increased mixture ignitability, resulting from reformation of the fuel when injected into the hot residual gas as discussed in Section 7.4.1.3. At 1200 RPM, ignition was generally most advanced with injection at IVO.

Analysis of Residual Gas Trapping on Ignition

Though Figures 7.9 and 7.10 show that combustion phasing is affected by injection timing, probably through changes in the igniteabiliy of the charge, it is predominately controlled by the quantity, temperature and other qualities of the residual gases. Zhao et al [95] studied the following five effects of recycled burned gases on four stroke CAI combustion:

i) Charge heating effect: Increased charge temperature due the presence of hot burned gases
ii) Dilution effect: Reduction in oxygen content due to increased burned gas quantity
iii) Heat capacity effect: Increase in charge heat capacity, primarily due to high quantities of H_2O and CO_2 present in burned gas.
iv) Chemical effect: Chemical reactions involving H_2O and CO_2 present in burned gas.
v) Stratification effect: Burned gases, fresh charge and fuel are not fully mixed.

By isolating the different effects through modelling and experimental techniques they were able to conclude the following:

i) The charge heating effect is responsible for advanced ignition timing and reduced combustion duration.
ii) The dilution effect does not affect ignition timing but was found to extend combustion duration. It also slows the heat release rate when present in large quantities.
iii) The heat capacity effect reduces the heat release rate and hence extends combustion in a similar way to the dilution effect.
iv) The chemical effect was found to have little effect on combustion phasing
v) Stratification permits ignition to take place in the high temperature region at the fresh residual gas interface. It is probable that complete mixing of the same gases would result in insufficient temperature to allow auto ignition.

Since the above investigation concluded that ignition timing was affected only by the charge temperature and stratification effects, a much simplified version of the above analysis was applied to this study using the data from the engine tests. An equation was developed to calculate the initial overall charge temperature (at IVC) in order to investigate any correlation with ignition timing. The steady flow energy equation shows that the internal energy of a mixture is equal to the sum of energy possessed by each component prior to mixing. In this case, the internal energy of the mixture at IVC, U_{Mix}, can be determined by the addition of internal energies possessed by the residual gases, U_R and inducted air, U_A, i.e.,

$$U_{Mix} = U_A + U_R \qquad (7.1)$$

However,

$$U_A = M_A . Cv_A .T_A , \tag{7.2}$$

$$U_R = M_R . Cv_R .T_R \tag{7.3}$$

And

$$U_{Mix} = M_{Mix} . Cv_{Mix} .T_{Mix} \tag{7.4}$$

where M_R, M_A and M_{Mix} are the residual, inducted and total gas masses respectively and T_R, T_A and T_{Mix} are the component and mixed gas temperatures. Cv_R and Cv_A are the constant volume heat capacities of the two components while Cv_{mix} is the average of the Cv_R and Cv_A values. Combining equations 7.1 - 7.4 and rewriting in terms of temperature, gives the overall mixture temperature, T_{Mix},

$$T_{Mix} =. \frac{(M_R . Cv_R .T_R) + (M_A .Cv_A .T_A)}{(M_{mix} .Cv_{mix})} \tag{7.5}$$

The equation includes only the charge heating effect and, since it assumes the charge to be fully mixed, allows any influence of stratification to be isolated. The heat capacity and dilution properties of the residual gas are included only in terms of their contribution to the overall charge temperature.

The results from this analysis are shown in Figure 7.11. They show that at low speed, the overall charge temperature falls by about 25°C across the operating range as the load is increased. The 2400RPM results show the opposite trend with charge temperature increasing with load, with a change in temperature across the operating range of around 100°C. Although it was anticipated that as ignition timing advanced, the overall charge temperature would increase, Figures 7.9 and 7.11 show an opposite trend. The most likely explanation for this is the strong effect of charge stratification on the combustion, neglected in this analysis, though this appears to function in a subtly different way at each engine test speed. At low speed the ignition timing generally becomes more advanced as load increases (Figures 7.9 and 7.10) and, while exhaust gas temperature increases (Figure 7.12), the estimated homogenous initial charge temperature falls (Figure 7.11) due to the

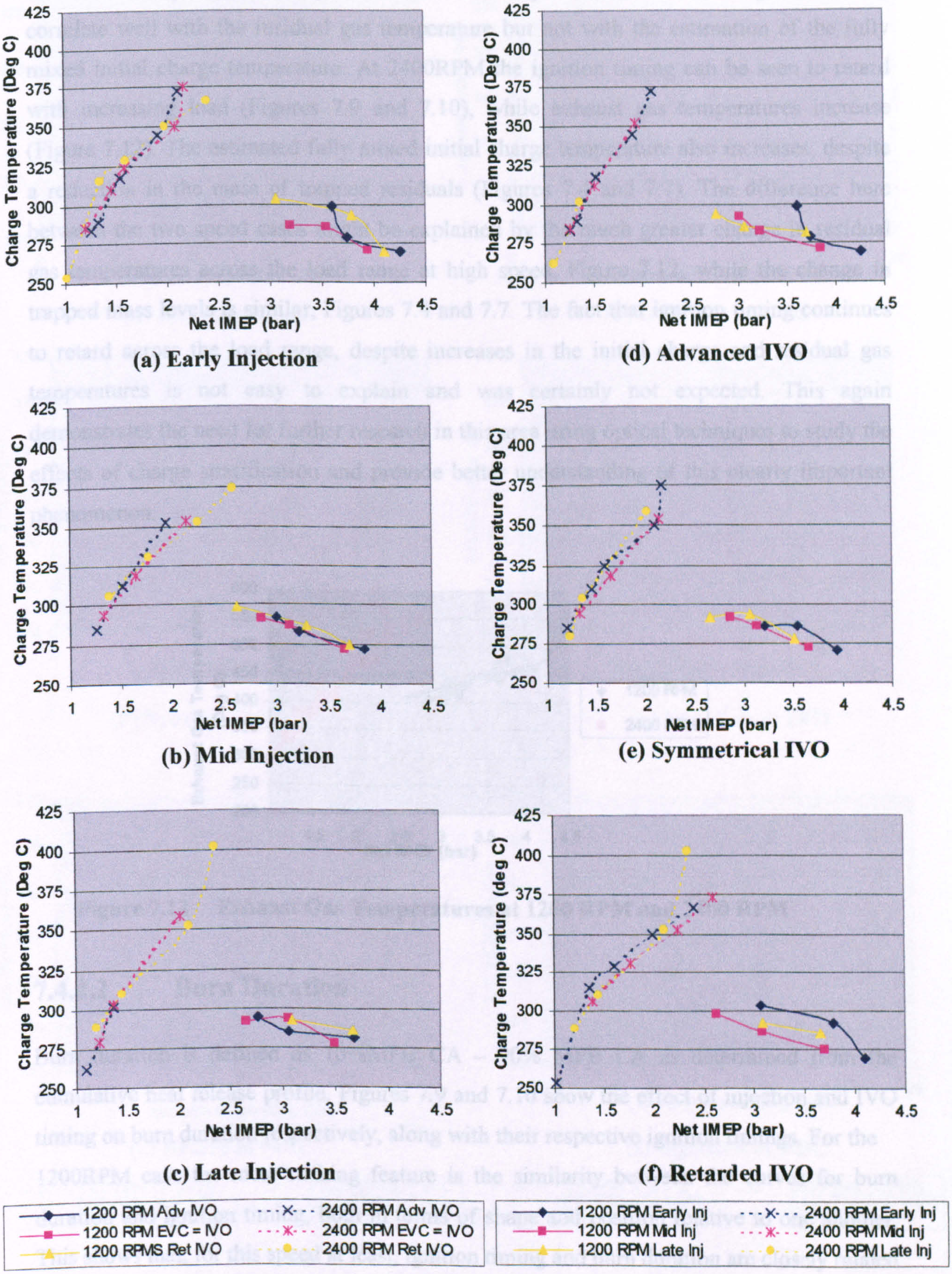

Figure 7.11 Variation in Initial Charge Temperature with Injection and IVO Timing

reduction in the amount of trapped gas (Figures 7.4 and 7.7). This suggests that strong stratification is present in the cylinder at the time of ignition, since trends in ignition timing correlate well with the residual gas temperature but not with the estimation of the fully mixed initial charge temperature. At 2400RPM the ignition timing can be seen to retard with increasing load (Figures 7.9 and 7.10), while exhaust gas temperatures increase (Figure 7.12). The estimated fully mixed initial charge temperature also increases, despite a reduction in the mass of trapped residuals (Figures 7.4 and 7.7). The difference here between the two speed cases might be explained by the much greater change in residual gas temperatures across the load range at high speed, Figure 7.12, while the change in trapped mass levels is similar, Figures 7.4 and 7.7. The fact that ignition timing continues to retard across the load range, despite increases in the initial charge and residual gas temperatures is not easy to explain and was certainly not expected. This again demonstrates the need for further research in this area using optical techniques to study the effects of charge stratification and provide better understanding of this clearly important phenomenon.

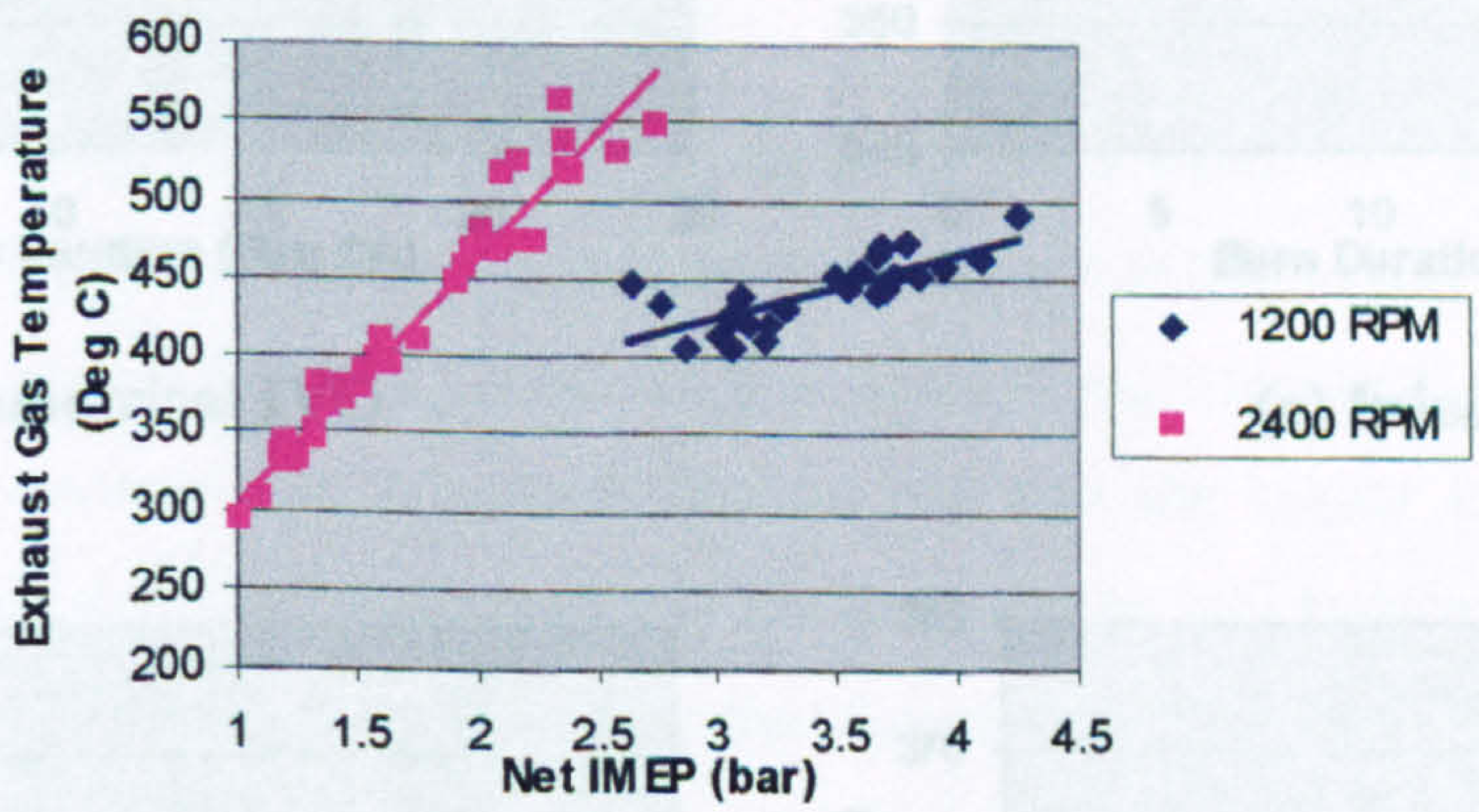

Figure 7.12 Exhaust Gas Temperatures at 1200 RPM and 2400 RPM

7.4.2.2 Burn Duration

Burn duration is defined as 10%MFB CA – 90% MFB CA as determined from the cumulative heat release profile. Figures 7.9 and 7.10 show the effect of injection and IVO timing on burn duration respectively, along with their respective ignition timings. For the 1200RPM case the most striking feature is the similarity between the curves for burn duration and ignition timing, both in terms of shape and position relative to one another. This shows that, for this speed at least, ignition timing and burn duration are closely related i.e. if combustion begins early then the burn duration will be short and visa versa and Figure 7.13 shows that this relationship is close to linear. This is not surprising, since early ignition (just before or around TDC in this case) is likely to produce both very fast rates of

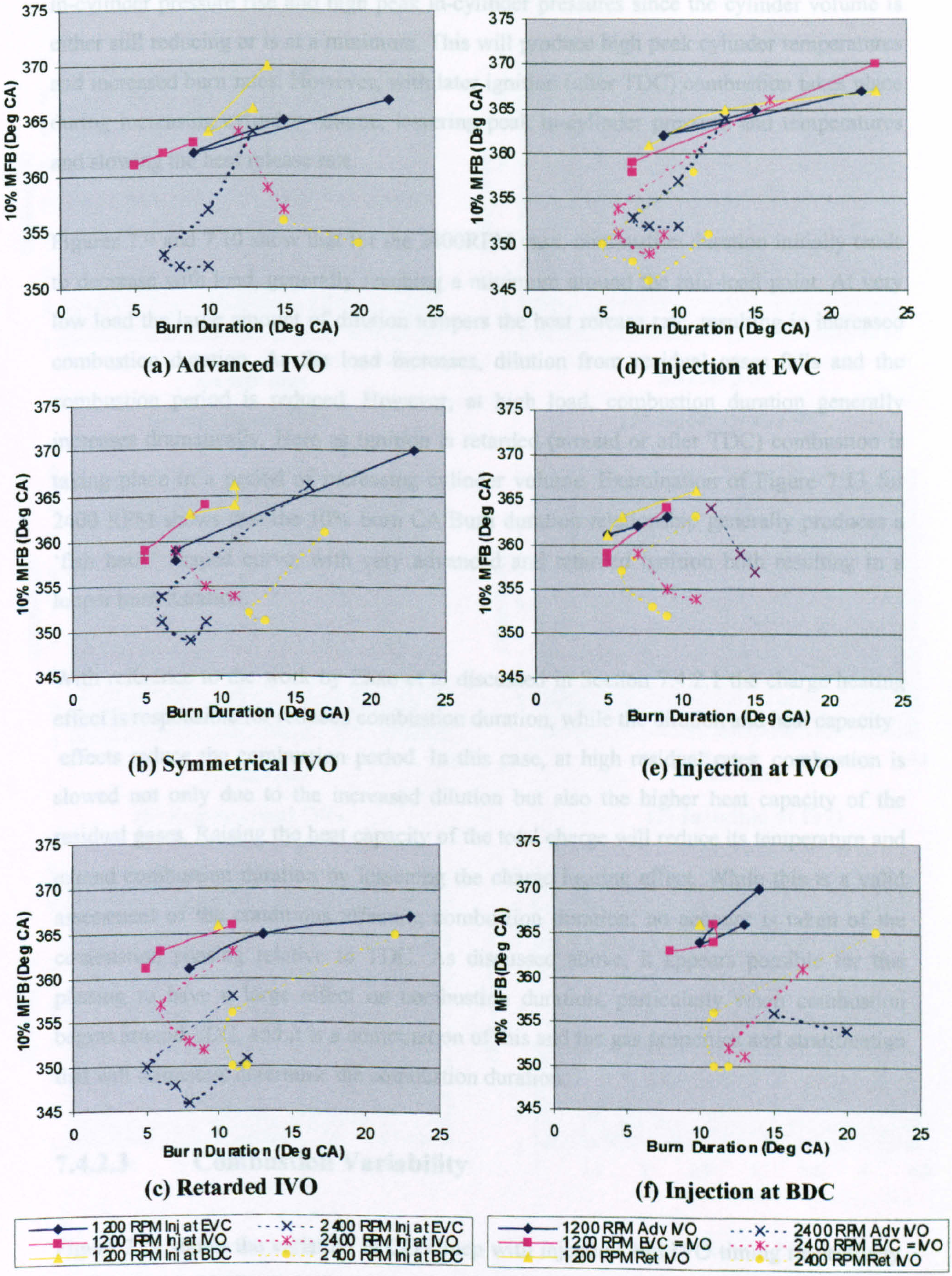

Figure 7.13 Relationship Between 10% MFB CA and Burn Duration with IVO and Injection Timing

in-cylinder pressure rise and high peak in-cylinder pressures since the cylinder volume is either still reducing or is at a minimum. This will produce high peak cylinder temperatures and increased burn rates. However, with later ignition (after TDC) combustion takes place during increasing cylinder volume, lowering peak in-cylinder pressure and temperatures and slowing the heat release rate.

Figures 7.9 and 7.10 show that for the 2400RPM case, combustion duration initially tends to decrease with load, generally reaching a minimum around the mid-load point. At very low load the large amount of dilution tempers the heat release rate, resulting in increased combustion duration. As the load increases, dilution from residual gases falls and the combustion period is reduced. However, at high load, combustion duration generally increases dramatically. Here as ignition is retarded (around or after TDC) combustion is taking place in a period of increasing cylinder volume. Examination of Figure 7.13 for 2400 RPM shows that the 10% burn CA/Burn duration relationship generally produces a 'fish hook' shaped curve, with very advanced and retarded ignition both resulting in a longer burn duration.

With reference to the work by Zhao et al discussed in Section 7.4.2.1 the charge heating effect is responsible for reduced combustion duration, while the dilution and heat capacity effects reduce the combustion period. In this case, at high residual rates, combustion is slowed not only due to the increased dilution but also the higher heat capacity of the residual gases. Raising the heat capacity of the total charge will reduce its temperature and extend combustion duration by lessening the charge heating effect. While this is a valid assessment of the conditions affecting combustion duration, no account is taken of the combustion phasing relative to TDC. As discussed above, it appears possible for this phasing to have a large effect on combustion duration, particularly when combustion begins around TDC, and it is a combination of this and the gas properties and stratification that will ultimately determine the combustion duration.

7.4.2.3 Combustion Variability

Figure 7.14 shows the variation in COVimep with injection and IVO timing respectively. At low speed COVimep is in the range or 2 to 5%, generally regarded as acceptable in terms of vehicle driveability. No particular trends can be identified with regard to the effects of IVO and injection timing across the load range.

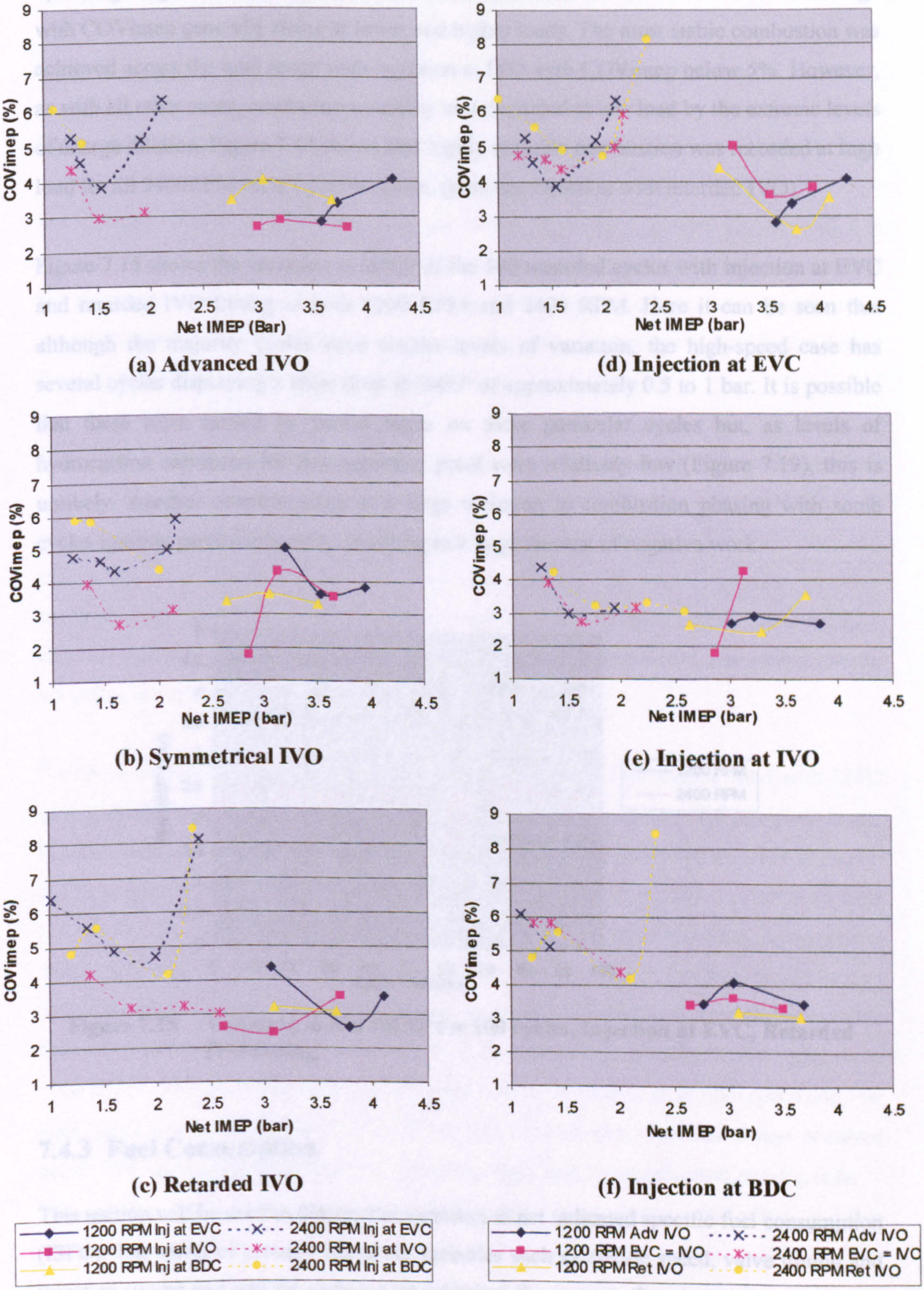

Figure 7.14 Variation in COVimep with IVO Timing and Injection Timing

High speed operation was generally much less stable, particularly at the extremes of the operating range. In each case, combustion was most stable in the centre of the load range with COVimep generally rising at lower and higher loads. The most stable combustion was achieved across the load range with injection at IVO with COVimep below 5%. However, as with all other cases, combustion stability was degraded at low load by the extreme levels of charge dilution. Figure 7.14 shows that highly unstable combustion was recorded at high load for all 2400RPM early injection cases, (plus late injection with retarded IVO).

Figure 7.15 shows the variation in IMEP of the 100 recorded cycles with injection at EVC and retarded IVO timing at both 1200 RPM and 2400 RPM. Here it can be seen that although the majority cycles have similar levels of variation, the high-speed case has several cycles displaying a large drop in IMEP of approximately 0.5 to 1 bar. It is possible that these were caused by partial burns on these particular cycles but, as levels of hydrocarbon emissions for this operating point were relatively low (Figure 7.19), this is unlikely. Another possible cause is a large variation in combustion phasing with some cycles igniting particularly early, resulting in a large amount of negative work.

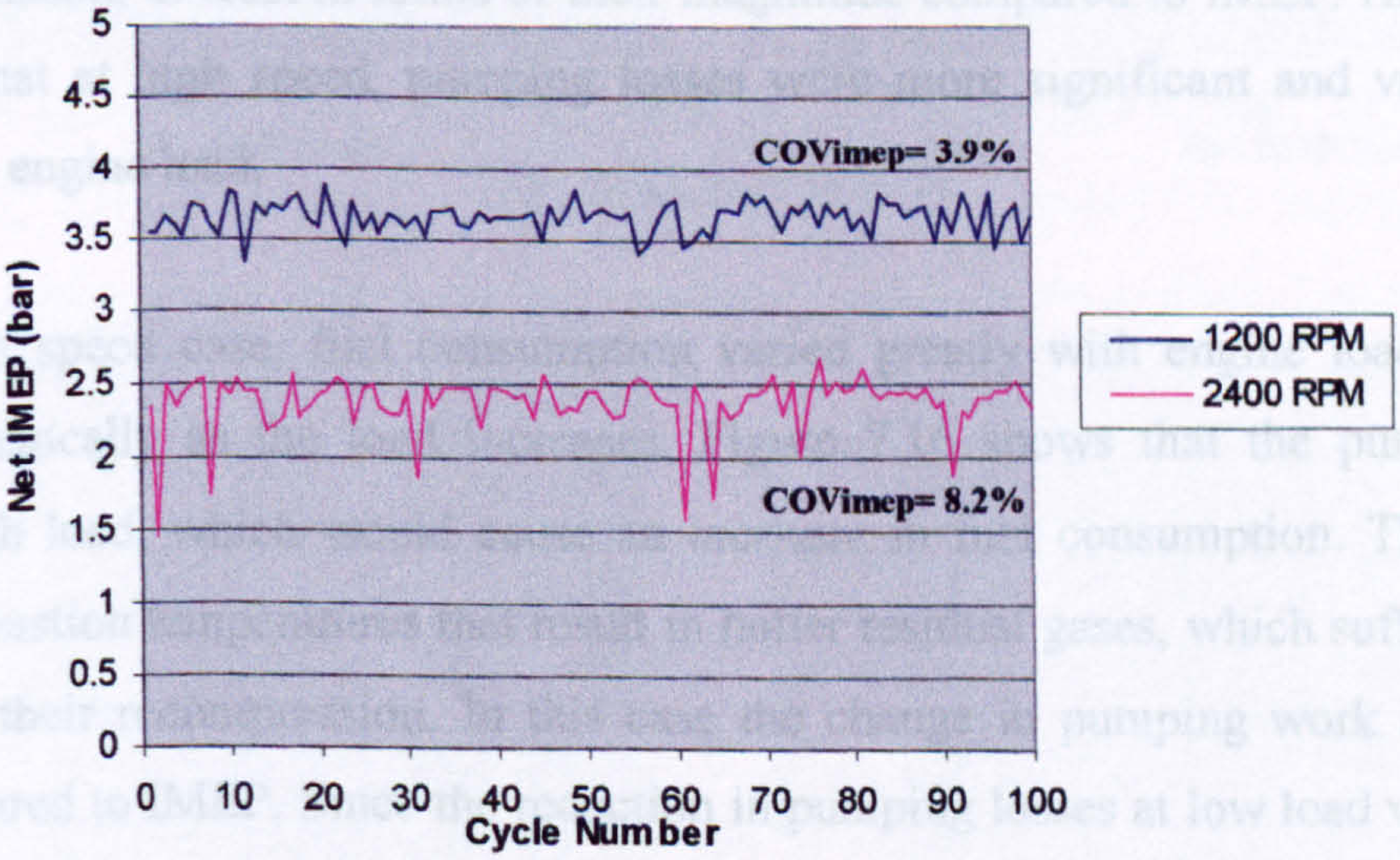

Figure 7.15 Variation in Net IMEP for 100 cycles, Injection at EVC, Retarded IVO timing

7.4.3 Fuel Consumption

This section will be used to discuss the variation in net indicated specific fuel consumption (ISFC). The effect of primary operating variables such as engine speed, valve timing and injection timing and will be analysed. In addition, the impact of variations in combustion phasing, pumping work, hydrocarbon emissions and combustion stability that result from changes in operating conditions will also be discussed.

7.4.3.1 Effect of Load and Speed

Figure 7.16 shows the net indicated specific fuel consumption (ISFC) and pumping work against engine load for different IVO timings respectively. Unlike a conventional homogenous charge SI engine that must use intake throttling to control engine load, this type of CAI engine uses valve timings to control the gas exchange process. For this reason the pumping losses normally associated with throttling during part load operation are absent. However, small amounts of pumping losses are incurred due to heat losses during the recompression of residual gases (Figure 7.2).

In the low and mid load range, low-speed operation yielded much lower fuel consumption compared to high speed. However, at high load fuel consumption was comparable for both speeds. Since the fuel consumption is calculated on an indicated output basis frictional effects can be neglected. Figure 7.16 shows that pumping losses for low speed operation are fairly constant, at least in terms of their magnitude compared to IMEP. However, they also show that at high speed, pumping losses were more significant and varied greatly according to engine load.

For the high speed case, fuel consumption varied greatly with engine load with ISFC falling dramatically as the load increases. Figure 7.16 shows that the pumping losses increase with load, which would cause an *increase* in fuel consumption. This is due to higher combustion temperatures that result in hotter residual gases, which suffer more heat loss during their recompression. In this case the change in pumping work is significant when compared to IMEP. Since the reduction in pumping losses at low load would tend to reduce fuel consumption, the increase in fuel consumption at low load must therefore come from other sources, the most likely of which is the combustion phasing. Referring again to Figures 7.9 and 7.10, which show the 10% burn times for each case, at high speed and low load, ignition occurred at least 8° CA BTDC and in many cases ignition always occurred before TDC across the load range. It is therefore likely that the combustion phasing is far from optimal, with a large amount of negative work being done on the piston and this could harm the fuel consumption to the extent shown in Figure 7.16 . One possible solution would be to retard the combustion phasing by operating with a leaner mixture and lower burned gas temperature.

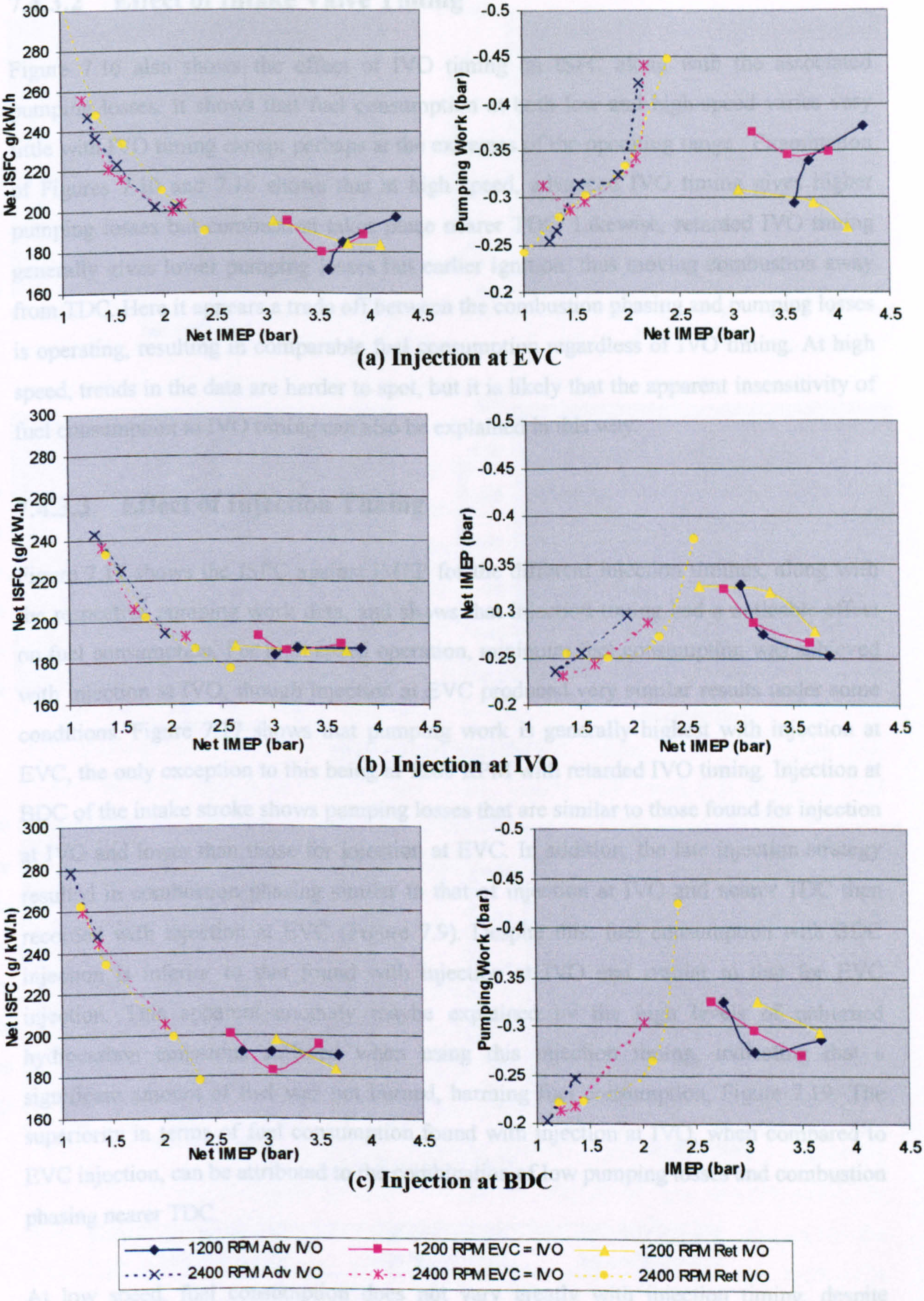

(a) Injection at EVC

(b) Injection at IVO

(c) Injection at BDC

Figure 7.16 Variation in ISFC and Pumping Work with IVO Timing

7.4.3.2 Effect of Intake Valve Timing

Figure 7.16 also shows the effect of IVO timing on ISFC along with the associated pumping losses. It shows that fuel consumption at both low and high-speed varies very little with IVO timing except perhaps at the extremes of the operating range. Examination of Figures 7.10 and 7.16 shows that at high speed, advanced IVO timing gives higher pumping losses but combustion takes place nearer TDC. Likewise, retarded IVO timing generally gives lower pumping losses but earlier ignition, thus moving combustion away from TDC. Here it appears a trade off between the combustion phasing and pumping losses is operating, resulting in comparable fuel consumption regardless of IVO timing. At high speed, trends in the data are harder to spot, but it is likely that the apparent insensitivity of fuel consumption to IVO timing can also be explained in this way.

7.4.3.3 Effect of Injection Timing

Figure 7.17 shows the ISFC against IMEP for the different injection timings, along with the respective pumping work data, and shows that injection timing had a noticable effect on fuel consumption. For high speed operation, minimum fuel consumption was achieved with injection at IVO, though injection at EVC produced very similar results under some conditions. Figure 7.17 shows that pumping work is generally highest with injection at EVC, the only exception to this being at 1200 RPM with retarded IVO timing. Injection at BDC of the intake stroke shows pumping losses that are similar to those found for injection at IVO and lower than those for injection at EVC. In addition, the late injection strategy resulted in combustion phasing similar to that of injection at IVO and nearer TDC than recorded with injection at EVC (Figure 7.9). Despite this, fuel consumption with BDC injection is inferior to that found with injection at IVO and similar to that for EVC injection. This apparent anomaly maybe explained by the high levels of unburned hydrocarbon emissions suffered when using this injection timing, indicating that a significant amount of fuel was not burned, harming fuel consumption, Figure 7.19. The superiority in terms of fuel consumption found with injection at IVO, when compared to EVC injection, can be attributed to the combination of low pumping losses and combustion phasing nearer TDC.

At low speed, fuel consumption does not vary greatly with injection timing, despite significant differences in pumping work and combustion phasing in each case. It is likely that there was a trade-off in these two effects resulting in broadly similar fuel consumption with each injection timing.

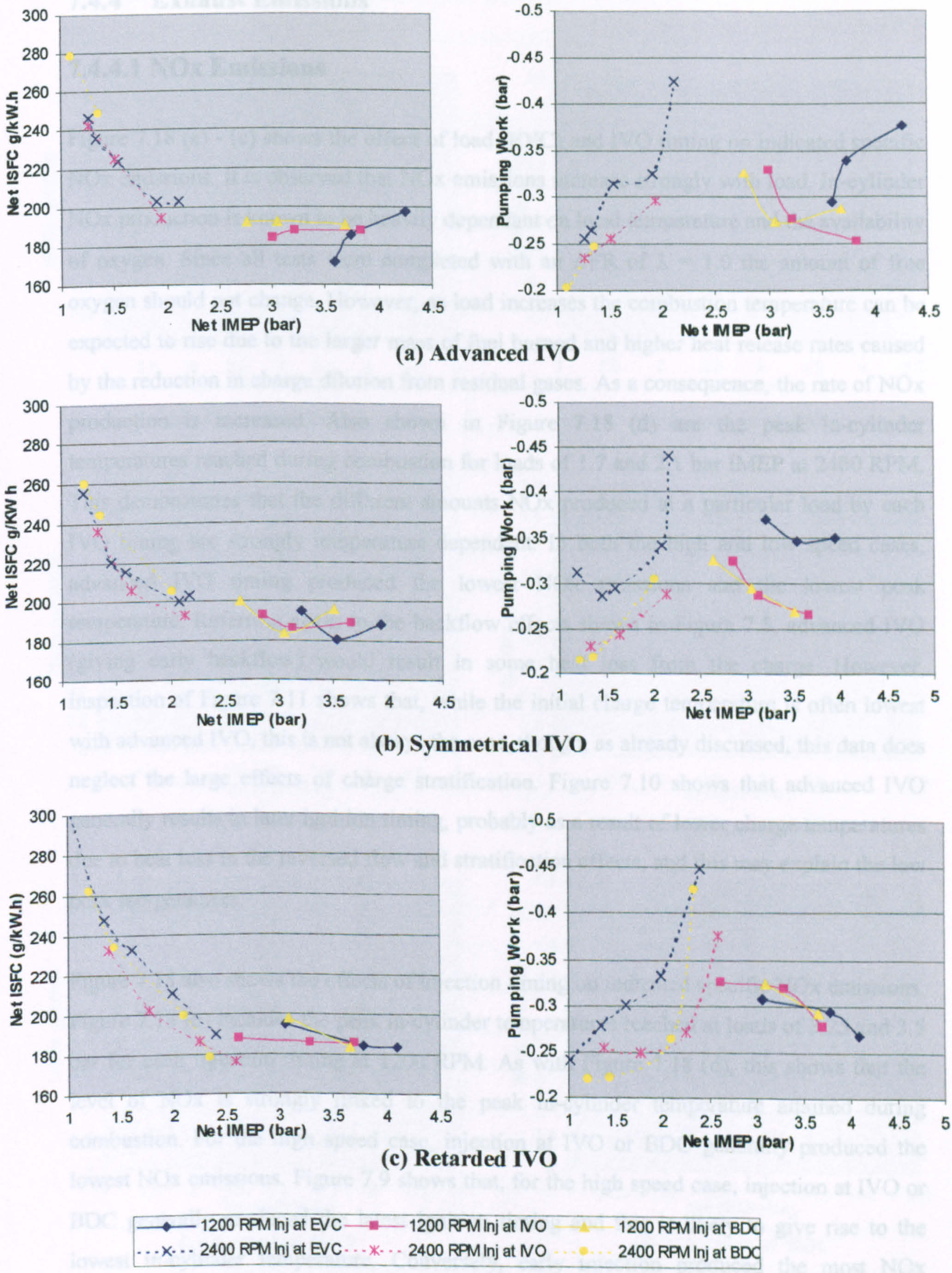

Figure 7.17 Variation in ISFC and Pumping Work with Injection Timing

7.4.4 Exhaust Emissions

7.4.4.1 NOx Emissions

Figure 7.18 (a) - (c) shows the effect of load (EVC) and IVO timing on indicated specific NOx emissions. It is observed that NOx emissions increase strongly with load. In-cylinder NOx production is known to be heavily dependant on local temperature and the availability of oxygen. Since all tests were completed with an AFR of $\lambda = 1.0$ the amount of free oxygen should not change. However, as load increases the combustion temperature can be expected to rise due to the larger mass of fuel burned and higher heat release rates caused by the reduction in charge dilution from residual gases. As a consequence, the rate of NOx production is increased. Also shown in Figure 7.18 (d) are the peak in-cylinder temperatures reached during combustion for loads of 1.7 and 2.1 bar IMEP at 2400 RPM. This demonstrates that the different amounts NOx produced at a particular load by each IVO timing are strongly temperature dependent. In both the high and low speed cases, advanced IVO timing produced the lowest NOx emissions and the lowest peak temperature. Referring again to the backflow effects shown in Figure 7.5, advanced IVO (giving early backflow) would result in some heat loss from the charge. However, inspection of Figure 7.11 shows that, while the initial charge temperature is often lowest with advanced IVO, this is not always the case, though, as already discussed, this data does neglect the large effects of charge stratification. Figure 7.10 shows that advanced IVO generally results in later ignition timing, probably as a result of lower charge temperatures due to heat loss in the reversed flow and stratification effects, and this may explain the low peak temperatures.

Figure 7.18 also shows the effects of injection timing on indicated specific NOx emissions. Figure 7.18 (b) includes the peak in-cylinder temperatures reached at loads of 3.25 and 3.5 bar for each injection timing at 1200 RPM. As with Figure 7.18 (d), this shows that the level of NOx is strongly linked to the peak in-cylinder temperature attained during combustion. For the high speed case, injection at IVO or BDC generally produced the lowest NOx emissions. Figure 7.9 shows that, for the high speed case, injection at IVO or BDC generally produced the latest ignition timing and this is likely to give rise to the lowest in-cylinder temperature. Conversely, early injection produced the most NOx emissions and had the earliest ignition timing At 1200 RPM the highest NOx emissions and in-cylinder temperatures were generally attained with injection at IVO and Figure 7.9 also shows that mid injection results in earlier ignition timing. The lowest NOx emissions

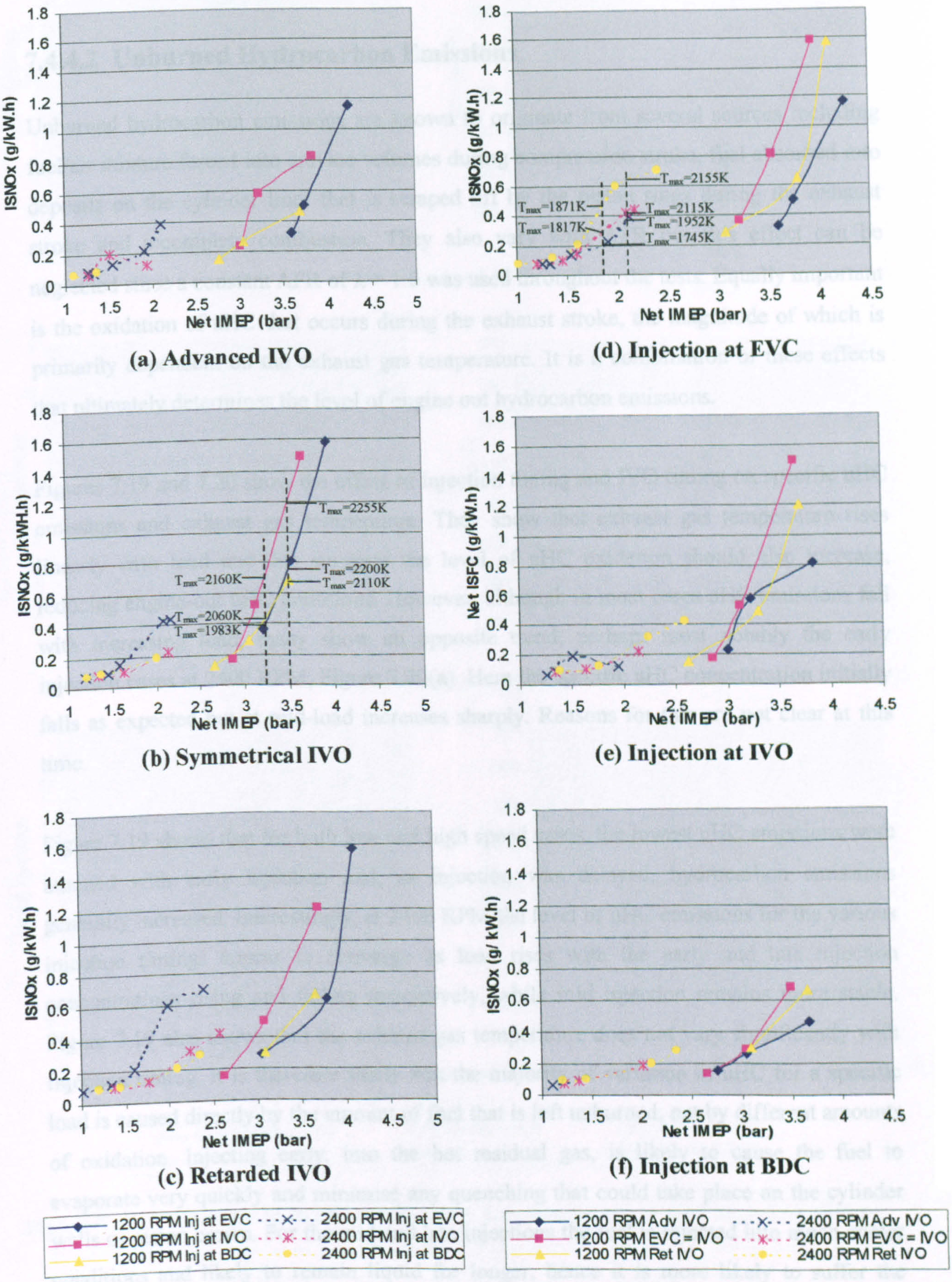

Figure 7.18 Variation in ISNOx Emissions with Injection Timing and IVO timing

throughout the range were produced with late and early injection at low and high load respectively. Again the reason for this appears to be the later combustion phasing.

7.4.4.2 Unburned Hydrocarbon Emissions

Unburned hydrocarbon emissions are known to originate from several sources including fuel/air mixture forced into crevice volumes during compression stroke, fuel absorbed into deposits on the cylinder liner that is scraped off by the piston rings during the exhaust stroke and incomplete combustion. They also vary with AFR but this effect can be neglected since a constant AFR of $\lambda = 1.0$ was used throughout the tests. Equally important is the oxidation of uHC that occurs during the exhaust stroke, the magnitude of which is primarily dependent on the exhaust gas temperature. It is a combination of these effects that ultimately determines the level of engine out hydrocarbon emissions.

Figures 7.19 and 7.20 show the effect of injection timing and IVO timing on specific uHC emissions and exhaust gas temperature. They show that exhaust gas temperature rises linearly with load and this suggests the level of uHC oxidation should also increase, reducing engine-out uHC emissions. However, although in most cases uHC emissions fall with increasing load, many show an opposite trend, perhaps most notably the early injection cases at 2400 RPM, Figure 7.20(a). Here the specific uHC concentration initially falls as expected but at mid-load increases sharply. Reasons for this are not clear at this time.

Figure 7.19 shows that for both low and high speed cases, the lowest uHC emissions were attained with early injection and, as injection was delayed, hydrocarbon emissions generally increased. Interestingly, at 2400 RPM the level of uHC emissions for the various injection timings appear to converge as load rises with the early and late injection concentrations rising and falling respectively, while mid injection remains more stable. Figure 7.19 also shows that the exhaust gas temperature does not vary significantly with injection timing. It is therefore likely that the majority of variation in uHC for a specific load is caused directly by the amount of fuel that is left unburned, not by different amounts of oxidation. Injecting early, into the hot residual gas, is likely to cause the fuel to evaporate very quickly and minimise any quenching that could take place on the cylinder walls or piston crown. For the mid and late injections the fuel is injected into much cooler conditions and likely to remain liquid for longer, hence it is more likely to suffer the effects of quenching. In addition, Urushihara et al [9] found that injection during the

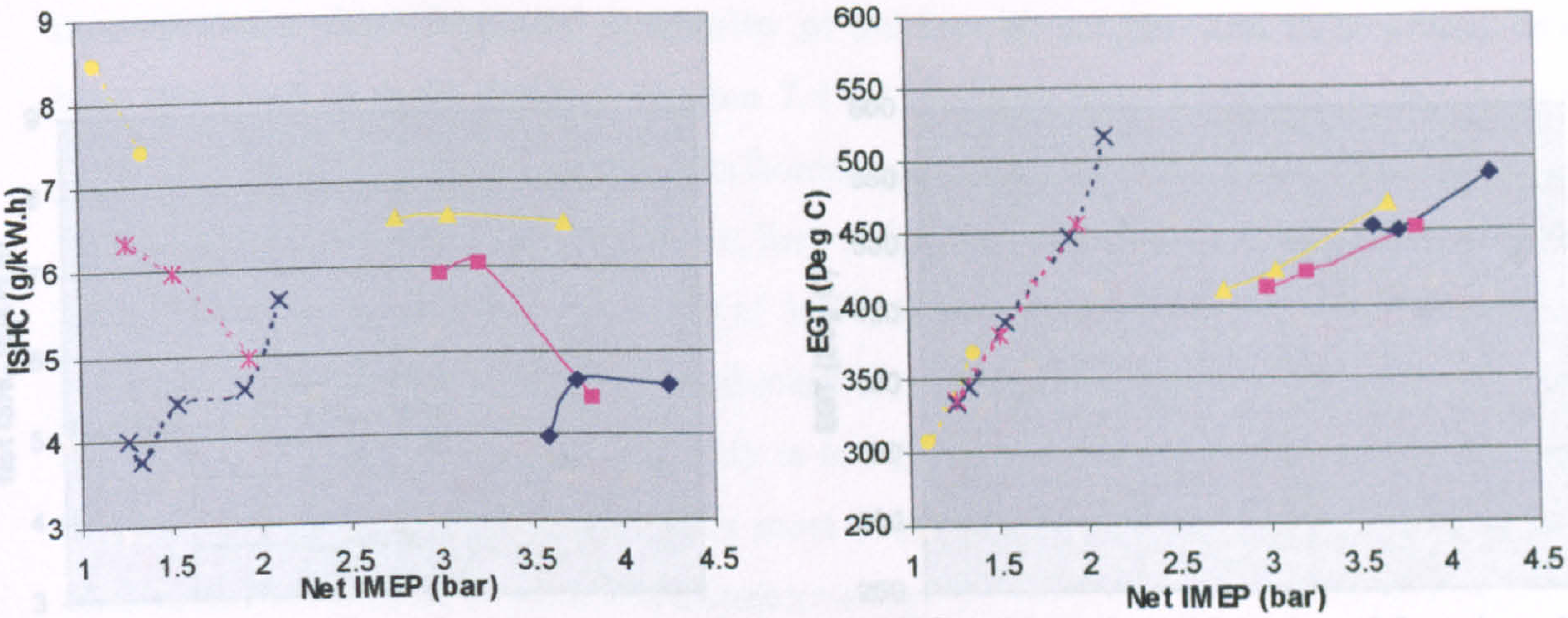

(a) Advanced IVO

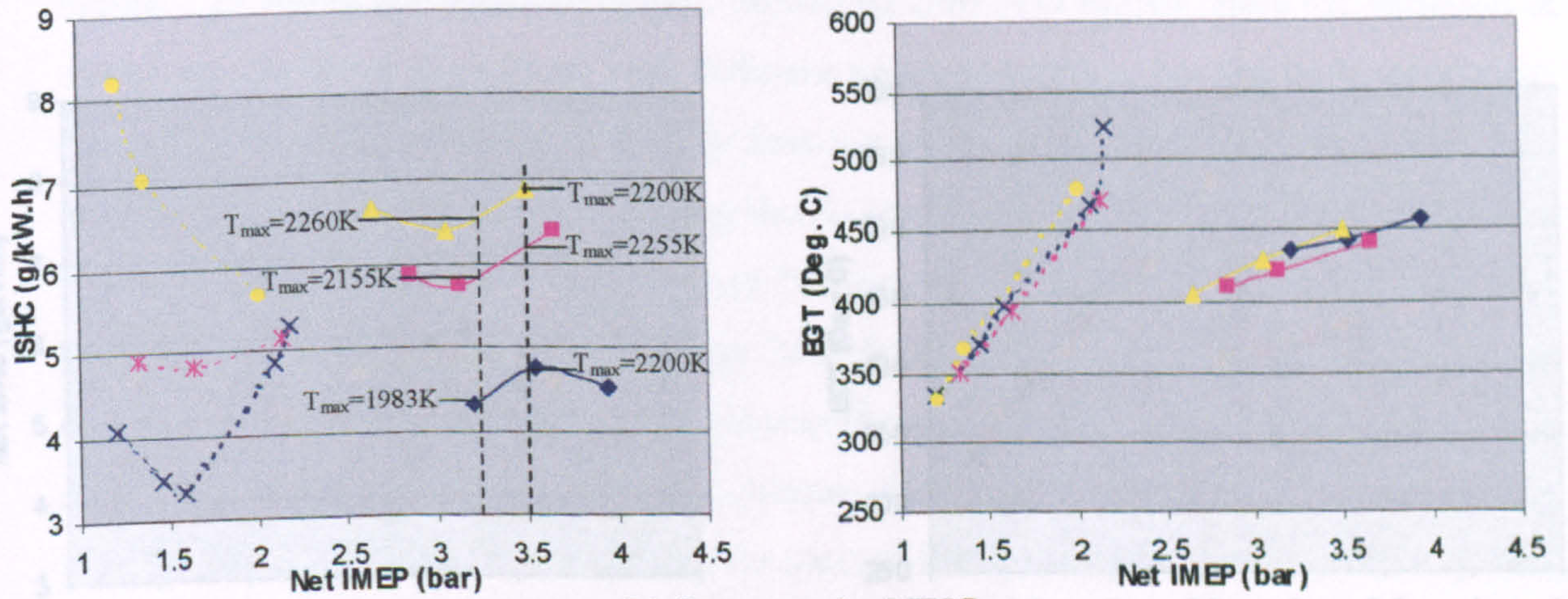

(b) Symmetrical IVO

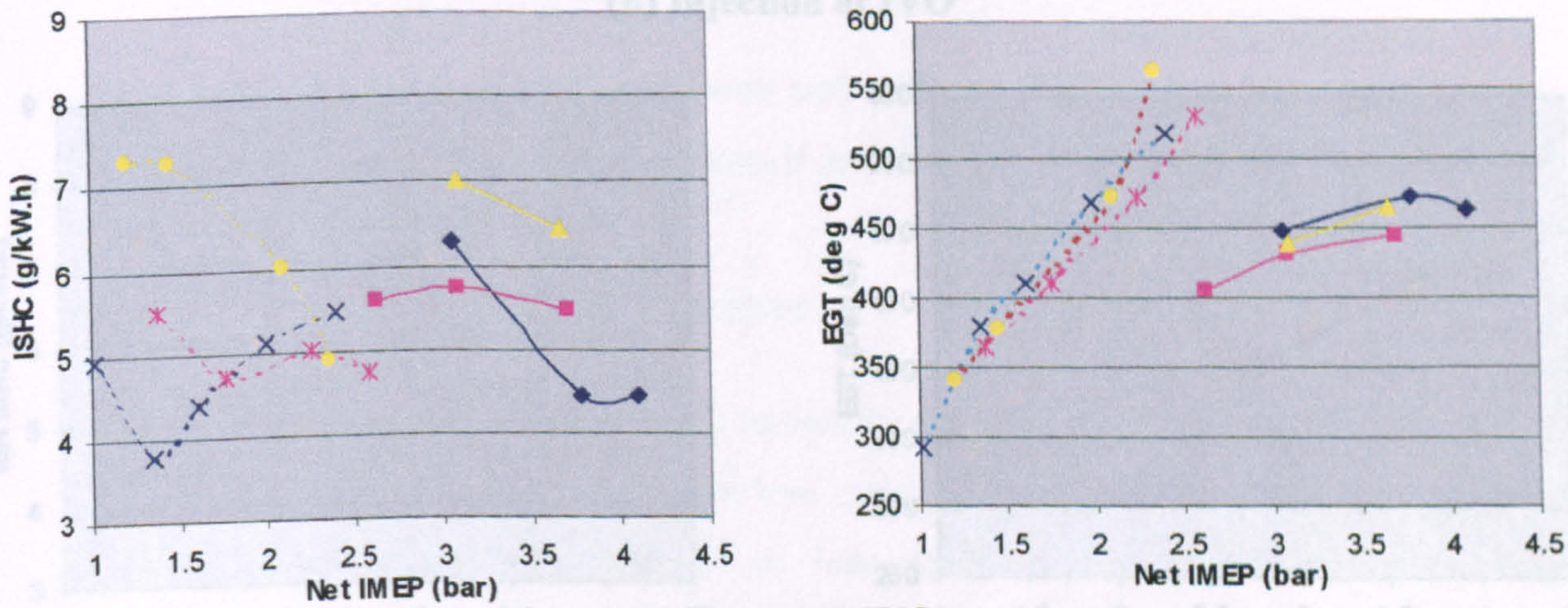

(c) Retarded IVO

Figure 7.19 Variation in ISHC and Exhaust Gas Temperature with Injection Timing

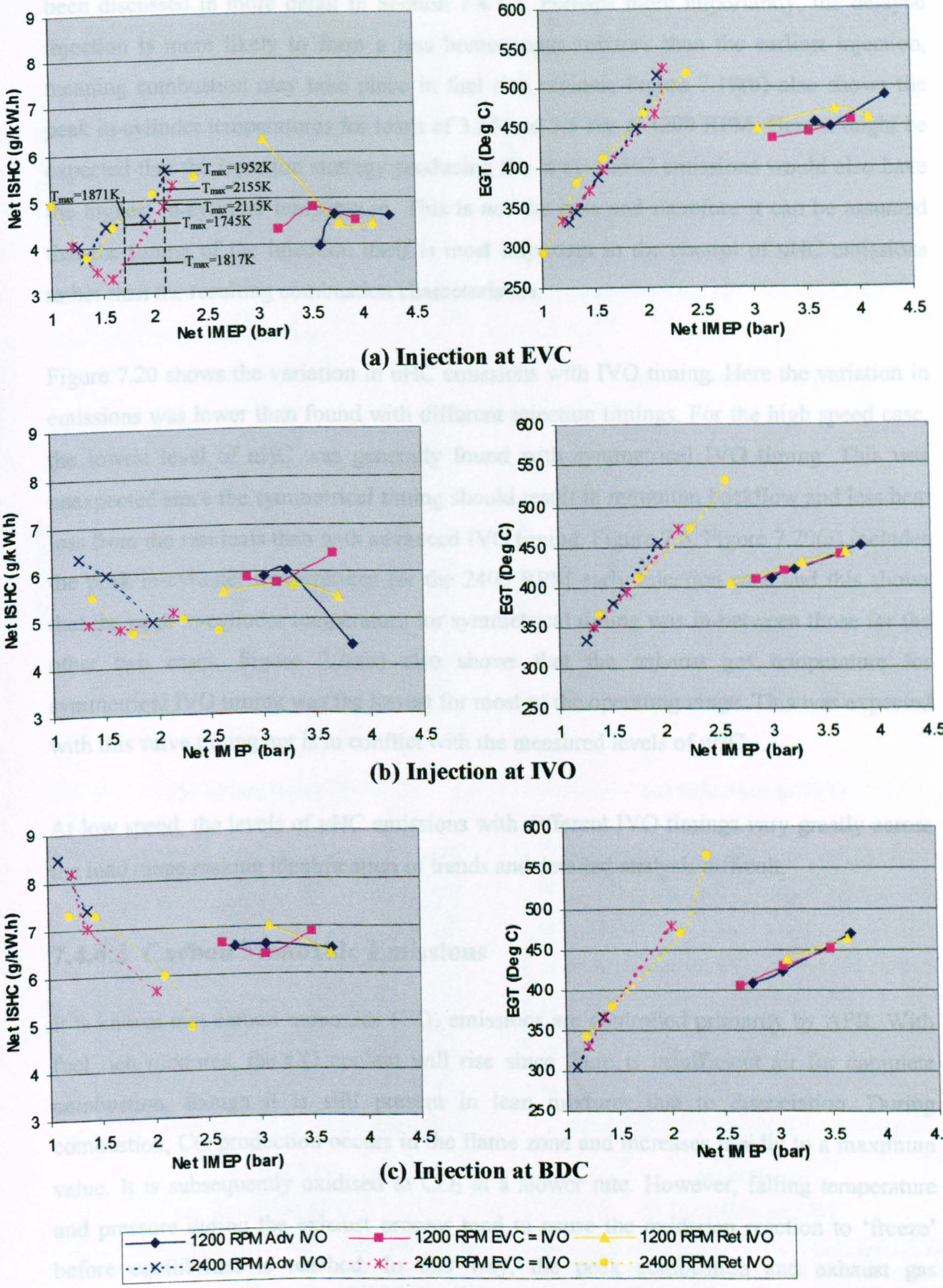

Figure 7.20 Variation in ISHC Emissions and Exhaust Gas Temperature with IVO Timing

recompression phase increased ignitability of the fuel air mixture and these effects have been discussed in more detail in Section 7.4.1.3. Perhaps more importantly, the delayed injection is more likely to form a less homogenous mixture than the earliest injection, meaning combustion may take place in fuel rich regions. Figure 7.19(b) also shows the peak in-cylinder temperatures for loads of 3.25 and 3.5 bar at 1200 RPM. Here it might be expected that the injection strategy producing the lowest uHC emissions would also have the highest in-cylinder temperature. This is not the case and therefore it can be assumed that the timing of the injection itself is most important in the control of uHC emissions rather than the resulting combustion characteristics.

Figure 7.20 shows the variation in uHC emissions with IVO timing. Here the variation in emissions was lower than found with different injection timings. For the high speed case, the lowest level of uHC was generally found with symmetrical IVO timing. This was unexpected since the symmetrical timing should result in minimum backflow and less heat loss from the residuals than with advanced IVO timing, Figure 7.5. Figure 7.20(a) includes the peak in-cylinder temperatures for the 2400 RPM early injection case and this shows that the peak in-cylinder temperature for symmetrical timing was in-between those for the other two cases. Figure 7.20(a) also shows that the exhaust gas temperature for symmetrical IVO timing was the lowest for most of the operating range. This was expected with this valve timing but is in conflict with the measured levels of uHC.

At low speed, the levels of uHC emissions with different IVO timings vary greatly across the load range making identification of trends and detailed analysis difficult.

7.4.4.3 Carbon Monoxide Emissions

It is known that carbon monoxide (CO) emissions are controlled primarily by AFR. With fuel rich mixtures, the CO content will rise since there is insufficient air for complete combustion, though it is still present in lean mixtures due to dissociation. During combustion, CO production occurs in the flame zone and increases rapidly to a maximum value. It is subsequently oxidised to CO_2 at a slower rate. However, falling temperature and pressure during the exhaust process tend to cause the oxidation reaction to 'freeze' before equilibrium is reached. In this way, the peak combustion and exhaust gas temperatures affect exhaust gas CO concentrations. Generally, low exhaust gas temperatures result in higher levels of CO since less oxidation takes place.

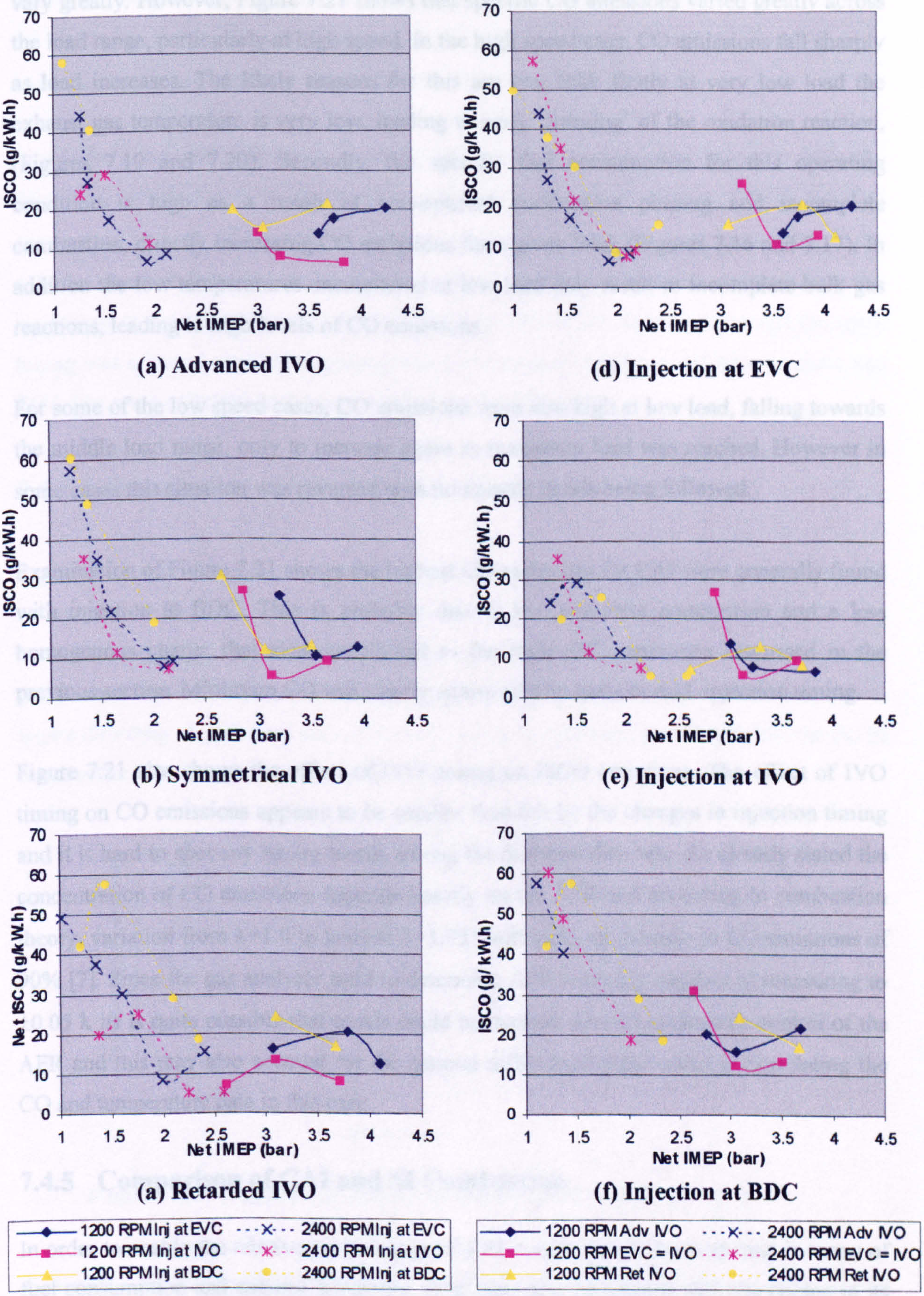

Figure 7.21 Variation in ISCO Emissions with Injection Timing and IVO Timing

Since the AFR was held at $\lambda = 1.0$ for all experiments the CO emissions were not expected vary greatly. However, Figure 7.21 shows that specific CO emissions varied greatly across the load range, particularly at high speed. In the high speed case, CO emissions fall sharply as load increases. The likely reasons for this are two fold: firstly at very low load the exhaust gas temperature is very low, leading to early 'freezing' of the oxidation reaction, (Figures 7.19 and 7.20). Secondly, the specific fuel consumption for this operating condition is high as a result of non-optimal combustion phasing and incomplete combustion, directly increasing CO emissions for a given load, (Figures 7.16 and 7.17). In addition the low temperatures encountered at low load may result in incomplete bulk gas reactions, leading to high levels of CO emissions.

For some of the low speed cases, CO emissions were also high at low load, falling towards the middle load range, only to increase again as maximum load was reached. However in some cases this situation was reversed with no notable trends being followed.

Examination of Figure 7.21 shows the highest CO emissions for CAI were generally found with injection at BDC. This is probably due to less complete combustion and a less homogenous charge that also contributed to the high uHC emissions discussed in the previous section. Minimum CO was mainly achieved with early or mid injection timing.

Figure 7.21 also shows the effect of IVO timing on ISCO emissions. The effect of IVO timing on CO emissions appears to be smaller than felt by the changes in injection timing and it is hard to spot any strong trends among the different data sets. As already stated the concentration of CO emissions depends heavily on the AFR and according to combustion theory, variation from $\lambda=1.0$ to lambda $\lambda=1.025$ will yield an increase in CO emissions of 90% [7]. Since the gas analyser used to determine AFR was only capable of measuring to $\pm 0.05\ \lambda$ its is quite possible that trends could be masked through inadequate control of the AFR and this may also account for the general difficulties experienced in correlating the CO and temperature data in this case.

7.4.5 Comparison of CAI and SI Combustion

In order to enable the relative performance of CAI combustion to be evaluated in terms of fuel consumption and exhaust emissions, tests were also completed with the engine in its conventional spark ignited mode. The only changes made to the engine were the replacement of the short duration camshafts with a pair having conventional production timings and the installation of a throttle and plenum chamber to the intake. The fuel injection and spark drivers remained unchanged, as did the measurement systems. As with the CAI tests, the engine was operated with an AFR of λ = 1.0. This time, however, only one injection timing was used, taking place at 90°CA ATDC in the intake stroke.

In order to allow and effective comparison between the two combustion types to be made, data were required over a comparable load range. The load range in IMEP for CAI combustion at each of the test speeds was determined from the post processing of the cylinder pressure data. The engine was then tested in SI mode at various points across this load range at the original test speeds of 1200 and 2400 RPM. At each test point the spark timing was adjusted until MBT timing was achieved and emissions, cylinder pressure and EGT data were collected in the same manner as the CAI tests.

7.4.5.1 Comparison of Fuel Consumption

Figure 7.22 shows that the maximum reduction in fuel consumption obtained with CAI combustion varies from 9% to 17% over the load and speed range tested. For both test speeds, the biggest reduction in ISFC was obtained at the lower end of the load range. The main reason for this is the large pumping losses suffered by SI engines at low load due to intake throttling. As the load increases, throttling is reduced and pumping losses for the SI combustion fall, along with the reduction in fuel consumption.

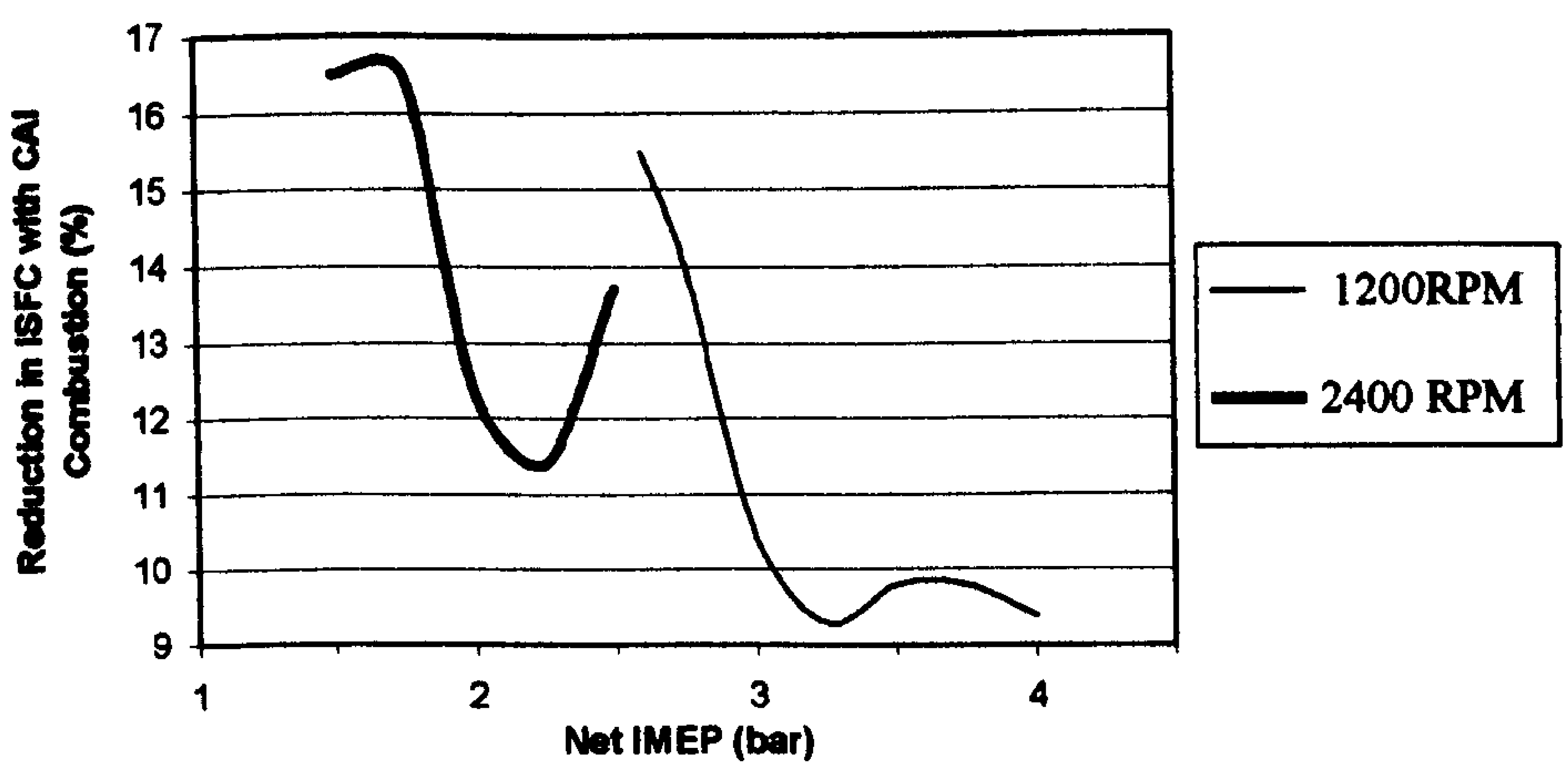

Figure 7.22 Maximum Reduction in ISFC with CAI Combustion

A smaller contributor to the reduced fuel consumption is the increased cycle efficiency of CAI combustion. The extremely rapid combustion around TDC following auto-ignition means that heat addition takes place at near constant volume leading to higher thermal efficiency.

7.4.5.2 Comparison of NOx Emissions

Figure 7.23 shows the maximum reduction in NOx emissions obtained with CAI combustion when compared to the engine operating in its conventional SI mode. It can be seen that the reductions in NOx emissions achievable from CAI combustion are in the region of 98 to 80%. Though the NOx emissions in SI mode did increase slightly with load the percentage change was over two orders of magnitude less than with CAI combustion.

The significant reduction in NOx emissions with CAI combustion can again be attributed to the low temperatures encountered with CAI combustion. As local in-cylinder temperatures increase to 1800K and higher, NOx production rates increase exponentially. With SI combustion the burned gas region is subject to compression and can reach 2500K, well above the threshold required for major NOx production. With CAI combustion, however, the temperature of the cylinder contents remains relatively uniform throughout the event due to the absence of the hot burned gas found in SI combustion. Thus, significant NOx production is only witnessed if the bulk charge temperature exceeds 1800K.

Also shown in Figure 7.23 is the nearest load point where the 1800K threshold is crossed. For the 2400 RPM case, the reduction in NOx emissions decreases rapidly as this point is passed. For low speed the threshold is passed shortly after minimum load after which the reduction in NOx falls steeply.

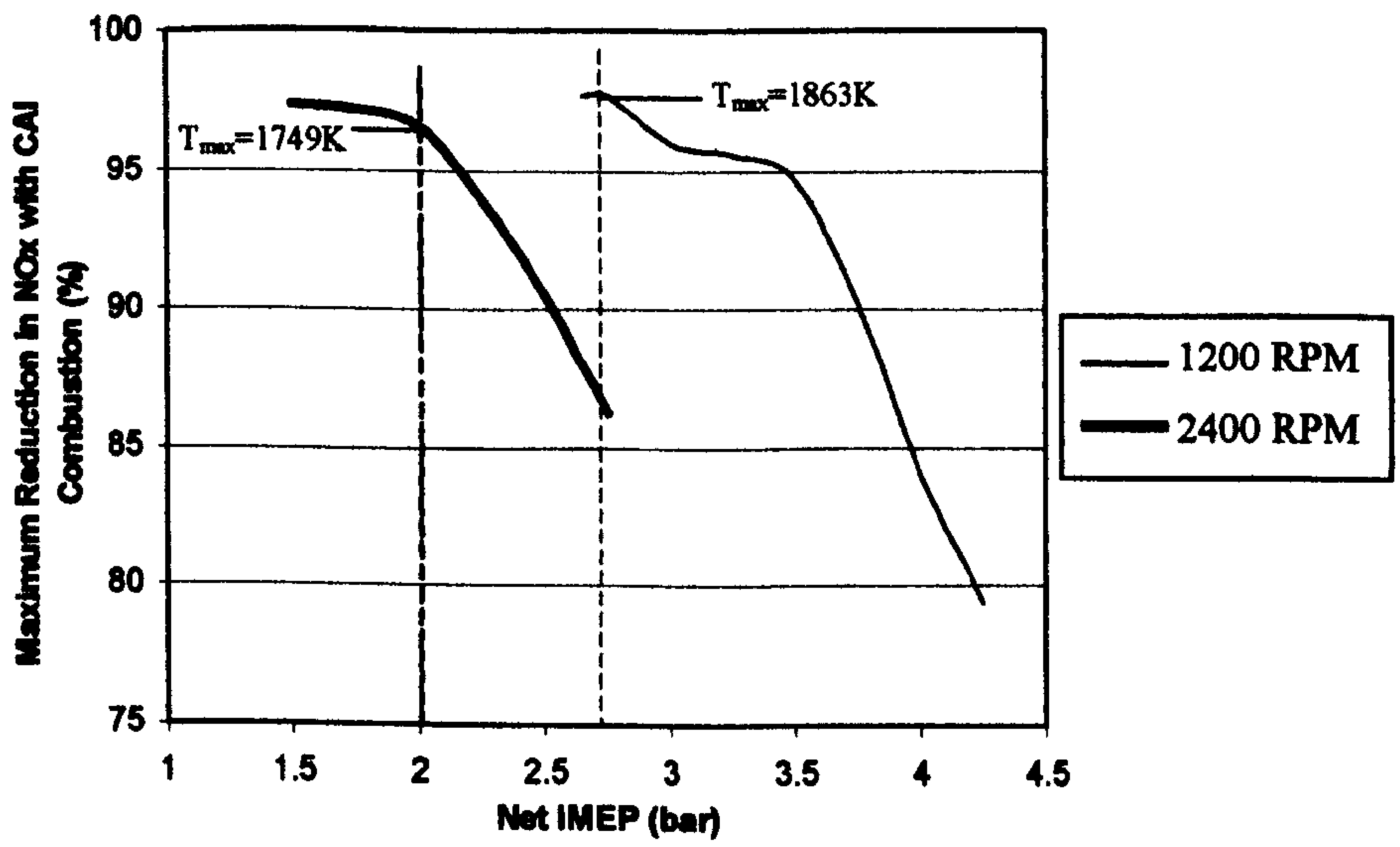

Figure 7.23 Maximum Reduction in NOx Emissions with CAI Combustion

7.4.5.3 Comparison of Unburned Hydrocarbons Emissions

Figure 7.24 shows that the maximum reduction in uHC emissions with CAI combustion was between 10 and 58%. Though this demonstrates the potential of CAI combustion to achieve low uHC emissions the comparison may not be completely fair since the effects of injection timing on SI combustion were not explored. In fact, with the low in-cylinder and exhaust gas temperatures experienced with CAI combustion, a reduction in uHC emissions was not anticipated.

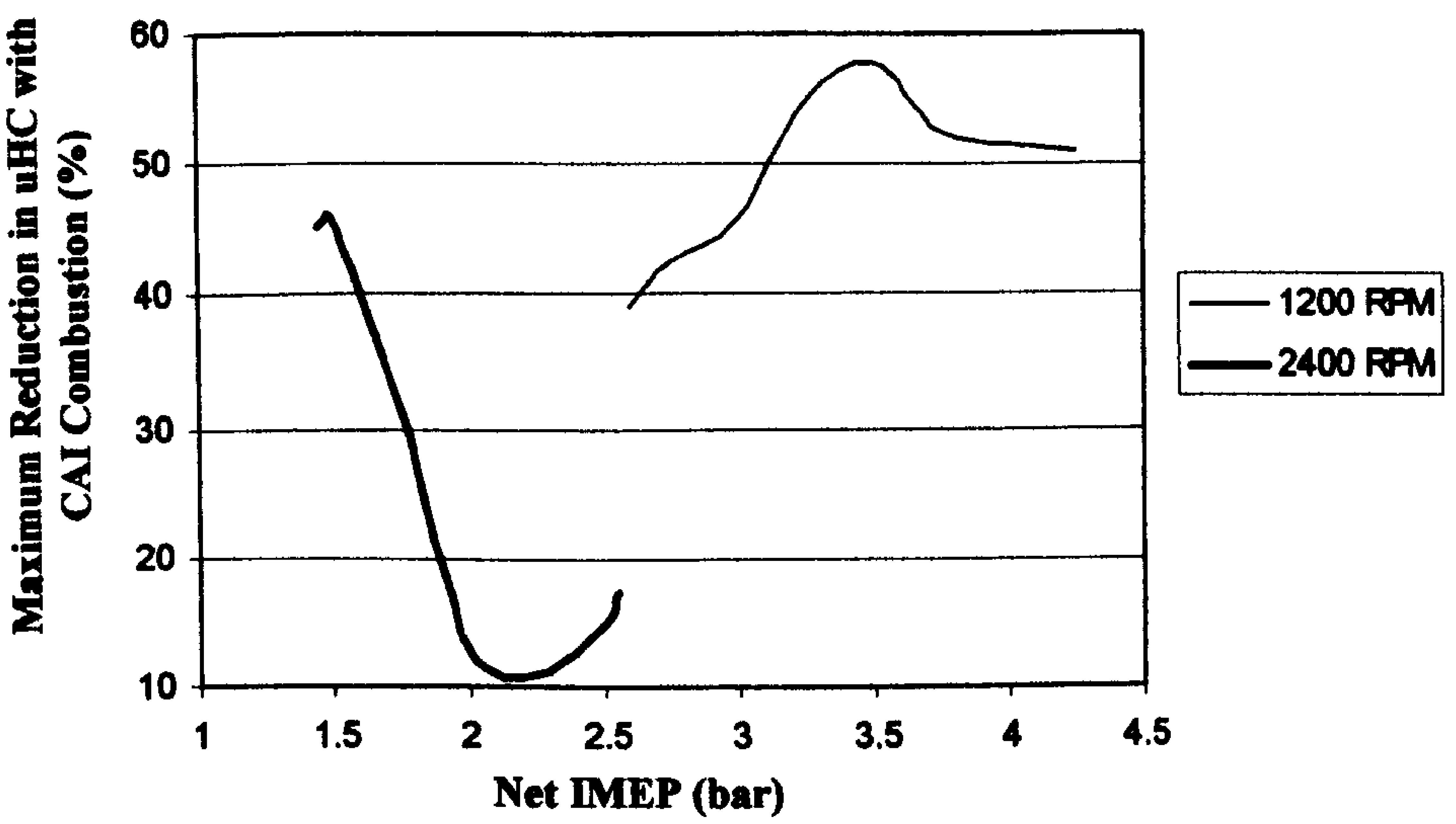

Figure 7.24 Maximum Reduction in uHC Emissions with CAI Combustion

7.4.5.4 Comparison of CO Emissions

Figure 7.25 shows the maximum reduction in CO emission with CAI combustion. The reduction achieved was between 34 and 87% depending on engine speed and load. At both of the tested engine speeds the biggest reductions were found around the middle of the load range.

In the high speed case the CO reduction steadily increases with load to the 2.5 bar IMEP operating point, then falls significantly as full load is reached. Since the CO emissions levels for SI combustion were relatively stable, the shape of the curve broadly represents the inverse of those found in Figure 7.21 for these operating conditions.

In a similar manner, the stable levels of CO production from the low speed SI operation across the load range mean that the shape of the curve can mainly attributed to the concentrations found with CAI operation, also shown in Figure 7.21.

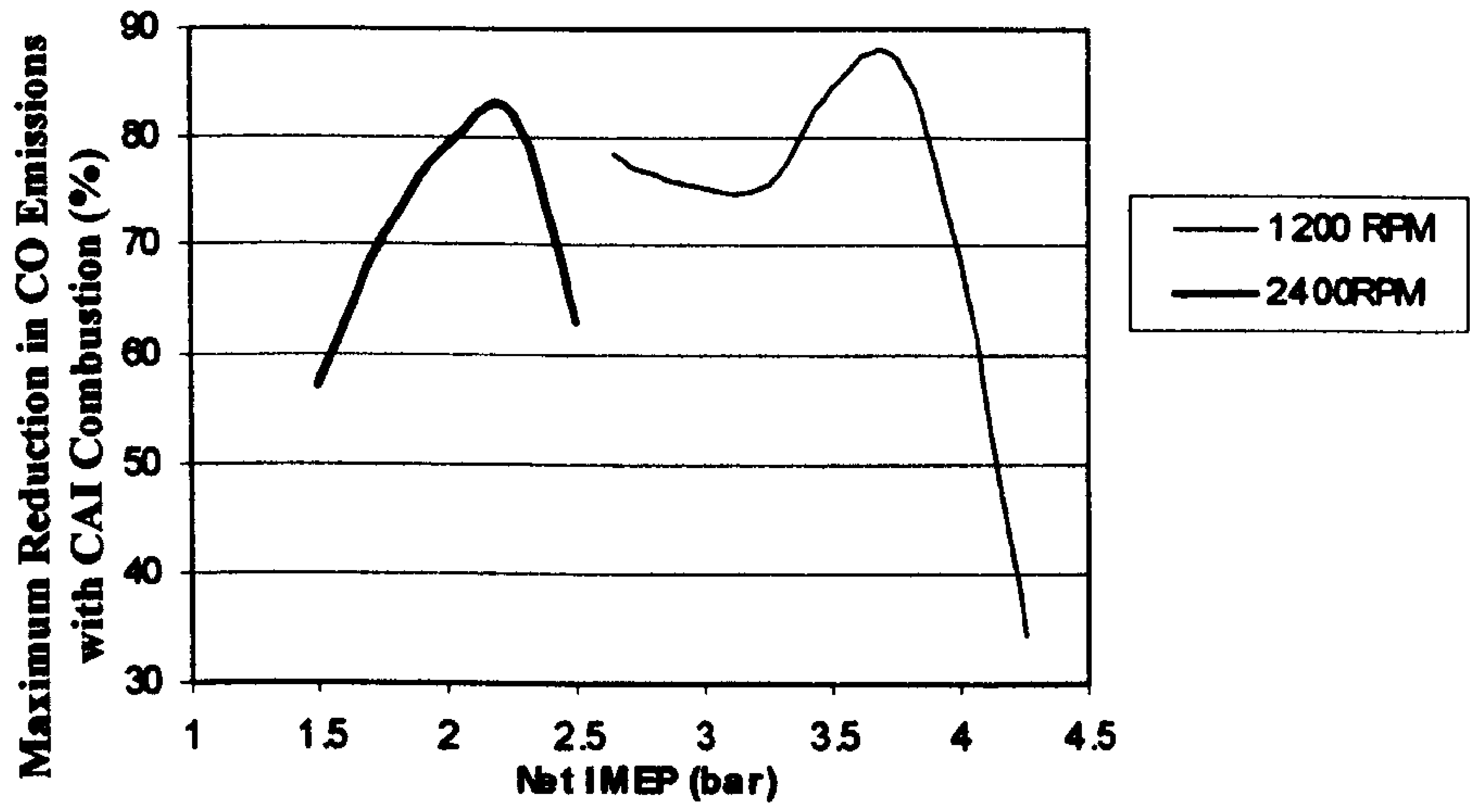

Figure 7.25 Maximum Reduction in ISCO Emissions with CAI Combustion

7.5 Summary

The intention of this section is to summarise the pertinent points arising from the analysis and discussion of the experimental data obtained from the CAI and SI engine tests.

i) As expected, engine load was most dependent upon EVC timing and the resulting amount of trapped residual gas. Operating ranges of 1 to 2.5 bar and 2.5 to 4 bar were attainable at 2400 RPM and 1200 RPM respectively. Injection at EVC extended the operating range due to increased mixture ignitability via fuel reformation activated by the high temperatures present. Injection during the recompression period also increased maximum load by up to 18%.

IVO timing was found to have a smaller effect on engine load than injection timing, although the IVO timing required to achieve maximum output varied according EVC timing.

ii) Ignition timing appears to be dependent on the amount of trapped gases and their temperature. If the amount of trapped gas is high, then their temperature is generally low and visa versa. It is a combination of these effects that appears to control ignition timing. Ignition generally occurred earlier at high speed, particularly at low load. Here the large amount of trapped residuals encourages early auto-ignition. As the load increases the amount of trapped residuals reduces, ignition is retarded. At low speed, ignition timing was generally most advanced in the middle of the load range and was retarded with both reducing and increasing loads due to reduction in the temperature and mass effects respectively.

Injection during the recompression process has two conflicting effects that can be used to influence ignition timing. Firstly, as already mentioned, the fuel can undergo a reformation process that increases its ignitabilty but, for this to be effective, the residual gases must be at a sufficiently high temperature. Secondly, injection into the residual gases lowers their temperature and pressure. This is turn admits more fresh charge further reducing the overall charge temperature and delaying ignition. At high speed, injection at EVC resulted in the most advanced ignition timing due the increased ignitabilty. However, it appears that the temperature threshold for reformation to take place was not reached during low speed operation and here injection at IVO, with an increased percentage of trapped gas, gave the most advanced ignition timing.

iii) Combustion duration appears to be directly related to ignition timing and, if ignition takes place just before or around TDC, combustion is likely to be fast. However, if levels of charge dilution from residual gases are high then this will slow the heat release rate, extending the combustion period.

iv) While combustion stability at low speed was good, at high speed it was only within acceptable limits over the whole load range when injection at IVO was employed.

v) Fuel consumption for CAI combustion was most influenced by combustion phasing and, to a lesser extent, pumping losses. At high speed and low load, the very early combustion had a large detrimental effect on fuel consumption. A reduction in fuel consumption of between 9% and 17% was realised with CAI combustion compared to SI operation. This was due to reduced pumping losses and faster combustion.

vi) NOx emissions with CAI combustion increased sharply with load and were directly linked to peak in-cylinder temperatures which in turn could be linked to combustion phasing.

With CAI combustion NOx emissions were reduced by 80% to 98% when compared to operation in the SI mode. This reduction can be attributed to the greatly reduced in-cylinder temperatures experienced with CAI combustion.

vii) Early injection resulted in the lowest levels of unburned hydrocarbons, with concentrations rising as injection was delayed. Since exhaust gas temperatures varied little with injection timing, the variations in uHC can be attributed to the amount of fuel left unburned, rather than the level of oxidation that takes place. The superior performance of early injection is most likely as a result of increased fuel ignitability due to its reformation in the recompression process, while later injection resulted in a less homogenous mixture and combustion of locally fuel rich mixtures in some areas.

With CAI, a maximum reduction in uHC emissions of between 10% and 58% was realised over SI combustion.

viii) Carbon monoxide emissions varied greatly with CAI combustion, with high levels present at low load, particularly at high speed. It is likely this was caused by incomplete bulk gas reactions due to low in-cylinder temperatures. Highest CO concentrations were generally found with late injection timing and this was probably due to fuel rich combustion in some areas due to the less homogenous charge. A reduction in CO emissions of between 34 and 87% was achieved with CAI combustion.

Chapter 8

Conclusions and Recommendations for Further Work

Chapter 8 Conclusions and Recommendations for Further Work

8.1 Conclusions

8.1.1 In-Cylinder Flow Field and Liquid Fuel Spray Measurement using Particle Image Velocimetry

A PIV system has been used to measure the in-cylinder flow conditions during the intake and compression strokes of the Ricardo Hydra engine fitted with a prototype Orbital GDI cylinder head. In addition, the technique was used to measure the liquid fuel spray from the Orbital air assisted injection system.

The in-cylinder airflow velocity maps showed that no significant large-scale vortices were formed and, as a result, no organised flow regimes such as swirl or tumble were witnessed. This is probably beneficial to the operation of the air-assisted injection system, since, being of the spray guided type, any such flows might disrupt the stratification that is desired during the late injection mode. The PIV system itself worked very well, giving detailed measurements of the in-cylinder conditions

Application of the PIV system to the fuel spray gave reasonable results. However, good data was often very sparse within the individual cycle velocity maps, meaning that fairly harsh data processing was required to obtain average images that could be considered representative. This meant that, while reasonable average flow maps could be obtained, most details of the spray were lost.

One of the objectives in this part of the study was to examine any interaction between the in-cylinder air motion and fuel spray. However, since the fuel spray does not appear to be particularly affected by the in-cylinder air motion, no further investigation was pursued.

8.1.2 Characterisation of In-Cylinder Fuel Distribution using Laser Induced Exiplex Fluorescence

A laser induced exciplex fluorescence system has been used to examine the in-cylinder fuel distribution in a single cylinder optical engine with a prototype cylinder head featuring an air-assisted injection system. Images of injected fuel in both its liquid and vapour phases were obtained. Initially, the dopants were excited using a laser sheet to give images of a thin plane passing through the spray. In an attempt to obtain images of the whole spray structure, experiments were also completed with expanded laser beams. The tests were completed using two different injection timings to represent homogenous and stratified charge modes.

During testing, problems were encountered with attenuation of the laser light due to absorption where high densities of vaporised fuel were present. For this reason, the expanded beam experiment was carried out 3 times with the laser beam entering the cylinder from a different direction on each occasion. Averaging the left and right illuminated images appears to be an effective means of approximating the true spray shape when severe laser attenuation is present. It offers the means to at least partially overcome the problem of laser absorption, without the need to supply the beam from both directions simultaneously.

The late injection timing produced a consistently narrow spray and good stratification. However, towards the end of the compression stroke, some of the stratification was lost, although it was felt that this could be improved by using a piston with a bowl in the crown

When using the early injection timing, the results were quite different. The spray was initially quite narrow but quickly developed into, what appeared to be, a wide cone. The last set of images shows that a fairly homogenous charge is left at the end of the compression stroke. This change of spray shape is a function of the cylinder pressure during the injection period.

When using the expanded beam with illumination from below, the liquid image apparently shows that liquid fuel is impinging the piston, while the horizontally illuminated images fail to show this. This maybe because the fluorescence is actually coming from fuel despotised on the piston surface and, since the piston window is very slightly recessed from the piston crown, may not experience excitation when the laser enters from the side.

A typical symptom of cross talking between the emissions of the two phases is appearance of the much stronger liquid fluorescence signal on vapour side. Inspection of the results show significant differences between the images of the two phases, suggesting that cross talking is not a serious problem in this case.

During the analysis of the results, some anomalies were found to exist between the different measurement planes and illumination methods, the reasons for which are not clear. It is felt that additional experiments would be needed, while paying extra attention to these problems, to provide answers to this.

8.1.3 Engine Experiments with CAI Combustion

CAI combustion was realised in the Ricardo Hydra engine by trapping large amounts of exhaust gas through early exhaust valve closure. The effects of valve and injection timing and engine speed on exhaust emissions, fuel consumption and operating range were explored. Tests on the same engine with SI combustion were then completed to allow comparison of the two combustion types.

8.1.3.1 Effect of Injection Timing

Injection timing was found to affect all aspects of CAI combustion including engine output, combustion stability, fuel consumption and emissions. These effects can be categorised as follows:

Combustion Phasing Effect

Under certain conditions, injection during the recompression phase can be used to increase fuel ignitability and advance ignition timing. For maximum efficiency, combustion should be rapid and occur around TDC. However, high heat release rates from rapid combustion result in high peak cylinder pressures and temperatures, leading in high NOx emissions. Over advanced ignition harms fuel consumption through increased negative work on the piston and also leads to very fast combustion, which increases NOx emissions through high in-cylinder temperatures. In this work combustion phasing did not appear to have a large effect on uHC emissions.

Mixture Quality Effect

Earlier injection tends to result in a more homogenous mixture, better combustion quality and less fuel quenching, reducing uHC and CO emissions. The poor combustion with late injection resulted in high fuel consumption due to the large amount of unburned fuel in the exhaust stream.

Charge Cooling Effect.

Early injection can increase engine output through maximisation of the charge cooling effect. However, this tends to lead to an increase in pumping work, damaging fuel consumption.

From this it can be concluded that, although injection timing is a very useful as a means of controlling CAI combustion, its use results in a number of trade-offs between exhaust emissions, engine output and efficiency. However, targeted use of each injection strategy according to operating conditions could result in much improved overall performance. Additionally, the use of a split injection strategy might allow the compromises to be lessened.

8.1.3.2 Effect of Valve Timing

With CAI combustion, engine load was most dependent upon EVC timing and the resulting amount of trapped residual gas. However, intake valve timing played an important part in charge formation and the phasing of the resulting combustion. This appears to stem from its role in creating different in-cylinder distributions of exhaust gas and fresh charge by varying the amount and type of back flow either side of the intake process. Estimations of the overall (homogenous) charge temperature at IVC showed that the overall temperature of the charge was not a major factor in controlling ignition timing, prompting the assertion that the type and level of stratification of residual gases wasimportant to the performance of the engine. The changes in combustion phasing, brought about by variation in IVO timing, were also found to affect NOx formation and fuel consumption.

8.1.3.3 Effect of Engine Speed

The main effect of engine speed was on the amount of residual gas trapped in the cylinder. The reduced time available for the gas exchange process at high speeds resulted in high levels of trapped gas for any given EVC timing. The extra trapped gas and reduced time available for heat loss often caused the ignition timing to be very advanced at high engine speed, increasing fuel consumption through extra negative work on the piston.

8.1.3.4 Comparison with SI Combustion

A reduction in fuel consumption of between 9% and 17% was realised with CAI combustion compared to SI operation. This was due to reduced pumping losses and faster combustion.

With CAI combustion, NOx emissions were reduced by 80% to 98% when compared to operation in the SI mode. This reduction can be attributed to the greatly reduced in-cylinder temperatures experienced with CAI combustion. A maximum reduction in uHC emissions of between 10% and 58% was realised with CAI over SI combustion, while CO emissions were reduced by between 34 and 87%.

8.2 Recommendations for Further Work

8.2.1 In-Cylinder Flow Field and Liquid Fuel Spray Measurement using Particle Image Velocimetry

As already discussed, the inclusion the fuel injection event in the airflow PIV experiments might allow any intrusion of the fuel spray into the in-cylinder airflow to be better assessed. These experiments could be easily completed using the equipment already available.

Since the PIV results obtained here were completed using the 'full lift' production type camshafts, it would be interesting to see how the CAI short duration camshafts affect the in-cylinder airflow. Again, this could be completed without any modifications or extra equipment.

Further use could be made of the PIV system as part of an investigation into the trapped and fresh gas stratification present during the CAI combustion. If a seeding material is chosen that can withstand temperature of the residual gases and the compression event, but is destroyed by the combustion (so is subsequently absent from the residual gas) it may be possible to obtain a clear picture of the mixing and stratification phenomena. In addition, information of the intake air flow-field and fuel spray motion could be gained. Since the illumination would be via a laser sheet, this would allow certain planes to be isolated and measured as desired. However, in order to allow PIV measurements to be taken in a fired engine, the optical configuration used previously would require significant upgrading to withstand the elevated temperatures and pressures of combustion.

8.2.2 Characterisation of In-Cylinder Fuel Distribution using Laser Induced Exiplex Fluorescence

One obvious limitation of the LIEF system presented here is its inability to provide quantitative measurements of air fuel ratio. Therefore, the development of such a system could yield much useful and detailed information on the in-cylinder conditions.

Even as a qualitative system, its application to a fired GDI CAI engine could provide a large amount of information relating to the fuel evaporation process, charge stratification and ignition and combustion behaviour. However, as with the PIV system, the engine would require substantial reworking to allow optical accesses to be used in the fired engine.

8.2.3 Engine Experiments with CAI Combustion

While analysis of the engine test data yielded some interesting discoveries, many phenomena could not be easily or fully explained. Also, the research has prompted many questions that had not been considered before the work was undertaken. In addition, due to time constraints, the potential effect of many available control parameters were either only partially explored or ignored completely. For these reasons, completion of following additional work should provide much in the way of useful and interesting data:

i) One of the main conclusions to be drawn from this part of the project is just how the important the interaction between the residual and fresh gases is to the subsequent CAI combustion. However, with the data available at this time, it is almost impossible to extend this conclusion by commenting on the specific effects of such phenomena as backflow and stratification. Therefore, further work would be necessary to improve understanding in this area. Much of the work could be completed by CFD modelling of the gas exchange process and subsequent combustion, though this would require validation with data from equivalent experimental work using a fired optical engine. Completion of this experimental work would require the engine to be significantly reworked in order to allow the use of optical accesses within the combustion environment. The main purpose of the extra tests would be to try and establish if and how stratification of the fresh and residual charge affects CAI combustion. This could be achieved by applying the PIV and LIEF techniques to the intake, injection and compression events.

ii) This study has found that injection timing has a significant effect on many aspects of CAI engine performance. However, due to time constraints it was only possible to perform tests with 3 injection timings. Therefore, a better understanding of injection timing effects could be gained by repeating the tests over a bigger range of injection timings. Another possibility would be to split the injection into two (or more) events throughout the available injection window, since, for example, this might allow some of the advantages of early and late injection to be enjoyed simultaneously.

iii) During this work, the amount of IVO/EVC combinations that could be tested was limited. However, the apparent significance of the early and late backflow phenomena on the final charge state would suggest that this could be an area well worth expanding upon.

iv) One important engine control variable not exploited in this work due to time constraints was the modulation of AFR. Though minor fuel consumption benefits may arise from increasing the AFR, due to increased cycle efficiency, it is most likely to be of benefit as extra means of controlling combustion phasing, both in terms of ignition timing and burn duration. This would allow more optimal tuning of the system, with the potential to provide a better trade off between the various emissions and fuel efficiency.

References

1. "Climate Change UK Programme", UK Department of the Environment Transport and the Regions, February 2001

2. "The Kyoto Protocol to the United Nations Framework Convention on Climate Change" UNFCCC Document No. FCCC/CP/1997/Add.1, March 1998

3. Euro III-V legislated emissions levels, Vehicle Certification Agency (VCA), obtained from http://www.carfueldata.org.uk/ June 2004

4. "California Exhaust Emissions Standards and Test Procedures for 2004 and Subsequent Model Passenger Cars. Light Duty Trucks and Medium Duty Vehicles, California Environmental Protection Agency Air Resources Board" (CARB), June 2004

5. Johnson, T. V., "Mobile Emissions Control technologies in review, International Conference on 21st Century Emissions Technology." IMechE Conference Transactions 2000-2, ISBN 186058 322 9 , 2000

6. Hentschel, W. "Optical Diagnosis for combustion process development of direct-injection gasoline engines." Proceedings of the combustion institute, volume 28, 2000/pp. 119-1135

7. Weiss, M., Heywood , J., et al., "On the Road in 2020: A Life Cycle Analysis of New Automobile Technologies," MIT Energy Laboratory Report EL00-003, MIT, Cambridge, MA. 2000

8. Stone, R,. "Introduction to internal combustion engines", Third Edition, p.171, Macmillan Press, ISBN 0-333-86058 322 9, 2000

9. Searles, R.A., "Emission catalyst technology – challenges and opportunities in the 21st century." International conference on 21st century emissions technology, IMechE, Conference Transactions 2000-2, ISBN 1 86058 322 9, 2000

10. Salvat, O., et al., "Passenger car serial application of a particulate filter system on a common rail direct injection diesel engine," SAE paper 2000-01-0473, 2000

11. Oppenheim, A. K., "The knocking syndrome: its cures and its victims," SAE paper 841339, 1984

12. Onishi, S., Hong Jo, S., Shoda, K., Do Jo, P. and Kato, S., "Active thermo-atmosphere combustion (ATAC) – A new combustion process for internal combustion engines," SAE paper 790507, 1979

13. Noguchi, M., Tanaka, Y., Tanaka, T., Takeuchi, Y., "A study on gasoline engine combustion by observation of intermediate reactive products during combustion," SAE paper 790840, 1979

14. "Honda readies activated radical combustion two-stroke engine for production motor-cycle," Automotive Engineer, pp.90-92, SAE publications, January 1997

15. Shawcross, D., Pumphrey, C. and Arnall, D., "A five million kilometre, 100 vehicle fleet trial of an air assisted direct fuel injected, automotive 2-stroke engine," SAE paper 2000-01-0898, 2000

16. Najt, P. M. and Foster, D. E., "Compression-ignited homogenous charge combustion," SAE paper 830264, 1983

17. Lavy, J., Dabadie, J., Angelberger, C., Duret, P. (IFP), Willand, J., Juretzka, A., Schaflien, J. (Daimler Chrysler), Ma, T. (Ford), Lendress, Y., Satre, A.(PSA Peugeot Citroen), Shultz, C., Kramer, H. (PCI – Hiedelberg University), Zhao, H., Damiano, L. (Brunel University), "Innovative ultra-low NOx controlled auto-ignition combustion process for gasoline engines: the 4-SPACE project," SAE paper 2000-01-1837, 2000

18. Pucher, G. R., Gardiner, D. P., Bardon, M. F. and Batissa, V., "Alternative combustion systems for piston engines involving homogenous charge compression ignition concepts – a review of studies using methanol, gasoline and diesel fuel," SAE paper 962063, 1996

19. Olsson, J. Johansson, B., "Closed loop control of an HCCI engine," SAE paper 2001-01-1031, 2001

20. Urushihara, T., Hiraya, K., Kakuhou, A., Itoh, T., "Expansion of HCCI operating region by the combination of direct injection, negative valve overlap and internal fuel reformation," SAE paper 2003-01-0749, 2003

21. Aoyama, T., Hattori, Y., Mizuto, J., Sato, Y., "An experimental study on premixed-charge compression ignition gasoline engine," SAE paper 960363, 1996

22. Li, J., Zhao, H., Ladommatos, N. and Ma, T. "Research and development of a controlled auto-ignition (CAI) combustion in a 4-stroke multi-cylinder gasoline engine" SAE Paper 2001-01-3608, 2001

23. Koopmans, L., Strom, H., Lundgren, S., Backlund, O and Denbratt, I., "Demonstrating a SI-HCCI-SI mode change on a Volvo 5-cylinder electronic valve control engine," SAE Paper 2003-01-0753.

24. Aoyama, T., Hattori, Y., Mizuto, J., Sato, Y., "An experimental study on premixed-charge compression ignition gasoline engine," SAE paper 960363, 1996

25. Christensen, M. and Johansson, B., "Influence of mixture quality on homogenous charge compression ignition", SAE paper 982454, 1998

26. Oakley, A., "Experimental investigations on controlled auto ignition combustion in a four-stroke engine," PhD Thesis, Brunel University, 2001

27. Christensen, M., Hultqvist, A, and Johansson, B., "Demonstrating the multi fuel capability of a homogenous charge compression ignition engine with variable compression ratio," SAE paper 1999-01-3679, 1999

28. Sjoberg, M., Edling, L., Eliassen, T., Magnusson, L. and Angstrom, H., "GDI HCCI: Effects of injection timing and air swirl on fuel stratification, combustion and emissions formation." SAE paper offer #02P-27

29. Li, Y., Zhao, H., Peng, Z., Ladommatos, N., "Particle image velocimetry measurement of in-cylinder flow in internal combustion engines - experiment and flow structure analysis", Proc Instn Mech Engrs Vol. 216 Part D

30. Thring, R. H., "Homogenous-charge compression – ignition engines," SAE paper 892068

31. Flowers, D., Aceves, S., Smith. R., Torres, J., Girard. J, and Dibble, R., "HCCI in a CFR engine: experiments and detailed kinetic modelling," SAE paper 2000-01-0328, 2000

32. Duret, P. and Lavy, J., "Process for controlling self-ignition in a 4-stoke engine," US patent 6 082 342

33. Zhao, H., Li, J., Ma, T. and Ladommatos, N., "Performance and analysis of a 4-stroke multi –cylinder gasoline engine with CAI combustion" SAE paper 2002-01-0420, 2001

34. Hultqvist, A., Christensen, M., Johansson, B., "The application of ceramic and catalytic coatings to reduce the unburned hydrocarbon emissions from a homogenous charge compression ignition engine," SAE Paper offer # 00FL-185

35. Li, Y., Zhao, H,. Peng, Z,. Ladommatos, N. "Analysis of a tumble and swirl motions in a four-valve SI engine", SAE paper 2001-01-3555

36. Hutchison, A., Wicker, R., "DISI fuel spray effects during simulated injection timing", SAE paper 2001-01-2026

37. Liou, T. –M. and Santavicca, D. A. , "Cycle resolved LDV measurements in Motored IC engine." Trans. AMSE, J. Fluids Engng, June 1985, 107, 232-240

38. Fansler, T. D. and French, D. T. , "Cycle-resolved laser velocimetry measurements in reentrant-bowl-piston engines." SAE paper 880377, 1988

39. Glover, A. R., Hundleby , G. E and Hadded, O., "The development of scanning LDA for the measurement of turbulence in engines." SAE trans. J. engines, 1988, 97, 6.604 – 6.616

40. Fraser, R. A. and Bracco, F. V. "Cycle-resolved LDV integral length-scale measurements in an IC engine." SAE paper 88021, 1988

41. Lorenz, M. and Presher, K. "Cycle resolved LDV measurements on a fired SI engine at high data rates using a conventional modular LDV system." SAE paper 900054, 1990

42. Lee. D. W., "A Study of airflow in an engine cylinder," NACA report 653, 1939

43. Ronnback, M., Wang, X. L. and Linna, J. R. "Study of induction tumble by particle tracking velocimetry in a 4-valve engine." SAE paper 912376, 1991

44. Neuber, H. J., Spiegel, L. and Ganser, J. "Particle tracking velocimetry, a power tool to shape the in-cylinder flow of modern multi-valve engine concepts." SAE paper 950102

45. Fan. L., Reitz, R. D. and Trigui, N. "Intake flow simulation and comparison with PTV measurements." SAE paper 1999-01-0176, 1999

46. Reuss, D. L., Adrian, R. J., Landreth, C. C., French D. T. and Fansler, T. D. "Instantaneous planar measurements of velocity and large-scale vorticity and strain rate in an engine using particle image velocimetry." SAE paper 890616, 1989

47. Nino, E., Gajdeczko, B. F. and Felton, P. G. "Two-color particle image velocimetry in an engine with combustion." SAE paper 930872

48. Reeves, M., Garner, C. P., Dent, J. C and Halliwell, N. A. "Particle image velocimetry measurements of in-cylinder flow in a multi-valve internal combustion engine." Instn Mech Engrs, Part D, Journal of Automobile Engineering 1996, 210 (D), 63-70

49. Khalighi, B, and Huebler, M. S. "A transient water analogue of a dual-intake-valve engine for intake flow visualisation and full field velocity measurements." SAE paper 900059, 1990

50. Shack, D. H and Reynolds, W. C. "Application of particle tracking velocimetry to the cyclic variability of the pre-combustion flow field in a motored axisymmetric engine." SAE paper 910475, 1991

51. Church, W. and Farrell, P. V. "Effects of intake port geometry on large scale in-cylinder flows," SAE paper 980484, 1998

52. Reuss, D. L., Bardsley, M. ., Felton, P. G., Landreth, C. C. and Adrian, R. J. "Velocity, Vorticity and strain rate ahead of a flame measured in an engine using particle image velocimetry." SAE paper 900053, 1990

53. Li. Y., Zhao, H., Leach, B., Ma. T., and Ladommatos, N. "Optimisation if in-cylinder flow for fuel stratification in a three-valve twin-spark-plug engine." SAE paper 2003-01-0635, 2003

54. Rouland, E., Trinite, M., Dionnet, F., Floch, A. and Ahmed, A. "Particle image velocimetry in a high tumble engine for in-cylinder flow structure analysis." SAE paper 972831, 1997

55. Arcoumanis, C., Green, H. G. and Whitelaw, J. H., "Velocity and concentration measurements in a model diesel engine." Expts fluids, 1985, 3, pp. 270-276

56. Arcoumanis, C., Whitelaw, J. H. and Wong, K. Y. "Gaseous simulation of diesel engine sprays." SAE paper 890793, 1989

57. Green, H. G., Whitelaw, J. H. and Wong, K. Y. "Air fuel mixture characteristics of reciprocating engines. Combustion. Science and Technology." 1988, 59, pp. 225-246

58. Kadota, T., Zhao, F.-Q. and Miyoshi, K., "Rayleigh scattered measurements of transient fuel vapour concentration in a motored SI engine." SAE paper 900481, 1990

59. Zhao, F.-Q., Kadota, T. and Takemota, T. "Rayleigh scattered measurements of transient fuel vapour concentration fluctuation in a motored SI engine," Proc. Int. Symp. Comodia 90, pp. 377-382

60. Espey, C., Dec, J., Litzinger, T. A and Santavicca, A. "Quantitative 2D Fuel Vapour concentration imaging in a firing DI diesel engine using planar laser induced Rayleigh spectroscopy." SAE paper 940682, 1994

61. Johnston, S. C. "Pre-combustion fuel /air distribution in a stratified charge engine using laser Raman spectroscopy." SAE paper 791433, 1979

62. Johnston, S. C. "Raman spectroscopy and flow visualisation of stratified charge engine combustion." SAE paper 800136, 1980

63. Miles, P. and Dilligan M., "Quantitative in-cylinder fluid composition measurements using broad band spontaneous Raman scattering." SAE paper 960828, 1996

64. Heinze, T. and Schmidt, T. "Fuel air ratios in a spray, determined between injection and auto ignition by pulsed spontaneous Raman scattering," SAE paper 892102, 1989

65. Zhao, F.-Q., Taketomi, M., Nishida, H. and Hiroyasu, H. "PLIF measurements of the cyclic variation of mixture concentration in an SI engine." SAE paper 940988, 1994

66. Baritaud, T. A. and Heinze, T. A. "Gasoline distribution measurements with PLIF in a SI engine," SAE paper 922355, 1992

67. Deschamps, B., Snyder, R. and Baritaud, T., "Effect of flow and gasoline stratification in a four-valve SI engine, " SAE paper 941993, 1994

68. Nakada, T., Kokita, H. and Itoh, T. Comodia 94, pp. 177-182, 1994

69. Urushihara, T., Nakata, T., Kaduhou, A. and Takagi, Y., JSAE review, 1996, 17, pp. 239-244

70. Hishinuma, T., Urushihara, T., Kaduhou, A and Itoh, T., JSAE Review, 1996, 17, pp. 239-359

71. Diwakar, R. Fansler D. T, . French D. T. , Ghandhi, J. B. , Dasch, C. J. and Heffelfinger, D. M. "Liquid and vapour fuel distributions from an air-assist injector – an experimental and computational study." SAE paper 920422, 1992

72. Shimizu, R., Matumoto, S., Furuno, S., Murayama, M., and Kojima, S. "Measurement of air-fuel mixture distribution in a gasoline engine using LIEF technique." SAE Paper 922356, 1992

73. Kim, J. U., Golding, B. "Exiplex fluorescence visualisation systems for pre-combustion diagnostics of an automotive gasoline engine." SAE paper 960826, 1996

74. Münch, K. U., Krämer, H. and Leipertz, A. "Investigation of fuel evaporation inside the intake of a SI engine using laser-induced exiplex-fluorescence with a new seed." SAE paper 961930, 1996

75. Fröba, A. P., Rabenstein, F., Münch, K. U. and Leipertz, A. "Mixture of triethylamine (TEA) and Benzene as a new seeding material for the quantitative two-dimensional laser-induced exiplex fluorescence imaging of vapour and liquid fuel inside SI engines." Combustion and flame 112: 199-209 (1998)

76. Ipp, W., Wagner, V., Krämer, H., Wensing, M. and Leipertz, A. "Spray formation of high pressure swirl gasoline injectors investigated by two-dimensional mie and LIEF techniques." SAE paper 1999-01-0498, 1999

77. Kornmesser, C., Müller, T., Beushausen, V. "Applicability of different exiplex tracers and model fuels for investigation of mixture formation in direct injection gasoline engines." Fifth international symposium on diagnostics and modelling of combustion in internal combustion engines, 2001

78. Melton, L, and Verdiect, J. "Vapour/liquid visualisation in fuel sprays, proceedings of 20th symposium (Int.) on combustion," pp. 1283-1290, 1984

79. Melton, L, and Verdiect, J. "Vapour/liquid visualisation in fuel sprays Combustion, science and technology," Volume 42, pp. 217-222, 1985

80. Bardsley, M., Felton, P. and Bracoo, F., "2-D visualisation of a hollow cone spray in a cup-in-head, ported, IC engine," SAE paper 880521, 1988

81. Tabata, M. , Kataoka, M. , Tanaka, T. and Yamakawa, M. "Measurement of fuel distribution in the piston cavity of direct injection SI engine by using LIF." SAE paper 2000-01-0240, 2000

82. Fujimoto, M. and Tabata, M. "Effect of swirl rate on mixture formation a spark ignition engine based on 2-D laser visualisation technique." SAE paper 931905, 1993

83. Melton, L. A. "Final report to the Texas higher education co-ordinating board, energy research applications program," contract 27, 1993

84. Law, C, K., "Some recent advances in droplet combustion, AIP conference proceedings," 197, pp. 321-337, 1989

85. Ghandhi, J. B., Felton, P. G., Gajdeczko, B. F. and Bracco, F. V. "Investigation of the fuel distribution in a two-stroke engine with an air-assisted injector," SAE paper 940394, 1994

86. Shimizu, R., Matumoto, S., Furuno, S., Murayma, M. and Kojima, S. "Measurement of air fuel mixture distribution in a gasoline engine using LIEF technique." SAE paper 922356

87. Reeves, M., Garner, C.P., Dent, J.C. and Halliwell, N.A., "Study of barrel swirl in a four-valve optical engine using particle image velocimetry", Comodia 1994

88. Raffel, M,. Willert, C.E. and Kompenhaus, J. "Particle Image Velocimetry", Springer, Hiedelberg

89. Westerweel, J., Darbiri, D., and Gharib, M., "The effect of a discrete window offset on the accuracy of cross correlation analysis of PIV Recordings", Exp. Fluids Vol. 23, 1997

90. Zhao, H. and Ladommatos, N., "Engine Combustion Instrumentation and Diagnostics", p. 74, ISBN 0-7680-0665-1, SAE International, 2001

91. Piepmeier, E.H. " Theory of laser-saturated atomic resonance fluorescence", Spectrochimica Acta, Vol27B pp 431-433, 1972

92. Stone, R,. "Introduction to internal combustion engines", third edition, p.526, Macmillan Press, ISBN 0-333-86058 322 9, 2000

93. Randolph, A., "Methods of processing cylinder pressure transducer signals to maximise data accuracy," SAE Paper 900170

94. Stone, R,. "Introduction to internal combustion engines", third edition, p.151, Macmillan Press, ISBN 0-333-86058 322 9, 2000

95. Zhao, H., Peng, Z., Williams, J. and Ladommatos, N., "Understanding the effects of recycled burnt gases on the controlled auto-ignition (CAI) combustion in a 4-stroke gasoline engines", SAE paper 2001-01-3607, 2001

96. Stone, R,. "Introduction to internal combustion engines", third edition, p.99, Macmillan Press, ISBN 0-333-86058 322 9, 2000

Appendix A Engine Component Detail Drawings

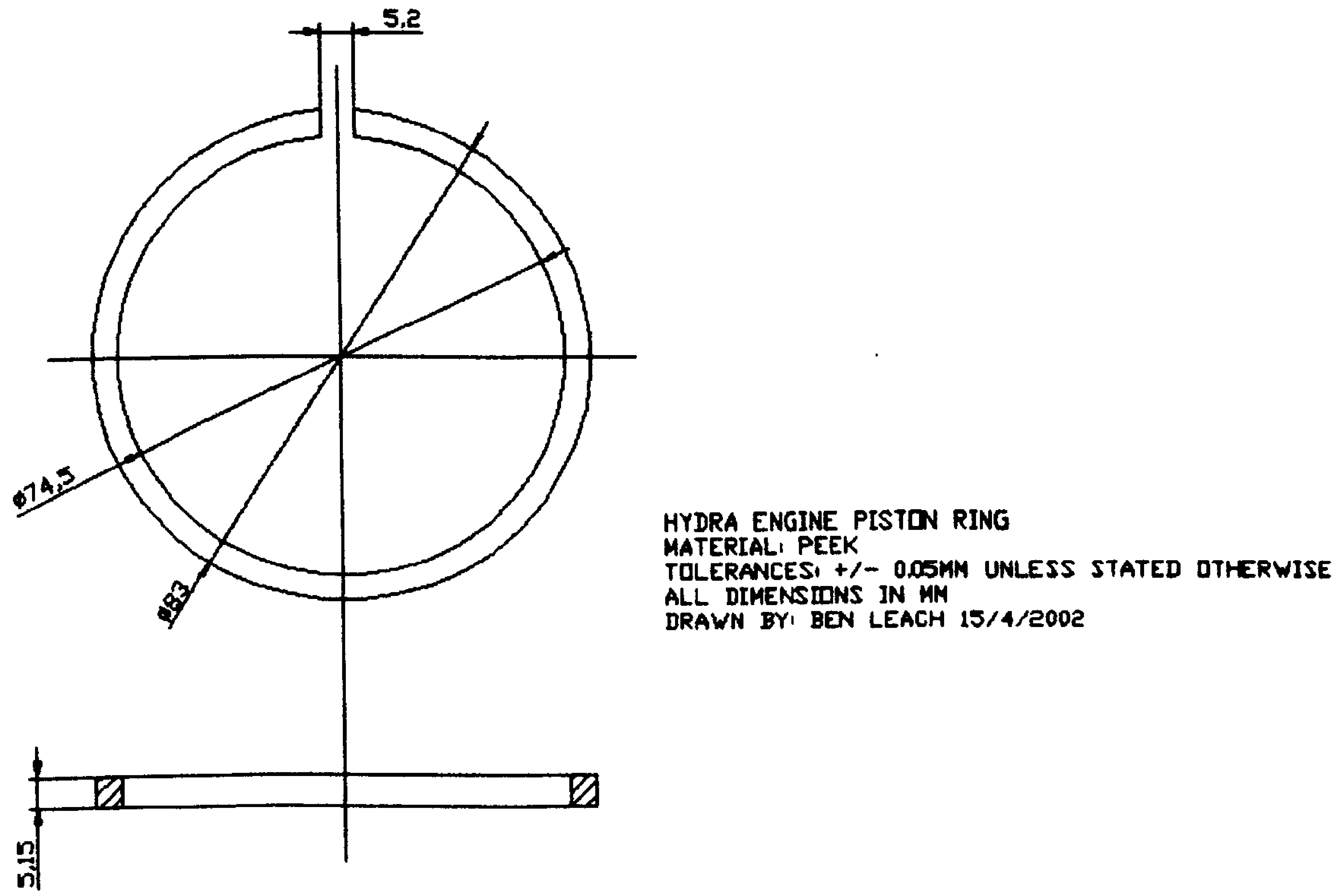

Figure A1 Detail Drawing of 'PEEK' Piston Rings

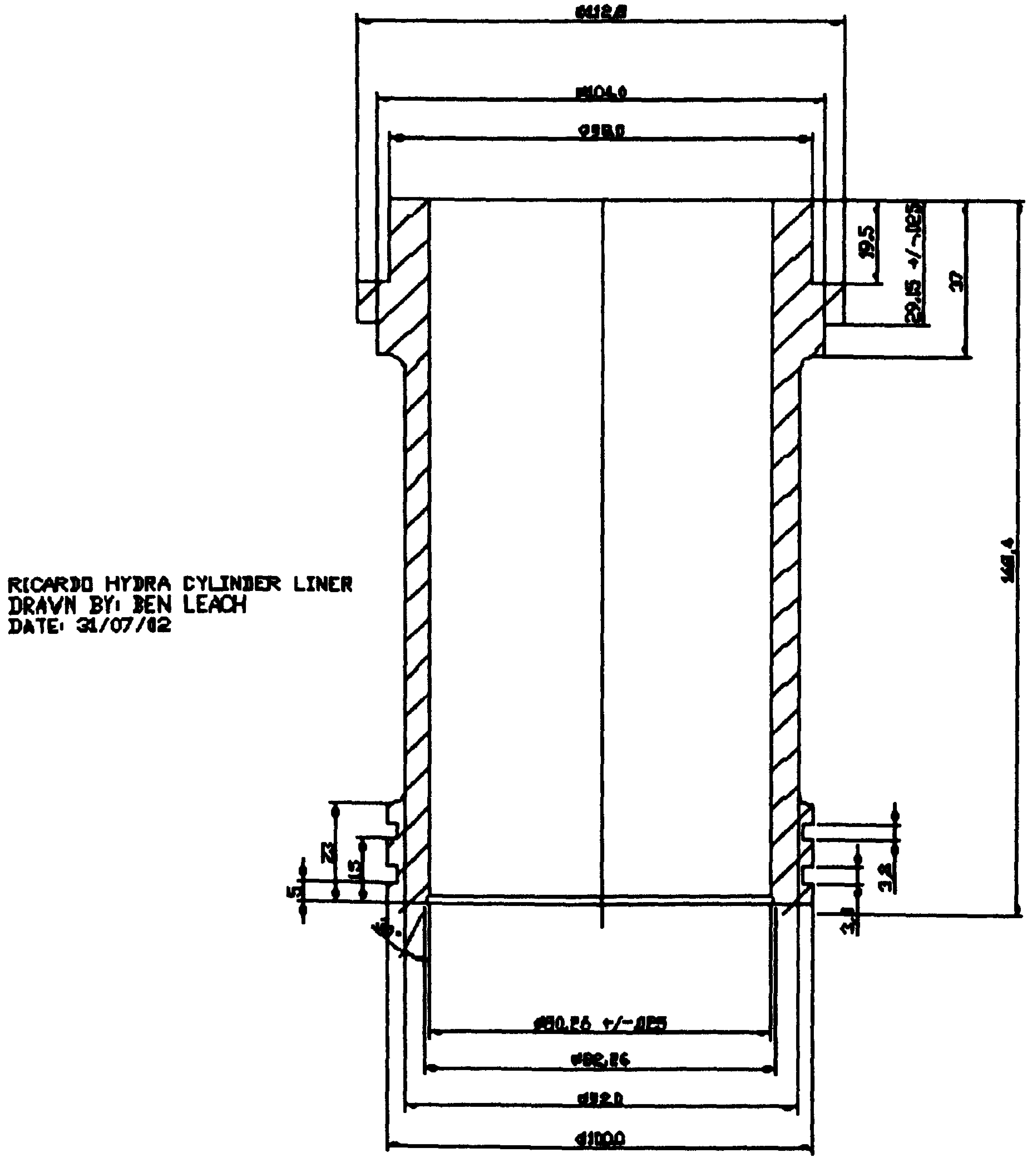

Figure A2 **Detail Drawing of Cylinder Replacement Cylinder Liner**

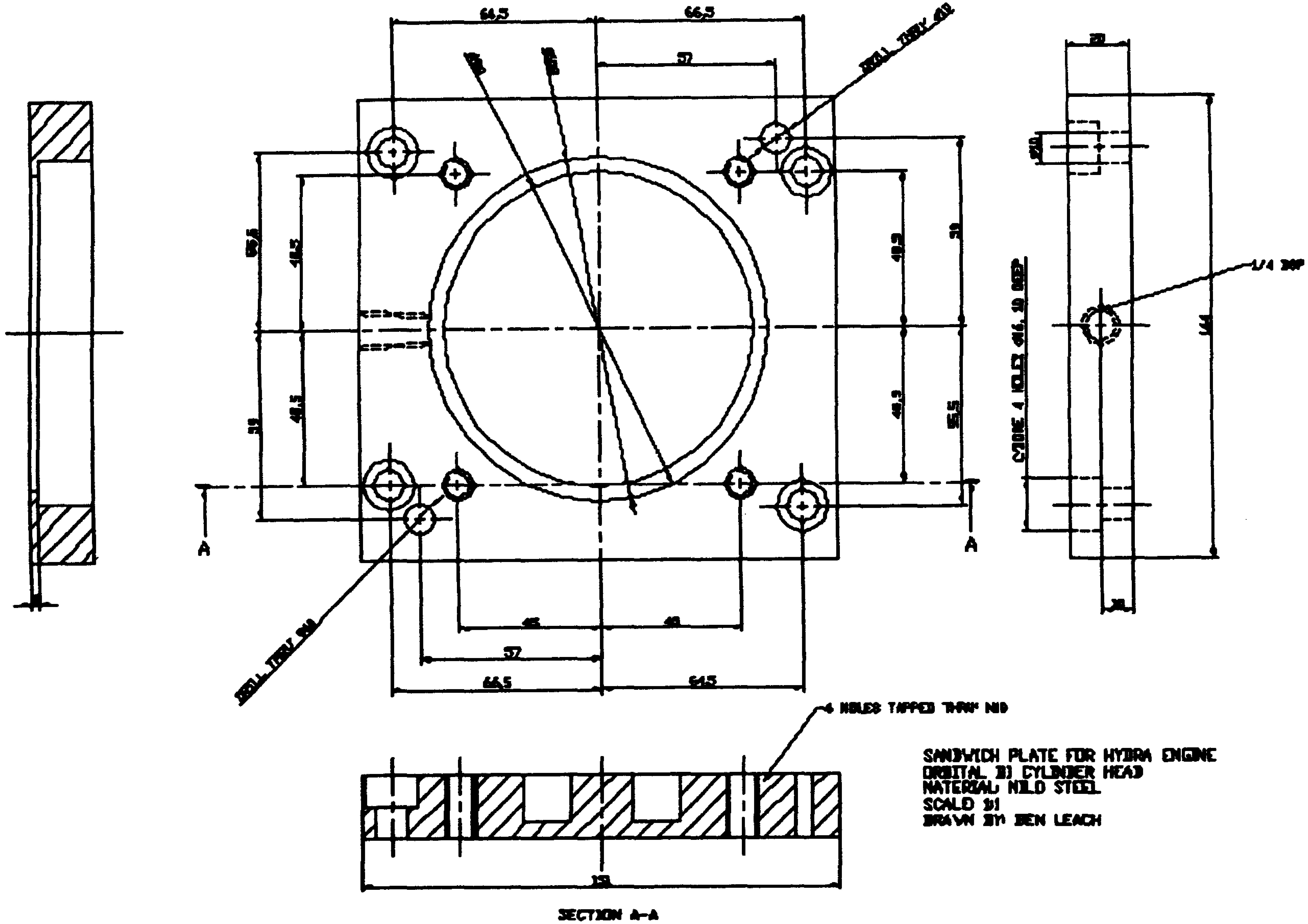

Figure A3 **Detail Drawing of Cylinder Head Sandwich Adaptor Plate**